# Multi-scale analysis of the mechanics of branched actin material.

Magid Badaoui

## To cite this version:

Magid Badaoui. Multi-scale analysis of the mechanics of branched actin material.. Biological Physics [physics.bio-ph]. Université Paris Cité, 2023. English. NNT : 2023UNIP7074 . tel-04544187

HAL Id: tel-04544187
https://theses.hal.science/tel-04544187

Submitted on 12 Apr 2024

## Université Paris Cité

École doctorale Physique en Île-de-France n°564

Institut Jacques Monod - UMR 7592

Équipe *Organisation spatiale de la cellule*

# Multiscale analysis of the mechanics of branched actin material

Par **Magid BADAOUI**

Thèse de doctorat de **Physique**

Dirigée par **Serge DMITRIEFF**

Présentée et soutenue publiquement le 24/11/23 devant un jury composé de :

| | | | |
|---|---|---|---|
| Verena RUPRECHT | Directrice de Recherche | CRG Barcelone | *Rapportrice* |
| Ulrich SCHWARZ | Professeur d'Université | Université d'Heidelberg | *Rapporteur* |
| Andrew CALLAN JONES | Chargé de Recherche | MSC | *Examinateur* |
| Olivia DU ROURE | Directrice de Recherche | PMMH | *Examinatrice* |
| Alphée MICHELOT | Directeur de Recherche | IBDM | *Examinateur* |
| Serge DMITRIEFF | Chargé de Recherche | IJM | *Directeur de Thèse* |
| Nicolas BORGHI | Directeur de Recherche | IJM | *Membre invité* |

*À mes parents,*

# Analyse multi-échelle de la mécanique de l'actine ramifiée

La polymérisation de filaments d'actine contre une membrane peut générer des forces importantes entraînant l'endocytose chez la levure ou la formation de lamellipodes à l'extrémité de cellules motiles comme les kératocytes. Cette polymérisation est thermodynamiquement favorable car l'ajout d'un monomère s'accompagne d'une diminution du potentiel chimique. Cependant, la croissance du filament ralentie lorsqu'une contrainte lui est opposée, évaluant la force de décrochage à quelques pN. Si ce schéma est bien établi pour un filament unique, il n'est pas évident de le transposer à un réseau composé de centaines de filaments comme le lamellipodium. Plus généralement, comprendre l'émergence de caractéristiques à grande échelle à partir des propriétés moléculaires reste un défi majeur en biologie. Ainsi, l'objectif global de cette thèse est d'étudier l'émergence des propriétés mécaniques de l'actine ramifiée d'un point de vue numérique, théorique et statistique. Pour ce faire, nous nous appuyons sur des simulations numériques de réseaux à grande échelle dans lesquelles les caractéristiques macroscopiques peuvent être mesurées.

Dans la première partie de notre travail, nous utilisons des simulations stochastiques (dynamique de Langevin) pour créer des réseaux ramifiés en croissance soumis à une contrainte mécanique externe, imitant ainsi la résistance de la matrice extracellulaire. Précisément, nous étudions comment les propriétés stationnaires du système sont déterminées à la fois par la force de décrochage et par la contrainte. Pour un réseau de filaments avec une force de décrochage infinie, la vitesse de croissance présente un maximum lorsque la contrainte tend vers zéro et diminue ensuite comme une loi de puissance de la contrainte. Une théorie mécanique des réseaux ramifiés fondée sur l'enchevêtrement des filaments s'accorde sur cette loi de puissance. La valeur maximale à faible contrainte peut être expliquée par la traînée du réseau, qui devient ici le principal facteur déterminant. Par l'étude de filaments plus réalistes nous montrons qu'il existe un seuil de force de décrochage à partir duquel le mouvement est possible. Ce seuil est proportionnel à la contrainte externe. Enfin, pour mieux comprendre le régime de faible contrainte, nous avons étudié les réseaux à croissance libre et avons montré qu'ils s'adaptent d'eux-mêmes en ralentissant et en devenant plus denses.

Dans la deuxième partie, nous cherchons à quantifier l'information qui peut être obtenue à partir de statistiques réalisées sur de nombreuses simulations. Plus précisément, nous cherchons à identifier les combinaisons de paramètres (e.g. rigidité de l'actine, longueur du filament) qui influencent le plus les observables de notre système ramifié (e.g. densité, module d'Young). Afin de les identifier, nous appliquons des outils issus de la théorie de l'information aux statistiques générées par nos simulations, ces dernières ayant été répétées en appliquant de petites modifications aux paramètres. Sur la base de travaux antérieurs sur la dynamique des microtubules, nous avons calculé la matrice d'information de Fisher (MIF) associée qui permet de quantifier la dépendance observable-paramètre. En supposant que chaque observables suit localement une distribution normale, et grâce à une meilleure utilisation des statistiques de simulation, nous avons pu obtenir un calcul plus efficace de la MIF. L'analyse des vecteurs et valeurs propres de la MIF fournit une hiérarchie de modes de sensibilité dans l'espace des paramètres. Ces modes peuvent être interprétés géométriquement comme les directions pour lesquelles les caractéristiques du réseau sont le plus influencées par les paramètres. Ainsi, nous avons caractérisé notre système branché avec ses principaux modes de sensibilité, correspondant à une dimension effective de notre système, dont la valeur, deux, a été confirmée à l'aide d'un modèle analytique.

**Mots clefs:** biophysique, actine, polymérisation, réseau, mécanique, simulations, information, dimensionnalité, réduction

# Multiscale analysis of the mechanics of branched actin material

Polymerization of actin filaments against membranes can generate significant forces, leading to endocytosis in yeast or to the formation of lamellipodium protrusions at the leading edge of motiles cells like keratocytes. This polymerization is thermodynamically favorable, as the addition of a monomer is accompanied by a decrease in chemical potential. However, filament growth slows down when a stress opposes its growth, with a stall force of a few pN. While this picture is well established for a single filament, it is not clear how it translates to a network of hundreds of filaments like the lamellipodium. More generally, understanding the emergence of large-scale characteristics from molecular properties remains a major challenge in biology. Thus, the overall aim of this thesis is to understand the emergence of the mechanical properties of branched actin from a numerical, theoretical and statistical point of view. To achieve this, we rely on numerical simulations of large-scale networks in which macroscopic characteristics can be measured.

In the first part of our work, we use stochastic simulations (Langevin dynamics) to create growing branched networks subjected to external mechanical stress, mimicking the resistance of the extracellular matrix. Specifically, we investigate on how stationary properties of the system are determined by both stall force and stress. For a network made of filaments with an infinite stall force, the growth velocity exhibits a maximum when the stress tends towards zero and then decreases as a power law of the stress. A mechanical theory of branched networks based on filaments entanglement agrees with this power law. The maximum value at low stress can be explained by the drag of the network, which becomes the main determining factor here. By studying more realistic filaments, we show that there is a stall force threshold above which movement is possible. This threshold is proportional to the external stress. Finally, to better understand the low-stress regime, we studied free-growing networks and showed that they self-adapt by slowing down and densifying.

In the second part, we aim at quantify the information that can be obtained from statistics carried out on numerous simulations. More specifically, we seek to identify the combinations of parameters (e.g. actin stiffness, filament length) that most influence the observables of our branched system (e.g. density). To identify them, we apply tools from information theory to the statistics generated by our simulations, which have been repeated by applying small modifications to the parameters. Based on previous work on microtubule dynamics, we have calculated the associated Fisher information matrix (FIM), which quantifies the observable-parameter dependence. By assuming that each observable locally follows a normal distribution, and by a better use of simulation statistics, we were able to obtain a more efficient calculation of the FIM. Analysis of the eigenvectors and eigenvalues of the FIM provides a hierarchy of sensitivity modes in the parameter space, which can be interpreted geometrically as the direction in which network characteristics can be most influenced by the parameters. Thus, we characterize our branched system with its main sensitivity modes, corresponding to an effective dimension of our system. We find that this system has two effective dimensions, which has been confirmed using an analytical model.

**Keywords:** biophysics, actin, polymerization, network, mechanics, simulations, information, dimensionality, reduction

# Résumé substantiel

La seconde moitié du vingtième siècle a vu les collaborations entre physiciens et biologistes s'intensifier. Ces derniers, se sont entre autres consacrés à la compréhension des principes régissant la régulation cellulaire , en se penchant particulièrement sur des aspects tels que le développement, la morphogenèse et le cycle cellulaire. Aujourd'hui, la recherche portant sur les propriétés mécaniques des cellules et de leurs composants revêt une importance croissante, contribuant de manière significative à notre compréhension des phénomènes biologiques, notamment au niveau cellulaire. Le cytosquelette est l'acteur central de la régulation mécanique des cellules : ce réseau de biopolymères intracellulaire assure un rôle essentiel dans le maintien des propriétés structurales et mécaniques des cellules, qu'il s'agisse d'eucaryotes, de bactéries ou d'archées. Il s'agit d'un système actif, caractérisé par la polymérisation et la dépolymérisation qui assurent un renouvellement constant de ses composants, en utilisant l'hydrolyse de l'ATP. Les fonctions du cytosquelette englobent diverses tâches cruciales, notamment la régulation de la forme cellulaire, le trafic membranaire et la contraction des cellules musculaires. En outre, il assure un rôle fondamental dans le processus de division cellulaire Le cytosquelette se décline en trois principales familles : les microtubules, les filaments intermédiaires et l'actine.

L'actine fait l'objet de notre étude. Il s'agit d'une protéine versatile, qui se présente sous de très nombreuses formes et qui se situe la plupart du temps sous la membrane. Elle est l'élément du cytosquelette le plus largement étudié. L'actine s'associe à de nombreuses autres protéines, notamment les moteurs moléculaires, les protéines de coiffe et les protéines de nucléation telles que Arp2/3, pour créer, maintenir ou détruire des structures qui remplissent des fonctions biologiques spécifiques. Parmi ces structures, citons le lamellipode, le filopode, l'actine corticale et le podosome. Notre attention se porte sur les réseaux d'actine branchés, qui constituent une structure élémentaire présente dans de nombreux contextes tels que le lamellipode et le podosome. La polymérisation des filaments d'actine contre une membrane peut engendrer des forces significatives, entraînant des phénomènes tels que l'endocytose chez les levures ou la formation de lamellipodes à l'extrémité de cellules motiles comme les kératocytes. La polymérisation de l'actine est thermodynamiquement favorable, car l'ajout d'un monomère s'accompagne d'une diminution du potentiel chimique. Cependant, la croissance du filament ralentit de manière exponentielle en présence d'une contrainte mécanique externe, avec une force de décrochage estimée à quelques piconewtons. Cette diminution de la vitesse de croissance s'explique par le fait que l'application d'une force réduit la probabilité qu'un intervalle suffisamment large entre le filament et la membrane permette l'insertion d'un monomère. Ce modèle stochastique dit du "cliquet brownien", a été validé expérimentalement.

Bien que ce schéma soit bien établi pour un filament individuel, son application à un réseau composé de centaines de filaments, comme dans le cas du lamellipode, demeure complexe. De nombreuses études expérimentales se sont penchées sur les propriétés mécaniques et la vitesse de croissance des réseaux d'actine branchés. En général, elles ont confirmé que la croissance ralentissait en présence d'une contrainte externe, bien que des divergences notables subsistent en fonction des conditions expérimentales. Dans notre travail, nous passons en revue l'état actuel des connaissances relatives à la croissance des filaments individuels, des faisceaux de filaments et des réseaux d'actine branchés. Nous soutenons ainsi l'idée que ces réseaux branchés s'adaptent en réponse aux contraintes extérieures, réduisant leur vitesse de croissance et ajustant leurs propriétés mécaniques, en devenant plus rigides lorsque la contrainte augmente. Plusieurs modèles théoriques et simulations ont été proposés pour étayer ces constats.

Toutefois, une analyse plus approfondie de la littérature met en lumière certaines limites des travaux actuels que nous abordons dans notre propre recherche. En particulier, la force requise pour immobiliser des réseaux d'actine branchés n'a été que peu explorée, et sa dépendance à la force de décrochage individuelle des filaments n'a pas encore été clairement établie. De manière plus générale, l'impact de la force de décrochage sur la dynamique des réseaux demeure méconnu, et le processus d'adaptation des réseaux aux contraintes, en termes de vitesse ou de module d'élasticité, n'a pas encore été encadré théoriquement. Enfin, l'évolution des propriétés mécaniques du réseau dans le temps, en dehors de toute intervention biologique, requiert une exploration plus approfondie. Plus généralement, la compréhension de l'émergence de caractéristiques à grande échelle à partir des propriétés moléculaires demeure un défi majeur en biologie, thématique que nous abordons dans la seconde partie de notre travail.

Ainsi, l'objectif global de cette thèse est d'étudier l'émergence des propriétés mécaniques de l'actine ramifiée, en adoptant une approche numérique, théorique et statistique. Pour ce faire, nous nous appuyons sur des simulations numériques de réseaux à grande échelle, au sein desquelles les caractéristiques macroscopiques peuvent être mesurées.

Dans la première partie de notre étude, nous avons employé des simulations stochastiques basées sur la dynamique de Langevin (en utilisant l'outil de simulation de cytosquelette Cytosim) pour générer des réseaux ramifiés en croissance soumis à une contrainte mécanique externe. Cette contrainte reproduit la résistance de la matrice extracellulaire. Initialement, nous positionnons des protéines de nucléation Arp2/3 à la base d'un cylindre qui définit notre espace de travail. Ces protéines sont libres de diffuser aléatoirement à la surface du cylindre. Lorsqu'une de ces protéines de nucléation s'approche suffisamment d'un filament, elle s'y attache, induisant ainsi la création d'un nouveau filament. Le processus démarre avec quelques filaments pour amorcer la croissance du réseau, et le réservoir de protéines de nucléation est alimenté à un taux constant. Le réseau ainsi formé croît de manière substantielle, nous permettant d'étudier ses propriétés. La contrainte appliquée est maintenue constante, elle peut être assimilée à l'implémentation numérique d'un microscope à force atomique. Après une série d'étalonnages visant à affiner les paramètres de notre système, nous avons examiné comment les propriétés stationnaires du réseau sont influencées à la fois par la force de décrochage individuelle des filaments et par la contrainte mécanique.

Pour un réseau de filaments présentant une force de décrochage infinie, la vitesse de croissance atteint un maximum constant lorsque la contrainte tend vers zéro, puis diminue conformément à une loi de puissance en fonction de la contrainte. Une théorie mécanique des réseaux ramifiés, basée sur le concept d'enchevêtrement des filaments est cohérente avec cette loi de puissance. Dans une autre partie de notre recherche, nous avons approfondi les aspects théoriques liés à cette théorie mécanique des réseaux ramifiés. La valeur maximale de la vitesse de croissance à faible contrainte peut s'expliquer par la traînée exercée par le réseau, celle-ci devient le facteur déterminant lorsque la contrainte imposée est faible. En étudiant des filaments plus réalistes, nous avons démontré l'existence d'un seuil de force de décrochage en deçà duquel le mouvement n'est pas possible pour des contraintes non négligeables. Ce seuil est proportionnel à la contrainte externe. Par conséquent, nous pouvons caractériser la transition entre la phase de non-mouvement et la phase de mouvement (qui suit la loi de l'enchevêtrement) au moyen d'une surface seuil. Cependant, nous n'avons pas pu établir une correspondance directe entre la valeur de cette surface seuil et une surface caractéristique issue des caractéristiques physiques de notre système. Enfin, pour mieux appréhender le régime de faible contrainte, nous avons étudié les réseaux à croissance libre, montrant qu'ils s'auto-ajustent en ralentissant et en devenant plus denses avec le temps.

Plus précisément, les nouvelles couches de filaments se développent en présence d'une plus grande quantité de matériel et sont donc soumis à une force de traînée plus significative. Cela entraîne un ralentissement du réseau. Une approche théorique, en partie fondée sur la théorie de l'enchevêtrement, a confirmé ces résultats numériques.

Dans la seconde partie de notre travail, nous cherchons à quantifier l'information que nous pouvons extraire des statistiques provenant d'un grand nombre de simulations. Plus précisément, notre objectif est d'identifier les combinaisons de paramètres (par exemple, la rigidité de l'actine ou la longueur d'un filament) qui exercent la plus grande influence sur les observables de notre système ramifié, tels que la densité ou le module d'élasticité. Pour parvenir à cette identification, nous avons appliqué des outils issus de la théorie de l'information aux données statistiques générées par nos simulations, en réalisant de légères variations des paramètres à chaque itération.
S'inspirant de travaux antérieurs portant sur la dynamique des microtubules, nous avons calculé la matrice d'information de Fisher associée, qui nous permet de quantifier la dépendance entre les observables et les paramètres. De manière générale, l'infirmation de Fisher mesure la dépendance d'un modèle probabiliste par rapport à un paramètre. Techniquement, il s'agit de la variance de la fonction de score qui est elle même la dérivée de log-vraisemblance. Dans le contexte d'un système comportant plusieurs paramètres, on parle de matrice d'information de Fisher. L'analyse des espaces propres de la matrice d'information de Fisher révèle les combinaisons de paramètres qui exercent la plus grande influence sur le système, conduisant à ce que l'on nomme la "compression de l'espace des paramètres". Après avoir décrit l'estimation numérique de la matrice de Fisher pour un système biologique complexe, en l'occurrence la dynamique des microtubules, nous avons identifié les limitations de cette approche qui se fonde sur une estimation de la densité de probabilité du système. Afin de minimiser les effets du bruit d'estimation sur les espaces propres, nous avons opté pour une étude locale des effets induits par les variations de paramètres sur les moments de la loi de probabilité. De plus, pour maximiser l'information obtenue, nous avons considéré des ensembles d'observables, ce qui a permis une caractérisation plus détaillée des espaces propres.
Ainsi, en supposant que chaque observable suit localement une distribution normale, et grâce à une utilisation plus efficace des statistiques de simulation, nous avons développé une méthode plus précise pour le calcul de la matrice de Fisher en estimant localement les dérivées premières et la matrice de covariance. L'analyse des vecteurs propres et des valeurs propres de la matrice de Fisher a permis d'établir une hiérarchie des modes de sensibilité dans l'espace des paramètres. Ces modes peuvent être interprétés géométriquement comme les directions dans lesquelles les caractéristiques du réseau sont le plus fortement influencées par les paramètres. Finalement, nous avons caractérisé notre système ramifié en identifiant ses principaux modes de sensibilité, déterminant ainsi une dimension effective pour notre système, dont la valeur, égale à deux, a été confirmée grâce à un modèle analytique. Nous détaillons les limites de notre travail et proposons plusieurs voix d'améliorations et potentielles applications afin d'étendre ces résultats statistiques. Nous estimons par ailleurs que cette approche pourrait se révéler fructueuse pour orienter des collaborations entre expérimentateurs et théoriciens.

# Acronyms

- ABP: Actin Binding Protein
- ADP: Adenosine Diphosphate
- AFM: Action Force Microscopy
- ARP: Actin Related Protein
- ATP: Adenosine Triphosphate
- FI: Fisher Information
- FIM: Fisher Information Matrix
- GDP: Guanosine Diphosphate
- GTP: Guanosine Triphosphate
- NPF: Nucleation Promoting Factor
- PCA: Principal Component Analysis
- PSC: Parameter Space Compression
- PDF: Probability Density Function
- RG: Renormalization Group
- SD: Standard Deviation
- SDEM: Standard Error of the Mean
- SVD: Singular Value Decomposition
- WASP: Wiskott–Aldrich Syndrome protein

# Remerciements

Je souhaite avant tout exprimer mes plus sincères remerciements envers les membres du jury. Mes rapporteurs, Verena Ruprecht et Ulrich Schwarz, ainsi que mes examinateurs Olivia du Roure, Alphée Michelot et Andrew Callan-Jones. Je les remercie pour l'intérêt manifeste porté à mon travail, leur lecture attentive de ce manuscrit ainsi que pour leurs précieux commentaires et suggestions. Je remercie à nouveau Andrew Callan-Jones, mon tuteur scientifique, et Nicolas Borghi mon parrain de thèse, pour leurs nombreux conseils formulés lors des comités de suivi. Tout naturellement, je tiens à exprimer ma profonde reconnaissance envers mon directeur de thèse, Serge Dmitrieff, sans qui rien de tout cela n'aurait été possible. Je le remercie pour son soutien, sa clairvoyance scientifique et sa bienveillance constante. Je tiens, au-delà de son encadrement, à saluer ses engagements humanistes et écologiques.

Je souhaite également remercier les nombreux scientifiques avec qui j'ai eu le privilège de discuter. Ces échanges ont été précieux pour moi. Parmi eux, je citerais : Martin Lenz, Olivia du Roure et Julien Heuvingh du PMMH, Guillaume Romet-Lemonne et Antoine Jegou de l'IJM, ainsi que Jim Sethna de l'Université Cornell. Je souhaite aussi exprimer ma gratitude envers Alix Silvert et Olivier Kirsh de la plateforme IPOP-UP, ainsi que Joel Marchand de l'IJM, pour leur assistance informatique sans laquelle mes nombreuses simulations auraient pris (encore) plus de temps.

L'enseignement a joué un rôle central durant mes trois années de thèse. J'ai une pensée chaleureuse pour mes collègues du campus Saint-Germain-des-Prés, en particulier Anne Baudot, dont je souhaite saluer l'engagement envers les étudiants. Une fois n'est pas coutume, je remercie mes élèves de la L1 Sciences Biomédicales pour les nombreux et riches moments que j'ai passés auprès d'eux. J'espère qu'ils garderont un souvenir amusé de mes explications sur les moments de force, que je ne les ai pas usés à introduire des ressorts à chaque fois que l'occasion se présentait. J'ai beaucoup appris à leur contact et leur souhaite le meilleur, à toutes et tous. Je profite de ce passage pour exprimer ma reconnaissance envers tous les enseignants qui ont pu stimuler ma curiosité générale ou mon intérêt pour les sciences tout au long de mon parcours académique. J'aurais une mention spéciale pour mes deux années en CPGE au lycée Faidherbe de Lille, auquel je reste profondément attaché.

J'ai mené cette recherche au sein de l'équipe de Nicolas Minc à l'Institut Jacques Monod. Pendant trois ans, j'ai eu le privilège de travailler aux côtés de scientifiques talentueux se penchant sur des questions cruciales liées au développement et à l'organisation interne de la cellule. Bien que physicien de formation, les discussions scientifiques, les réunions de groupe et les séminaires ont rythmé ma vie académique, développant en moi un goût prononcé pour ces sujets. Je remercie chaleureusement Nicolas Minc pour son accueil, ses critiques pertinentes concernant mon travail, ainsi que nos échanges passionnés sur le football. Je tiens à exprimer ma gratitude envers tous les collègues, anciens et actuels, avec qui j'ai partagé de très bons moments à discuter science, sport ou cuisine.
Je mentionnerai : Jeremy, Javad, Amir, Aude, Maribel, Charlotte, Jordan, Célia, Camille, Ilaria, Yannis, Louis, Jing, Tony, Christophe et Camilia. J'ai forcément un mot particulier pour nos discussions politico-geek avec Jeremy et pour mes autres voisins de bureau, Jing et Maribel, dont je suis obligé de mentionner les crèmes hydratantes.

Durant ces trois années, j'ai bénéficié d'un soutien inestimable de la part de mes amis. Il m'est malheureusement difficile de tous les énumérer. Néanmoins, je pense tout naturellement à mes anciens colocataires, Alex et Sam (sans oublier notre chatte Miso) avec qui j'ai partagé mes deux premières années de thèse dans un appartement à l'air un peu trop sec. Je les remercie pour les précieux moments passés ensemble (sauf FIFA), et je m'excuse d'avoir eu à expliquer un nombre incalculable de fois mon sujet en leur présence. Bravo pour leur patience. Je pense aussi à Pierre qui fut pendant quelques mois notre quatrième colocataire et qui, je l'espère, sera meilleur philosophe que joueur de Catan. Mes pensées vont aussi à tous les amis que nous avons hébergés ou accueillis à la Misoloc, notamment les membres du Think Tank. Mes remerciements s'étendent également à mes amis de prépa, de Lyon, du master, à toutes les personnes dont la rencontre m'aura enrichi. Enfin, je tiens à adresser un remerciement spécial à Estelle, dont la présence est devenue essentielle dans ma vie.

Mes plus profonds sentiments vont à ma famille. Je remercie du fond du cœur mes parents, à qui je dois tant, et auxquels je dédie cette thèse. Merci pour leur amour.
Je pense aussi à mes deux frères, Amine et Bilal, heureux que les choses restent aussi simples même lorsque je suis traité comme un invité. Je tiens également à remercier, dans ma famille, ceux qui m'ont soutenu pendant cette thèse et durant toutes mes études, qu'ils soient en France ou en Algérie. J'ai une pensée singulière pour ma grand-mère, dont l'affection semble sans limite malgré toutes les épreuves qu'elle a pu rencontrer.
Mes derniers mots iront à mon grand-père, qui nous a quitté en janvier 2021 après une longue maladie. Il occupe une place éternelle dans mon cœur.

# Summary

# Introduction

> *Faites rhizome et pas racine, ne plantez jamais! Ne semez pas, piquez! Ne soyez pas un ni multiple, soyez des multiplicités!*
>
> ---
>
> Gilles Deleuze et Félix Guatarri - **Mille Plateaux**

Since the second half of the twentieth century, physicists have approached the question of what is at stake in living processes, essentially through the lens of statistical physics. Erwin Schrödinger, one of the fathers of quantum mechanics, had the insight of an *aperiodic crystal* a decade before Watson and Crick, wherein genetic information would reside in the configuration of covalent chemical bonds. This unique structure aimed to elucidate the physical and chemical foundations of biological events and genetic inheritance [1]. In particular, scientists have investigated the emergence of biological order and identity through fluctuations and chaos, establishing the theoretical framework of dissipative structures to account for deviations from the second law of thermodynamics [2] or developing pioneering studies on morphogenesis [3]. In addition, since early studies on the motility of cells [4], soft matter advances, the active matter framework and the advent of new experimental and numerical tools have fostered a closer collaboration between physicists and biologists. This interdisciplinary approach seeks to understand the underlying principles governing cellular regulation, with specific attention to developmental processes, morphogenesis, and the regulation of the cell cycle. Collaborations focusing on the study of the mechanical properties of cells, including their origins and self-regulation processes, are particularly noteworthy.

A fundamental aspect of cellular self-regulation is attributed to the cytoskeleton: a dynamic network of intracellular polymers that endows the cell with most of its mechanical and architectural properties. The cytoskeleton operates as an active system, constantly undergoing polymerization and depolymerization processes to renew its components. Consequently it is permanently pushed out of equilibrium due to the continuous energy consumption of its components. The functions of the cytoskeleton encompass various crucial tasks, including the regulation of cell shape, membrane trafficking, and muscle cell contraction. Additionally, it plays a fundamental role in cell division mechanisms [5]. The influence of the cytoskeleton extends beyond mechanical frameworks, as it impacts processes such as protein transport, regulation of gene expression or cell differentiation and proliferation. The comprehensive scope of the cytoskeleton's involvement in cellular processes cannot be exhaustively enumerated, as ongoing research in this field continually reveals new roles and functions. Depending on their designated tasks, cytoskeletal structures exhibit different organization patterns, leading to distinct mechanical behaviors. Consequently, fibers can aggregate collectively to form stable networks, with their defined properties emerging from both the individual fiber characteristics and the external biological and mechanical environment. This observation prompts scientists to question the emergence of collective order in a manner that transcends reductionist principles, as stated by P.W. Anderson in his work "More Is Different." [6]. Specifically, today, there is no comprehensive understanding of how macroscopic mechanical properties manifest from microscopic parameters. Deciphering this enigma stands as a significant challenge in the realm of cell biology and soft matter physics.

The overall objective of this thesis is to understand the emergence of mechanical properties within actin networks through numerical, theoretical, and statistical perspectives. The manuscript is structured into two distinct parts, each addressing a specific problem investigated during my PhD research.

The first part focuses on the issue of stress adaptation in growing branched actin networks. Following an introduction to the components of the cytoskeleton, actin dynamics, and mechanics, I will present simulation-based results obtained on the adaptation of network growth speed. The findings reveal how both filament properties (in particular stall force) and external stress collectively determine the velocity of the actin network in this particular scenario.

More generally, the mechanical features of branched actin networks are contingent upon molecular properties, including actin filament stiffness or stall force. However, given the overlapping roles of many molecular properties, perturbations at the molecular level can affect the mechanical features of the network in a limited number of ways.

In this second part, the objective is to identify the specific combinations of molecular properties that exert the most significant influence to the features of the system. To achieve this, the study employs information theory tools to analyze the statistical data generated by the simulations. This approach enables novel means of characterizing systems by capturing the essential features of their compressed parameter space, in between black boxes and the spherical cow [1]

> *Bon voilà toute l'introduction. J'en conviens parfaitement, elle ne sert à rien du tout, mais, puisqu'elle est écrite, qu'elle reste. Sur ce, au fait.*
>
> Fiodor Dostoïevski - **Les Frères Karamazov**

---

[1] Milk production at a dairy farm was low, so the farmer wrote to the local university, asking for help from academia. A multidisciplinary team of professors was assembled, headed by a theoretical physicist, and two weeks of intensive on-site investigation took place. The scholars then returned to the university, notebooks crammed with data, where the task of writing the report was left to the team leader. Shortly thereafter the physicist returned to the farm, saying to the farmer, "I have the solution, but it works only in the case of spherical cows in a vacuum."

# Part I

# The stress adaptation of growing branched actin networks

# Introduction

Actin, a highly versatile protein and a key component of the cytoskeleton, plays a crucial role in cell motility. When assembled into networks, actin can generate forces through two main mechanisms: motor contractility and polymerization. Motors within the actin network can induce significant contractile stresses, leading to mechanical contraction [7]. In addition, polymerization of actin filaments against membranes can generate substantial forces, resulting in various processes such as endocytosis in yeast [8], lamellipodium protrusions at the leading edge of motile cells such as keratocytes [9] or propulsion of intracellular pathogen [10]. This thesis will specifically focus on actin polymerization as a force generation mechanism [11], to overpass mechanical stress induced by membranes or cytoplasmic material.

More precisely, the growth of an actin filament is governed by the difference in chemical potential between the monomers in solution and those attached to the filaments. Thermodynamically, it is more favorable for an actin monomer to join the barbed end of a filament rather than diffuse freely in solution. The conversion of this chemical energy into a mechanical energy generates a force. The addition of a new monomer occurs when thermal fluctuations create sufficient space for its stochastic insertion, despite counteracting forces [12], [13]. However, filament growth becomes increasingly unfavorable when an opposing mechanical stress hinders its expansion. The stall force, estimated to be a few pN, represents the point at which filament growth is impeded [14]. While this picture is well established for individual fibers, it remains unclear how it applies to a network composed of hundreds of fibers. Determining the individual contribution of the fiber to the behavior of the network poses a significant challenge. Several theoretical and experimental relationships between network growth velocity and applied stress have been proposed, with a variety of predictions directly linked to experimental conditions and theoretical assumptions. In this study, we investigate the relationship between stress and velocity in branched actin networks. Through a minimalist simulation model in physiologically relevant conditions, we explore the roles of stress and stall force in determining the velocity.

The manuscript begins by reviewing the actin machinery and the process of individual force generation. Subsequently, we delve into the established findings on the rheology of actin structures, specifically focusing on the stress-velocity relationship in branched actin systems. Then, we provide a brief introduction to our simulation tool, Cytosim, along with an explanation of our force generation model. Finally, we present our results concerning stress dependence and stall force, separately.

# Chapter 1

# Cytoskeleton and actin

The evolution of cells has led to the development of complex and diverse structures. Today, biological classifications categorize cellular life into three domains: Archaea, Bacteria, and Eukaryota. Despite their differences, all cells are enclosed by a membrane and contain genetic material. Eukaryotic cells, have organelles that compartmentalize different functions within the cell, such as the nucleus that contains DNA. In contrast, cells lacking organelles are referred to as prokaryotes (bacteria and archea). The cytoskeleton, present in eukaryotic cells, plays a crucial role in providing mechanical support and maintaining the structural integrity of the cell. It is also determining for cell division and cellular transport.

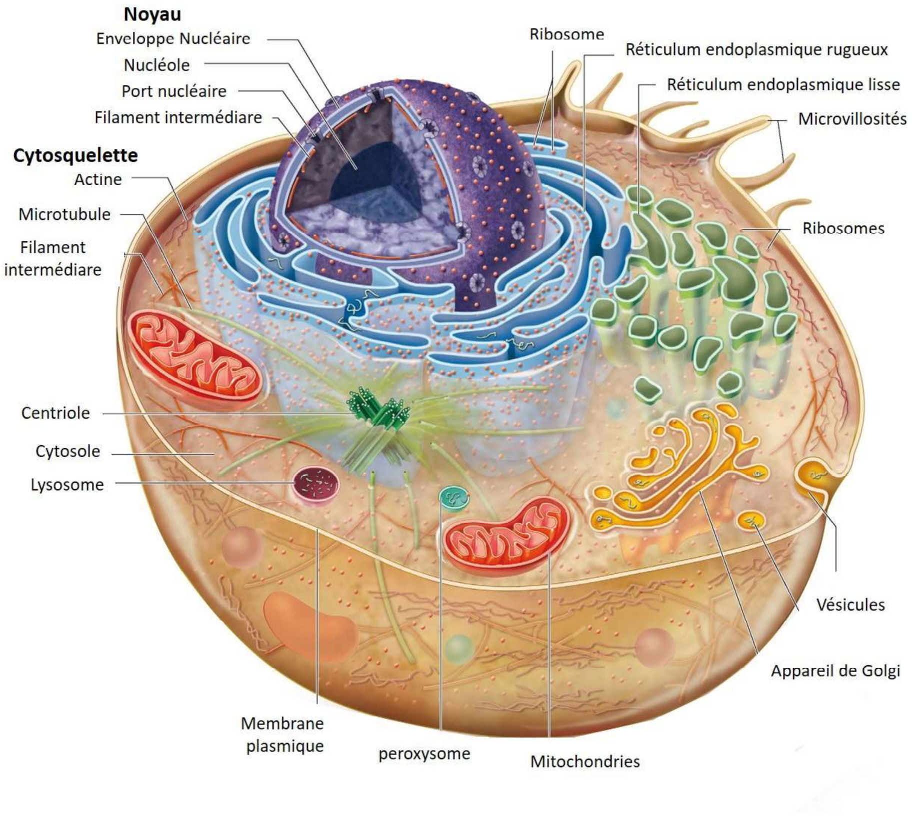

Figure 1.1: Eukaryotic cell, adapted from Raven, G.B Johnson, Mason et al. 2017.

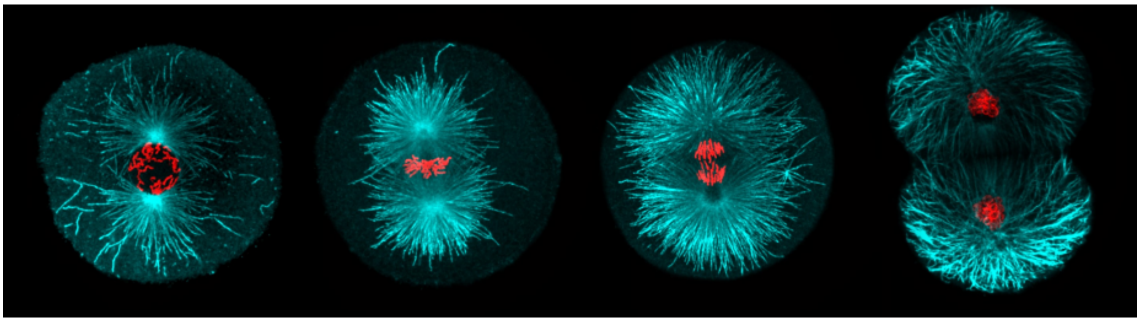

Figure 1.2: First division of a sea urchin embryo with DNA in red and microtubules in green - with the courtesy of Jérémy Sallé - Minc Lab.

## 1.1 The cytoskeleton

The cytoskeleton is composed of various fibers that are formed through polymerization and regulated by associated proteins. It is typically divided into three types: microtubules, intermediate filaments, and actin filaments. From a physicist's perspective, these fibers are considered dynamic, semi-flexible filaments in an non-equilibrium state [15]. Let's take a closer look at microtubules, intermediate filaments and actin with their characteristics and functions.

### 1.1.1 Microtubules

Microtubules are hollow tubes with a diameter of approximately 24 nm. They consist of $\alpha$-tubulin and $\beta$-tubulin subunits that associate as dimers and can form protofilaments when associated to guanosine triphosphate (GTP). Thirty protofilaments come together to create a microtubule, GTP hydrolysis occurs during the growth process. Due to their heterodimeric composition, microtubules exhibit a polarity, with a plus end and a minus end. When the nucleotides at the growing tip are completely hydrolyzed, the microtubule becomes unstable and undergoes depolymerization, a process known as catastrophe [16].

Microtubules are the most rigid fibers having a persistence length of approximately 5 mm [17], which is much larger than the typical cell size. Thus, they play a crucial role in defining cellular shape and serve as tracks for intracellular motor proteins like dyneins or kinesins [18]. In addition, microtubules are responsible of DNA segregation during mitotis, through the formation of complex assembles called mitotic spindles [19], as seen in Figure 1.2. They also form large structures called asters, which help drive the male pronucleus to the center during fertilization, facilitating its fusion with the female pronucleus. The centering mechanism of microtubule asters is partly governed by geometric principles [20].

### 1.1.2 Intermediate filaments

Intermediate filaments represent a diverse family of apolar fibers with diameters ranging from 8 to 12 nm. The most studied types of intermediate filaments are vimentins, lamins, and keratins. Intermediate filaments assemble into fibers through a slower dynamics compared to other cytoskeletal fibers, they maintain a relatively stable structure over time. Their persistence length varies between a few hundred nanometers and a few micrometers, making them the most flexible cytoskeleton fibers. As a result, intermediate filaments provide an important part of the mechanical support to the cell. Vimentin, the major intermediate filament in most animal cells plays an important role in maintaining cell integrity under high deformations. Nuclear lamins form a protective shell around the nucleus and act as mechanosensors to preserve chromatin. Keratin, is widely known for its presence in structures such as hair or nails [21].

### 1.1.3 Actin

Actin monomer proteins form microfilaments, also known as F-actin, which play crucial roles for various motile and morphogenesis processes such as migration, endocytosis or organelles dynamics [5].

The individual units of actin, referred to as G-Actin (globular actin), are compact, small globular proteins of approximately 42 kDa, measuring about 5.5 nm in diameter [22]. Each G-Actin monomer consists of a single polypeptide chain composed of 375 amino acids, which undergoes precise folding to adopt a well-defined structure. G-Actin can be subdivided into four distinct domains arranged in two lobes. These lobes create two distinct clefts or gaps between them. The upper gap functions as a binding site for a nucleotide: adenosine triphosphate (ATP) or adenosine biphosphate (ADP), (multicolor sticks in Figure 1.3 (Left)). It also serves as a binding site for a divalent cation such as calcium ($Ca^{2+}$) or magnesium ($Mg^{2+}$) (green dot in Figure 1.3, (Left)) [23]. The lower gap serves as a binding site for other actin-related proteins (ARPs), including profilin. The process of filament formation, referred as polymerization, occurs through this lower gap as new actin monomers are added to the growing filamentous structure.

The asymmetry observed at the level of the monomer is translated at the fiber scale, where the actin filament display polarization. At each end, the dynamics are governed by the association $k_{on}$ and dissociation rates $k_{off}$ of actin monomers. Under physiologically salt conditions, the disparity in these rates leads to a directional growth. Specifically, actin filament grow more rapidly from the *barbed end* (+) compared to the *pointed end* (-). At steady state, ATP-G-Actin is mostly added at the barbed end, while ADP-G-Actin dissociates from the pointed end, see Figure 1.4. During filament assembly, actin monomers undergo a conformational change that triggers the ATPase activity of the protein. It has been shown that this conformal change is enabled by the $Mg^{2+}$ cation located at the upper cleft [25] [26].

During the process, there is a rapid hydrolysis of ATP (rate of 0.3 $s^{-1}$), followed by a slower release of inorganic phosphate (Pi) (rate of 0.002 $s^{-1}$). The surplus of ATP in the system facilitates the regeneration of ATP-G-Actin through a nucleotide exchange mechanism. This ensures the availability of monomers for polymerization. Thus, actin filaments exhibit treadmilling, where the rates of polymerization and depolymerization are balanced, resulting in a constant filament length.

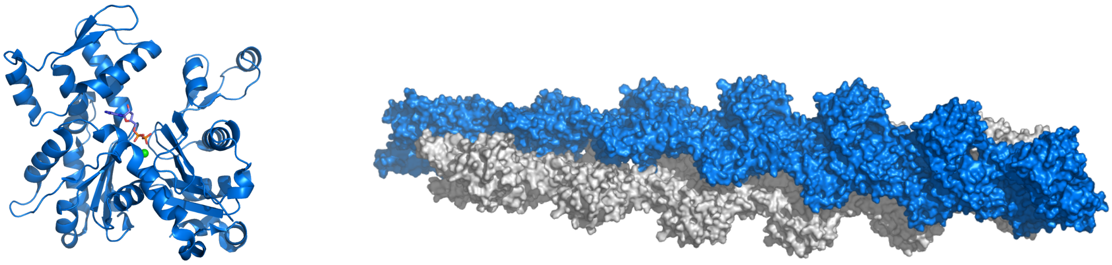

Figure 1.3: (Left) Ribbon diagram of G-Actin adapted from [24]. (Right) Representation of a 13 monomers F-Actin, work of Thomas Splettstoesser.

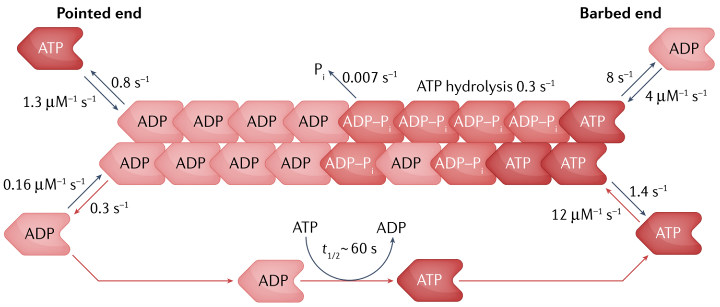

Figure 1.4: Actin dynamics at both ends with associations and dissociation rates, from [30].

Once assembled, the filament exhibits a right-handed helix structure of two protofilaments with a 37 nm step and a diameter of 7 nm [27], see Figure 1.3, (Right). Their persistence length is of the order of 10 µm [17] [28]. In addition, actin filaments are rather resistant to stretching, bending being their main elastic response [29].

## 1.2 Regulation of actin assembly

In eukaryotic cells, the dynamic process of actin polymerization and the diverse range of observed structures are facilitated by actin-related proteins (ARPs). These proteins play a regulatory role in actin polymerization and exert influence on the formation of well-defined structures. They inhibit uncontrolled and spontaneous polymerization focusing assembly at needed sites. For instance, they help to maintain a pool of actin monomers, to restrict the length of filaments or to cross-link filaments into networks or bundles.

### 1.2.1 Nucleators

Actin fiber nucleation from a small number of monomers is energetically unfavorable until a four-monomer oligomer is formed [31]. Cells employ various mechanisms, including the recruitment of nucleators, to overcome this energetic barrier. These nucleating proteins not only facilitate the formation of new filaments but also play a role in determining the architecture of the resulting actin network.

#### Formins

One class of nucleators involved in the regulation of cytokinesis and stress fibers formation is known as formins. In budding yeast, two specific formins, Bni1p and Bnr1p, are responsible for orchestrating the assembly of actin cables. These actin cables are bundles that facilitate polarized growth and the segregation of organelles within the cell [32]. Formins initiate the process of actin polymerization by interacting with G-actin monomers and remain associated with the growing barbed-end of the filament with their FH2 domain. They not only stabilize oligomers but also catalyze the nucleation of actin filaments with their scaffold shape. By maintaining their connection to the barbed-end, formins actively participate to the elongation of the filament, resulting in the generation of straight, linear fibers [33]. Formins can also segregate profilin-actin monomers with their FH1 domain making them accessible and ready for polymerization [30], see Figure 1.5. Similarly but with a different underlying mechanism, an other class of proteins the Ena/VASP family proteins catalyzes the elongation of the filament barbed-end [34].

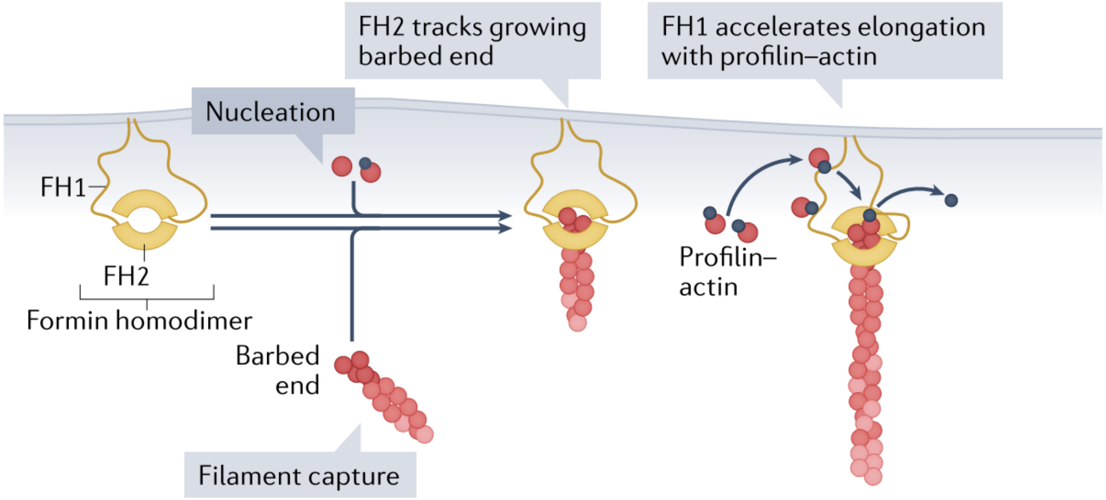

Figure 1.5: Acceleration of the barbed-end elongation of F-Actin by formins, from [30].

### Arp2/3

The Arp2/3 complex constitutes the other primary class of nucleators involved in actin dynamics. Unlike formins that generate straight linear filaments, the Arp2/3 complex is responsible for producing branched filament networks. These branched networks are abundant in cells, at the leading-edge lamellipodium of migrating cells or at the sites of endocytosis for instance. The Arp2/3 complex is composed of seven sub-units, including Arp2 and Arp3, as well as five scaffolding sub-units. Basically, when the complex binds to the side of an existing filament, Arp2 and Arp3 undergo reorganization, coming closer together and providing a template for the elongation of a daughter filament. The branching occurs at a conserved angle of 1.23 rad (approximately 70°) with respect to the mother filament [35]. To enhance the stability of the daughter branch, two subunits of the mother branch undergo a conformational change [36]. While the cooperative action between the Arp2/3 complex and the mother branch is crucial for branch generation, the involvement of nucleation-promoting factors (NPFs) is required to activate Arp2/3 and initiate the branching process [37]. These NPFs, activated by GTPases such as Rac1 and Cdc42, are anchored to lipid bilayers and play a role in triggering endocytosis in the case of WASP family proteins or promoting cell migration for the WAVE family proteins.

### NPFs

As the dynamics and functional implications of nucleation-promoting factors (NPFs) are crucial for our modelisation, we will delve further into their characteristics and functional aspects. When these proteins become associated with cell membranes, they exhibit a carboxy-terminal (C-terminal) region known as the “WCA domain”. This WCA domain can be further divided into four distinct domains. The first domain is the WH2 (W) domain, which has the ability to bind to actin monomers. The central (C) domain and the acidic (A) domain can bind to the Arp2/3 complex. Lastly, the WCA domain contains a proline-enriched (P) domain, which facilitates binding to other actin-related proteins (ARPs) such as profilin or myosin. The (P) domain, in particular, may play an important role in delivering G-Actin enriched with profilin, thereby promoting branching in the actin network [38].

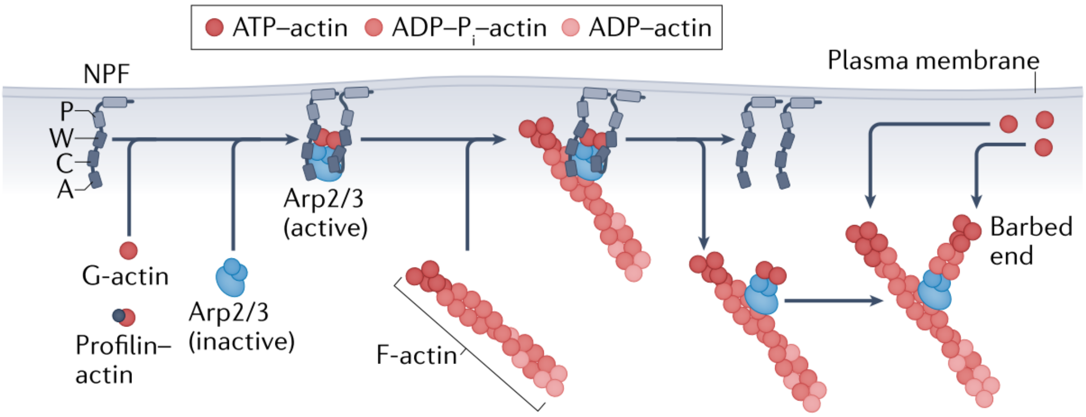

Figure 1.6: Activation of Arp2/3 by NPFs and formation of a new branch, from [30].

The activation of the Arp2/3 complex requires the presence of two NPFs. Once bound to the Arp2/3 complex along with two actin monomers, a conformational change is triggered in the complex. This conformational change allows the scaffolding units of Arp2/3 to attach to the mother filament, thereby stabilizing the entire structure. Subsequently, when the WCA domain of the NPFs detaches from the complex, it allows for the growth of the daughter filament. This liberation of the NPFs enables its availability for future activation, see Figure 1.6.

### 1.2.2 Regulators

Regulatory mechanisms play a pivotal role in governing the processes of polymerization, depolymerization, and the maintenance of the G-Actin reservoir. Three distinct protein families are distinguished, profilin, capping proteins, and severing proteins.

#### Profilin

Profilin prevents the spontaneous initiation of filaments elongation by binding to the G-Actin polymerization site. In doing so, it sequesters monomers from the pool of polymerizable G-Actin molecules. However it has been demonstrated that the complex formed by profilin and actin can bind to the barbed end of the filament, promoting its directed elongation [39]. In addition, profilin acts as a catalyzer in the nucleotide exchange process, facilitating the conversion of ADP-bound actin monomers, which have limited polymerization capabilities, into ATP-bound actin monomers that readily polymerize. As a result, profilin enhances the polarity of filaments. Profilin exhibits a higher affinity for polyproline sequences compared to actin. This affinity enables profilin to readily bind to the FH1 domains of formin proteins, leading to an acceleration of filament elongation. This phenomenon also applies to NPFs such as the WASP-family proteins and their (P) domain [38].

#### Capping proteins

Capping proteins exert their regulatory function by binding to the barbed end of growing actin filaments, thereby preventing the addition of new monomers. This action halts filament elongation and restricts the filament's length [40]. Furthermore, recent research has revealed the involvement of capping proteins in the branching process.

The WH2 (W) domain of NPFs can bind to actin monomers and interact with filament barbed ends that are not capped by other binding proteins. This mechanism, known as "barbed end interference" hinders the binding of NPFs to globular actin, which impedes the activation of Arp2/3 complex. Consequently, capping proteins promote branching [41]. Capping proteins exhibit a Brownian ratchet dynamics, which means their response to stress is similar to that of actin monomers. This characteristic has a significant impact on how branched actin networks adapt their architectural organization in response to changing loads [42].

### Severing proteins

The ADF/cofilin protein family represents a prominent group of severing proteins. Overall, these proteins facilitate the disassembly of actin filaments by inserting themselves between actin monomers, thereby catalyzing filament severing. In addition, they also promote depolymerization at both ends of the filament [43]. During this process, ADF/cofilin proteins form protein-rich domains along the filament, leading to a conformational change that modifies the twist of the fiber. Consequently, a mechanical torque is exerted, further enhancing the severing mechanism [44]. It is worth to note that the fragmentation is happening at the boundaries between bare and ADF/cofilin-decorated segments. In addition, ADF/cofilins have a low affinity with ATP-actin sub-units, targeting ADB-bound ones, which preserves the integrity of networks on their growing site.

## 1.2.3 Cross-linkers and molecular motors

While regulators are important to control the assembly, disassembly and the pool of actin, they poorly participate to connect filaments to each others to generate structures. This is, at first glance the role of crosslinkers and molecular motors.

### Cross-linkers

Cross-linking proteins create physical connections between actin filaments. By doing so, they contribute to the stabilization of higher-order structures such as lamellipodia or filopodia [45]. These cross-linkers typically possess two actin-binding domains (ABDs), with each domain connecting to an individual actin fiber. The distance between ABDs influences the ability to establish connections between filaments and affects the mechanical properties of the cross-linker. In addition, the flexibility of the link between the ABDs impacts the mechanical response of the system. Small crosslinkers like fascin, fimbrin or $\alpha$-actinin ($\sim$ 10 - 40 nm) form compact bundles, whereas larger and more compliant ones like filamin ($\sim$ 150 nm) form looser bundles or mesh-like networks [46].

Overall, an increase in connectivity through cross-linking leads to an increase in the stiffness of the actin network [15]. However, it is worth noting that the attachment and detachment kinetics of cross-linking proteins are considerably rapid compared to artificial polymers. They can attach to and detach from actin filaments on a timescale of the order of seconds to tens of seconds. Theses rates, vary between the different forms of cross-linkers [47], temperature and the force applied. This finding is crucial in understanding why cells exhibit stiffness on short timescales but possess a softer and more flow-like behavior on longer timescales. The rapid dynamics of cross-linkers allow them to rearrange and contributes to the overall mechanical response [48].

### Molecular motors

Molecular motors are a class of proteins capable of undergoing conformational changes to move along fibers in an ATP-dependent manner. This energy consumption enables them to perform work and permits directed motion. Among these motors, myosins specifically associate with actin fibers and exhibit movement toward the barbed end of the filament. Myosins are composed of a tail region that is connected to one or two heads, which can attach to and detach from actin fibers. Myosin I consists of a single head domain, with its tail region connected to a vesicle. When organized in groups, these myosins transport vesicles along actin fibers in proximity to the plasma membrane, facilitating processes such as endocytosis or exocytosis.

On the other hand, myosin II functions as a dimer, featuring two heads. This class of myosins is primarily responsible for generating muscle contraction in the majority of muscle cells by connecting several fibers. In actin bundles, Myosin II activity can induce contraction forces of the order of 100 pN [49]. In addition Myosin II contraction has been shown to induce actin filament fragmentation, as contraction can induce buckling and lead to breakage [50].

## 1.3 Actin structures

Therefore, the polymerization of actin filaments and their interaction with actin binding proteins give rise to a wide range of structures. Notably, rapidly growing filaments have a tendency to form a fine meshwork, while slowly elongating fibers organize themselves into tightly packed bundles. This architectural diversity is governed by kinetic factors. The unique arrangement of each filament contributes to the distinct mechanical properties and biological functions of the resulting structure. In the subsequent discussion, we will present a concise summary of several common actin structures, as illustrated in Figure 1.7.

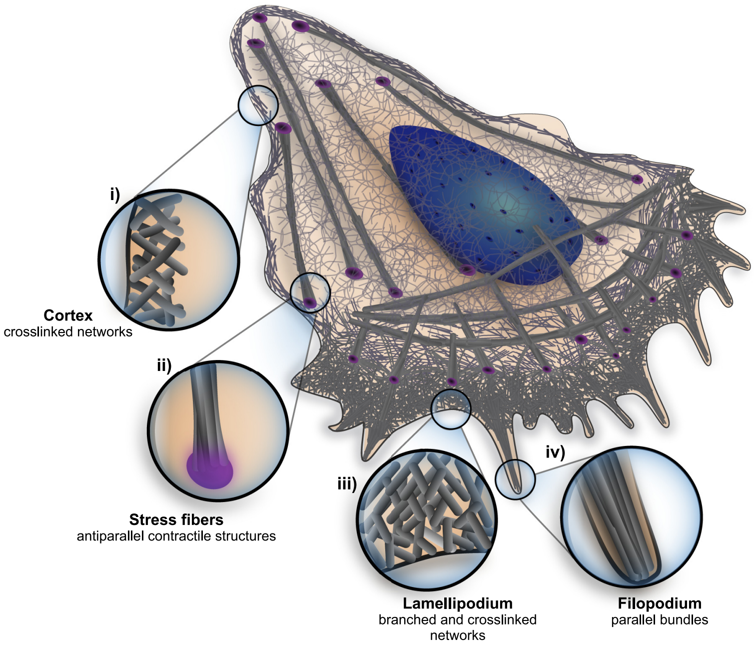

Figure 1.7: Scheme of the main actin structures in an eukaryotic cell, from [5].

## Filopodium

Filopodia are assemblies of elongated fibers that exhibit parallel growth, with their barbed ends directed towards the cell membrane [51]. This orientation is achieved through the involvement of formins and Ena/VASP proteins, which help anchor the barbed ends at the tip by facilitating polymerization. The individual fibers within filopodia are interconnected by small and tight crosslinkers like fascin. With a diameter of a few hundred nanometers, filopodia can extend to lengths of a few micrometers. On average, they consist of about ten to thirty fibers. Studies have demonstrated that an optimal number of thirty fibers permits to prevent buckling when the fiber count is low and to avoid high diffusion of G-Actin when there is an excessive number of fibers [52]. As filopodia grow, they induce deformations in the cell membrane, enabling them to explore their surroundings at the tip and sense the environment. They protrude at velocities about 0.16 $\mu$m.s$^{-1}$.

## Lamellipodium

Lamellipodia are almost two-dimensionally growing, branched structures that are stabilised by cross-linking proteins, see Figure 1.8. These protrusions help the cell sense their environment and enable movement through crawling motility. WAVE Nucleation Promoting Factors (NPFs) located at the cell membrane activate the Arp2/3 complex, which triggers nucleation of new actin branches and causes membrane deformation. Branch elongation is limited by capping proteins that promote the orientation of short branches towards the membrane to activate the branching process. The structure of the lamellipodium adapts to mechanical forces, resulting in a denser actin network and a wider distribution of branching points [53].

## Cortical actin

The cortex is a thin layer of cross-linked filaments, beneath the plasma membrane that is contractile due to the presence of myosins motors. It is large of a few hundred nanometers and also composed of actin bundles. Its dynamics plays an important role in cell shape changes [54]. For instance, the induced cortical contractility, balanced by the osmotic pressure difference explains the rounding of cells just before division [55].

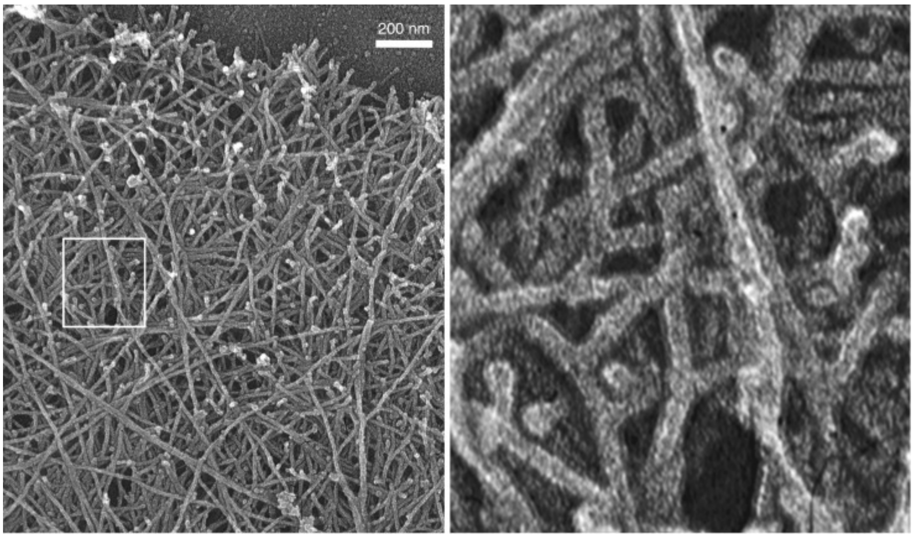

Figure 1.8: Actin filament organization in a lamellipodium at the leading edge of a fish epidermal keratocyte, from [56].

### Stress fibers

Stress fibers are bundles of elongated fibers that exhibit an anti-parallel orientation. These fibers are interconnected throughout the structure by $\alpha$-actinin cross-linkers and non-muscle myosin II motors. Stress fibers extend over significant portions of the cell and have the ability to anchor to focal adhesion points. The contractility generated by stress fibers contributes to the maintenance of these focal adhesions. By anchoring to these points, stress fibers are able to probe and assess the mechanical properties of their surrounding environment. This enables them to adapt their structure in response to the stiffness of the environment, which is crucial for cell motility [57]. Stress fibers also play important roles in processes such as morphogenesis, cell migration, and mechanotransduction.

### Endocytosis

During endocytosis, external materials, such as nutrients or signaling molecules, are engulfed by the cell through the formation of membrane protrusions facilitated by branched actin networks. The branching of actin filaments in endocytosis patches is activated by proteins belonging to the WASP family. Once the membrane protrusion surrounds the external material, the endocytosis patch undergoes budding, leading to the internalization of the cargo and the formation of a vesicle containing the substances within. This process allows the cell to regulate various cellular functions such as nutrient uptake, receptor internalization or membrane remodeling.

### Podosomes

Podosomes are adhesion sites that establish connections between the actin cytoskeleton and the extracellular matrix, see Figure 1.9. In macrophages cells, for example, podosomes play a role in sensing the stiffness of the surrounding extracellular environment by generating forces that can reach tens of nN, as measured by atomic force microscopy (AFM) [58]. A podosome typically consists of a central core rich in actin filaments that protrude into the extracellular space, surrounded by an adhesion ring. The protrusion of the core is made possible by the counteracting forces exerted by the adhesion ring through traction. The forces generated by the protrusive action of podosomes surpass the force produced by the polymerization (pNs) of actin fibers at the core membrane. To explain this phenomenon, a recent model based on the storage of elastic energy within bent filaments has been proposed and investigated. In this model, the actin network within podosomes acts as spring-loaded material, enabling podosomes to exert nN forces that overcome the limits of actin polymerization [59].

Furthermore, podosomes and endocytosis structures highlight the importance of branched actin force generation, which can rely on the stored elastic energy through polymerization. Overall, these diverse cytoskeletal organizations and processes highlight the versatility and importance of actin dynamics in various cellular functions.

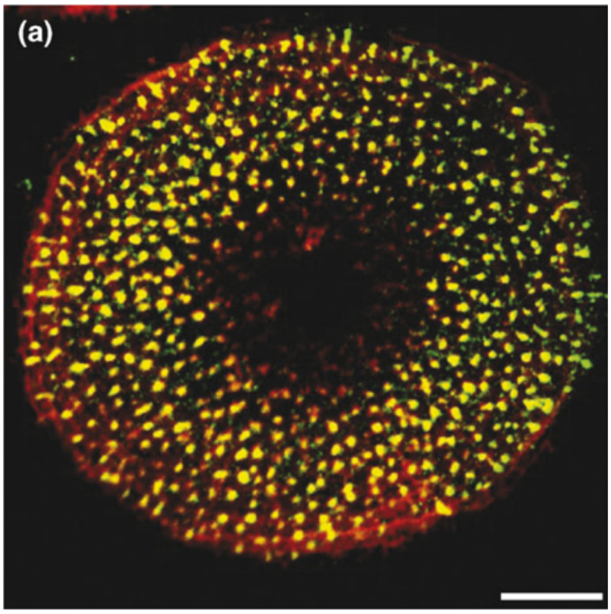

Figure 1.9: Confocal immunofluorescence image of podosomes in a primary human macrophage. F-actin (red) and WASP (green) colocalize in the core structure of podosomes (yellow) (scale bar = 10 $\mu$m), from [60].

# Chapter 2

# Actin mechanics and rheology

In order to execute diverse essential cellular functions, actin relies upon its intrinsic semi-flexible filament nature [15], and on the variety of network configurations. Before delving into investigations on network mechanics, we provide a concise introduction of the mechanics of semi-flexible polymers and a brief overview of viscoelasticity.

## 2.1 Semi-flexible polymer

### 2.1.1 Worm-like chain model

Bio-polymers, particularly those found in the cytoskeleton, are composed of proteins that are significantly larger than the atomic or molecular scales. As a result, they form fibers that are more rigid compared to synthetic polymers. They serve as prime examples of semi-flexible fibers, exhibiting configurations that deviate from the random coil structures commonly observed in polymer physics, demonstrating distinct elastic and viscoelastic properties.

In general, a polymer is considered semi-flexible when its resistance to bending, or bending modulus, is sufficiently high to overcome entropic effects. While bending modulus promotes straight conformations, maximizing entropy typically leads to the formation of random coils. In their native state, semi-flexible polymers display minor thermal fluctuations around a relatively straight inextensible conformation. In fact, in the total absence of thermal fluctuations ($T = 0$), it appears as a rod with the countour length $L_c$ identical to the shortest length between the two ends $L$. However, thermically induced transverse fluctuations ($T > 0$) lead to the contraction of $L$, such that $L < L_c$, see Figure 2.2, (Right).

To quantitatively describe the regime of thermal equilibrium, the persistence length serves as an intuitive measure, representing the contour length at which significant bending fluctuations occur. In the case of the widely used worm-like chain (WLC) model, the bending energy is described by the following expression:

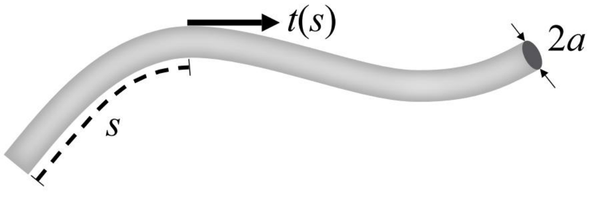

Figure 2.1: Scheme of a semi-flexible polymer of radius $a$, $\vec{t}(s)$ defines the local orientation of the fiber on the curvilinear abscissa $s$, from [15].

$$H_B = \frac{\kappa}{2}\int \mathrm{d}s \left|\frac{\partial \vec{t}}{\partial s}\right|^2 \tag{2.1}$$

With $\kappa$ the bending modulus, $s$ the curvilinear abscissa and $\vec{t}(s)$ the tangent vector along the chain, see Figure 2.1:

$$\vec{t}(s) = \frac{\partial \vec{r}}{\partial s}, \text{ with } \vec{r}(s) \text{ the chain position}$$

Moreover, considering that the bending modulus $\kappa$ is measured in units of energy multiplied by length, and taking into account that $k_BT$ is the inherent energy scale resulting from Brownian fluctuations, the expression for the persistence length arises naturally as $\ell_p = \kappa/k_BT$.

Indeed, it is possible to demonstrate this relationship by considering that small variations in orientation are independent degrees of freedom that adhere to the equipartition theorem. Thus it can be shown that the correlation function of the orientation vector decays according to the following expression:

$$< \vec{t}(s) \cdot \vec{t}(s') >= e^{-|s-s'|/\ell_p} \text{ where } \ell_p = \frac{\kappa}{K_BT} \tag{2.2}$$

Hence, when a fiber is in a thermal equilibrium at temperature T, the persistence length serves as a geometric measure of its stiffness. It is crucial to note that this quantity is only meaningful in the context of thermal equilibrium, and Brownian fluctuations.

### 2.1.2 Buckling threshold

We now assume that our fiber of length $L_c << \ell_p$ is under tension or compression $\tau$, along an axis $x$. For the sake of simplicity, we just consider a single transverse deflection $u(x,t)$. Moreover, if we consider that the chain is in-extensible, the end-to-end contraction of the chain $\Delta L = L_c - L$ can be approximated as :

$$\Delta L \approx \frac{1}{2}\int \mathrm{d}x \left|\frac{\partial u}{\partial x}\right|^2 \tag{2.3}$$

Thus, the energy with bending and tension terms is :

$$H = \frac{1}{2}\int \mathrm{d}x \left[\kappa\left(\frac{\partial^2 u}{\partial x^2}\right)^2 + \tau\left(\frac{\partial u}{\partial x}\right)^2\right] \tag{2.4}$$

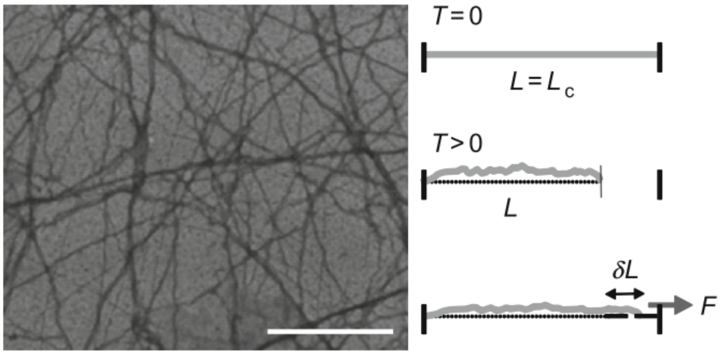

Figure 2.2: (Left) Electron microscopy image of F-actin network with a 1 $\mu$ m scale bar. (Right) Variation of the end-to-end length $L$, adapted from [61].

Then, if $u(x)$ is represented by its Fourier Series decomposition:

$$u(x,t) = \sum_q u_q \sin(qx) \tag{2.5}$$

We obtain the following expression for the energy:

$$H = \frac{L_c}{4} \sum_q (\kappa q^4 + \tau q^2) u_q^2 \tag{2.6}$$

Here, for $\tau$ positive, each term in the sum contributes positively so that increasing $u_q$ goes with increasing the overall stored energy, which accounts for stability. However, in the scenario of compressive stress where $\tau$ is negative, this is no longer the case when $\tau < -\kappa q^2$. Here increasing the value of $u_q$ leads to a decrease in energy, indicating instability. This onset, known as buckling instability, occurs at the smallest possible value of $q$ determined by the length of the fiber: $q_l = \pi/L_c$. This leads to the expression of the buckling force threshold:

$$\boxed{F_{Buckling} = \kappa \left(\frac{\pi}{L_c}\right)^2} \tag{2.7}$$

### 2.1.3 Force extension response

As seen in Figure 2.2, right, at room temperature, Brownian fluctuations reduce the end-to-end distance below the contour length. Here we will review the overall force response of F-Actin, plotted in Figure 2.3. In general, for small positive or negative forces the filament behaves like a linear entropic spring (red dotted line). Then for forces larger than 0.1 pN, as the end-to-end distance is approaching the contour length, the entropic spring becomes non-linear. In the case of an in-extensible fiber the force required for extension quickly diverges (black dotted curve). As actin-filaments are not completely inextensible, their length can be extended beyond the contour length for forces larger than 100 pN (blue dotted line) [29]. Under compression, the buckling force is $\sim$ 0.4 pN, which allows for a large range of distances under nearly constant force. The overall picture is summarized in the dark line [62]. In addition, it is worth to note that the helicity of F-Actin induces coupling between bending and twisting [63].

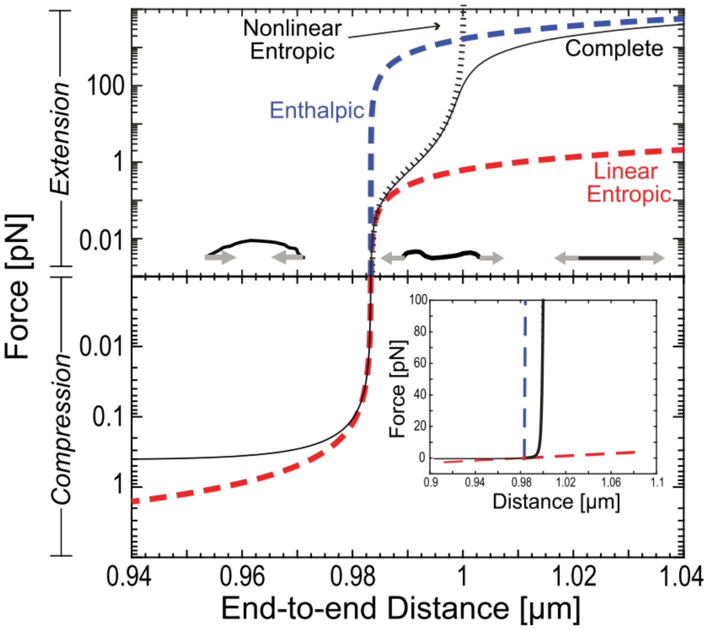

Figure 2.3: Force extension of an actin filament with a 1 $\mu$m contour length, normal-log plot, from [62].

## 2.2 Viscoelasticity

### 2.2.1 Solid and liquids

Solid materials exhibit elastic behavior, which refers to the capacity to return to their original configuration after deformation. When a stress $\sigma$ is applied to a material, it induces a corresponding strain $\epsilon$, and vice-versa. The elastic modulus, specifically describes the relationship between stress and strain. In the case of a uni-axial stress situation, where the material is subjected to compression or tension, the Young modulus E characterizes the elastic response of the material:

$$\sigma = E \ \epsilon \tag{2.8}$$

In addition, different kinds of elastic modulus can be defined, depending on the direction of the applied stress. For instance, as introduced before, the bending modulus $\kappa$ measures the resistance to bending while the shear modulus $G$ measures the response to a shear deformation.

In simple materials, the elastic modulus remains constant regardless the applied strain, indicating a linear elastic behavior. However, when the material exhibits a dependence on the strain ($E = E(\epsilon)$), it deviates from linearity. When the elasticity increases with increasing applied stress, materials are said to be *stress-stiffen*, in contrast when the elasticity decreases they are *stress-soften.*

Additionally, beyond the yield point, the material undergoes irreversible plastic deformations, losing its elastic behavior. Moreover, the relationship between the bending modulus $\kappa$ and the Young Modulus $E$ is the following for a semi-flexible polymer [64]:

$$\kappa = \frac{\pi}{4} E a^4 \tag{2.9}$$

In contrast to solids, liquids are characterized by their viscosity. The stress experienced by a liquid is determined by the rate at which it undergoes strain, with this relationship being governed by its viscosity, also known as dynamic viscosity. The viscosity of a liquid weighs the strain rate, indicating how resistant the liquid is to flow under the influence of applied stress [65].

$$\sigma = \eta \, \dot{\epsilon} \tag{2.10}$$

### 2.2.2 Complex materials

In general, cytoskeletal polymer networks exhibit viscoelastic behavior, characterized by a combination of elasticity (response to deformation) and viscosity (response to the rate of deformation). At short time scales, these networks display elastic behavior, meaning they can store and recover energy upon deformation. However, at longer time scales, they exhibit viscous behavior due to the rearrangement of the network structure. For instance, the viscoelastic response of the cell cortex, plays a crucial role in maintaining cell integrity and shape.

Viscoelastic properties are not limited to cytoskeletal networks but are also observed across different scales and structures. Developing tissues, for example, demonstrate dynamic organization and reorganization, indicating fluid-like characteristics in their material properties over long time scales. However, when subjected to mechanical deformations, they exhibit elastic relaxation [66]. The adaptation and response of epithelial tissues to stress or laser ablation have been extensively studied, revealing their viscoelastic properties [67]. At the cellular scale, viscoelastic properties have been identified as markers of cancer cells.

In addition, recent studies have shed light on the significance of cytoplasmic viscoelastic properties in the proper alignment of the mitotic spindle during the initiation of cell division. These properties play a crucial role in facilitating symmetric division when disrupted [68]. Interestingly, it has been observed that viscoelastic properties depend on the size of the object being moved. This phenomenon arises due to hydrodynamic interactions between the moving object and the static cell surface [69].

In order to characterize and quantify viscoelastic properties, different combinations of springs and dashpots arranged in parallel or series are employed to construct models that replicate the observed behavior. For example, the Maxwell model consists of a spring and a dashpot connected in series, while the Kelvin-Voigt model comprises a spring and a dashpot connected in parallel.

### 2.2.3 Rheology measurements

Given the frequency-dependent nature of viscoelastic properties in biopolymer networks, it is advisable to investigate their response under periodic stimulation. Consequently, in order to characterize their linear response, oscillatory shear strain is applied to the material, and the resulting stress is measured. The in-phase response corresponds to the shear elastic modulus, representing the storage of mechanical energy within the material. On the other hand, the out-of-phase response corresponds to the viscous loss modulus, representing the dissipation of mechanical energy within the material. By employing a rheometer, we can determine the shear modulus $G$, which consists of a real part denoting the elastic response $G'$ and an imaginary part denoting the viscous response $G''$.

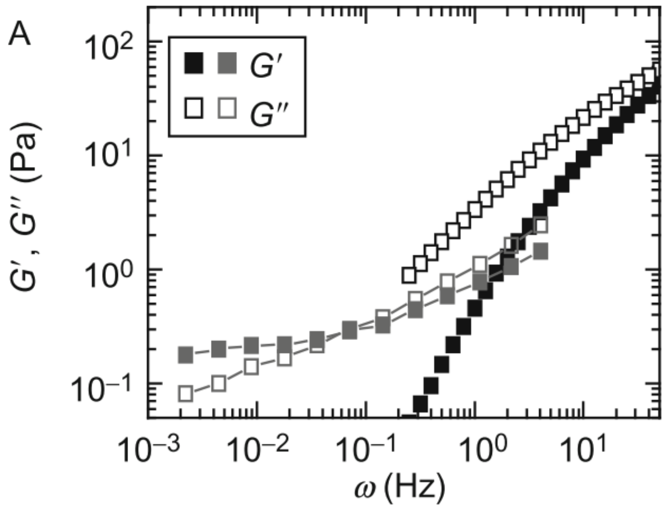

Figure 2.4: Frequency-dependent elastic and viscous modulus of a solution of flexible polymers (black) and a F-Actin newtork (grey), from [61].

$$G(\omega) = G' + iG'' \tag{2.11}$$

Therefore, the behavior of materials can vary between solid-like and liquid-like states depending on the frequency. This phenomenon is particularly relevant when studying the dynamics of F-Actin, as it exhibits frequency-dependent behavior, see Figure 2.4. In contrast to flexible polymer solutions (represented by black symbols), which predominantly manifest viscous properties over a broad range of frequencies, the solution containing F-Actin filaments (represented by grey symbols) primarily demonstrates the prevalence of the elastic modulus at frequencies below 0.1 Hz, but transitions to a dominance of viscosity at higher frequencies. Consequently, it is necessary to consider the influence of frequency-dependent dynamics when constructing mechanical models. Moreover, the dynamics and rates at which crosslinkers attach to and detach from F-Actin filaments assume a pivotal role in determining the frequency-dependent behavior.

## 2.3 Rheology of actin networks

### 2.3.1 Free networks

#### Entangled networks

In the absence of crosslinkers, filaments assemblies tend to form homogeneous networks with filaments evenly spaced at a relative uniform distance known as the mesh size $\xi$. When the persistence length $\ell_p$ of the filaments is significantly larger than the mesh size, it becomes feasible to express the mesh size in terms of the volume fraction $\phi$ and the radius of the fiber $a$.

$$\xi = \frac{a}{\sqrt{\phi}} \tag{2.12}$$

When filaments exceed the mesh size, they become entangled within the network, leading to motion constraints and the emergence of viscoelastic behavior, which occurs on a length scale basis [70]. It is noteworthy that this entanglement also artificially enhances network connectivity and prevents the realignment of filaments into bundles [71].

In Figure 2.5, the storage modulus $G'(\omega)$ and loss modulus $G''(\omega)$ are represented for a 1 mg.mL$^{-1}$ solution of F-Actin, both in the presence and absence of crosslinkers (specifically, biotin-neutravidin bonds with high irreversibility) [72]. This experimental findings of Koenderink et al. are compared to a theoretical framework proposed by Gittes and MacKintosh [73], which addresses the shear modulus of entangled and cross-linked networks at high frequencies, assuming an affine network behavior (where the macroscopic deformations closely resemble the microscopic deformations). According to the theory, the shear modulus at high frequencies is primarily determined by the relaxation of individual polymer chains in both solutions. Increasing the frequency results in a higher shear modulus. Specifically, on shorter time scales, fewer bending modes can relax, leading to reduced compliance and increased stiffness of the fiber. The authors derive the following scaling relationship:

$$G(\omega) \approx \frac{1}{15}\rho\kappa\ell_p\big(-2i\zeta/\kappa\big)^{3/4}\omega^{3/4} - i\omega\eta \tag{2.13}$$

The scaling relationship observed in the form of $\omega^{3/4}$ is noteworthy in the context of the mentioned system, where $\rho$ represents the filament density, $\kappa$ denotes the bending modulus, $\zeta$ is the lateral drag coefficient per unit length, and $\eta$ stands for the viscosity. Notably, the dependence of the elastic modulus $G'(\omega)$ on density $\rho$ is highly pronounced. Furthermore, this scaling relationship is independent of network parameters such as the mesh size $\xi$. Since filaments contribute independently to the shear modulus, there is no distinction observed between entangled and cross-linked networks, as indicated by the black lines in Figure 2.5.

In the figure presented, it can be observed that cross-linked networks display higher viscosity compared to entangled ones, and this observation aligns with theoretical predictions across a broader range of frequencies. The storage modulus of entangled networks consistently remains lower than that of cross-linked solutions, and coincides with theoretical expectations particularly at extremely high frequencies. At lower frequencies, the storage modulus of the non-cross-linked solution is approximately 0.2 Pa, corroborating previous conventional rheology measurements [48] [65] which exhibit the same plateau.

#### Rigidly crosslinked networks

As depicted in the Figure 2.5, the introduction of cross-linkers leads to a notable enhancement in both elastic and viscous moduli of the networks [48] [72]. Having examined the frequency-dependent behavior of actin rheology, we now shift our focus to its dependence on stress (or strain), thereby discerning different regimes based on variations in actin concentration and filament lengths.

In the presence of non-dynamic and rigid cross-linkers, it is assumed that the mechanical response is primarily determined by the flexibility of the actin filaments. Furthermore, when cross-linkers exhibit a high binding affinity and remain bound to F-Actin for extended periods, their dynamics can be neglected. In such cases, there is no active remodeling the network can only adapt through bending and tension. Avidin-biotin cross-links [72] [74] and scruin [75] serve as examples of this scenario.

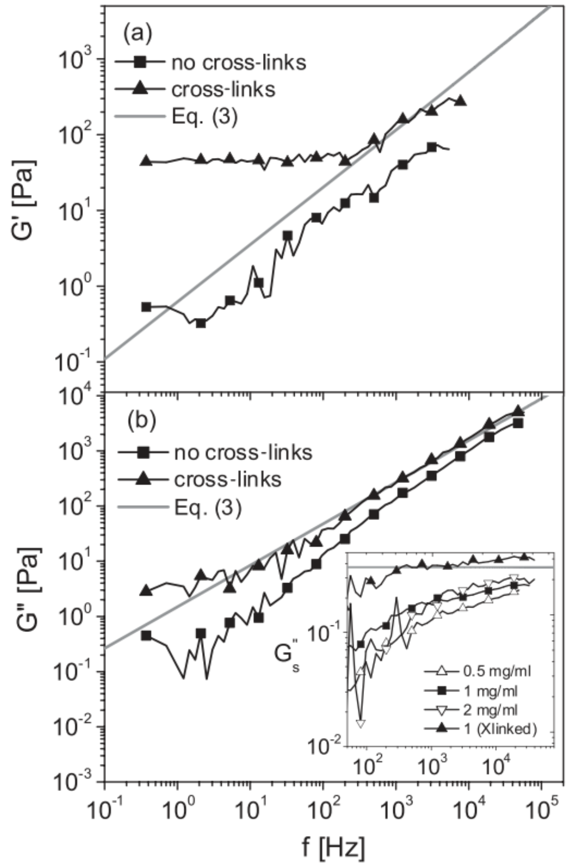

Figure 2.5: (a) Storage modulus $G'(\omega)$ and loss modulus $G''(\omega)$ (b) of a 1 mg.mL$^{-1}$ solution of F-actin filaments ($\sim$ 25 $\mu$M) against frequency $f$, from [72].

Two characteristic regimes govern the mechanics of actin networks. On the one hand, in networks composed of densely cross-linked long filaments, deformations exhibit self-similarity across macroscopic and microscopic length scales, thus referred to as affine networks. In this regime, the mechanical response is primarily governed by filament stretching [75], as illustrated in the bottom-left panel of Figure 2.6. Specifically, stretching occurs when applied stress restricts the range of accessible fluctuation configurations, known as the *affine entropic* regime. However, when the distance between cross-links $\ell_c$ is smaller than the persistence length $\ell_p$, the system resembles a dense network composed of macroscopic rods. In this scenario, stretching arises from the Young modulus of the filaments in an enthalpic response, referred to as the *affine mechanical* regime, as depicted in the right panel of Figure 2.6.

In stretch-dominated networks, an intriguing stress stiffening behavior is observed, as illustrated in Figure 2.7. This phenomenon arises from the nonlinear force-extension characteristics of individual filaments, as depicted in Figure 2.3. The storage modulus $G'$ increases until reaching a maximum stress $\sigma_{max}$ or strain $\gamma_{max}$, at which point the network "breaks". The breaking stress exhibits a linear relationship with the density of F-Actin filaments, indicating the rupture of individual filaments [65]. The maximum strain is proportional to the distance between cross-links, which scales approximately as $\ell_p \approx c_A^{-2/5}$ [75].

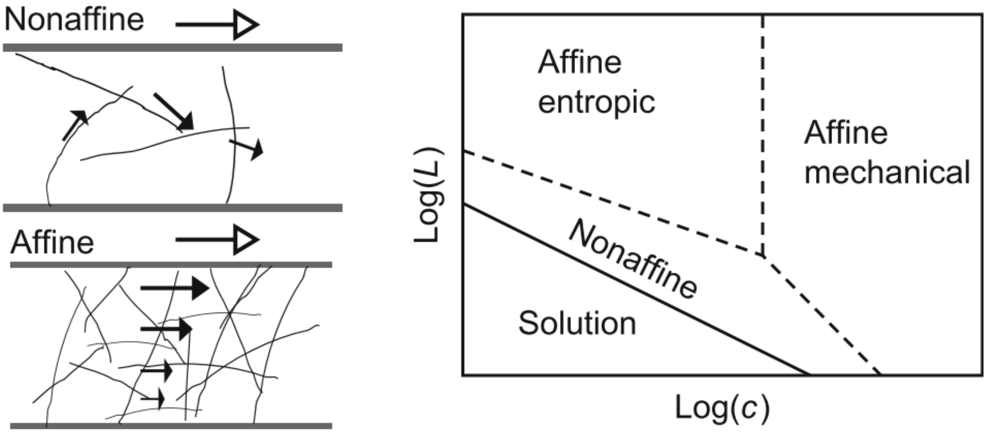

Figure 2.6: (Left) Schemes indicating the bend-dominated deformations in low density and sparsely cross-linked networks (top), and stretch-dominated deformations that occur in high density and densely cross-linked networks. (Right) Phase Space of the types of network deformations as a function of actin concentration log($c$) and filament lengths (presuming that every overlap has a rigid cross-linker, from [61].

On the other hand in the limit of poorly cross-linked networks with short filaments, stress imposed by an external shear result in *non affine* deformations throughout the network [76], see Figure 2.6, bottom-left. Indeed, under a shear stress, filaments will tend to bend and buckle resulting in a deformation that is not self-similar [75]. These bending-dominated networks soften under increasing stress [62] as seen in Figure 2.7. Thus, experiments and theory have demonstrated the complexity in even a model of system with rigid and nondynamic cross-linkers that can exhibit both enthalpic and entropic contribution to the mechanical response.

Both experimental findings and theoretical investigations have revealed the complex nature of systems even with rigid and non-dynamic cross-linkers, which display a combination of enthalpic and entropic contributions to the mechanical response. However, as discussed previously, physiological F-Actin cross-linking proteins have a finite binding affinity and a significant compliance. This affinity determines the timescale over which forces are efficiently transmitted through the network.

### Cross-linked dynamics limited networks

The contribution of cross-linkers kinetics and compliance has been studied *in vitro*. This dynamic nature enables networks to support stresses and reorganize in a “fluid-like” manner at long time scales. Here we will quickly review some studies that stress the impact of temperature, force and concentration on the systems’s properties. Firstly, temperature has been studied has a a way to alter the binding affinity of $\alpha$-actinin, resulting in modifications of bulk viscoelastic properties. At low temperature (around 6°C) networks are stiff and behaving like rigid-static cross-linked ones, whereas when the temperature is raised (to 25°C), the elastic modulus decreases drastically making the network become more “fluid-like” as expected [77]. Although temperature is rather unlikely to be a key control parameter *in vivo*, it highlights the importance to have dynamic cross-linkers to relax stress. More generally, the increase of binding affinity is associated with crosslinkers abnormalities which can favor kidney diseases [78].

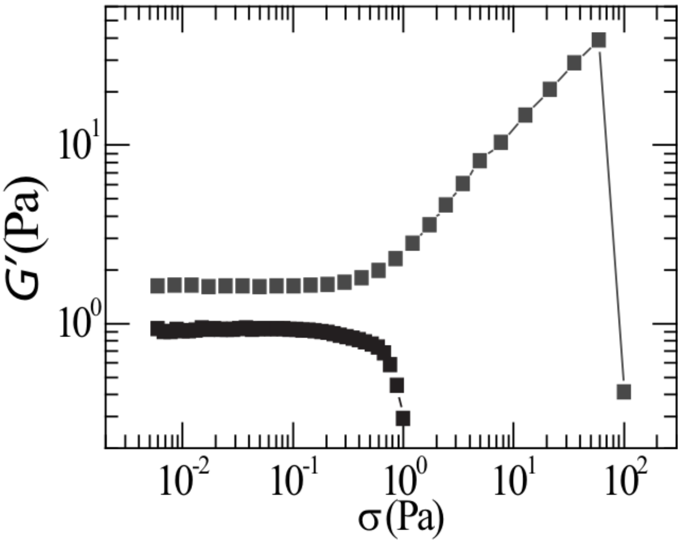

Figure 2.7: Shear Elastic modulus as a function of the applied stress for a network that is stretch dominated, which exhibit stress stiffening and failure (grey) and for a bending dominated one, which exhibit stress-softening (black), from [62].

In filamin-A networks, an increase in the length of cross-linkers results in a transition towards a more fluid-like structure, where the elastic modulus becomes highly sensitive to frequency. The modulus decreases more rapidly and exhibits lower overall values [79]. Remarkably, filamin-A networks demonstrate a non-linear stress-stiffening behavior similar to that observed in scruin networks. The elastic modulus increases by two orders of magnitude, reaching stiffness levels characteristic of living cells (around 1 kPa), as shown in Figure 2.8. This quantitative comparison between the characteristics of pre-stressed networks in vitro and the mechanical properties of adherent cells in vivo emphasizes the potential importance of non-linear elastic effects in determining the mechanical response of the cytoskeleton. Notably, in contrast to scruin networks where the concentration of actin was the limiting factor for network failure, in filamin-A networks, it is the concentration of cross-linkers that governs the breaking point [80].

In summary, freely self-assembling actin networks exhibit a wide range of mechanical behaviors, which are influenced by the lengths of the fibers and the nature and number of cross-linkers that connect them. However, these networks lack the specific structures and organization observed in living cells, as they arrange themselves in a loosely constrained environment. Overcoming this challenge of achieving directed dense structures has been performed by the discovery of the Arp2/3 machinery in the late 1990s: Cdc42 triggers the interaction between N-WASP and the Arp2/3 complex [81]. This breakthrough has allowed researchers to mimic cytoskeletal structures observed in living cells, such as *Listeria monocytogenes* motility using purified proteins [82]. Thus, mastering the Arp2/3 machinery enables the nucleation and elongation of actin filaments in a polarized manner on functionalized surfaces, achieving densities comparable to those observed in cells.

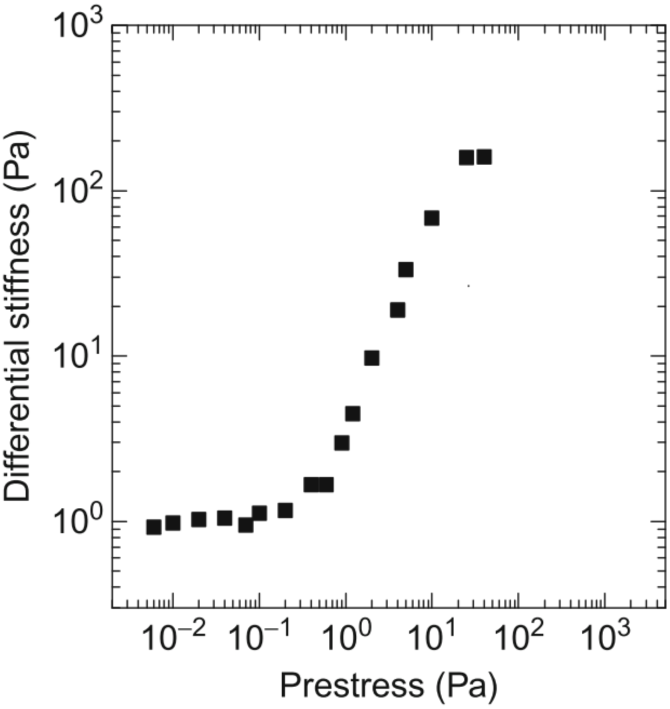

Figure 2.8: Differential shear modulus as a function of pre-stress (f = 0.2 Hz) for physiological relevant filamin-A networks, $c_A$ = 48 $\mu$M, R = 1/100, from [61] [80].

### 2.3.2 Constrained networks and stress adaptation

**Micro-pipettes and actin comet**

The team led by Cecile Sykes conducted the initial measurements of the mechanical properties of dense branched actin networks, primarily to quantitatively investigate the forces generated by branched-actin-based propulsion of *Listeria monocytogenes* [83], relying on purified proteins. The experimental setup involved attaching a bead coated with N-WASP to a force probe, a flexible rod capable of measuring forces through its deflection. Upon activation of Arp2/3 by the NPFs at the bead surface, a comet-like structure of actin formed and extended from the bead. The tail of this actin comet was held by a micro-pipette, which could apply pulling or pushing forces on the network, up to a few nN, as shown in Figure 2.9 (Left). The experimental solution comprised purified proteins, including actin, Arp2/3, profilin, ADF and gelsolin (a capping protein).

In the experiments, the actin comet was pulled at a velocity higher than the free-growing velocity of actin filaments, resulting in an elastic deformation of the comet tail ($v$ = 10 $\mu$m.min$^{-1}$). Since the contribution of the comet growth can be neglected, the force-displacement relationship of the system exhibits a linear response, allowing the determination of the rigidity of the comet, as shown in Figure 2.9 (Right). Using the dimensions of the structure, it becomes possible to estimate the Young Modulus of the material, the mean value was found to be 3.7 kPa. This value is notably higher compared to the elastic moduli discussed earlier, such as those of entangled networks, which are less than a pascal at low frequency measurements (as seen in Figure 2.5). This substantial difference highlights the distinct mechanical behaviors of actin networks. Furthermore, the stress required to tear the comet apart and break the gel-bead interface was estimated to be 250 Pa.

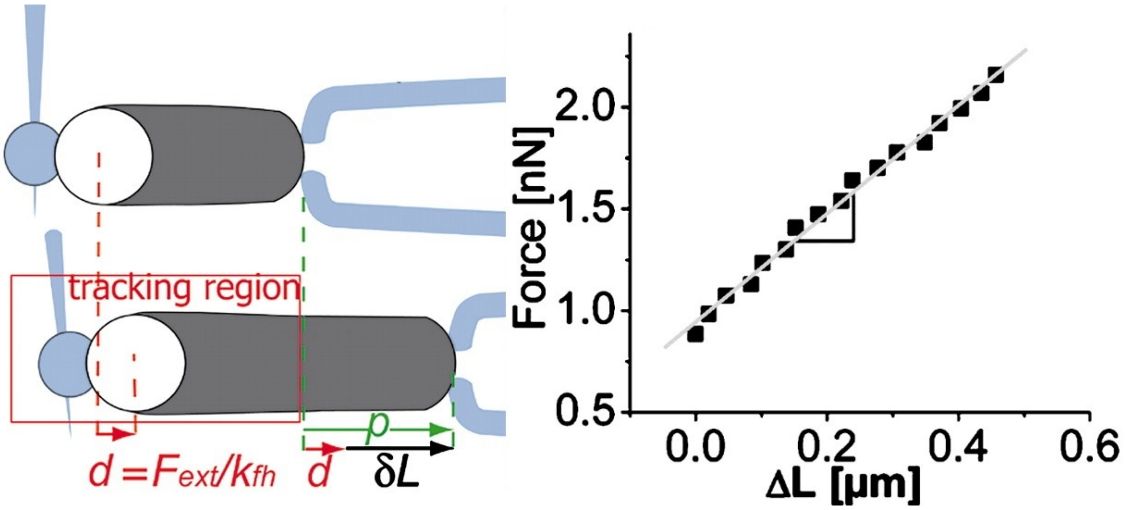

Figure 2.9: (Left) Experimental scheme: Actin comet in dark gray grows from the flexible handle bead in white and is held in its end by the comet holding micro-pipette: the deflection of the fiber, provides information on the force applied, (Right) Force as a function of the lengthening of the comet $\delta L$. The slope of 2.7 nN.$\mu$m$^{-1}$ corresponds to the comet rigidity, adapted from [83].

### AFM cantilever

Later, Dan Fletcher and his team employed a modified AFM (Atomic Force Microscope) cantilever to investigate the characteristics of dendritic actin networks. Their experimental setup allowed them to reach the stall force, which was not achieved in the previous work by Sykes team [84]. The AFM cantilever was coated with ActA, a nucleation-promoting factor found in *Listeria*, before being immersed in cytoplasmic extract from *Xenopus laevi* eggs. This functionalized surface triggered the formation of branches [85]. The cantilever exerted a restoring force that was proportional to its deflection, as depicted in Figure 2.10 (Right). By using AFM-based microrheology, Parekh et al., assuming minimal growth during their measurements, measured the frequency-dependent elastic and viscous moduli. In this setup, the functionalized surface was driven sinusoidally (shown in blue), and the force transmitted through the network was transduced by the cantilever, whose response was analyzed, Figure 2.10 (Left) [86].

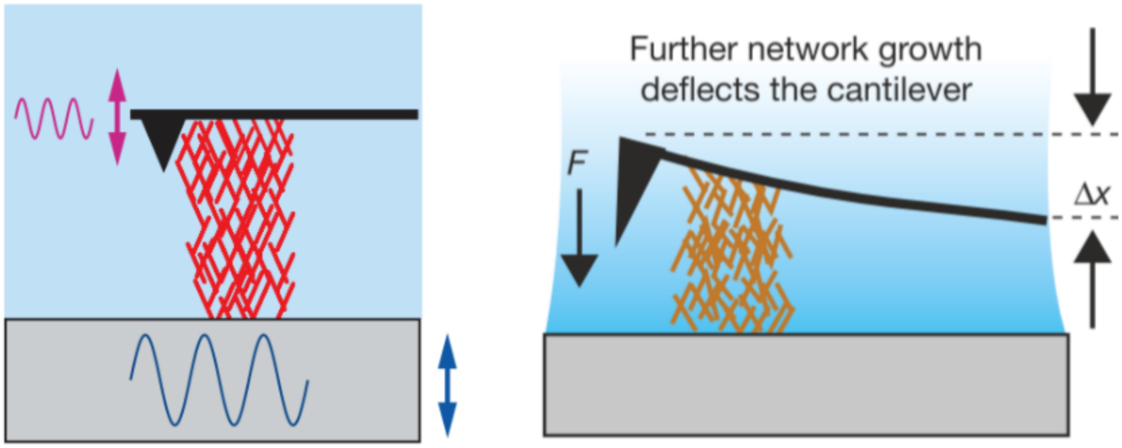

Figure 2.10: (Left) Cartoon illustrating the transmission of the sinusoidal surface displacement to the cantilever. (Right) Scheme of the growth of branched actin on the ActA coated AFM cantilever, adapted from [84] and [86].

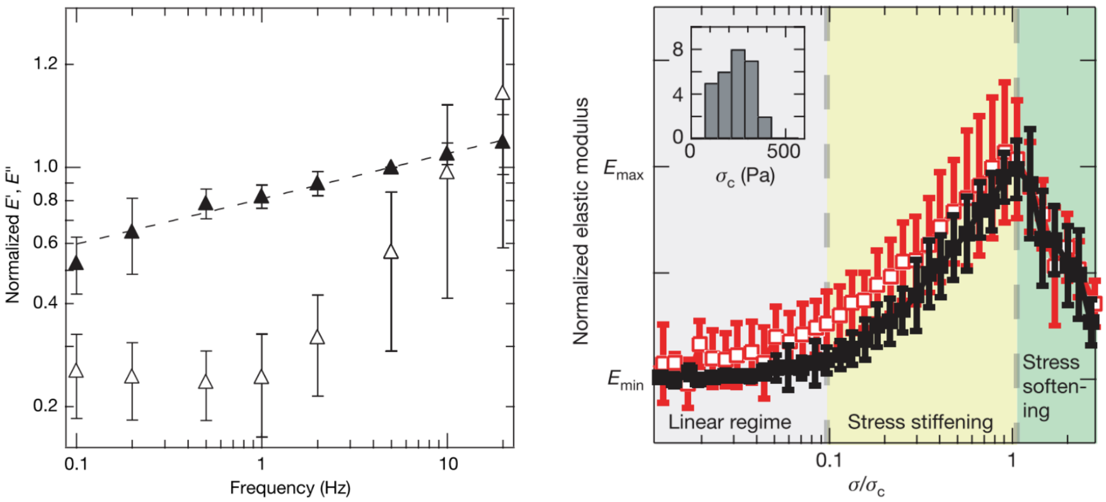

Figure 2.11: (Left) Frequency dependence of elastic (filled triangles, E') and viscous (open triangles, E") moduli. (Right) Averaged and normalized trace of nonlinear elasticity of actin networks: increased (black) and decreased stress (red).

As evident from Figure 2.11, the micro-rheology results demonstrate a frequency-dependent behavior with a predominance of the elastic response at low frequencies, while the viscous moduli increases and become dominant at higher frequencies, consistent with previous observations in Figure 2.4. The elastic modulus follows a power-law rheology with $E' \sim f^{\alpha}$, where $\alpha$ is approximately 0.13, yielding an average value of around 1 kPa.

Additionally, the stress dependence of the elastic modulus was explored under 5 Hz stimulation, revealing various regimes. Initially, there is a linear regime for stresses up to approximately 15 Pa that leads to a stress-stiffening behavior until a critical stress $\sigma_c$. Beyond $\sigma_c$, the elasticity gradually decreases. The stress-stiffening is attributed to entropic elasticity. Beyond $\sigma_c$ the stress-softening cannot be explained by the fracture of fibers or cross-linkers or by the network rearrangement since it is entirely reversible. The explanation lies in the fact that when the stress exceeds the threshold value, the compressional force surpasses the Euler buckling threshold. Buckling filaments display infinite compliance, rendering them unable to contribute to the network's elasticity. As a result, the network undergoes a transition where the stress-softening behavior becomes evident, and the elastic modulus decreases.

Ten years later, Peter Bieling and his team adapted the protocol used by Parekh et al [84]. to study the force-feedback of self-assembling branched actin networks [87]. To mimic the natural enrichment of WASP-family NPFs on cellular membranes, they enriched the base coverslip with the Arp2/3 activating region of WAVE1. Unlike Parekh et al., they loaded the system with purified components, including actin monomers, Arp2/3, capping proteins and profilin. The actin networks formed three-dimensional pillars, growing from WAVE1-coated squares with an area of 200 $\mu$m$^2$. Before the assembly initiation, an AFM cantilever was positioned over the coated surface to apply forces and measure the growing velocity, as depicted in Figure 2.12 (Top).

Indeed, by applying a constant force and using an optical feedback mechanism to maintain a constant deflection of the cantilever, they were able to study the stress adaptation of the growth velocity. Following a short adaptation phase, the network reached a steady-state condition characterized by a constant velocity regime, as depicted in Figure

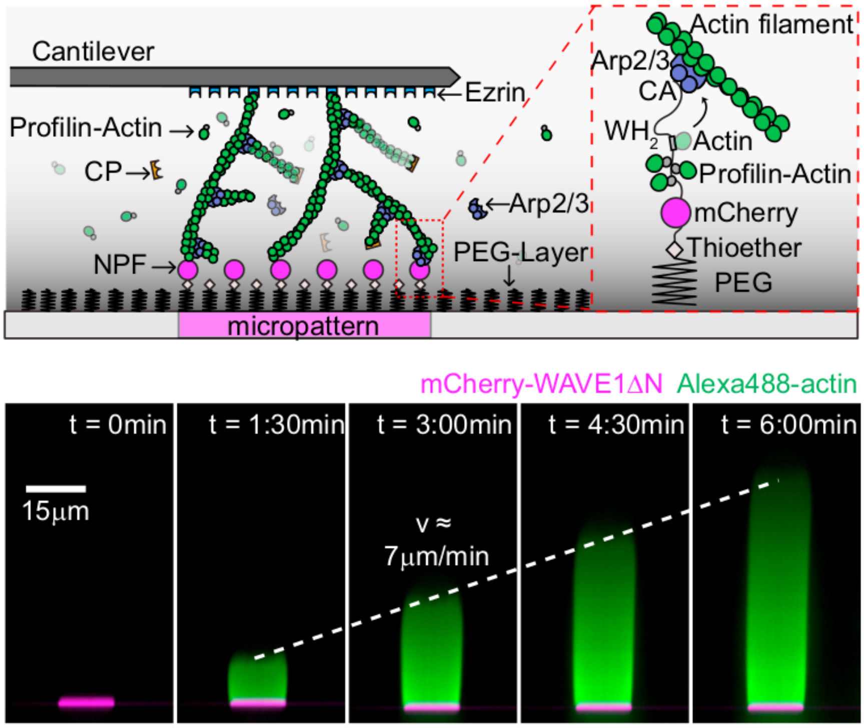

Figure 2.12: (Top) NPF patches, bound to a PEG passivated coverslip, rapidly assemble dendritic networks from profilin-actin, CP and Arp2/3. (Bottom) Confocal microscopy (reconstructed axial view) of actin assembly (Alexa488-actin, green) from WAVE1 micropatterns (magenta) after indicated time of protein addition, from [87].

2.12 (Bottom). This steady-state allowed the investigation of the effects of stress on both the velocity and the density of the network. Overall, when the stress increases, so does the density and the velocity decreases. The next section will likely delve into a detailed discussion of the observed effects on density and growth rate.

In their study, Bieling and his team used AFM-based micro-rheometry to investigate the material properties of the actin networks grown under various test loads. To stop the network growth, they introduced Latrunculin B, a compound that binds to actin monomers and halts polymerization, when the network reached a height of 10 $\mu m$. Surprisingly, when the growth stress was released, the height of the network increased only slightly (less than 10%), suggesting that the increase in density was more a result of architectural reorganization rather than elastic compression. The elasticity measurements fell within the range of $10^3$ to $10^4$ Pa, consistent with previous measurements, and both the elastic and viscous moduli increased with the growth stress.

The most striking finding was that when the response of the networks was investigated under various test loads, the networks were stiffer when the test load matched the original growth force experienced during assembly, as depicted in Figure 2.13 (Left). Similarly, the viscous modulus displayed a local minimum when the test load equaled the growth force. These results indicate that growing branched actin networks adapt to a specific growth force, becoming maximally stiff and minimally viscous at that load. This stress adaptation of the actin networks reveals a remarkable ability of the system to tailor its mechanical properties according to the mechanical environment it experiences during assembly.

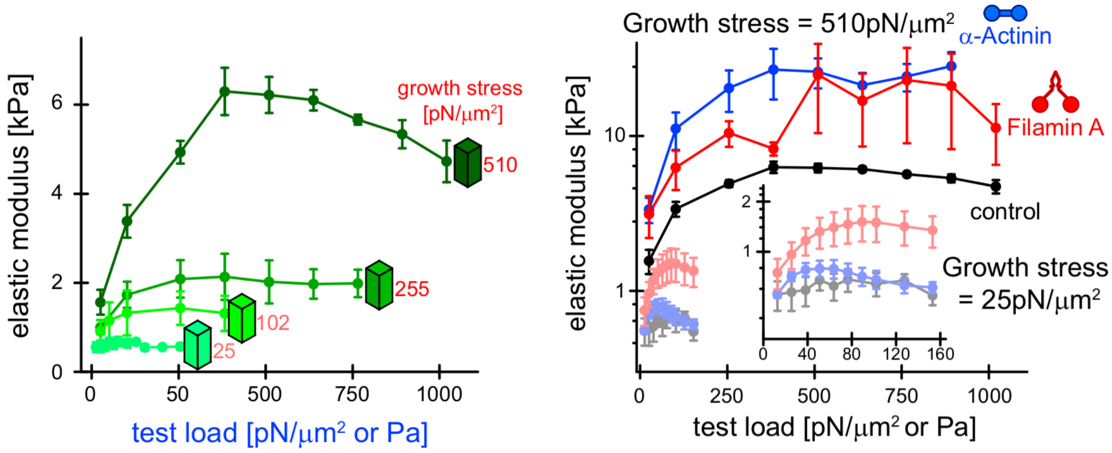

Figure 2.13: (Left) Network elasticity as a function of test load for networks assembled at different growth stresses as indicated. (Right) Network elasticity as a function of test load for networks assembled at a growth stress of 25 (light) or 510 pN.$\mu$m$^2$ (dark) growth stress and additionally crosslinked with either filamin-A (red) or $\alpha$-actinin (blue) or a buffer control (black)

Indeed, the study by Bieling and his team further confirmed the significant influence of crosslinkers on the elasticity of branched actin networks. The crosslinkers used, namely $\alpha$-actinin (short cross-linkers) and Filamin A (long cross-linkers), were introduced after the networks had terminated their growth with Latrunculin B. Both types of crosslinkers stiffened the network, although interesting differences in behavior were observed. For dense networks assembled under high forces, $\alpha$-actinin caused the most significant stiffening effect. However, in sparse networks assembled under low load, Filamin A has the greatest impact, as shown in Figure 2.13 (Right).

Notably, while crosslinkers did impact the stiffness of the networks, they did not qualitatively change the shape of the stress-stiffening curve. This finding indicates that the mechanical response of branched actin networks is primarily governed by their load-adaptive architecture rather than by the specific properties of the crosslinkers themselves.

### Magnetic colloids

Olivia du Roure and Julien Heuvingh's team has developed a micro-rheology measurement technique using supra-magnetic colloids to study the mechanics of dense branched actin networks. These colloids are coated with the VCA domain of neuronal WASP, which triggers the activation of Arp2/3. By using a minimal set of purified proteins, including G-Actin, Arp2/3, cofilin, and gelsolin, they activate the assembly of branched actin networks on the surface of these colloids. The growth of the gel is stopped after 15 min by dilution in buffer containing phalloidin, obtaining a stable network with a 650 nm thickness in average.

When a magnetic field is applied, the colloids become magnetic dipoles and self-assemble into chains of beads (Figure 2.14 Top-Inset). To measure the elastic modulus of the actin gel, they apply an increasing magnetic field which bring beads closer together, inducing a deformation of the gel between them. This allows them to measure the force required to compress the actin gel and bring the colloids closer together (Figure 2.14 Top). This technique enables access to the elastic modulus through a direct force-displacement relationship. An advantage of this method is that each pair of beads acts as a sensor, increasing the number of measurements for each batch of experiments.

Using this approach, they found that the average elastic modulus of the stable actin network was approximately 5200 Pa, in good agreement with other studies [88].

In the same work, they investigated the effects of varying Arp2/3 and gelsolin concentrations independently. While the estimated density of the network barely increased with increasing Arp2/3 or gelsolin, the gel exhibited a significant stiffening response in both cases, Figure 2.14 (Bottom), for the case of Arp2/3. When Arp2/3 concentration was increased further, the Young modulus reached a plateau, indicating a saturation of Arp2/3 activation by the NPFs. In fact, increasing the concentration of branching or capping proteins led to a decrease in the distance between branching points, which modified the origin of elasticity from an entropic stretching regime to a coupled enthalpic bending-stretching regime.

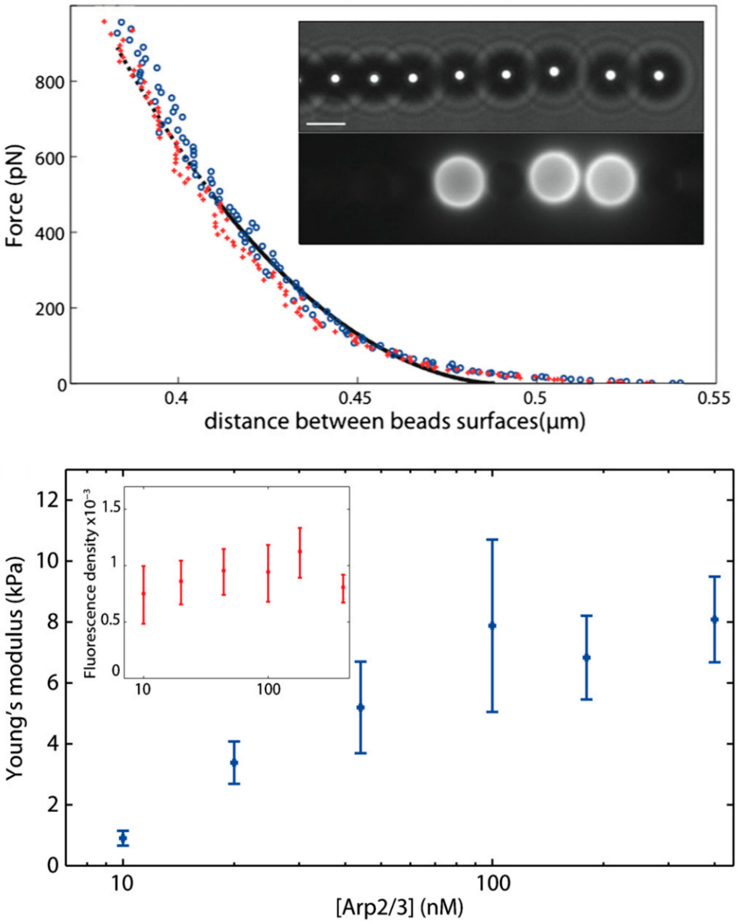

Figure 2.14: (Top) Typical force-distance curve. Compression in blue circles, decompression in red crosses with a Hertzian fit in black. Inset: BF (bright-field) and fluorescent images of a chain, with three beads covered by an actin gel. Scale bar = 4 $\mu$m.(Bottom) Young modulus of the gel as a function of increasing Arp2/3. Inset: Evolution of the fluorescence density as an estimate of the actin concentration.

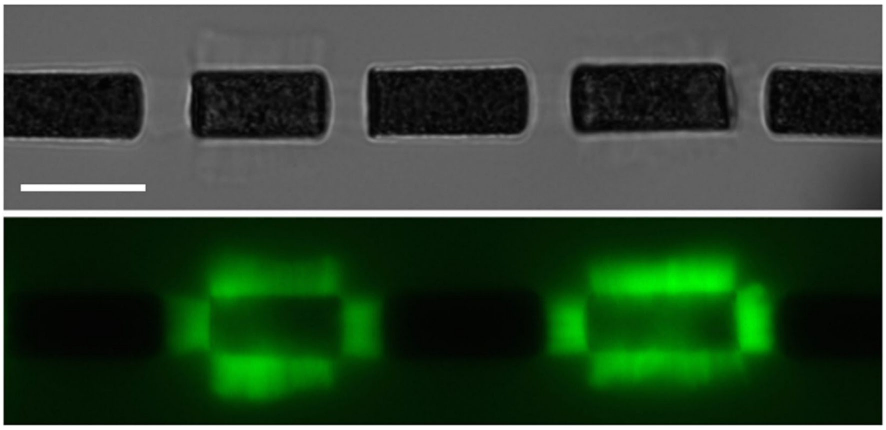

Figure 2.15: Chain of magnetic cylinders (6 $\mu$m in diameter) in an horizontal magnetic field. Top: Bright field image. Bottom: Fluorescent image (actin is labelled). Actin networks have grown from cylinders covered by the activator of the polymerization for around 15 minutes. Non actin-covered cylinders have been passivated. The cylinders are seen from the side, the circular faces being perpendicular to the image. Scale bar 10 $\mu$m, from [89].

In subsequent studies, the focus shifted to analyzing actin gels reconstructed from cell extracts still using the magnetic colloids technique. In collaboration with the team of Alphée Michelot, Planade et al. investigated the link between the elasticity of actin patches and the efficiency of endocytosis. They found that gels made from yeast cell extracts were significantly stiffer ($\sim$ 6000 Pa) compared to gels made from purified proteins ($\sim$ 900 Pa). This difference in stiffness could be attributed to the absence of connecting proteins, such as cross-linkers, or to variations in the network architecture induced by other accessory proteins present in the extract [90]. Moreover, in this study, they discovered a clear correlation between softer actin networks and a decreased efficiency of endocytosis.

However, one limitation of using magnetic colloids as force sensors is their round geometry at the interface, which introduces non-linearities in the force measurements. This challenge was overcome by a more recent technique that uses cylindrical-shaped colloids with a flat surface at the interface, providing more accurate results [89].

In Bauer et al. [89], pioneering results on actin mechanics at low stresses were presented, specifically investigating the behavior at stresses lower than 100 Pa with purified proteins. Actin gels grown on cylindrical structures (as shown in Figure 2.15) in a medium containing purified proteins were subjected to increasing stresses ranging from 0 to 30 Pa. The observed strain resulting from the applied stress was measured, providing access to the corresponding Young modulus. The stress-strain curve obtained from the experiments was not linear. Instead, it displayed a positive slope, which is a characteristic signature of stress-stiffening behavior. This phenomenon had been previously encountered in other studies involving actin suspensions [75] and gels [84] [87]. The inset of Figure 2.16 shows that the non-linear elastic modulus follows a global linear increase. However, it is noteworthy that the elastic modulus vanishes ($\sim$ 20 Pa) for stresses approaching or falling below 1 Pa. This particular behavior had not been previously reported, as most AFM measurements in previous studies were performed starting from stresses of 25 or 100 Pa.

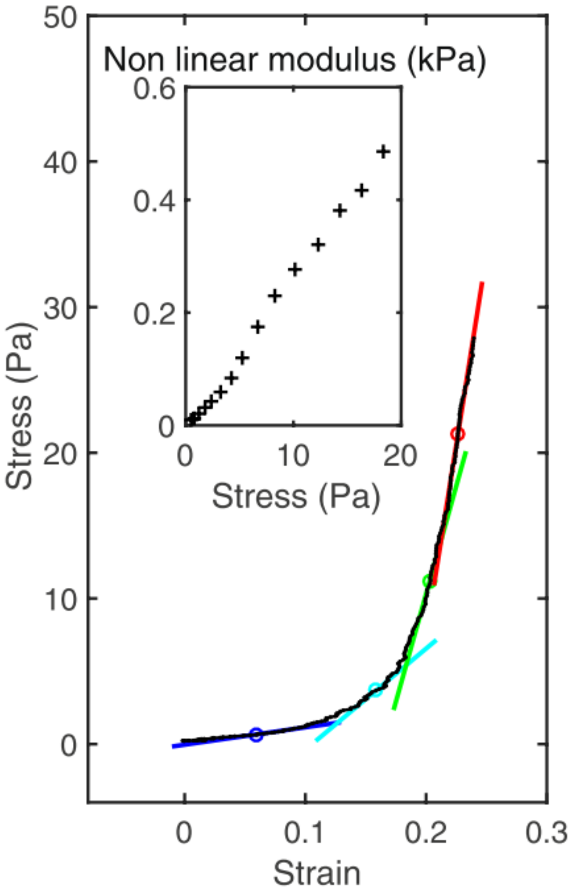

Figure 2.16: Stress-strain curve for a given actin network obtained by application of an increasing force. The tangent of the curve on four points is represented by short colored lines whose slope is a measure of the local non linear modulus. Insert: the non linear modulus measured all along the stress strain curve, from [89].

The authors hypothesise, that this vanishing stiffness at low stresses is the direct consequence of the origin of elasticity in branched networks. As branched networks without crosslinkers have a critical connectivity, they are expected to build-up their stiffness through entanglement which appear as the growing network is submitted to increasing load. Thus, almost free-growing gels exhibit a vanishing elasticity as they lack supplementary connections provided by entanglement. This suggests that the origin of elasticity in branched actin networks is strongly influenced by entanglement, and in the absence of such connections, the network exhibit a loss of stiffness. The study of this phenomenon is still a work in progress in the field, although we will provide recent theoretical aspects recently developed by researchers.

All in all, the uniqueness of growing branched actin networks lies in their dynamic nature, where they continuously define and redefine their properties in response to the chemical and mechanical environment, influencing the mesh size or the distance between branching points. This is evident in the significant differences observed between networks grown in purified protein mediums and those reconstructed from cell extracts. Furthermore, at some point, studying the elasticity of these gels boils down to the analysis of the load-dependent growth process of networks, whose first building block is actin force generation through polymerization.

In the subsequent discussion, we will delve into the theoretical and experimental aspects of the force generation process of polymerizing actin filaments, focusing on the force-velocity relationship. We will then provide an overview of bundles and branched networks growth in experiments and explore theoretical approaches and findings related to this process.

# Chapter 3

# Actin network force production

## 3.1 Force generation of actin filaments through polymerization

The Brownian ratchet is the paradigmatic conceptual framework for elucidating force generation mechanisms during polymerization processes. The model relies on the conversion of biochemical energy into mechanical energy. More fundamentally it is a stochastic model that is built upon thermal fluctuations. Here we will review the main approaches of the model and present some experimental results.

### 3.1.1 Stochastic approach

The model described in Peskin et al. [13] is widely acknowledged and frequently cited. It adopts a convection-diffusion approach to describe the phenomenon. A filament undergoes linear polymerization against a diffusing barrier, characterized by a diffusion coefficient denoted as $D$. A force $f$ is exerted on the filament, as illustrated in the inset of Figure 3.1. The insertion of a monomer into the gap between the wall and the polymer tip (position denoted as $x$) is feasible when the gap size exceeds half the monomer dimension ($\delta$), owing to the helical structure of actin. Consequently, the growth of the filament is influenced by both the applied force and the magnitude of fluctuations in the system.

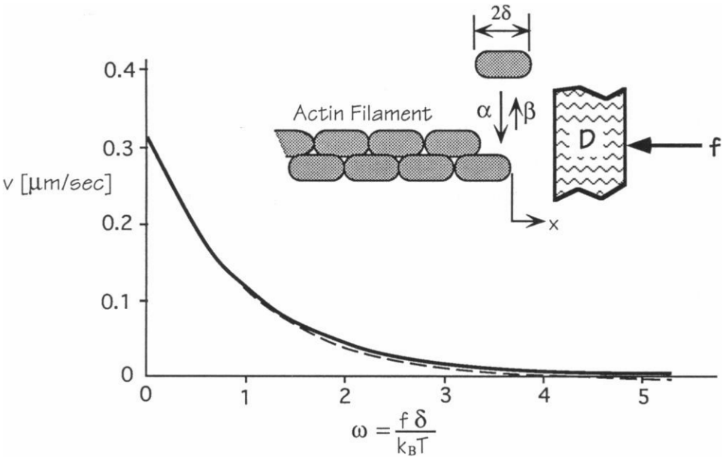

Figure 3.1: Velocity of elongation as a a function of $\omega = f\delta/k_BT$ (dimensionless force). The solid line represents the case when depolymerization is negligible ($\beta \to 0$). The dashed line is based on 3.3 when both polymerization and depolymerization are negligible compared to ideal ratchet velocity: $\alpha\delta, \beta\delta \ll 2D/\delta$, from [13].

In the context where the position $x$ is greater than or equal to the monomer size $\delta$ (i.e., $x \geq \delta$), the polymerization rate is represented by $\alpha$. Conversely, when $x$ is less than or equal to $\delta$ (i.e., $x \leq \delta$), the polymerization rate becomes null. Additionally, the constant depolymerization rate is denoted by $\beta$. In addition, $\alpha$ can be expressed as $\alpha = k_{on} \cdot M$, where $k_{on}$ represents the rate per monomer and $M$ denotes the monomer concentration. In the article, the authors derive the load-velocity relationship by treating the wall as a diffusing particle moving in a one-dimensional space with a diffusion coefficient $D$. The particle experiences a force field of magnitude $-f$, which imparts a drift velocity of $-Df/k_BT$ (where $k_B$ is the Boltzmann constant and $T$ is the temperature). The polymerization process, where a monomer attaches to the tip and extends the length by $\delta$, is analogous to the particle making a jump from position $x$ to position $x - \delta$.

Interestingly, rather than directly analyzing the diffusion of the particle itself, the focus of the study is on the system itself, represented as $c(x,t)$, which denotes the density of systems with gaps at position $x$ at time $t$. Thus, they describe the dynamics of systems in an ensemble at position $x$ and time $t$. Two situations can be distinguished, when the gap permits polymerization and when it is not wide enough. This leads to two equations:

$$\begin{aligned}
\frac{\partial c}{\partial t} &= D\frac{\partial^2 c}{\partial x^2} + \left(\frac{Df}{k_BT}\right)\frac{\partial c}{\partial x} + \alpha c(x+\delta,t) - \beta c(x,t), \;\; x \leq \delta \\
\frac{\partial c}{\partial t} &= D\frac{\partial^2 c}{\partial x^2} + \left(\frac{Df}{k_BT}\right)\frac{\partial c}{\partial x} + \alpha\big[c(x+\delta,t) - c(x,t)\big] + \beta\big[c(x-\delta,t) - c(x,t)\big], \;\; x \geq \delta
\end{aligned} \tag{3.1}$$

Furthermore, the authors propose the following expression for the steady state velocity:

$$v = \delta \frac{\alpha \int_\delta^{+\infty} c(x)\mathrm{d}x - \beta \int_0^{+\infty} c(x)\mathrm{d}x}{\int_0^{+\infty} c(x)\mathrm{d}x} \tag{3.2}$$

Here, $\int_\delta^{+\infty} c(x)dx$ represents the number of systems for which polymerization is made possible, while $\int_0^{+\infty} c(x)dx$ is the total number of systems in the ensemble. Thus, the upper term is the net growth rate for the ensemble, which has to be divided by the total number of systems and multiplied by the increment length $\delta$ to obtain the velocity per system.

Additionally, by assuming totally reflecting boundary conditions at the wall, i.e., $x = 0$ (when there is contact between the tip and the wall), where the monomer cannot be knocked off due to the polymerization free energy difference, and by enforcing the continuity of the density of states at $x = \delta$, two necessary boundary conditions are derived.

Despite the complexity of the model, an exact solution can be obtained for the system under certain conditions. This occurs when the rates of polymerization and depolymerization are much slower than the ideal Brownian ratchet velocity, specifically when $\alpha\delta$ and $\beta\delta$ are both much smaller than $2D/\delta$. In this regime, the formula is remarkably simple and stands as:

$$\boxed{v = \delta\big[\alpha e^{-\omega} - \beta\big]} \tag{3.3}$$

With $\omega = f\delta/k_BT$, the dimensionless force. Remarkably, in this limiting case, the formula does not depend on the diffusion coefficient of the load.

In Figure 3.1, the function is represented in dashed line using rates from [91]. From 3.3, it is straightforward to extract the stall force expression:

$$\boxed{f_s = -\frac{k_B T}{\delta} \ln\left(\frac{\beta}{\alpha}\right)} \tag{3.4}$$

Relying on values from [91], the stall force was estimated to be of the order of 10 pN *in vivo.*

### 3.1.2 Thermodynamical approach

Prior to Peskin et al. work, Hill had developed a model concerning force production associated with microfilament assembly and disassembly [12]. Although Hill model lacked a detailed mechanistic explanation of energy transduction, it offered simpler results through its thermodynamic approach. In this review, we will delve into Hill's work from 1981 and derive the force-velocity relationship. This result will serve as a crucial foundation for our simulations and analysis, allowing us to better understand the force generation mechanisms during microfilament dynamics and polymerization processes.

We consider a scenario in which a fiber exerts a constant force against a wall. The growth of the fiber is facilitated by a pool of $N_S$ sub-units, each of length $a$, which we assume to be present in a dilute solution.

#### Gibbs free energy

Let's call $\mu_s$ the chemical potential of sub-units in solution, at concentration $c$:

$$\mu_s = \mu_s^0 + RT\ln(c) \tag{3.5}$$

Where R is the gaz constant, T the temperature and $\mu_s^0$ the chemical potential at standard state. Let's note $\mu_0$ the chemical potential of the sub-unit attached to the polymer. For the sake of simplicity we will consider it independent of length and force (which meant to neglect the ATPase activity of actin at short time scales). We also have $\alpha$ the assembling rate per concentration, $\alpha'$ the disassembling rate and $F$ the applied force per mole.

At constant pressure and temperature, the Gibbs Free Energy $G$ is the Thermodynamic Potential, thus the quantity of interest. We write its variation induced by the assembly and disassembly of sub-units as :

$$\mathrm{d}G = -S\mathrm{d}T + V\mathrm{d}P - \mu_s\mathrm{d}N_s + \mu_0\mathrm{d}N_s + Fa\mathrm{d}N_s \tag{3.6}$$

$F$ is positive when we compress the filament, negative when we pull on it. Besides, as we assume temperature and pressure to remain constant, and considering (3.5) we get :

$$\mathrm{d}G = \left[\mu_0 - \mu_s^0 - RT\ln(c) + Fa\right]\mathrm{d}N_s$$

As it is a potential, and for this reaction to be spontaneous we must have $\mathrm{d}G < 0$, which means :

$$\mu_0 - \mu_s^0 - RT\ln(c) + Fa < 0 \tag{3.7}$$

At steady state, we have :

$$\begin{aligned} \mu_0 &= \mu_s^0 + RT\ln(c) - F_S a \\ \iff \mu_0 &= \mu_s - F_S a \end{aligned} \tag{3.8}$$

Where we have introduced the stall force per mole $F_S$. We define $\Delta\mu$ the difference between the chemical potential of the sub-unit attached to the polymer and the sub-unit in solution: $\Delta\mu = \mu_0 - \mu_s$. Thus, we get:

$$F_S = -\frac{\Delta\mu}{a} \tag{3.9}$$

In addition, we have for $\Delta\mu$:

$$\begin{aligned} \Delta\mu &= \mu_0 - \mu_s^0 - RT\ln(c) \\ &= RT\ln\left(\frac{c_e^0}{c}\right) \end{aligned} \tag{3.10}$$

With $c_e^0$ the equilibrium concentration, with no force. Using 3.10 and 3.9 we can derive the value of $F_S$:

$$F_S = \frac{RT}{a}\ln\left(\frac{c}{c_e^0}\right) \tag{3.11}$$

Then, the stall force expression is straightforward.

$$\boxed{f_s = \frac{k_B T}{a}\ln\left(\frac{c}{c_e^0}\right)} \tag{3.12}$$

Interestingly, this expression reveals the correspondence between the kinetic rates ratio of Peskin's expression 3.4 and the ratio of concentration here, in Hill's work.

In the same time, we can derive the equation linking equilibrium concentrations with and without force.

$$\frac{\ln(c)}{\ln(c_e^0)} = \frac{Fa}{RT}$$

The quantity $\left|\frac{Fa}{\Delta\mu}\right|$ can be seen as the free energy transduction efficiency (thermodynamics to mechanics).

### Detailed balance as an equilibrium condition

Considering that our system is at equilibrium, we must respect the Detailed Balance condition between attached and detached states :

$$P(A)P(A \to D) = P(D)P(D \to A)$$

With $P(D \to A) = \alpha c_e$ and $P(A \to D) = \alpha'$

Thus we obtain :

$$\frac{P(A)}{P(D)} = \frac{\alpha c_e}{\alpha'} \tag{3.13}$$

Moreover, as we are at equilibrium the probability of being in Attached or Detached States is given by the Boltzmann-Gibbs distribution:

$$P(A) = \frac{e^{-\bar{\beta}E_A}}{Z} \quad ; \quad P(D) = \frac{e^{-\bar{\beta}E_D}}{Z} \quad \text{with} \quad \bar{\beta} = 1/RT$$

Thus (3.13) becomes :

$$\frac{\alpha c_e}{\alpha'} = e^{-\bar{\beta}\Delta E_{AB}} \quad ; \quad \Delta E_{AB} = E_A - E_B \tag{3.14}$$

Or, we know that $\Delta E_{AB} = \Delta\mu + Fa$

Finally we obtain :

$$\frac{\alpha}{\alpha'} = \frac{e^{-\bar{\beta}\Delta\mu}}{c_e} e^{-\bar{\beta}Fa} \tag{3.15}$$

Besides, we know that $v_+ = \alpha ca$ and $v_- = \alpha' a$. In addition, $v = v_+ - v_-$.

Then, let's fix the value of $\alpha'$, because, as long as the the ratio is conserved the physics remains the same. Thus, we get the velocity of the system :

$$\boxed{v = \alpha' a\left[e^{-\bar{\beta}\left(\Delta\mu + Fa\right)} - 1\right]} \tag{3.16}$$

### 3.1.3 Elastic ratchet

In Mogilner et al. [11], they generalize the Brownian ratchet concept to incorporate the semi-flexible nature of actin filaments and accounts for the approximately orthogonal growth networks observed in lamellipodia, unlike the assumption of colinear growth for infinitely stiff filaments in Peskin et al.'s model [13].

The setup involves an actin filament of length $\ell$, anchored to a rigid actin network as a fixed support, and growing against an external load $f$ at an angle $\theta$ (see Figure 3.2). In this configuration, the gap required for adding a monomer is $\delta\cos(\theta)$, where $\delta$ represents half the size of a monomer, as mentioned earlier. The actin filament exhibits a persistence length denoted as $\lambda$ (approximately 1 $\mu$ m). The mechanical behavior of the system can be equated to that of a Hookean spring, where the elastic constant of the spring is expressed as follows:

$$\kappa(\ell, \lambda, \theta) = \frac{4\lambda k_B T}{\ell^3 \sin^2(\theta)} = \frac{\kappa_0(\ell, \lambda)}{\sin^2(\theta)} \tag{3.17}$$

The statistical motion of the tip, subjected to the restoring force of the spring and the load force, can be described by a Fokker-Planck equation. In the scenario where thermal fluctuations of the tip occur much more rapidly than the polymerization rate, it becomes feasible to solve the Fokker-Planck equation using perturbation theory.

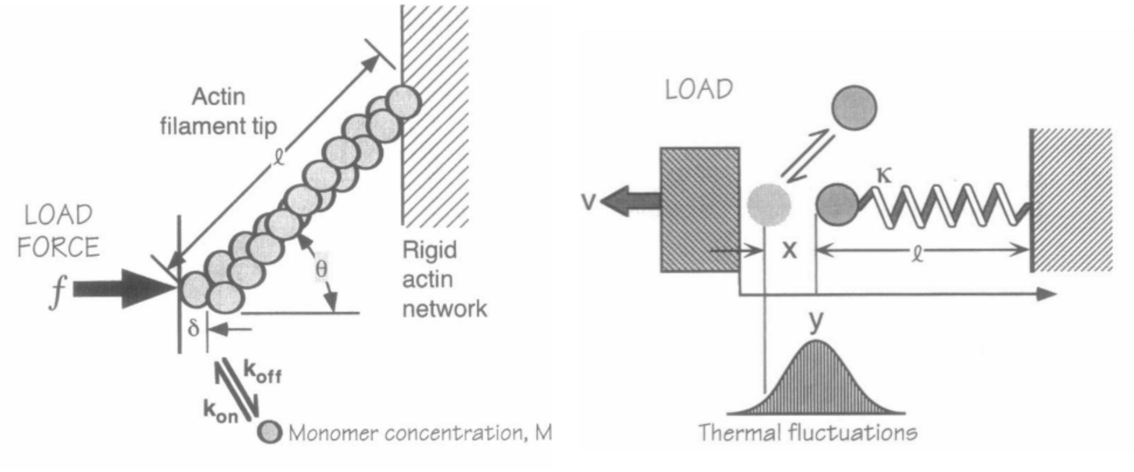

Figure 3.2: (Right) Scheme of the actin filament growing against the load at an angle $\theta$. (Left) Mechanical equivalent of the system with a Hookean spring of stiffness $\kappa$, adapted from [11]

As a result of this approach, the force-velocity relationship can be expressed as follows:

$$\boxed{v \approx \delta\cos(\theta)\left[k_{on}Mp(\theta,f) - k_{off}\right]} \tag{3.18}$$

The obtained result can be interpreted as the increment of length multiplied by the difference between the polymerization and depolymerization rates. The free polymerizing rate $k_{on}M$ is modulated by the steady-state probability of a gap with width $\delta\cos(\theta)$, denoted as $p(\theta, f)$. The expression for this probability, which we won't delve into the details here, depends on the flexibility of the filament, characterized by parameters $\ell$ and $\lambda$. The computation of this probability can be performed numerically, as demonstrated in the paper for motion analysis of *Listeria* or lamellipodium extension.

An interesting observation is that the velocity is not a monotonic function of the angle $\theta$ but instead exhibits a maximum at a critical angle $\theta_c$. This behavior arises because, on one hand, thermal fluctuations may not be able to bend a stiff filament that is pushing normally against the surface. On the other hand, a filament growing nearly parallel to the load cannot generate axial displacement. Hence, there must exist an optimal angle that allows for maximum force generation, as depicted in Figure 3.3 (Left). This finding highlights the significance of filament flexibility and angle in determining the force-velocity relationship and provides crucial insights into the mechanics of actin-based cellular processes.

In addition, it is possible to qualitatively estimate the stall force. At large forces, the filament becomes almost parallel to the wall, and we can approximate $\cos(\theta) \approx k_BT/f_s\delta$. In this state, the average equilibrium distance between the tip and the wall can be estimated as $y_0 \approx f_s/\kappa$. When the distance $y_0$ becomes equal to $\ell\cos(\theta)$, it indicates that the filament is bent nearly parallel to the load and the velocity drops to zero. This can be expressed as $\ell\cos(\theta) \approx \ell k_BT/f_s\delta \approx f_s/\kappa$. Tacking theses considerations into account, we can derive the following expression for the stall force per filament.

$$f_s \approx \frac{k_BT}{\delta l}\sqrt{\ell^2 + 4\lambda\delta} \tag{3.19}$$

Applying this framework, Mogilner et al. obtained the load-velocity curve for a crosslinked lamellipodium network with a 45° angle distribution comprising 5000 pushing filaments at the front. According to their model, they derived the stall force per filament, approximately $f_s \sim 5$ pN. Considering the collective contribution of all filaments, the total stall force for the lamellipodium was estimated to be $F_s \sim 25$ nN. The force-velocity curve is represented on Figure 3.3 (Right). Remarkably, their results are in good agreement with experimental measurements using micro-needles to assess the force required to halt the advancement of a keratocyte's lamellipodium. The experimental measurements indicated a stall force of approximately $\sim 45$ nN [92].

Additionally, their approach allows for the discrimination of different limiting regimes based on the values of two dimensionless parameters: $\omega$, representing the dimensionless work of the load, and $\epsilon = \kappa_0 \delta^2 / 2k_BT$, representing the dimensionless mean elastic energy stored in a filament. In situations where long microtubule bundles are subjected to large forces ($\omega \gg 1$), the bending energy becomes relatively low compared to the thermal energy ($\epsilon \ll 1$). Consequently, in this regime, the authors demonstrate that the assembly rate is predominantly determined by a deterministic Boltzmann factor $e^{f\Delta/k_BT}$, with $\Delta$ the displacement of the wall. This distinction between regimes, taking into account the relative contributions of bending energy and thermal energy, provides key insights into the dominant factors influencing the filament dynamics under different force conditions. For microtubule bundles experiencing large forces, the mechanical work exerted on the system becomes the primary driving force for the assembly rate, while the influence of bending energy diminishes due to its low magnitude compared to thermal energy. In a broader scope, this study significantly alters the results for low forces, revealing the existence of a local convex regime characterized by a slowly decreasing velocity. Nonetheless, when dealing with higher forces, the load-velocity curve maintains its convex nature. Let us now shift to describe some experimental results.

### 3.1.4 Experimental results

The initial investigations drawing evidences of force generation by single growing actin filaments were documented in Kovar et al's work. The barbed-end of an actin filament is anchored to the FH2 domain of formins, which are secured on microscopic slides, while the pointed-end is immobilized by myosin heads. Consequently, elongation at the barbed-end results in filament buckling between these two anchoring points, with segments as short as 0.7 $\mu$m displaying forces on the order of 1 pN. To our knowledge, direct measurement of force production by single actin filaments remains unexplored. However, researchers have gleaned insights from the collective motion of actin fiber bundles, which will be discussed in subsequent sections.

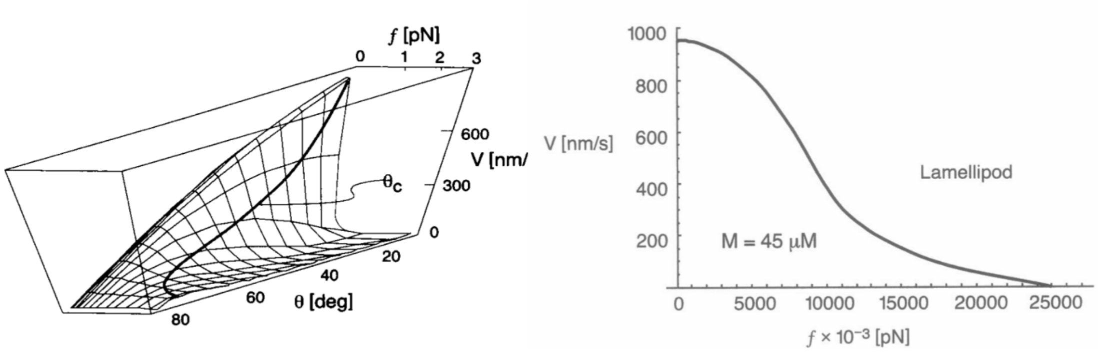

Figure 3.3: (Left) Velocity $v$ as a function of the load $f$ and filament incidence angle $\theta$. The critical angle $\theta_c$, for fastest growth depends on the load, its trajectory is shown on the $v(f, \theta)$ surface. (Right) Computed load-velocity curve for a network consisting of 5000 filaments actin on a membrane area of 5 $\mu$m x 0.2 $\mu$m.

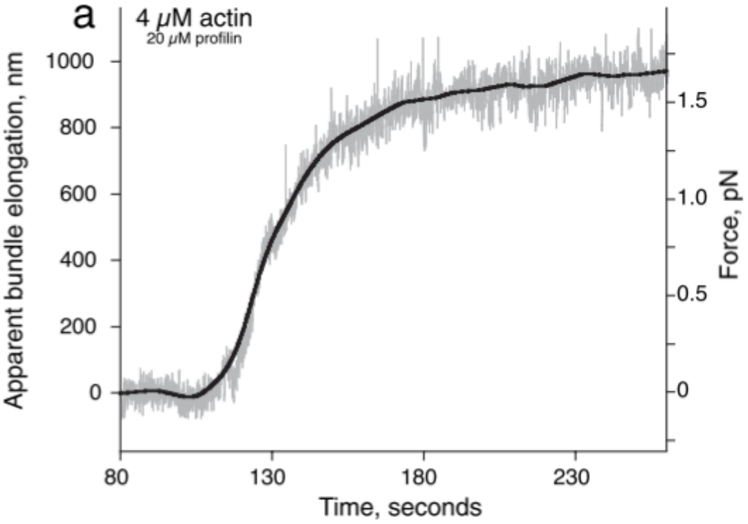

Figure 3.4: Force measurement for actin filament growth with monomeneric actin at 4 $\mu$M. Grey traces show raw data, the black line is the best-fit curve, adapted from [14].

Conversely, force-velocity relationships have been evaluated for growing microtubules, allowing for significant inferences. These microtubules are attached to a substrate on one end while the other end remains free, exerting force on a rigid barrier [93]. As the microtubules grow, they eventually buckle while continuing to elongate at a slower velocity. Analyzing the shape of the bent filament enables the computation of the corresponding stored elastic energy, facilitating the derivation of the force-velocity relationship, up to approximately 4 pN. Surprisingly, in these experiments, the velocity decreased more rapidly with the applied force than anticipated by the Peskin et al. model [13], which had overestimated the growth rate. This discrepancy could be attributed to the composite nature of microtubules, consisting of several proto-filaments, where only a limited number of them would contribute significantly to the work, leading to an accelerated exponential decay.

The subsequent section will delve into the investigation of aligned bundles of filaments or protofilaments, which have been the focal point of numerous scientific inquiries. Despite their apparent simplicity, these systems offer valuable insights into how geometric factors influence the overall dynamics of parallel ensembles, such as microtubules or actin bundles, changing the overall force-velocity shape or the stall force scaling.

## 3.2 Force production of filament bundles

### 3.2.1 Experimental results

Footer et al. [14] conducted an investigation into the growth capabilities of actin filaments and corroborated the presence of a stall force. To achieve this, they employed an optical trap to directly measure the positional effects of polymerization on eight parallel filaments. By assessing the displacement of the bead within the trap, they were able to calculate the associated force. In experiments with low G-Actin concentrations, they observed a stall force of approximately 1 pN for 2 $\mu$M actin and 1.5 pN for 4 $\mu$M, as depicted by the plateau in Figure 3.4. This observed small value aligns with theoretical predictions for their low concentration conditions involving only one filament.

A plausible explanation for this outcome lies in the likelihood that only the longest filament comes into direct contact with the barrier. This suggests that parallel bundles of actin filaments do not inherently collaborate to enhance force generation, necessitating a more intricate mechanism. Alternatively, the authors propose that actin bundles may exhibit lower efficiency in converting biochemical energy into mechanical work compared to other forms of actin filament organization. This idea will be revisited later, highlighting the trade-off between force and displacement for various structures, resembling a gear mechanism [94]. Moreover, Tsekouras et al. [95] propose an alternative explanation for this unexpected result, pointing to the influence of profilin, which is utilized to suppress spontaneous actin nucleation in Footer et al. [14]. Specifically, when profilin binds to actin monomers, it could interfere with ATP hydrolysis during polymerization, thereby modifying the thermodynamics of the system. This may contribute to the observed stall force behavior in the experiments.

### An interesting configuration

Furthermore, it is worth to mention the experiments carried out by Brangbour et al. [96], which, although not directly studying the growth of fiber bundles, provide valuable insights. In their study, they employed the magnetic beads setup detailed in the previous section to investigate the force-velocity response of individual growing actin filaments. To trap the barbed-end of the actin fiber and allow the pointed-end to grow freely, the beads were coated with gelsolin (which has an impact on the polymerization kinetics). The total number of gelsolin molecules per bead was denoted as $N_{GS}$. In the presence of G-actin, gelsolin initiated growth at the pointed-end, following this a magnetic field was applied to align the colloids, as previously described by Pujol et al. [88]. The magnetic force and the distance between the beads were monitored by adjusting the field accordingly.

The authors measured the bead-to-bead distances for various forces and obtained the corresponding velocities. In Figure 3.5, they plotted the velocity against the force for two actin densities. Increasing actin filament densities had no impact on the zero-force velocity but diminished the decay rate (with force). Both curves exhibited convex behavior, and the system appeared to approach zero force without any observed stall or negative velocity, suggesting no depolymerization induced by the applied force. Additionally, the authors investigated the effect of force on actin filament growth and found that the growth was unaffected by the load, contrary to what is predicted by the Brownian ratchet model. They performed experiments starting with growing filaments at a low load (0.8 pN) and then significantly increased the force to freeze the distance between the beads. Subsequently, the force was reduced back to its original value. Interestingly, the distance versus time before and after the application of the high force collapsed onto the same line, indicating that filaments grew at the same speed regardless of the load.

This rapid recovery suggests a soft elasticity which was found to be not compatible with buckling. Instead, the authors considered that elasticity originated from the soft biotin-gelsolin link that fixes fibers on the beads Thus, in response to increasing opposing forces, filaments tilt (without bending) which reduces the number of accessible configurations, which leads to entropic elasticity. This entropic repulsion was found to dictate the force-velocity profile, their entropic-based model successfully predicted the experimental points, as shown in Figure 3.5. This innovative setup presented an alternative to the Brownian ratchet mechanism, suggesting that the force-velocity behavior of those ensemble of filaments might be different from what was previously assumed, as they continue to grow as if they were in solution, disregarding their stall threshold.

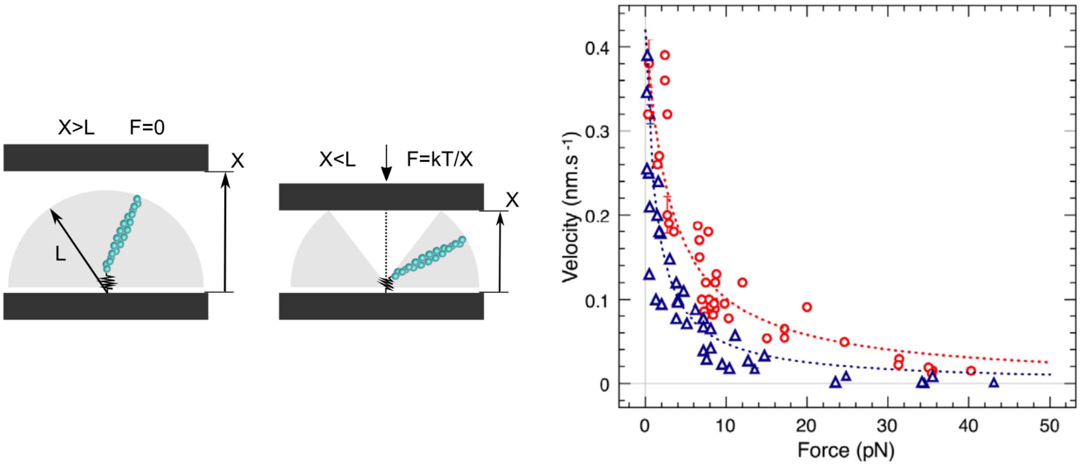

Figure 3.5: (Left) When the distance between black surfaces is large enough (X $\geq$ L), the filament explores the whole half sphere shaded on the figure because of thermal fluctuations. When X $\leq$ L, the accessible surface V decreases leading to an entropic repulsive force. (Right) Velocity versus force for different filament densities with $N_{GS} = 10000$ for red circles, $N_{GS} = 4000$ for blue triangles. The curves are the predictions of the model, adapted from [96].

Indeed, the experimental results discussed above shed light on the limitations of a simple Brownian ratchet approach when dealing with small fiber ensembles. The stall force of such ensembles may not scale directly with the number of filaments, and the dynamics of individual filaments might not be the sole limiting factor in certain complex structures. However, it is worth questioning the physiological relevance of the last system studied. Regrettably, there is a dearth of experimental results concerning small actin ensembles, despite the abundance of theoretical and numerical work on the subject. Nevertheless, the theoretical and numerical investigations have provided valuable insights, particularly regarding the scaling of the stall force in such ensembles. In the following sections, we will present some of these works, which have contributed significantly to our understanding of force generation in small fiber ensembles.

### 3.2.2 Theoretical and numerical approaches

In 1999 Mogilner et al. [97] extended upon their elastic ratchet framework to incorporate the findings of Dogterom's work on microtubules growth. It had been observed that the velocity decreased more rapidly with the applied force than predicted by the Brownian ratchet model. To account for this, the authors proposed that the force generated by the ensemble of filaments is not simply the sum of forces produced by individual filaments. Indeed certain proto-filaments positioned close to the membrane could not polymerize as rapidly due to insufficient space for the insertion of a tubulin dimer. Nonetheless, these filaments could indirectly support the growth of more distant fibers by effectively bearing a significant portion of the load.

They approached the system as a bundle of $N$ cross-linked filaments that polymerize independently against a perpendicular barrier. The authors made the assumption that the force influenced the assembly rate of sub-unit addition solely for filaments whose tips were closer than the size of a sub-unit ($x \leq \delta$), while the disassembly rate remained constant regardless of tip positions. Treating the tip distributions as a continuum, they numerically solved the model, focusing on the case of $k_{off} = 0$ where $k_{on} \gg k_{off}$.

Although their predicted velocity values were somewhat higher than observed experimentation, their results aligned notably well with the experimental trends. In their analysis, the authors quantified the number of *working filaments*, those falling within the $\delta$ range, and found that this count was smaller than $N$ but increased with the applied force. They further employed their model to predict the stall force, introducing a finite $k_{off}$ and found that it was scaling as the square root of the number of filaments:

$$F_{stall} = \frac{k_B T}{\delta} \sqrt{\frac{k_{on}}{k_{off}}} \sqrt{N} \tag{3.20}$$

The square root scaling of the stall force proposed by Mogilner et al. was subsequently scrutinized and questioned in subsequent studies, as thermodynamic considerations would generally suggest a simpler linear scaling. Addressing this, Van Doorn et al. [98] undertook a study using a discrete version of the model previously described. They paid particular attention to the treatment of the off-rate term. To facilitate computations, they introduced a step size $\sigma = \delta/N$ and arranged filaments at positions separated by $\sigma$ such that each position marked by $n$ ($x = n\sigma$) could accommodate at most one filament tip, as illustrated in Figure 3.6 (Left).

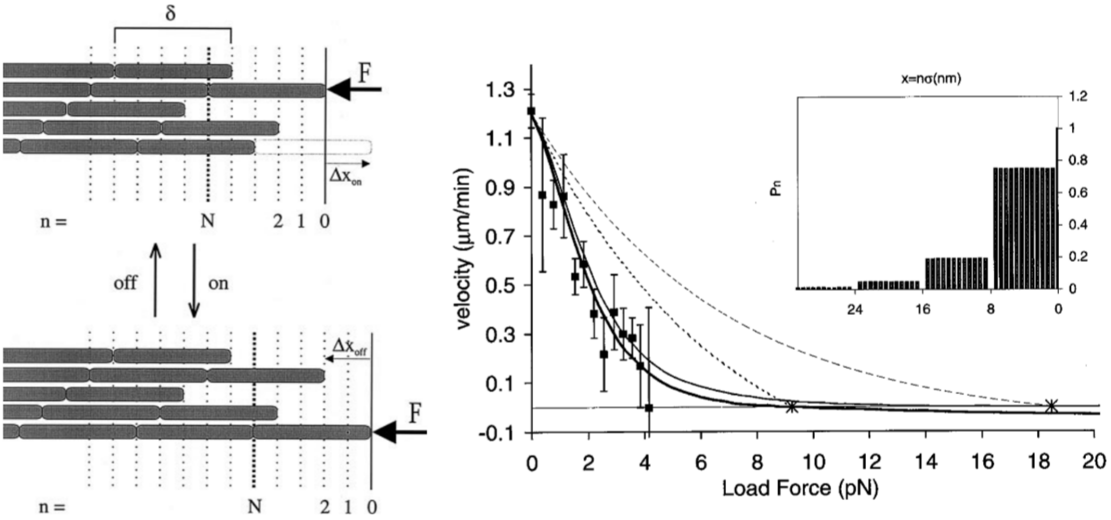

Figure 3.6: (Left) Discrete version of the Mogilner-Oster model for a polymer with $N = 5$ independently growing filaments. The addition of a monomer permits a displacement of the wall $\Delta x_{on}$, despite the force $F$. At the stall force, the two configurations are in equilibrium leading to detailed balance. (Right) The force-velocity relation for growing microtubules. Squares are the experiments from Dogterom et al. Solid lines are simulation results from the discrete theory: $k_{off} = 50$ min$^{-1}$ for the thick line, $k_{off} = 10$ min$^{-1}$ for the thin line. Dashed lines are the corresponding curves predicted by the Brownian ratchet model. The inset shows the probability distribution of filament tips at the stall force. Adapted from [98].

The authors conducted simulations to analyze the dynamics of the system, ultimately deriving the force-velocity relationship for a growing microtubule with $N = 13$, as depicted in Figure 3.6 (Right). Remarkably, the theoretical predictions closely matched Dogterom et al.'s experimental results, and importantly, the stall force obtained aligned with what is anticipated from thermodynamic considerations, specifically $F_{stall} = N \cdot f_s$. This finding reinforced the compatibility of the model with thermodynamics and highlighted the distinct shape differences compared to the Brownian ratchet, with the curve declining more steeply than an exponential decay. Furthermore, this result was achieved analytically. At the stall force, the net velocity is zero ($v_{pol} = v_{depol}$), implying that the detail balance condition can be imposed between pairs of tip configurations transformable by a single event (addition or removal). This condition led to the same stall force prediction as inferred from thermodynamic arguments:

$$F_{stall} = \frac{N k_B T}{\delta} \ln\left(\frac{k_{on}}{k_{off}}\right) \tag{3.21}$$

Subsequent findings provided further support for the linear scaling of the stall force through a more general analysis based on decomposition into polymerization cycles, specifically in the absence of lateral interactions between filaments [99]. In their study, Krawczyk et al. underscored that their analytical approach revealed the universal nature of the expression for models of this nature.

In a more recent study, a novel theoretical framework was proposed to address this problem by modeling the dynamics across a range of force values, rather than exclusively focusing on the stall force. This approach also accommodated an arbitrary number of filaments in contact with the moving wall [95]. Notably, this theoretical framework introduced the possibility of a condensation transition concerning the number of filaments at the wall. Given that multiple filaments could be in contact with the wall simultaneously, the manner in which the load was shared at these points needed precise specification.

When a monomer is added to the tip of a filament, it supports the full load and induces movement of the barrier ($k_{on} = U(f)$). During this step, the other filaments are considered free ($k_{on} = U_0$). Similarly, filaments are assumed to depolymerize freely ($k_{off} = W_0$), unless they are the sole filament in contact with the barrier ($k_{off} = W(f)$). Consequently, depolymerization results in work when only one filament interfaces with the barrier, as it leads to the barrier's motion. However, when multiple fibers interact with the load, a growing filament must exert work against the entire load. It is worth noting that this study adopts a "no-load sharing" scenario, distinguishing it from previous investigations [98] [99].

Applying these principles, the authors obtained equations of the dynamics and extended their analysis to the large $N$ limit to derive mean-field expressions. These expressions yielded the mean velocity of the moving barrier and the mean number of filaments in contact with the wall:

$$\begin{aligned} v &= \delta\big[U N_0 - W q\big] \\ N_0 &= \frac{(U_0 + W q - W_0) N}{U_0 + U(N-1) + (W - W_0) q} \end{aligned} \tag{3.22}$$

With $q = \langle \delta_{N_0=1} \rangle$ representing the time-averaged probability that there is only one filament in contact ($N_0 = 1$). Despite efforts, a method to extract $q$ directly from the equations could not be established. Consequently, its value was computed from simulations and subsequently incorporated into the mean-field theory. The outcome of this approach demonstrated remarkable agreement between simulations based on exact equations (using the Gillespie algorithm) and the predictions of the mean-field theory, as depicted in Figure 3.7. These graphs emphasize the occurrence of a condensation transition as the force increases. At low forces, the barrier velocity closely approximates its maximum value, determined by the free-polymerization velocity, and only a small number of fibers contact the barrier, leading to $q \approx 1$. This scenario is referred to as the *non-condensed* regime. Conversely, at higher loads, filaments accumulate at the barrier, the velocity approaches stall, and $q \approx 0$, constituting the *condensed* regime. After the initial plateau, the velocity decline exhibits a convex shape.

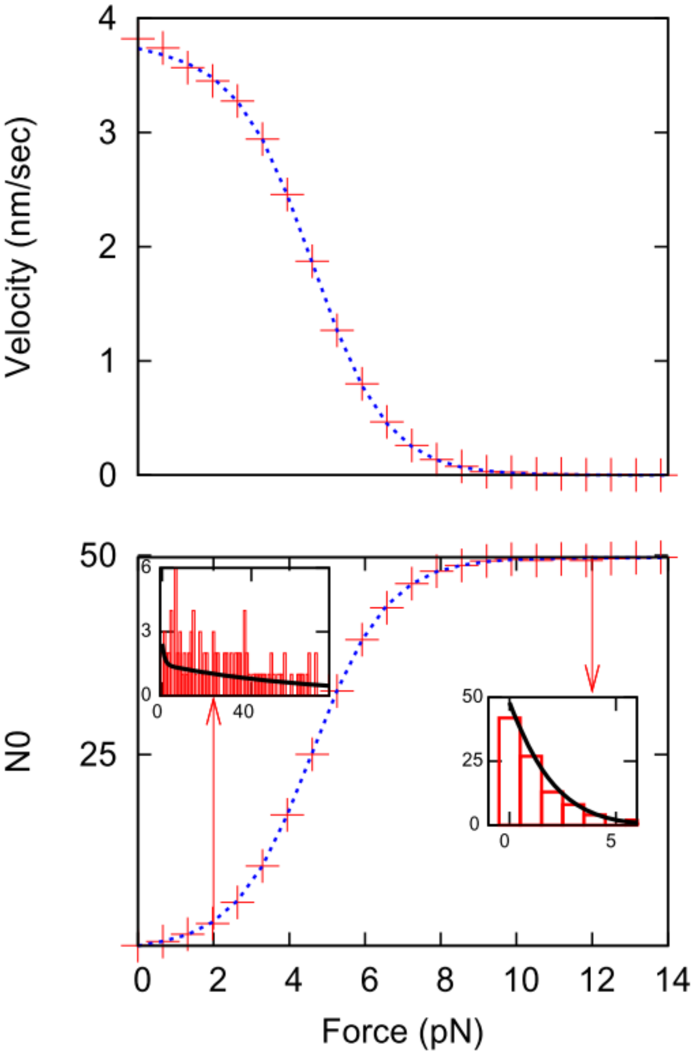

Figure 3.7: (Top) Mean velocity of the barrier versus the force. (Bottom) Mean number of filaments in contact with the barrier. Red cross symbols represent the simulations results, the blue dotted-line is the mean-field prediction based on 3.22, with $N = 100$. The inset represent the tips density profiles (red bars) with the mean-field theory predictions (black lines) as a function of the distance to the barrier, for *non-condensed* (left) and *condensed* regimes (right). From [95]

Then, having established the linear scaling of the stall force, the authors delved into studying the system's behavior as it approaches stall. This examination was motivated by the observation (seen in Figure 3.7 - Top) that the velocity approaches zero at forces significantly below the stall force. To quantify this effect, the authors introduced the notion of an *apparent* stall force, defined as the force at which the velocity drops to less than a small fraction $\alpha = 2.5\%$ of its initial value. This concept bears particular relevance in experimental scenarios where this threshold might correspond to the resolution limit of velocity measurements. Near stalling ($q \ll 1$), their calculations yielded the following approximation:

$$F_{apparent\ stall} \simeq \frac{k_B T}{\delta} \ln\left(1 + \frac{N}{\alpha} - N\right) \tag{3.23}$$

In the simulated regime, the calculated value of the apparent stall force was approximately 12.7 pN, force for which the velocity approaches the resolution limit of measurement. In addition, their theoretical analysis indicated that *condensation* occurs at this apparent stall force, a noteworthy observation that is evident in the graph. Consequently, the apparent stall force, scaling logarithmically with the number of filaments ($\ln(N)$), appears to be a significant quantity at this scale.

In summary, the paper highlighted the gradual approach to stalling, pointing out that this slow process could result in the underestimation of the true stall force. However, the authors acknowledged that their model might be too simplistic to comprehensively address various *in vivo* scenarios. Expanding beyond the parallel organization would likely be necessary to capture the complexities of real-world situations. Additionally, none of the discussed models accounted for the nucleation of filaments from existing ones, a phenomenon evident in branched systems. This omission underscores the need for more intricate models to truly capture the dynamics of force generation in complex actin networks.

More generally, while unraveling the mechanisms underlying polymerization-driven mechanical power, the previously mentioned approaches disregard the influence of growth on the pre-existing network. By focusing solely on surface interactions, these models overlook potential viscoelastic changes within the bulk of the system, which could impact its overall behavior. Notably, as discussed earlier, branched actin networks are particularly prone to undergoing viscoelastic adaptations in response to stress [87]. However, as pointed out in the work of Tsekouras et al., the intricate interplay between buckling and polymerization forces complicates the isolation of each contribution to the system's behavior. In the subsequent section, we will provide an overview of experimental and theoretical findings concerning the force-velocity behavior of growing branched actin networks. Many experimental results will be drawn from the same studies that were examined in the preceding section, where the mechanics of such networks were discussed. This approach aims to provide a comprehensive understanding of how branched actin networks respond to mechanical forces and how their growth dynamics interact with their mechanical properties.

## 3.3 Force velocity relationship in growing branched actin networks

### 3.3.1 Experimental results

Here we review experimental works (that have for the most been introduced in section 2.3.2) which describe the effects of loads on branched actin growth distinguishing between micro-pipette, AFM and magnetic cylinder experiments.

#### Micro-pipette and actin comet

In the case of *Listeria Monocytogenes* the load-adaptation of velocity is an important feature, as the bacteria needs to cross cell membranes to propagate. In the beginning of the twenty-first century, indirect approaches relying on increasing the viscosity of the medium led to opposing results: (bio-mimetic bead propulsion) [100] (*Listeria*) [101]. In addition, people strived to assess the value of the propulsive force, though the investigation range was limited to $\sim 100\ pN$. Beyond providing information on branched actin mechanics, experiments realized by Marcy et al., applied larger forces up to a few nN to probe the velocity response [83]. Indeed, Gerbal et al. suggested that forces of the order of a nN were necessary to slow down the bacteria, relying on a mesoscopic elastic analysis [102]. We will come back to their theoretical analysis and results later on in subsection 3.3.2.

Using the experimental setup previously presented in subsection 2.3.2, they applied pulling (negative) and pushing (positive) forces yielding to a force-velocity plot, see Figure 3.8 (c). The force applied is maintained through a feedback loop system as seen in (a), the constant velocity is fitted on the lengthening increase $\delta L$. The velocity at a given force is normalized, measuring the zero-force velocity $V_{F=0}$ for each flexible handle. In average the zero force velocity was around 2 $\mu$m.min$^{-1}$. Overall, there is a linear decrease for pulling forces, whereas the velocity decreases more gently for pushing forces, leading to a velocity roughly equal to 20 % of the zero load one at the maximum applied force. Although the stall force could not be reached experimentally, it was estimated to 7 nN by the fitting curve.

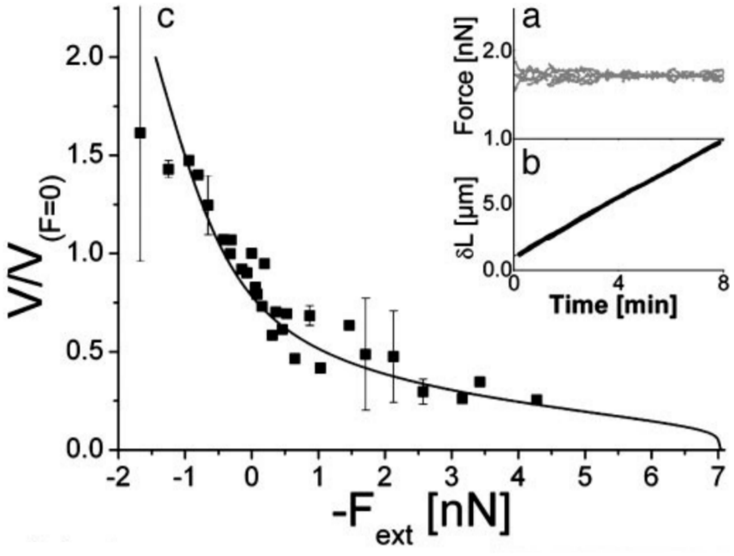

Figure 3.8: Force-velocity diagram : Typical measurement for one point with the Force (a), set to 1.7 nN, and the lengthening (b) $\delta L$ as a function of time. (c) The velocity is normalized by the velocity at zero force measured for each flexible handle, and fitted with an expression from [102] analysis.

### AFM cantilever

Dan Fletcher and his team took up the challenge of studying the velocity of networks approaching their stall force [84]. In those work they present the actin network growth against a flexible cantilever, relying on an AFM assay, as previously detailed in subsection 2.3.2. As the cantilever exerts a restoring force that is proportional to its deflection ($K_{AFM} \sim 20$ - 30 pN.$\mu$m$^{-1}$), the growing network faces an increasing load until stall. This force microscopy technique is capable of exerting forces up to hundreds nN in a flat nucleating surface which avoids ambiguities caused by the curvature of the substrate.

As seen in Figure 3.9, a load independent phase precedes the stall phase, where the elongation rate decreases until a stall at a force of 294 nN, which corresponds to a pressure of $\sim$ 1 kPa. Notably, the observed convex shape differs from previous experimental concave decrease as predicted by the Brownian ratchet [12] [13] or elastic gel models [102]. At first glance, the load independent phase could whether be explained by actin force-independent kinetics or by load adaptation as seen in the auto-catalytic [103] model which will be introduced in subsection 3.3.2. To lift the indeterminacy, the team performed force-reduction experiments.

Surprisingly, by reducing the force during the load-independent phase and by maintaining it at constant value, the velocity quickly increased maintaining a constant value for long times, as seen in Figure 3.10. This result discarded both results as no change in velocity was expected in the first hypothesis, while the short increase (second time scale) should lead to an exponential decay toward the original value in auto-catalytic model. In the same way, Parekh et al. showed that their could be two velocities for the same applied stress, exhibiting the load history dependence. This hysteresis phenomenon is explained by the structural remodelling of the network with an increase of filaments pushing the load.

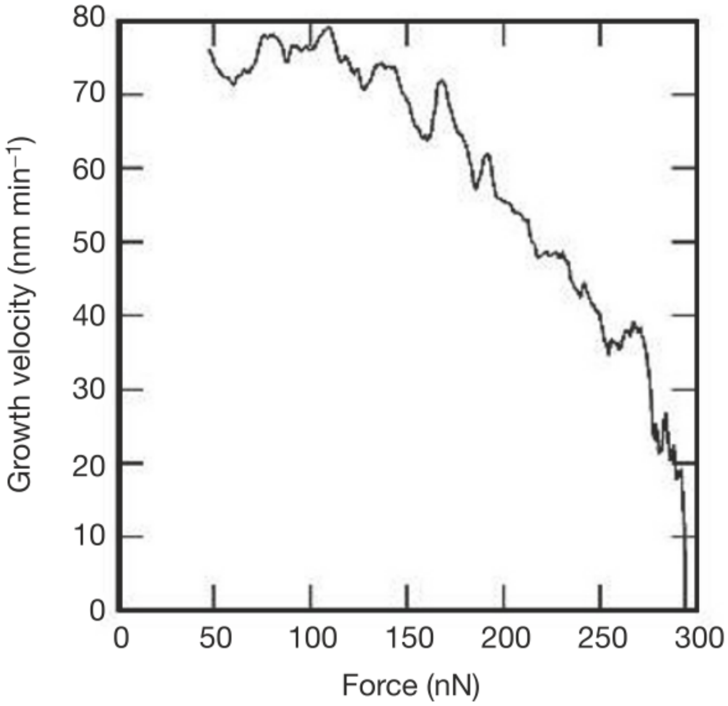

Figure 3.9: Force-velocity relationship for the experiment: A load independent phase precedes the stall one, from [84]

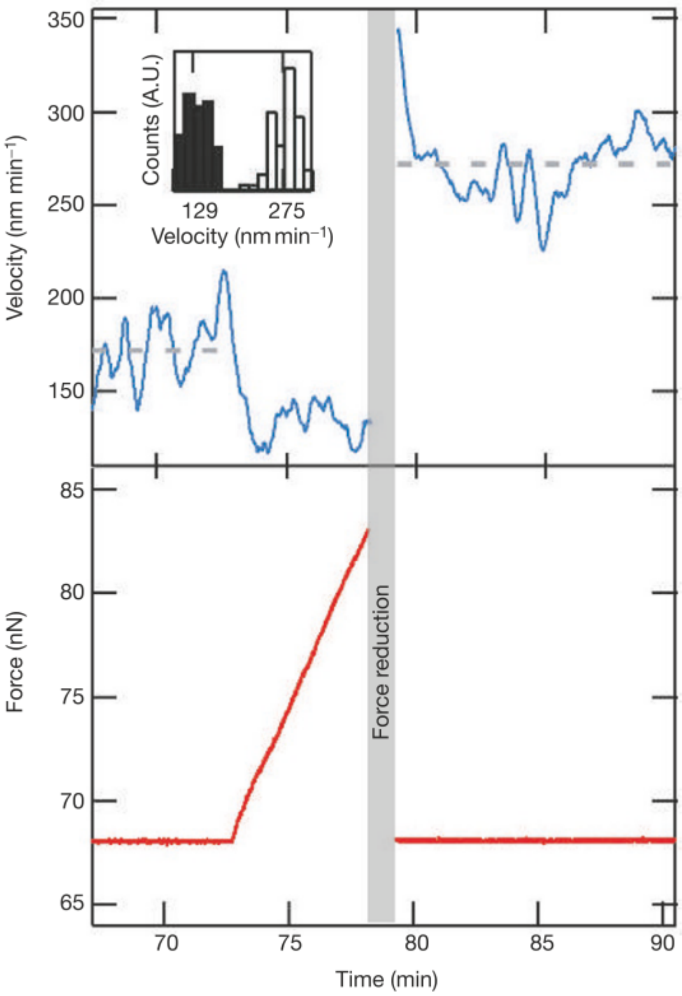

Figure 3.10: Force reduction experiments showing two stable velocities at a single force. (Bottom) After remaining constant for 73 min, force is allowed to increase to 83 nN before being reduced to its initial value of 68 nN 6 min after. (Top) The increase of the force in the second phase causes a decrease of the velocity, during the last phase the velocity increases to a value higher than the original one demonstrating multiple stable growth rate for a single force, from [84]

In Bieling et al. [87], the researchers measured the steady-state growth velocity of branched actin networks while applying a constant stress, as shown in Figure 3.11. Remarkably, the measured velocity exhibited a sharp decrease under small loads but did not completely stall until the load exceeded 1250 Pa, which is comparable to stresses observed in crawling cells [61]. The observed velocity curve, though convex, did not follow a simple exponential decay as expected by elastic Brownian ratchet models of a fixed number of growing filaments [13]. The more gradual decrease at higher forces suggested a possible load-dependent effect on filament density, which was further confirmed in the same study.

By using TIRF microscopy, they found that the density of the actin filaments increased as the applied stress was increased. Furthermore, they examined the energy efficiency (mechanical power over the energy consumption rate) of the growing actin networks and found that it was highly load-dependent. At higher forces, the energy efficiency increased from 3% to 14%. This indicated that under high load, polymerizing filaments appeared to share the mechanical burden more evenly.

Overall, the changes in velocity and density under different stress conditions seemed to nearly compensate each other, as the flux of actin (product of velocity and density) exhibited only a weak decrease with increasing stress. This delicate balance between velocity and density suggests that the growth of branched actin networks is tightly regulated to adapt to varying mechanical environments, possibly to optimize mechanical performance and energy efficiency. It remains to be seen to what extent this adaptation can be explained by physical criteria.

Investigating more precisely the density increase, Fletcher and his team deciphered that it was primarily due to an increase in polymerizing filaments, but that it was, more significantly resulting from a change in the network's architecture. Surprisingly, they found that this architecture adaptation did not involve a change in filament length. The mean filament length remained constant at approximately 300 nm regardless of the applied load. This discovery led to the understanding that there was a close match between the load response of filament elongation and capping.

They later confirmed this by showing that capping proteins indirectly stimulated Arp2/3 activity by inhibiting the interaction between NPFs and free barbed-ends, a mechanism known as "barbed-end interference" [41]. They further demonstrated that capping proteins also followed Brownian ratchet dynamics, similar to actin monomers [42]. This revelation indicated that the same theoretical framework is governing both force-response processes, which explains the high regulation of filaments length for changing loads. All in all, the Brownian ratchet not only underlies the ability of growing filaments to generate forces but also plays a critical role in their capacity to dynamically modify their architecture in response to mechanical loads.

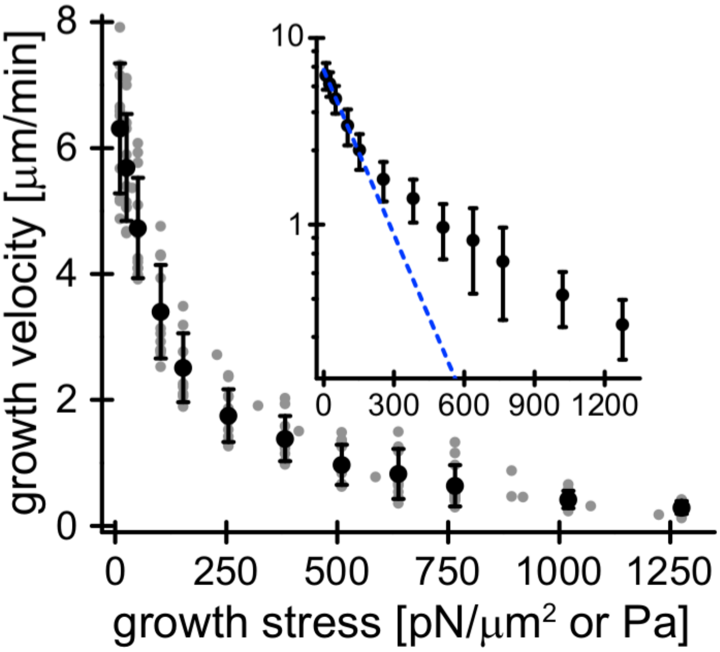

Figure 3.11: Steady-state growth velocities of branched actin networks as a function of growth stress. Raw data in grey, averages in black with SD. Inset: semi-logarithmic plot with a single exponential fit (dashed blue line) stresses the divergence with the Brownian ratchet, from [87].

### Magnetic colloids

In their study previously introduced in section 2.3.2, Bauër et al. [89] provided evidences of a stress stiffening behavior and a non linear response at small stresses with magnetic colloids. In addition, they were able show the slow down of network assembly as force is increased. They gradually increased the magnetic field and studied the displacement as a function of time. As they only focus small displacement (less than 100 nm), they assume that the imposed stress is constant during these growth steps, see Figure 3.12 (Left). From this they can extract the velocity as the function of the stress as seen in Figure 3.12 (Right). Even though the overall shape (convex) is similar to previous studies in rather close conditions (with purified proteins), the obtained velocities at zero force are remarkably slow: around 0.2 $\mu$m.min$^{-1}$ here, $\sim$ 2 $\mu$m.min$^{-1}$ in [83], 8 $\mu$m.min$^{-1}$ in [87]. To date, this difference has not been discussed, nor explained.

In the next section we will provide some theoretical results and insights on branched actin growth. We will explore two sides of the literature that have been lacking in parallel growth models: the importance of the elastic nature of filaments in networks as well as the interplay between branching, capping and elongation which is key for the formation of branched structures. While the second has been extensively studied and has recently performed significant advances, we think that the role of elasticity in branched networks is lacking theoretical and quantitative studies.

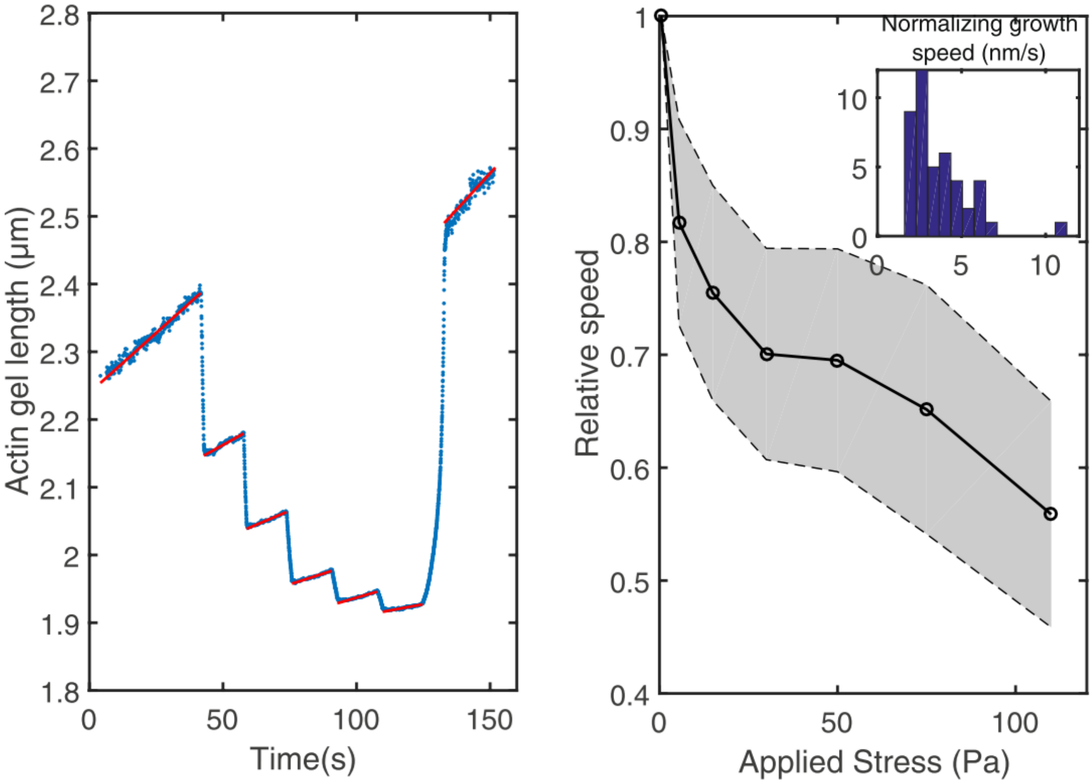

Figure 3.12: (Left) Actin gel length measured by the distance between the faces of two cylinders as a function of time. The magnetic field is increased by 15 s steps from 3 mT to 80 mT. The displacement as a function of time is fitted at each step of constant magnetic field (red lines). (Right) Normalized speed as a function of applied stress for several actin networks, inset: distribution of the normalizing velocity measured at low stress. The shaded area represents the 95% confidence interval, from [89].

### 3.3.2 Theoretical and numerical approaches

**Gerbal et al.**

One of the initial theoretical investigations into network response were led by Gerbal et al. in their work on the elastic model of *Listeria monocytogenes* propulsion [102]. This study introduced a continuous elastic gel model to elucidate how the accumulation of actin filaments into the tail leads to the bacterium's propulsion. In this model, filaments are cross-linked, and the tail is firmly attached to the bacterium. This conceptual framework refutes the notion of propulsion based on a simplistic Brownian ratchet model, where the filaments exert force on the bacterium without any attachment. Observations suggest that the propulsion of *Listeria monocytogenes* relies on the relaxation of a continuous elastic medium. The addition of a new filament through polymerization induces elastic deformation in the gel: the incorporation of a new layer compresses the previously formed layers. To simplify the system, the authors employ a two-gel model, with an internal gel produced at the back hemisphere and an external gel generated on the surface of the cylinder, as illustrated in Figure 3.13 (Left).

Computationally, by equating the forces exerted on the bacterium, it becomes feasible to determine the velocity of the entire structure. Here, we will outline the steady-state outcomes derived from the simplified one-dimensional model. In this scenario, the authors exclusively consider the propulsion within the internal gel, treating it as a purely elastic medium characterized by a constant strain. They also account for the dependence of polymerization speed at the surface on the applied force, which encompasses the Brownian ratchet mechanism. Incorporating these factors along with volume and mass conservation assumptions, they arrive at the following expression:

$$v_p = \frac{v_{p0}}{1 + F_{ext}/YS_b} e^{-(F_{ext}ad^2)/(k_BTS_b)} \tag{3.24}$$

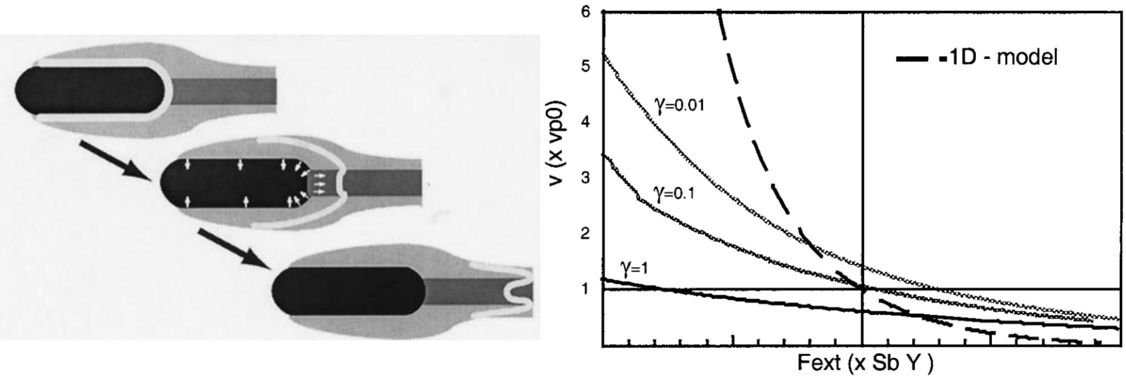

Figure 3.13: (Left) Elastic model of the propulsion of the material: new filaments are polymerized and expand the older layers, inducing a stress in the gel. The motion is caused by the relaxation of this stress in the tail. In light grey is depicted the internal gel, in dark grey the external one. (Right) Force-velocity curve for the two gel model for various values of the friction parameter $\gamma$. The dashed-line is the curve obtained for the one-dimensional model. Adapted from [102]

In this equation, Y represents the Young modulus of the gel (approximately $10^3$ to $10^4$ Pa), $S_b$ is the cross-sectional area of the bacterium, $v_{p0}$ denotes the velocity at zero force, $d$ stands for the mesh size, and $a$ corresponds to the length of a monomer. The velocity not only exhibits exponential decay but also decreases more rapidly as it scales inversely with $F_{ext}$, as depicted in Figure 3.13 (Right).

The inverse term captures the elastic compression, while the exponential term accounts for the change in polymerization speed. Additionally, the term $YS_B$ emerges as the characteristic force of the model, which is on the order of 1 nN. However, due to the omission of filament depolymerization, their analysis does not yield a stall force.

In the two-gel model, the authors also consider the normal polymerization of fibers at the surface of the bacterium, leading to the expansion of older layers outward and the accumulation of elastic energy. This radial energy accumulation is subsequently released in the tail. Intriguingly, the authors augment this elastic motor with the force induced by filament surface friction. Transient links formed by actin fibers at the surface result in a friction force that is parameterized by a drag coefficient $\gamma$. The resulting curves obtained from numerical simulations are illustrated in Figure 3.13 (Right) for various drag values. The overall shape of the curves remains consistent with the one dimension model, although the drag coefficient introduces a new dimension. Increasing friction or external force qualitatively yield similar effects, slowing down the movement of the bacteria. Notably, at zero force, the velocity no longer equals the polymerization rate. Depending on $\gamma$, the velocity can be greater or less than $v_{p_0}$, representing a significant departure from the one-dimensional model.

The analysis conducted by Gerbal et al. laid the groundwork for a significant theoretical framework in modeling the propulsion of *Listeria*. These fundamental insights were subsequently adapted to situations explored in studies like Marcy et al. [83], resulting in fitting models as depicted in Figure 3.8. Nevertheless, while these models incorporated both elasticity and polymerization, they assumed stiffness as a fixed parameter due to the presence of crosslinkers and the magnitude of applied stresses. De facto, these assumptions might not align with the specific scope of the study under consideration. In addition, they do not take into account the branching or the nucleating process and their effect on density.

### Carlsson

In 2003, Carlsson introduced a series of kinetic rate models based on the orientation-dependent number density of actin filaments [103]. In this work, he deliberately excludes the elastic nature of actin to underscore the impacts of branching and capping on the density of filament ends. Broadly, two variants are considered: one where new branches originate from existing ones (auto-catalytic behavior), and another where branches emerge independently (nucleation behavior), as depicted in Figure 3.14 (Top). Despite experimental evidence showing that branches indeed arise from existing filaments, the simulations in the auto-catalytic scenario suggest that the growth velocity should remain constant regardless of the applied force. This contradicts observations from experiments. In the nucleation hypothesis, the velocity decreases as force is applied, resembling the overall shape of the "tethered ratchet" model proposed by Mogilner et al. [104], as shown in Figure 3.14 (Bottom).

A plausible explanation for the unexpected behavior of the auto-catalytic model is rooted in one of the author's assumptions. Carlsson suggests that the rate of nucleation should increase under load due to the auto-catalytic nature of Arp2/3. However, this hypothesis had not been experimentally tested until a recent study led Li et al. [42] who demonstrated the opposite. Their work indicate that under compressive forces, the overall nucleation rate actually decreases. In this study they provide pioneering results on the molecular mechanism underlying load adaptation of branched networks. We will detail their main results and interpretations in a subsequent paragraph.

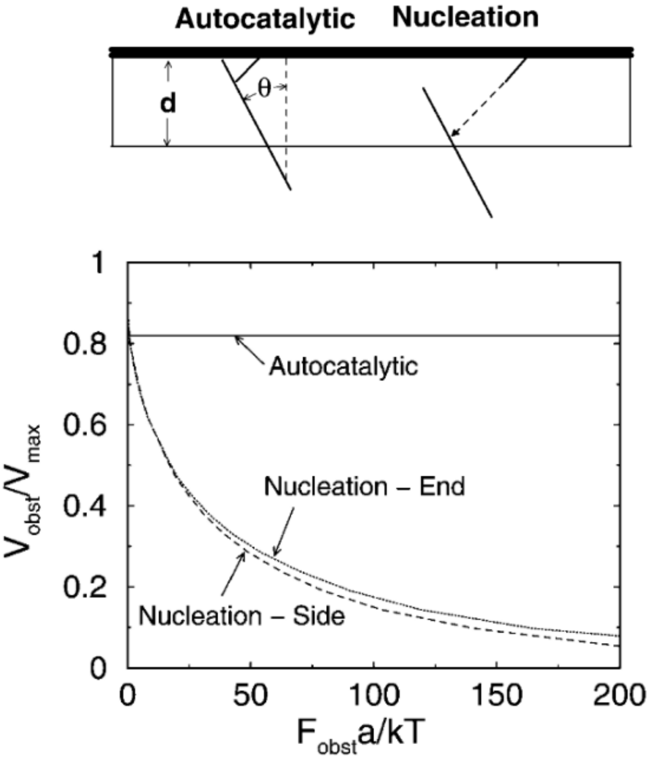

Figure 3.14: (Top) Scheme of an auto-catalytic vs nucleation-based branch generation process, with $d$ the branching layer thickness and $\theta$ the angle between filament and growth directions.(Bottom) Force-velocity for nucleation and auto-catalytic models, with side and end branching. $V_{max}$ is the maximum free-filament velocity, $F_{obst}$ the force exerted by the obstacle and $a$ the size of a monomer. Adapted from [103]

**Lee et al.**

Before concluding this section with the findings from Li et al. [42], it is worth mentioning a study by Lee et al. [105] that delved into the force generation process using Brownian dynamics simulations. In their work, Lee et al. investigated semi-flexible filaments that self-assemble into branched networks with Arp2/3 and exert force on a disk. Notably, unlike typical scenarios where Arp2/3 is activated by NPFs at the surface of the disk, in this case, the disk releases Arp2/3 from its rear side, inducing the formation of F-actin. To introduce a load on the disk, the authors applied a drag force by altering the disk radius $R_D$ and the viscosity experienced by the disk, denoted as $\eta_D$: $F_{drag} = \zeta_D V \propto 2\eta_D R_D V$. By doing so, they aimed to mimic the approach employed in the analysis of *Listeria*, where viscosity was increased by adding methyl-cellulose (well-known for its versatility of use) to the system [100] [101]. This adjustment does not influence the motion of free actin monomers, as they are much smaller than the mesh size of the methylcellulose polymer solution. The researchers also conducted simulations involving the application of a constant force on the disk, yielding similar results.

In Figure 3.15 (Left), velocity is plotted against the load force for different disk surfaces. Additionally, the experimental results from Parekh et al. [84] are shown on the same plot. Notably, the velocity remains constant until it reaches a certain point denoted as $F^*$, beyond which it begins to decline (typically in the range of 10 - 100 pN). The authors of the study observe that $F^*$ appears to scale proportionally with approximately half of the stall force ($0.5 \cdot F_{stall}$), which aligns with the observations made in the work by Parekh et al.

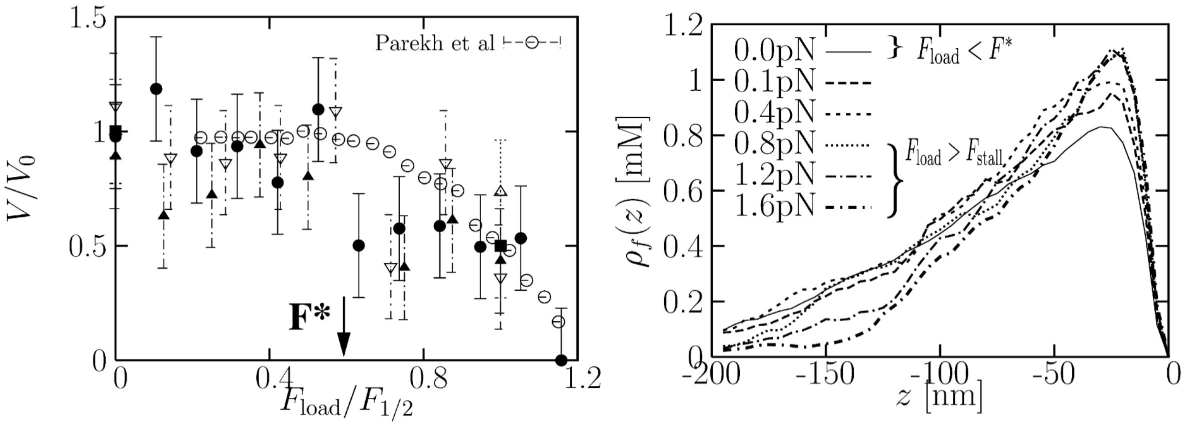

Figure 3.15: (Left) Velocity scaled by the zero force-velocity $V_0$ as a function of the force scaled by $F_{1/2}$, with $F_{1/2}$ the force when the velocity drops to half its free value: $V_0/2$. Data are shown for different disk sizes ( $R_D$= 30nm, △; 35nm, ■; 40cm, ▽; 45nm, ▲; and 50nm, ●) and compared to experimental results from Parekh et al. [84]. $F^*$ the maximum load the system can sustain while maintaining $V_0$, scales like $\approx 0.5 \cdot F_{stall}$. (Right) Steady-state density profiles of actin monomers in filaments, $\rho_f$, as a function of position $z$ in the frame of the moving disk, whose position is $z = 0$. Profiles are shown for different applied loads for flexible filaments $\ell_p = 0.01$ $\mu$m. Adapted from [105]

The simulations of Lee et al. had been done for a persistence length of $\sim$ 0.1 $\mu$m, which is particularly low ($\ell_p \approx 10$ $\mu$m) but much greater than the mesh size which ensures that they are in the correct regime. They repeated their experiments for stiffer and softer filaments and concluded that the constant behavior of $V$ at small loads is a property of stiff filaments that disappear for sloppy ones.

Furthermore, the study examined the impact of filament stiffness on their properties by analyzing the density profiles $\rho_f$ as a function of the distance to the disk ($z$). Right behind the disk, the density is near zero as the disk repels actin. Moving towards more negative $z$ values, the density increases, reaching a maximum (associated with Arp2/3 recruitment), before subsequently declining due to depolymerization. Of particular interest is the behavior observed for flexible polymers ($\ell_p = 0.01$ $\mu$m), as depicted in Figure 3.15 (Right). The system displays sensitivity to applied loads, with the maximum density increasing notably for higher forces due to buckling effects. Notably, under high $F_{load}$ conditions, the peak density eventually saturates.

This study reveals intriguing insights: for small loads and relatively rigid filaments, the velocity remains constant regardless of stress, as the velocity is determined by the polymerization rate. On the other hand, at high loads, the comet tail can withstand forces up to a certain threshold, reaching the stall point. This analysis underlines the fact that the force-velocity relationship is influenced by filament stiffness, resulting in a shorter plateau, even though stiffness does not affect the low-load regime.

### Li et al.

In the study conducted by Li et al. [42], researchers provide a molecular-level explanation for the phenomenon in which branched actin networks become denser when growing against an external load. They employed a similar experimental setup to that presented in [87], using actin pillars growing against an AFM tip. The researchers identified three crucial reactions that collectively define the structure of the network: nucleation, elongation, and capping.

Remarkably, they established that the capping process follows the dynamics of a Brownian ratchet, similar to elongation. This process decreases exponentially with the applied load. While the number of sites at which nucleation occurs (corresponding to immobilized NPFs at the surface) remains constant, nucleation decreases with load. This reduction is attributed to a phenomenon termed “barbed-end interference”. Essentially, the actin barbed-ends interfere with the WH2 (or V) domain of NPFs, hindering the activation of Arp2/3 proteins. Consequently, the applied force leads to an increase in the number of free barbed-ends, which can subsequently interact with a greater number of NPFs in non-nucleating complexes [41]. This negative feedback mechanism elucidates the decrease in Arp2/3 nucleation, a behavior that contradicts the auto-catalytic model proposed by Carlsson.

### Lappalainen et al.

Globally, the steady-state growth is sustained by the equilibrium between capping and nucleating rates:

$$R_{cap} = k_{cap}[\mathrm{CP}]E = R_{nuc} \tag{3.25}$$

Here, $k_{cap}$ is the capping rate constant (in $\mu\mathrm{M}^{-1}.\mathrm{s}^{-1}$), [CP] the capping rate concentration (in $\mu$ M) and $E$ the surface density of free barbed-ends (in $\mu\mathrm{m}^{-2}$).

In their recent review on the regulation of actin dynamics, Lappalainen et al. reevaluate this dynamic equilibrium and propose a comprehensive framework to explain steady-state growth (as depicted in Figure 3.16 (Left)) [30]. For the capping process, the reaction rate increases exponentially with the surface density. This increase occurs as the load is distributed across more filament ends, the reaction rate scales according to $\exp(-F_1 a/dAk_BT)$, where $d$ represents the density of barbed-ends and $A$ denotes the surface area of the membrane decorated with NPFs. On the other hand, branching (or nucleation) reaction rates decrease with density due to the finite pool of available NPFs and the phenomenon of “barbed-end interference”. By balancing these two reaction rates, a steady-state is established, resulting in an equilibrium density of the network.

When the external mechanical load increases from $F_1$ to $F_2$, this change has relatively minor effects on the branching process itself. However, it notably lowers the capping reaction rate curve due to the Brownian ratchet. Consequently, the system dynamically adjusts to a new steady-state characterized by reduced reaction rates (leading to a decrease in velocity) and higher network density (as illustrated in Figure 3.16 (Right)). This comprehensive model provides a coherent explanation for the observed phenomenon of network densification during growth against an applied mechanical load. In summary, these recent studies have successfully captured essential features of branched filament networks, shedding light on the intricate molecular mechanisms that underlie their behavior.

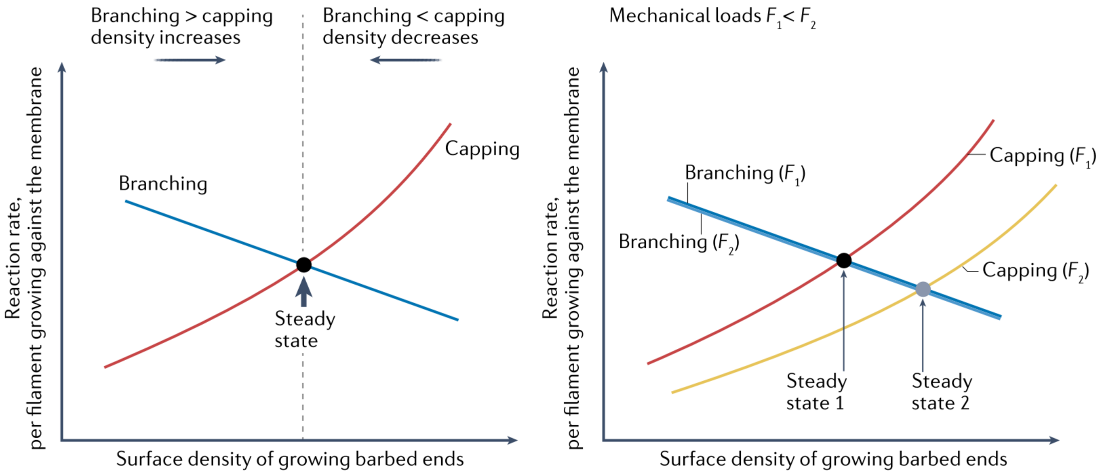

Figure 3.16: Molecular explanation for branched network mechanical adaptation. (Left) At steady-state, the surface density of growing barbed ends results from an equilibrium between branching and capping reaction rates. (Right) An increase of the mechanical load significantly changes the capping curve, slightly the branching one. This leads to the establishment of new steady state with increasing density. From [30]

Based on the information presented earlier, it is evident that several key aspects of the branched actin force generation problem remain to be explored. First and foremost, the determination of the stall force for branched filament networks in such complex structures is still an open question. Investigating the pivotal role of the stall force in this process would yield valuable insights. For instance, the condensation transition observed in the calculations of Tsekouras et al. [95] has not been demonstrated in the context of branched networks and could be an intriguing avenue of investigation. Secondly, the phenomenon of stress-stiffening in branched networks, which significantly influences the growth against a membrane, lacks comprehensive theoretical explanations. Understanding how the mechanical properties of these networks are affected by stress and how this relates to growth dynamics is a critical challenge that warrants further exploration. Finally, considering the aging of the network and the evolution of segments that have already experienced growth presents an additional layer of complexity. Investigating how the network properties change over time, and how this might impact force generation and overall behavior, is an intriguing avenue for future research. Addressing these key issues would contribute significantly to our understanding of the mechanics and dynamics of branched actin networks, providing insights into their intricate behavior under various conditions and mechanical constraints.

# Chapter 4

# A theoretical framework for branched actin elasticity

Prior to delving into the research carried out within this thesis, it is pertinent to highlight recent theoretical advancements that share a close affinity with our subject matter. In a yet-to-be-published study, Mehdi Bouzid and Martin Lenz address the issue of elasticity of branched network structures, placing a particular emphasis on the pivotal role of entanglement. These insights hold significant relevance to our investigations, as they furnish a comprehensive theoretical framework for understanding the stress-stiffening phenomenon.

## 4.1 Vanishing elasticity of branched networks

We first start by considering elasticity of branched networks without entanglement. In this context, the network is conceptualized as an assembly of discrete components interlinked with one another. This perspective allows us to treat it as an ensemble of $N$ interconnected vertices existing within a $d$-dimensional space. These vertices are arranged in adherence to stipulated conditions that dictate optimal distances and angles between them.

Dating back a century and a half, Maxwell introduced a fundamental principle to quantify the stability and elasticity of networks [106]. This principle treats interactions as constraints, and stipulates that the count of constraints must be equal to or exceed the number of internal degrees of freedom (d.o.f) to avert the emergence of soft deformation modes. We shall enumerate these d.o.f within the context of a minimal branched structure. With four vertices existing in three-dimensional space, the structure possesses a total of 12 d.o.f. Among these, 6 are classified as global d.o.f (comprising three translational and three rotational ones), thereby leaving 6 internal d.o.f. Notably, three constraints enforce the fixation of fiber lengths, while two angular constraints impose the linearity of the principal filament, and an additional constraint dictates the branching angle, as illustrated in Figure 4.1. As a result, the network attains an isostatic point, signifying the threshold between undercoordinated and overcoordinated regimes. Introducing a new branch entails the addition of a vertex, thereby accompanying it with three d.o.f and three constraints (one related to length and two to angles). Consequently, through this recursive process, the network consistently maintains its isostatic state.

In this context, as elucidated in [15], networks at the critical coordination point exhibit a diminishing linear elasticity as the thermodynamic limit is approached. Instead, they display non-affine displacements, wherein branches undergo substantial and uncoordinated movements when the network experiences compression. These substantial displacements facilitate the emergence of entanglement points, which in turn strengthens the network.

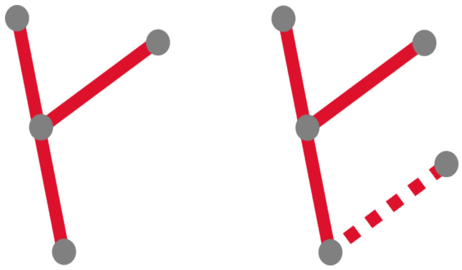

Figure 4.1: Scheme of the minimal structure of branched networks with four vertices and three edges (Left), and the appearance of a new branch with a new vertex on (Right).

Consequently, while the critical coordination of branched networks might seemingly obliterate their rigidity, it paradoxically enables its self-establishment through the creation of entanglement points induced by applied forces. These entanglement points contribute to the augmentation of the material's rigidity. In the subsequent section, we will elucidate the theoretical analysis conducted by Bouzid and Lenz in this context.

## 4.2 An analytical theory based on entanglement

The authors establish their theoretical framework by building upon Van Wyk's analysis of another weakly coordinated network, specifically sheep's wool [107]. Drawing inspiration from this work, they derive a Pressure-Volume relationship for branched systems, initially up to an integration constant. This constant is subsequently determined in a secondary step, specifically for networks that have grown under compressive stress.

The network is conceptualized as a unique filament of length $L$, radius $r$, and bending rigidity $\kappa$, placed within a confined volume $V$. As the volume is diminished, the filament undergoes compression, prompting it to coil and establish numerous contacts with itself. To further elaborate, the filament is subdivided into $L/r$ pseudo-monomers of length $r$, and it is naturally assumed that the number of contacts is proportional to the length of a monomer and its volume fraction $\phi \sim Lr^2/V$. Consequently, a mean-field approximation is derived for estimating the number of contacts.

$$N_{contacts} \approx \phi L/r \approx L^2 r/V \tag{4.1}$$

Thus the long filament can be seen as divided into $\sim N_{contacts}$ segments of characteristic length $\xi = L/N_{contacts} \approx V/Lr$, see Figure 4.2 (Left).

Within this confined volume defined by parameters $V$ and $P$, a typical segment of the filament maintains its bent configuration due to an applied force $f$. When an additional strain $\mathrm{d}\gamma = \mathrm{d}V/V$ is introduced (where $\mathrm{d}\gamma < 0$ signifies compression), it results in an increment of pressure $P$ by an amount $\mathrm{d}P$. Assuming that this added pressure is distributed among all the filaments in a horizontal cross-sectional plane and that the segments are, on average, separated by a distance of $\sim \sqrt{V/L}$, an expression for the increase in load experienced by a filament can be derived:

$$\mathrm{d}f \approx (V/L)\mathrm{d}P \tag{4.2}$$

Following this, the introduction of the additional strain $\mathrm{d}\gamma$ induces a relative displacement of the filament ends, given by:

$$\mathrm{d}y \approx -\xi \mathrm{d}\gamma = -\xi \frac{\mathrm{d}V}{V} \tag{4.3}$$

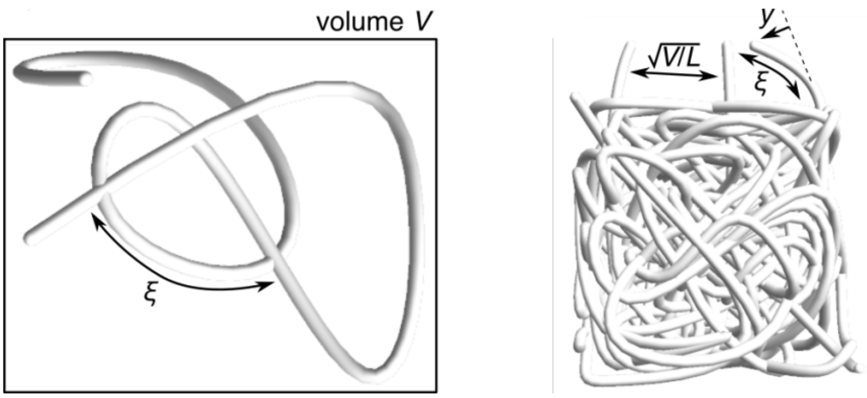

Figure 4.2: (Left) A filament confined in a volume $V$ finally randomly forms contact with itself. The characteristic length between consecutive contacts is $xi$. (Right) As filaments grow, the deflection y of a segment located at the growing surface of the network increases until it forms a contact with a neighboring filament, which is typically located at a distance $\sqrt{V/L}$. The typical segment length for which this happens fixes the value of $\xi$.

Now, if we consider the mechanics of a single bent filament segment, we note that moving its end by a length $\mathrm{d}y$ typically requires an elastic force $\mathrm{d}f = (\kappa/\xi^3)\mathrm{d}y$. As a result, we have:

$$\mathrm{d}P \approx \frac{L}{V}\mathrm{d}f \approx \frac{L}{V}\frac{\kappa}{\xi^3}\mathrm{d}y \quad \Rightarrow \quad \frac{\mathrm{d}P}{\mathrm{d}V} = -\bar{\gamma}\frac{\kappa L^3 r^2}{V^4}, \tag{4.4}$$

Here, $\bar{\gamma}$ represents an undetermined numerical pre-factor of order one. Integrating this equation across the volume $V$ yields the pressure-volume relationship for this system:

$$\begin{aligned} P &= \frac{\bar{\gamma}\kappa L^3 r^2}{3V^3} - P_0, \\ &= P_0\Big[\Big(\frac{V_0}{V}\Big)^3 - 1\Big], \end{aligned} \tag{4.5}$$

This expression reveals the existence of a resting volume $V_0$, directly related to the integration constant $P_0 = (\bar{\gamma}\kappa L^3 r^2)/3V_0^3$. This relationship is the main result from van Wyk theory [107] which leaves out an explicit expression of $P_0$. Additionally, Equation 4.5 introduces the ensuing stiffness-stress expression:

$$K = -V\frac{\mathrm{d}P}{\mathrm{d}V} = 3(P + P_0) \tag{4.6}$$

It is noteworthy that this theory might overestimate the stiffness at extremely low stresses, $K_0 = 3P_0$. This plateau might not accurately describe networks with finite length branches, which display stiffness that decreases according to their simulations. The authors emphasize the importance of considering the limitations of the infinite-filament-length hypothesis when the distance between contact points $\xi$ approaches the length of the branches. To determine the dependence of $P_0$ on the growth conditions of the network, the authors examine the scenario of growth under significant compressive stress $\sigma_0$. They assume that $\sigma_0$ is sufficiently large to ensure that $\xi$ remains smaller than the branch length. Consequently, during growth, filament deformation leads to the formation of contacts that increase and reinforce entanglement points, which persist even after the compressive force is removed. This accounts for the existence of a finite resting volume $V_0$ and pressure $P_0$.

Now, let us delve into the details of the entanglement process and derive an expression for $\xi(\sigma_0)$. With a surface density of filaments of $L/V$, each growing filament experiences a force $f \approx V\sigma_0/L$ during growth. Under this force, the deflection $y$ of a segment of length $\xi$ can be approximated as: $y \approx f\xi^3/\kappa$. The contact with a neighboring filament occurs when this deflection $y$ is on the order of the lateral distance between segments, $\sqrt{V/L}$, as seen in Figure 4.5. This growth-stability condition can be expressed as:

$$\frac{V\sigma_0}{L}\frac{\xi^3}{\kappa} = \sqrt{\frac{V}{L}} \tag{4.7}$$

Or, as $\xi \approx V/Lr$:

$$\xi(\sigma_0) \approx \left(\frac{\kappa}{\sigma_0}\right)^{2/7} r^{-1/7} \tag{4.8}$$

And then,

$$K_0 \approx P_0 \approx \frac{\kappa L^3 r^2}{V_0^3} \approx \frac{\kappa^{1/7}}{r^{4/7}}\sigma_g^{6/7} \tag{4.9}$$

Thus, we obtain the scaling of the plateau modulus:

$$\boxed{K_0 \approx \kappa^{1/7} r^{-4/7} \sigma_0^{6/7}} \tag{4.10}$$

In addition, as $\xi \approx V_0/Lr = V_0 r/Lr^2$, we get: $\xi \approx r/\rho_0$.

Then, using Equation 4.8, this naturally leads to:

$$\boxed{\rho_0 \approx \kappa^{-2/7} r^{8/7} \sigma_0^{2/7}} \tag{4.11}$$

In this regime, the formulas for the stiffness modulus plateau (4.10) and the equilibrium density (4.11) are solely dependent on the bending rigidity $\kappa$, the filament radius $r$, and the growth stress $\sigma_0$. Remarkably, the length of the filament does not play a significant role in this context, as it is replaced by the distance between contact points, which is uniquely determined by the three aforementioned parameters.

Hence, we believe that these scaling relationships offer valuable insights into the stress-stiffening phenomenon observed in branched actin networks, shedding light on the broader stress response mechanisms. These findings are poised to provide essential context for interpreting our research outcomes.

Furthermore, while the Brownian ratchet concept is well-established for individual fibers, its applicability to networks composed of numerous branched fibers remains less clear. Our study is designed to address this gap by predicting how the growth speed is influenced by fiber properties and external stress. Specifically, we aim to address the challenges raised in our earlier discussion, building upon observations from the existing literature. This includes investigating the stress response, the significance of the stall force, and the aging of networks. To achieve this, we rely primarily on Cytosim simulations, constructing a system akin to the setups employed in the studies by Bieling et al. and Li et al. [87] [42]. Arp2/3 complexes activated on a disk introduce new actin fibers from existing ones, generating an upward actin flow hindered by opposing stress.

In the subsequent section, we provide a concise introduction to Cytosim and detail our simulation setup and our force generation model. We then present our results, analyzing the response of velocity and density to stress, followed by an exploration of the influence of the stall force within the system. In the third step, we delve into the question of network evolution and aging.

# Chapter 5

# A numerical force velocity framework

## 5.1 The Cytosim environment

### 5.1.1 General description

To run simulations, we employ Cytosim, an open-source simulation engine founded on Langevin dynamics [108]. This software, accessible on GitLab equips users with a toolkit for simulating various cellular structures within a virtual cell environment. It enables the construction and manipulation of cytoskeletal structures such as asters or bundles. Cytosim's versatility has been demonstrated across several applications, including the exploration of disordered contractile cytoskeletal networks [109] and the organization of actin filaments [110].

Cytosim offers four primary object types, allowing for the representation of diverse structures: fibers, hands, solids, and spaces. Fibers are oriented line segments composed of connected points. Each point is identified by its position vector $\mathbf{r}_i$. Within a fiber, consecutive points are separated by a segmentation step $\mathrm{d}s$. Key characteristics of a fiber encompass its rigidity, length, directionality, and growth process. Hands are functional entities that can be free or attached to fibers, solids, or spaces as illustrated in Figure 5.1. When two hands are coupled, they can emulate motors or cross-linkers. The binding and unbinding rates, along with the binding range, are fundamental attributes of hands. Solids represent rigid assemblies of points, although they are not utilized in our study. Spaces generally define the boundaries of the simulated environment.

Cytosim incorporates forces acting on cytoskeletal structures. Considering their finite rigidity, fibers are amenable to bending, and their bending force can be computed: $F \sim \frac{\kappa}{\mathrm{d}s}(2\mathbf{r}_i - \mathbf{r}_{i+1} - \mathbf{r}_{i-1})$, see Figure 5.2. However, fibers cannot be compressed, a Lagrangian parameter enforces a constant step size ($\mathrm{d}s$) between points. Nonetheless, the tension applied during simulations can be extracted from the outputs. Attached couples are characterized by the rigidity of their link ($k$ in Figure 5.2), which behaves as a Hookean spring and responds to extension or compression. To confine a fiber within a space, a confinement force is implemented as another Hookean spring. Points located outside this confinement area experience a restoring force proportional to their displacement $\delta\mathbf{r}$ and the confinement stiffness $K_{confine}$, as illustrated in Figure 5.2. This feature will be important for our implementation of a numerical AFM. Furthermore, within Cytosim, objects are subject to steric repulsion effects still modeled as a Hookean spring of stiffness $K_{steric}$. Objects need to be close enough (within the range of a screen length) to feel each other.

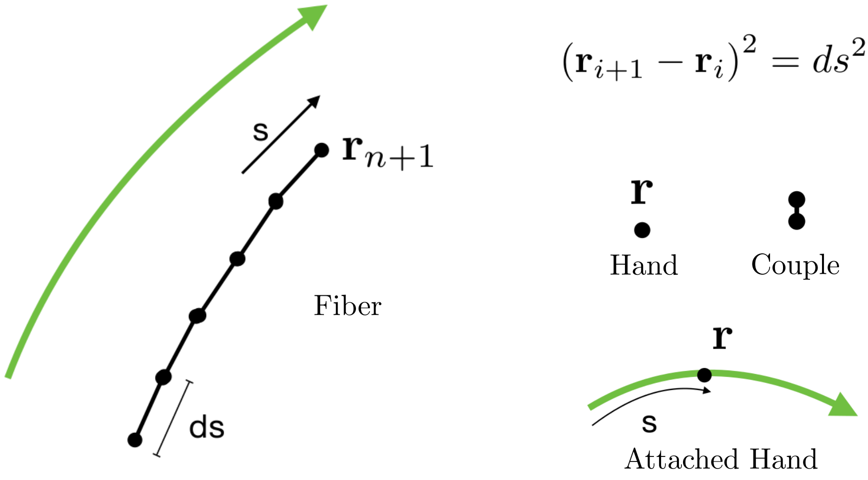

Figure 5.1: Numerical description of a fiber as a set of points $\{\mathbf{r}_i\}_i$ distanced by d$s$. Hands can be free or attached, two connected hands form a couple.

### 5.1.2 Simulation dynamics

Fibers, with a length of $L$, are composed of $p+1$ equidistant points separated by $\frac{L}{p}$ distance from each other. During fiber growth, new points are introduced, added while minimizing the difference $|\mathrm{d}s - \frac{L}{p}|$, where d$s$ represents the specified segmentation length in the model. This interpolation process is depicted in Figure 5.3.

Let us consider a scenario where we are dealing with $N$ fibers in a $d$-dimensional space. A vector $\mathbf{r}$ of size $Nd$ collects the positions of the points on the fibers. The governing equation for motion is a Langevin equation, which can be expressed as follows:

$$\mathrm{d}\mathbf{r} = \mu\mathbf{F}(\mathbf{r}, t)\mathrm{d}t + \eta(t) \tag{5.1}$$

The mobility coefficients are encapsulated within the matrix $\mu$ of dimensions $Nd \times Nd$. The forces acting on the points at time $t$ are represented by the matrix $\mathbf{F}(\mathbf{r}, t)$, also of dimensions $Nd \times Nd$. $\mathbf{F}(\mathbf{r}, t)$ encompasses various forces: bending rigidity, linker and confinement stiffness, and steric repulsion. Lastly, $\eta(t)$, also with dimensions $Nd \times Nd$, encapsulates the effects of random molecular collisions, leading to Brownian motion. This term, which is a Gaussian white noise, introduces randomness since the values differ for each simulation. Cytosim employs a pseudo-random number generator, and the random seed is derived from the clock time during initialization.

Crucially, Cytosim does not explicitly solve the system, as this would necessitate very small time steps to avoid instabilities. Instead, it employs an implicit approach, considering the current state of the system and the subsequent state. Equation 5.1 can thus be expressed as:

$$\delta\mathbf{r} = \mathrm{d}t\mu\mathbf{F}(\mathbf{r} + \delta\mathbf{r}) + \sqrt{\mathrm{d}t}\xi \tag{5.2}$$

At each time step, Cytosim solves the linear problem involving $\delta\mathbf{r}$ by diagonalizing a matrix of size $Nd \times Nd$, ultimately determining the positions of the points.

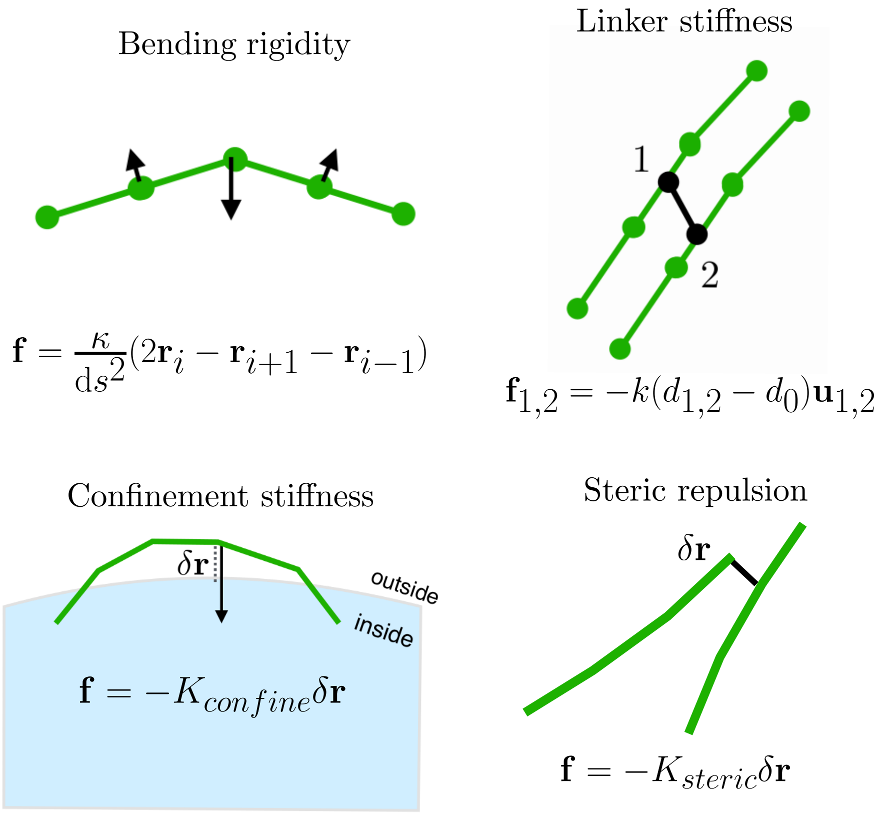

Figure 5.2: Implementation of forces in Cytosim: Bending rigidity, Linker stiffness, confinement stiffness and steric repulsion.

To simulate the Brownian ratchet dynamics, we incorporate the following expression for the growth of actin fibers within the Cytosim framework.

$$\boxed{v = v_0 e^{-\frac{f}{f_0}} - v_{dep} \quad ; \quad f \geq 0} \tag{5.3}$$

$f_0$ is the *growing force*, $v_0$ the polymerization velocity and $v_{dep}$ the de-polymerization velocity. The stall force is thus the following :

$$\boxed{f_s = f_0 \ln\left(\frac{v_0}{v_{dep}}\right)} \tag{5.4}$$

Identifying (3.12) and (5.4) we get :

$$f_0 = \frac{k_B T}{a} \tag{5.5}$$

In this context, the stall force $f_s$ becomes a crucial parameter for quantifying the dynamics of the fiber, along with the bending rigidity $\kappa$, length $l$, and radius $r$. With the understanding of the Cytosim framework and the foundational components required for constructing our model, we will proceed to elaborate on the simulation setup in the upcoming section.

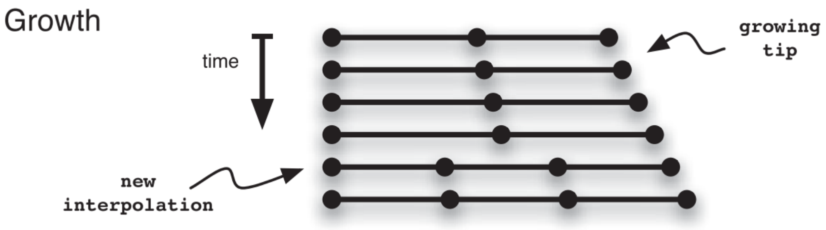

Figure 5.3: Dynamic fibers: the model-points of a fiber are updated when the tips grow, but they are always equally distributed over the fiber. Points are added or removed as necessary to ensure an optimal coverage.

## 5.2 The force generation model

### General description

In this section, we outline the force generation model that we employed within the Cytosim framework, emulating the environment introduced by Bieling et al. We initiate the simulation with a disk containing diffusing Arp2/3 nucleators on its surface, accompanied by a small number of initial fibers (5). The diameter of the base disk is denoted as $d = 1$ $\mu$m, corresponding to a surface area of approximately 0.8 $\mu\text{m}^2$, which is notably smaller than Bieling's experimental setup with an area of 200 $\mu\text{m}^2$. This choice stems from our desire to achieve dense network formations while controlling the numerical complexity. Indeed, our aim was to model a system with a significant surface area that would produce dense networks under stresses of around 500 Pa, without incurring excessive computational costs.

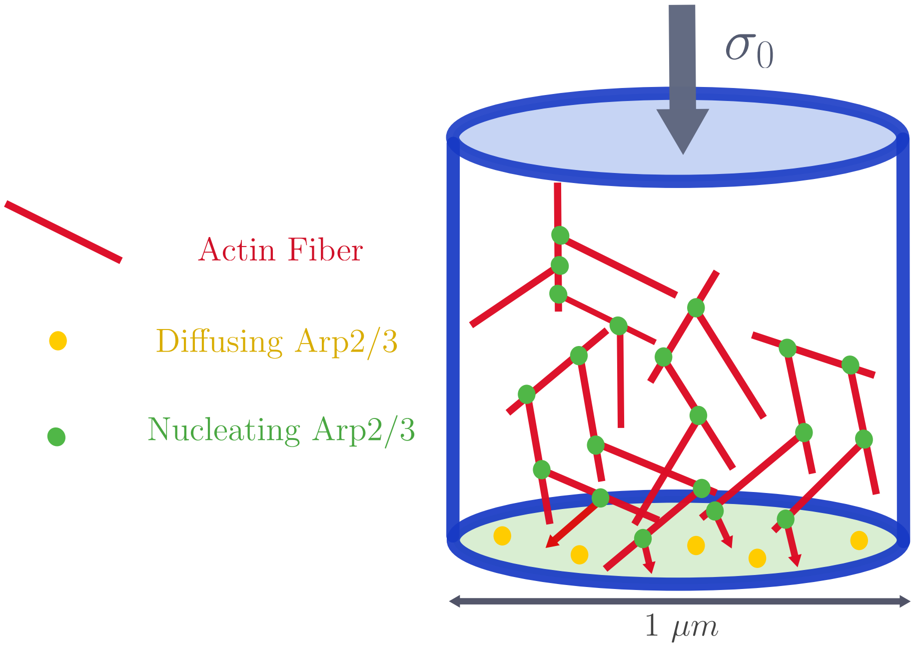

Figure 5.4: Scheme of the simulation system: A branched actin network is growing from the bottom and facing a stress $\sigma_0$.

In our entangled system, the characteristic length $\xi$ represents the distance between contact points, as defined in Equation 4.8. By leveraging the properties of our fibers (e.g., $\kappa = 0.0042$ pN.$\mu$m, $r = 0.005$ $\mu$m) and considering an intermediate stress value $\sigma_0 = 500$ Pa, we estimate the characteristic length as $\xi \sim 0.15$ $\mu$m. This choice ensures that we are operating in a regime where $\xi$ is much smaller than $d$, validating the accuracy of our simulations.

In a simulation, when a diffusing Arp2/3 (depicted in yellow in Figure 5.4) approaches a polymerized filament, it binds to the filament, transforms into a nucleator (depicted in green), and initiates the generation of a new polymerizing filament with a preserved branching angle of 70° between the mother and daughter branches. The source of Arp2/3 is renewed at a constant rate, thereby sustaining network expansion. This setup aims to replicate the in vivo activation of Arp2/3 by NPFs from the WASP family proteins on cellular membranes.

### 5.2.1 AFM implementation

To emulate external load, we apply a constant stress $\sigma_0$ to the growing network using a numerical AFM mechanism. At the beginning the AFM tip is positioned at `leq_piston` = 0.1 $\mu$m, which corresponds to the height of the cylinder. The stress applied opposes the motion of the network and influences its properties, as depicted in Figure 5.4. Here we will explain its functioning.

Fibers that reach the upper boundary exert a force depending on their penetration length, as seen in Figure 5.2. The cumulative contribution of all fibers determines the stress applied by the entire system $-\sigma_{top}$, which is the opposite of the stress applied by the AFM tip to the top of the network. If the stress $\sigma_{top}$ is below the target stress $\sigma_0$, the tip moves downward; however, if it exceeds $\sigma_0$, the tip moves upward to maintain the stress at the desired value.

Naturally, the tip does not move if its new length is lower than the original length of the piston: `leq_piston` = 0.1 $\mu$m. This avoids the collapse of the AFM at early moments of growth when there are not enough pushing fibers to challenge $\sigma_0$. In addition, the AFM displacement cannot exceed a certain threshold per time step: `max_displacement`, to avoid a too rapid growth. Details on the parameters of the simulations like the time step or the `max_displacement` value are provided in Appendix A.1.1, an extract of the numerical AFM algorithm is presented in Appendix A.1.2. Thus, the displacement of the piston d$x$ is:

$$\mathrm{d}x = \frac{\Delta\sigma S}{K_{confine}\alpha} \tag{5.6}$$

$\Delta\sigma = \sigma_{top} - \sigma_0$ is the difference of stress, $\alpha$ the attenuation parameter and $K_{confine}$ the stiffness of confinement. As the determination of $K_{confine}$ and $\alpha$ are of crucial interest for our study we present some methods verification here. For our simulations we fixed the value of the attenuation $\alpha$ arbitrary at 1 and focused on $K_{steric}$. In fact, later simulations showed us that it only has a small impact on the average displacement, see Appendix A.1.2, Figure A.2.

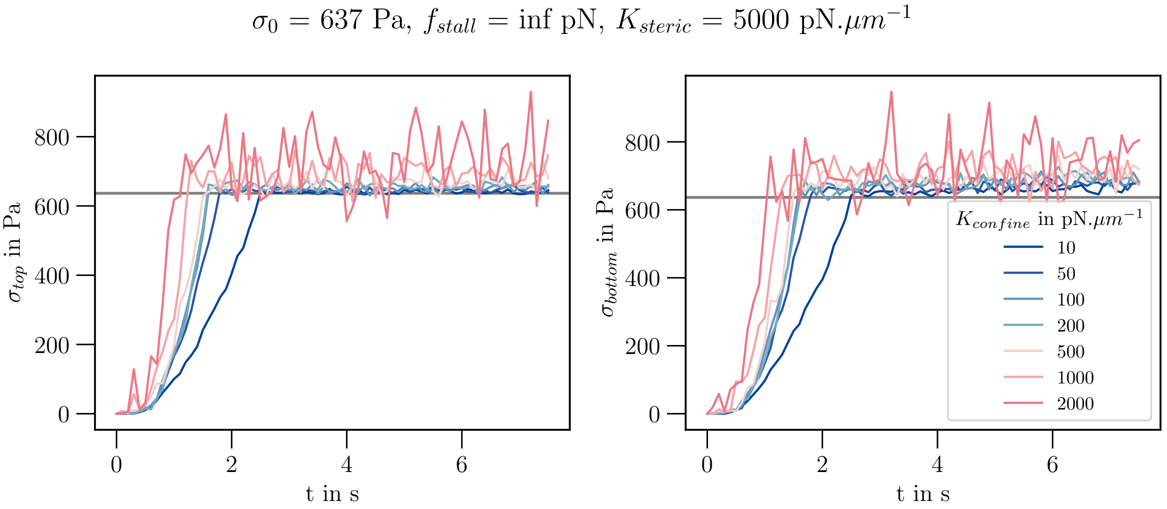

Figure 5.5: Stress measured by penetration length computation for top $\sigma_{top}$ (Left) and bottom $\sigma_{bottom}$ (Right) as a function of time $t$ for various $K_{confine}$, with: $\sigma_0$ = 637 Pa, $f_s$ = inf pN and $K_{confine}$ = 5000 pN.$\mu$m$^{-1}$. The horizontal grey line is the target stress $\sigma_0$.

In Figure 5.5, we count the number of penetrating fibers to compute the applied stress at the top (Left) and at the bottom (Right) for various potential stiffness $K_{confine}$. we compare it with the target stress $\sigma_0$. Remarkably the stress applied at the bottom corresponds to the one applied at the top, which accounts for a homogeneous transmission of the stress, which is particularly important as fibers are growing from the bottom. When $K_{confine}$ is too low the network takes more time to reach its steady-state as more fibers are required to apply a stress approaching the target one. Consequently, this may lead to an overshoot in density before reaching the expected steady state causing a delay in the response. However when $K_{confine}$ is too high, the system reaches the steady-state quicker but looses in precision and fluctuates more. Overall, between these two extremes the system behaves in a similar manner. This can also be observed in Appendix A.1.2, Figure A.1 (Center), with networks growing at the same velocity when $K_{confine}$ is within [50 - 1000] pN.$\mu$m$^{-1}$. We fixed $K_{confine}$ = 1000 pN.$\mu$m$^{-1}$, although we recognize that it could have been better to use something close to 200 pN.$\mu$m$^{-1}$ to reduce stress fluctuations.

The steric potential stiffness $K_{steric}$ accounts for the ability to overlap fibers and to store some elastic energy in their contact. Ideally, $K_{steric}$ should be really high to get as close as possible to a high core repulsion. However this goes with increasing the simulation time as it is more complex to find a satisfying configuration in our dense regimes. Also, increasing $K_{steric}$ goes with an increase of the velocity as depicted in Figure 5.6 for infinite stall force fibers. As a trade-off, we fixed $K_{steric}$ = 5000 pN.$\mu$m$^{-1}$. The same behavior has been observed for finite stall force fibers.

### 5.2.2 Length of actin

We consider filaments with a defined maximum length $\ell$ of 0.3 $\mu$m, mimicking the effect of capping proteins. Filaments grow according to the numerical implementation of the Brownian ratchet model, as described in Equation 5.3. Once a filament reaches its maximal length, it maintains this length. Since capping proteins exhibit dynamics consistent with a Brownian ratchet mechanism, the average length of the filament remains independent of the applied stress. This choice simplifies the system and ensures physiological

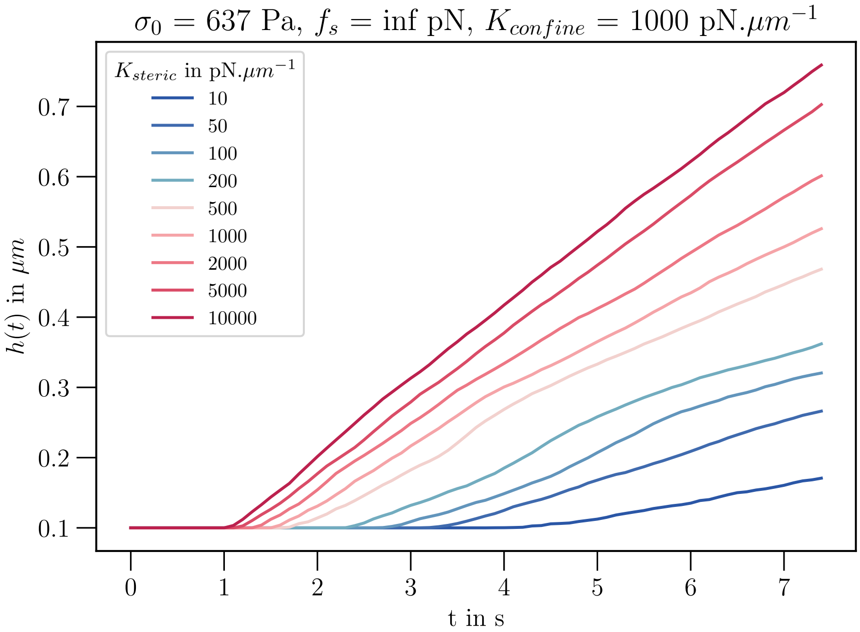

Figure 5.6: Height $h(t)$ as a function of time $t$ for various steric stiffness $K_{steric}$, with: $\sigma_0 = 637$ Pa, $f_s$ = inf pN and $K_{confine}$ = 1000 pN.$\mu$m$^{-1}$

relevance, as both capping proteins and actin monomers respond to stress in a similar manner. Throughout the simulations, $v_0$ was set at 1 $\mu$m.s$^{-1}$, and $v_{dep}$ at 0.1 $\mu$m.s$^{-1}$. The *growing force* value, $f_0$, was adjusted to explore the impact of the stall force $f_s$. To streamline the simulation process, we set the Arp2/3 nucleation rate (500 Arp2/3 s$^{-1}$) and the system size ($d = 1$ $\mu$m) to values that reduce the time spent in the transitional regime, where the network's applied stress falls below the AFM target. Notably, no accumulation of Arp2/3 was observed in the steady-state condition, see Appendix A.1.3. The influence of the quantity of actin on the velocity has been explored and discussed further in section 6.3.2. We present in Figure 5.7, snapshots extracted from a simulation.

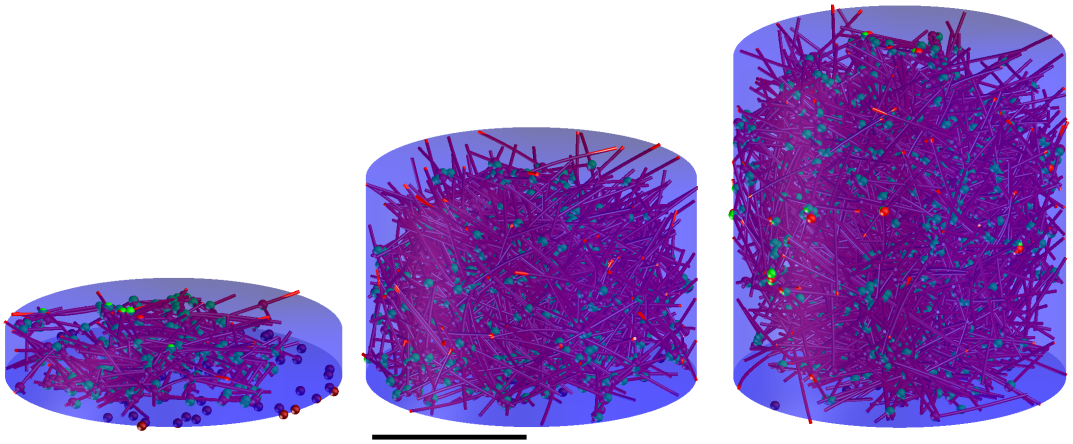

Figure 5.7: Simulation of a growing branched actin network with infinite stall force under $\sigma_0 \approx$ 60 Pa, at different times. (Left) $\tau = 0.7$ s, (Center) $\tau = 2.5$ s, (Right) $\tau = 4.5$ s. Scale bar = 0.5 $\mu$m. Actin filaments are in red, diffusing Arp2/3 are in red, activated ones in green.

Finally, our numerical simulation setup enables the investigation of stress adaptation in branched networks under various conditions, with a particular emphasis on velocity and density changes. As previously mentioned, our analysis revolves around the opposing stress $\sigma_0$ and the dependency on the stall force $f_s$. To isolate the stress contribution, we initially focused on filaments with infinite stall force, ensuring that they always reach their final length (0.3 $\mu$m) with a constant velocity of 0.9 $\mu$m.s$^{-1}$.

# Chapter 6

# Results

## 6.1 Infinite stall force

We conducted a total of 300 simulations of our system, varying the value of the applied stress $\sigma_0$, while considering filaments with infinite stall force. After a stress-dependent transition period, a growing steady-state was observed, characterized by nearly constant velocity. Notably, the network's growth rate slows down as the applied stress increases, as depicted in Figure 6.1 (Left). Simultaneously, within the same time as the velocity, the network's density reaches a stationary value. The network becomes denser as the applied stress is increased, as shown in Figure 6.1 (Right). However, it is worth noting that for low applied stress, the density continues to increase, which seemingly contradicts the expectation of a constant velocity, given that the actin flux must be conserved. Indeed, since we consider filaments with infinite stall force, they quickly reach their finite length (in $\tau = 0.3\underline{3}$ s), which maintains a constant actin flux (see Figure A.6 for the mean length of actin and for the volume in Appendix A.2.2). This particular discrepancy will be addressed and discussed in section 6.3.

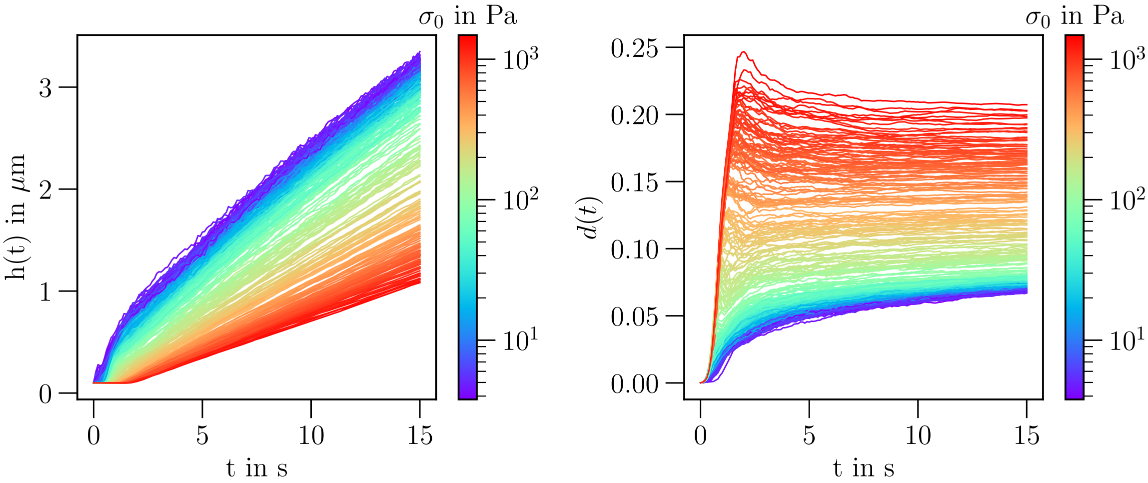

Figure 6.1: Height $h(t)$ (Left) and density $d(t)$ (Right) of the network as a function of time $t$ for various stress $\sigma_0$ with $f_s = \inf$ pN.

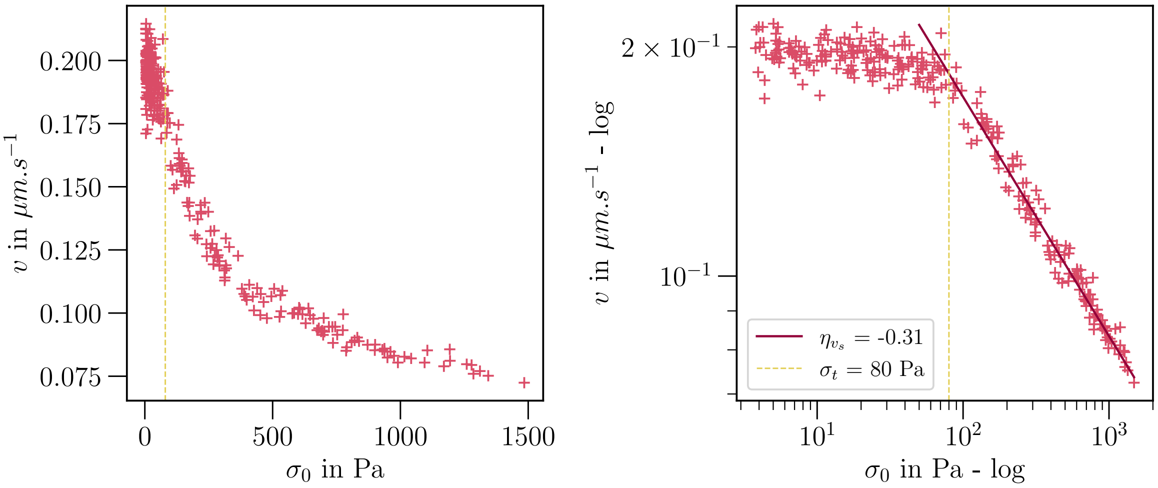

Figure 6.2: Near-stationary velocity for various stress in normal (Left) and log-log scales (Right), with $f_s = \inf$ pN. We see a power-law behavior for high stress after a constant value phase that ends around 80 Pa (yellow dotted line). The fit for the power-law scaling is represented in the log-log plot.

Analyzing the nearly stationary velocity as a function of stress reveals a decreasing convex shape that does not reach stall due to the continuous recruitment of Arp2/3 complexes that generate new filaments (we detail the stationary velocity and density estimations and discuss the stability of measurement in Appendix A.2.1). The log-log representation of this relationship highlights a transition between two distinct phases, as shown in Figure 6.2. For stress values lower than $\sim$ 80 Pa, the velocity appears to remain relatively constant, albeit with fluctuations. In the high-stress regime, the velocity exhibits a power-law decay, scaling as $v \propto \sigma^{\eta_{v_s}}$ with $\eta_{v_s}$ = - 0.31. Similarly, the near-stationary density follows a two-phase behavior, as observed in Figure 6.3. Beyond the transition, the density scales with the stress as $\rho \propto \sigma^{\eta_{d_s}}$ with $\eta_{d_s} = 0.34$, ensuring that the flux ($j = \rho v$) remains constant regardless of the applied stress.

We now compare the scalings we obtained to those of the entanglement theory, from which we have the equilibrium density in Equation 4.11. From this, we can derive the expression of the growth velocity $v$, with $j$ the flux of actin:

$$\rho_0 = \kappa^{-2/7}\sigma_0^{2/7}r^{8/7} \quad ; \quad v = j\kappa^{2/7}\sigma_0^{-2/7}r^{-8/7} \tag{6.1}$$

The alignment of their theoretical predictions with our simulation outcomes is satisfying ($2/7 \approx 0.29$). Consequently, we can deduce from these results that in scenarios where $\xi \leq \ell$, the system's mechanics adhere to the entanglement theory. However, when the distance between contact points $\xi$ approaches $\ell$, velocity and density are no longer governed by the network's mechanics. To illustrate, at $\sigma_0 = 50$ Pa, we observe $\xi \sim 0.28$ $\mu$m, which is comparable to $\ell = 0.3$ $\mu$m. This signifies a departure from the entanglement regime as predicted by the theory. Exploring how velocity manifests at low stress becomes essential, as one would anticipate it to be solely determined by the polymerization rate. Nevertheless, a substantial disparity between our observed value $v(\sigma_0 \to 0) \sim 0.2$ $\mu$ m.s$^{-1}$ and the fiber's intrinsic velocity $v_0 = 0.9$ $\mu$m.s$^{-1}$ emerges. Section 6.3 provides insights on this subjects.

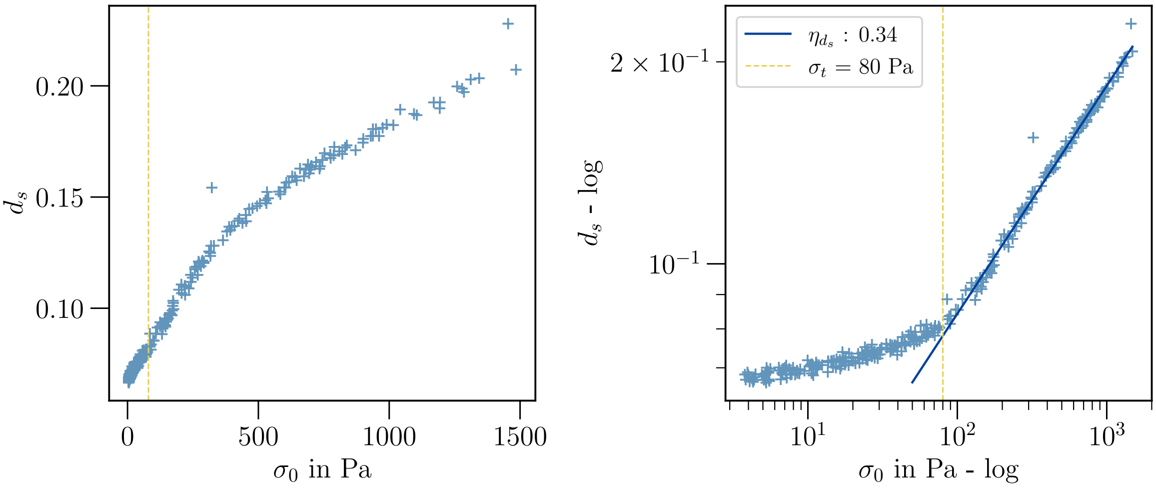

Figure 6.3: Near-stationary density for various stress in normal (Left) and log-log scales (Right), with $f_s$ = inf pN. We see a power-law behavior for high stress after a constant value phase that ends around 80 Pa (yellow dotted line). The fit for the power-law scaling is represented in the log-log plot.

Furthermore, although our outcomes exhibit the same general trend as Bieling et al. and Li et al. (increase of velocity and decrease of density with stress), the rate of decay for the velocity is considerably slower in our case. Specifically, their decay is characterized by a two-exponential decline (a rapid and a minor one), in contrast to our observations, see Figure 3.11. Currently, we lack an explanation for such discrepancies.

Now, turning our attention to the impact of stall force, we sought to investigate if the same two-phase behavior persists when working with more realistic fibers with finite stall force. We computed the stall force corresponding to a physiologically relevant growing force $f_0$, as described in Equation 5.5. Given $k_B T = 0.042$ pN.$\mu$m and $a = 0.0025$ $\mu$m (half the size of a G-Actin monomer), we determined $f_s \approx 3.87$ pN. In this context, analogous simulations yielded outcomes largely akin to those observed previously, featuring a constant phase followed by power-law decay, see Appendix A.3.1. It is worth noting that the constant phase appeared to persist over a wider stress range, and the decay seemed steeper. However, the transition between the two regimes is less sharp.

## 6.2 Stall force transition

To further explore the complex interplay between stall force and growth dynamics, and to investigate the observed change in slope, we conducted an extensive series of simulations covering a broad range of stall force and stress values. This study involved 300 simulations distributed randomly across stall force values ranging from $10^{-4}$ to $10^4$ pN. We selected stress values from a predefined list spanning between 64 and 1910 Pa. When stress levels are low, the growth velocity exhibits little dependency on stall force, which is consistent with the expectation that growth should not rely significantly on stall force in the absence of stress. However, as stress levels increase, stall force becomes a limiting factor. At low stall force, for stresses roughly above 500 Pa, network growth ceases. Interestingly, once a certain threshold stall force is surpassed, velocity appears to become independent of stall force, as depicted in Figure 6.4. However, the data presented in this figure does not provide enough information to draw conclusions about the stress dependency of the transition.

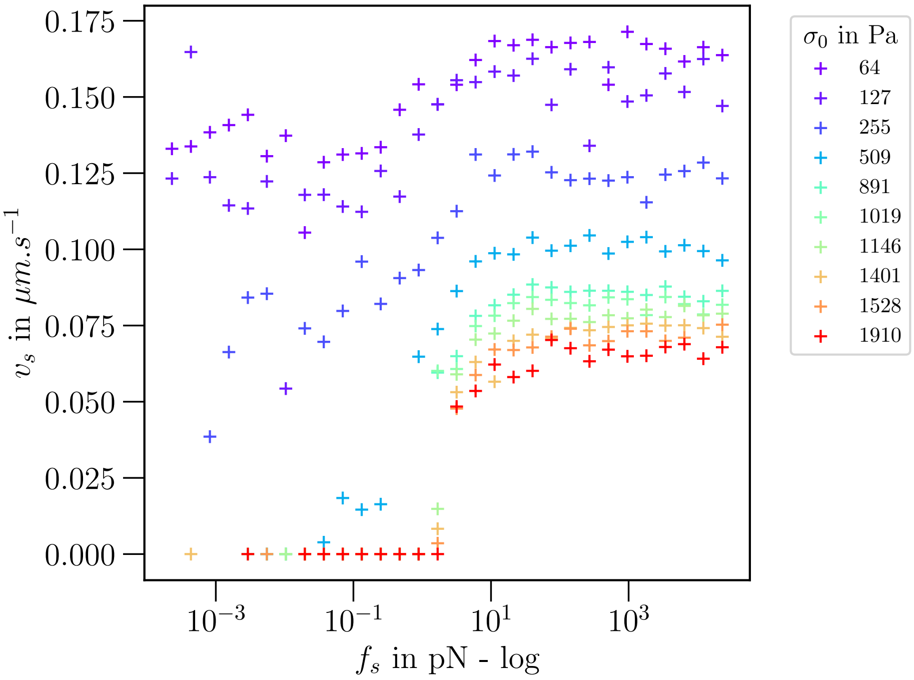

Figure 6.4: Appearance of a stall force transition threshold for different stress values: Stationary velocity $v_s$ as a function of stall force $f_s$, for various stress values $\sigma_0$, x-axis in log.

We explored the dependence of the stall force transition on the applied stress by conducting simulations over a smaller range of stall forces, with an increased number of simulations (1000) and for high stress [500 - 1900] Pa. Our results indicate that the stall force transition value is indeed dependent on the applied stress, as demonstrated in Figure 6.5. The stall force required for growth varies with stress, as all points collapse on a single threshold. In addition, we see that once growth becomes feasible, network behavior appears consistent regardless of the stall force and obeys the entanglement theory as shown by the $\sigma_0^{-2/7}$ scaling.

As $f_s/\sigma$ has unit of surface, the observed transition can be characterized by a fixed surface value $s_{tr} \approx 2.02 \times 10^{-3}$ $\mu$m$^3$. However, it has been challenging to link this value to any simple characteristic surface of the system, whether it is the total surface area of the system $S = 7.8 \times 10^{-1}$ $\mu$m$^2$, or the short cross-sectional area of an actin filament: $s_0 = 7.8 \times 10^{-5}$ $\mu$m$^2$. To date, we have not been able to find a satisfying candidate. However, the closest surface value seems to be the cross-section of actin in its long axis: $s_{long} = 3 \times 10^{-3}$ $\mu$m$^3$ for a perfectly polymerized filament. It is possible to reduce this value by considering the distance between contact points $\xi$ instead of the total length of actin, which would give an associated cross-sectional area of $\approx 1.5 \times 10^{-3}$ $\mu$m$^3$ at 500 Pa. It is indeed intriguing to observe that the detachment of velocity from ground is associated with entanglement, which appears to play a critical role in powering the system.

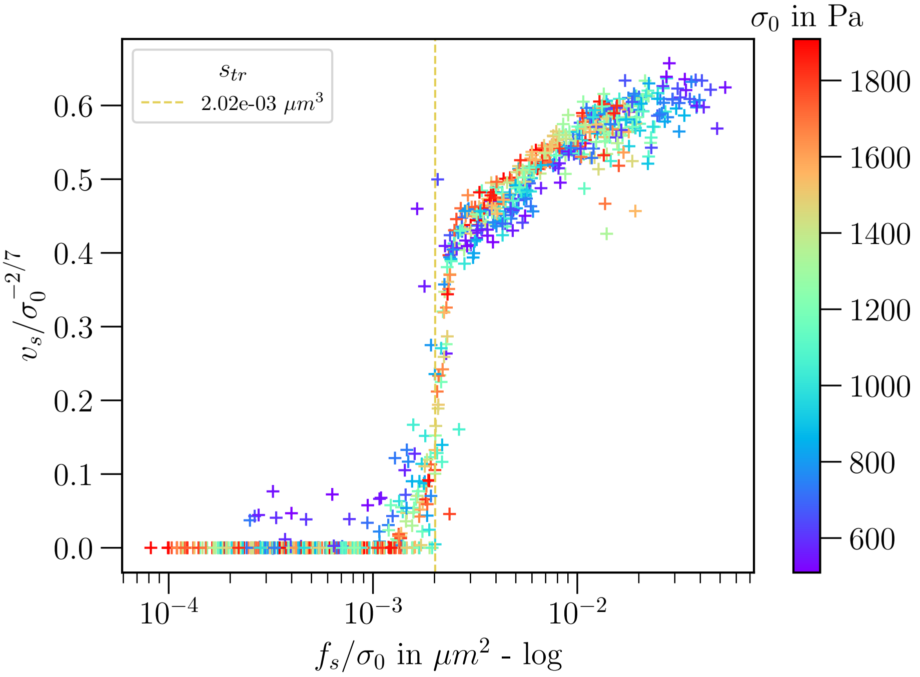

Figure 6.5: Re-scaled velocity with respect to entanglement theory versus stall force over stress for different stress values. The yellow dotted-line represents the transition surface $s_{tr}$.

In addition, one could be tempted to weight the surface transition value with the density of the system although it is a stress-dependent quantity. However it has been shown that random packing of cylinders would ultimately reach a maximum density function of their aspect ratio $\ell/(2r)$, which is different from 1 [111]. In our case it would be of the order of  0.2 which is coherent with Figure 6.1. While those observations provides valuable insights, further research may be needed to conclusively establish this relationship and understand the underlying mechanisms in more detail.

Exploring the determinants of velocity at small stresses when entanglement theory fails to offer a suitable explanation, represents a crucial avenue for further inquiry. Disregarding explanations predicated on Brownian ratchet behavior and simplistic scaling with fibers velocity underscores the necessity to consider alternative factors. Notably, the incorporation of network drag within Cytosim emerges as a compelling prospect. As evident from A.5, Figure A.16, there is a substantial augmentation in stress experienced at the bottom $\sigma_{bottom}$ over time, which is particularly remarkable for low initial stress values $\sigma_0$. Investigating this hypothesis holds the potential to furnish valuable insights into the system's response to low external forces.

## 6.3 Drag dominated regime

### 6.3.1 Estimation of the drag of the network

The total drag of the network, as implemented in our simulations, was computed in accordance with the approach detailed in [112]. This computation was specifically conducted for our simulations of infinite stall force, as illustrated in Figure 6.6 (Left). Since there are no complex hydrodynamic interactions in Cytosim, the network's drag is a cumulative result of individual fiber drags, primarily contingent on their respective lengths. Mathematically, this is expressed as follows:

$$\Gamma(t) = \sum_{i=1}^{N_{fibers}(t)} \frac{3\pi\eta\ell_i(t)}{\ln\left(\frac{\ell_i(t)}{2r}\right) + 0.312} \tag{6.2}$$

Here $\eta$ represents the dynamic viscosity of the medium, $\ell_i(t)$ denotes the length of fiber $i$ at time $t$, and $r$ signifies the radius of the fiber. Additionally, $N_{fibers}(t)$ represents the count of fibers at time $t$. When comparing the stress associated with drag, $\sigma_{drag}(t) = \Gamma(t)v(\sigma_0)$, with the externally applied stress $\sigma_0$, it becomes evident that under conditions of low opposing stress, the network's drag governs the motion, as shown in Figure 6.6 (Right).

Subsequently, our investigation shifted to examine the behavior in scenarios where no external force was applied. In Figure Appendix A.9, we presented velocity profiles for a network subject to no applied force but possessing finite stall force. Both the height and density profiles exhibited continuous trends with low stress levels. Consequently, we postulate that analyzing the behavior of this limiting case can yield insights applicable to the broader regime. Given the continual increase in the number of fibers over time, exerting a pronounced influence on motion, we hypothesize that the network's motion should slow down as a consequence.

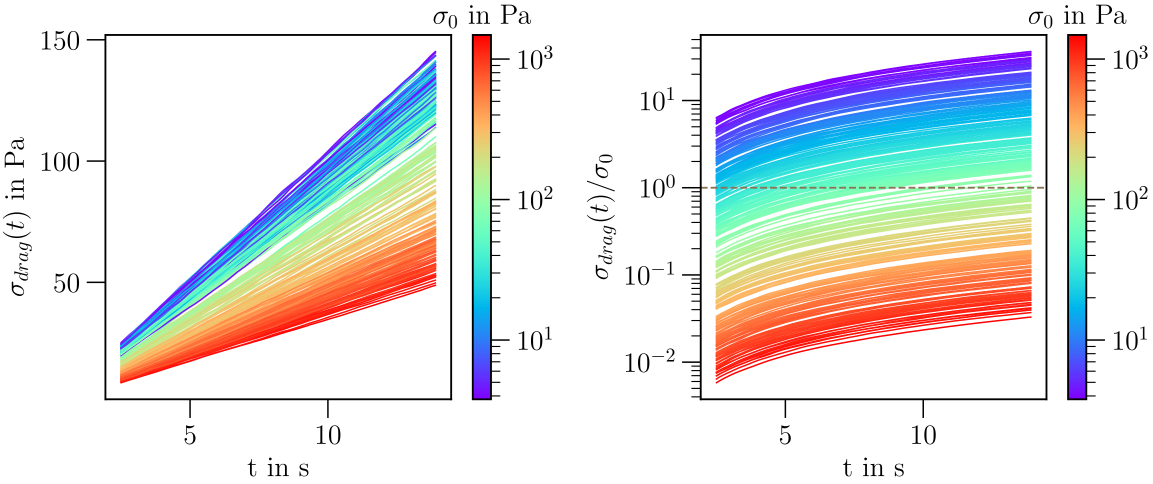

Figure 6.6: (Left) Drag stress $\sigma_{drag}(t)$ as function of time $t$ for various stress $\sigma_0$. (Right) Ratio of the drag stress over the imposed stress: $\sigma_{drag}(t)/\sigma_0$ as a function of time for various $\sigma_0$, with $f_s$ = inf pN. The brown dotted-line represents the equality threshold.

### 6.3.2 Free growth and adaptation

In the absence of applied stress, we assume that the Arp2/3 rate, denoted as $k_{Arp2/3}$, emerges as the pivotal parameter governing network growth as it determines the actin mass at any given moment. To assess its significance, we conducted 100 simulations with varying values of $k_{Arp2/3}$ in the absence of external force. The results are presented in Figure 6.7, where the left panel displays the network's height $h(t)$, and the right panel shows the network's density $d(t)$. As expected, higher values of $k_{Arp2/3}$ correspond to increased velocities and greater network density. Nevertheless, it is noteworthy that, over time, the network experiences a deceleration and a densification, which can be attributed to the increase in network drag.

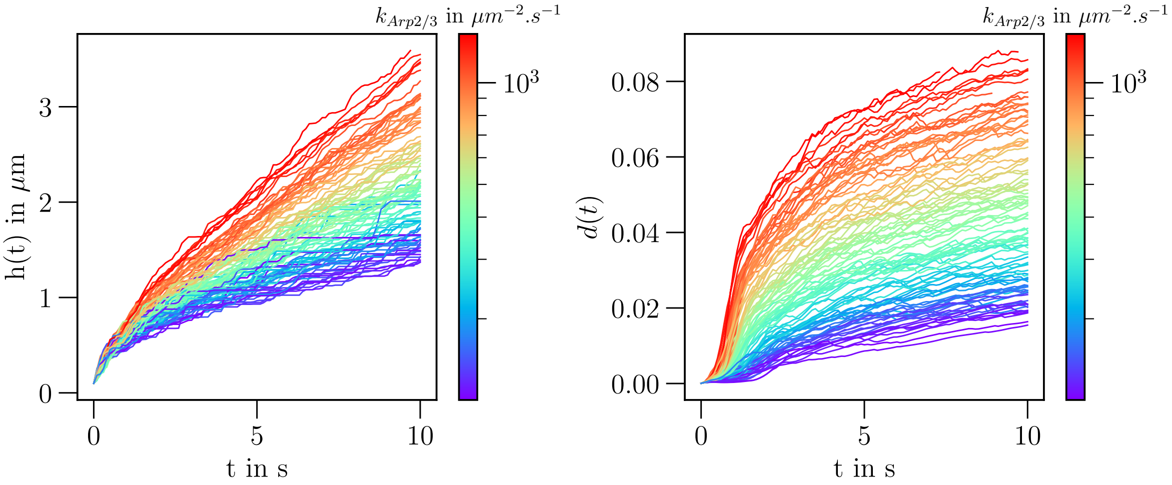

Figure 6.7: Height $h(t)$ (Left) and density $d(t)$ (Right) as a function of time $t$ for various $k_{Arp2/3}$ with $f_s = \text{inf}$ pN.

Indeed, as the network expands, newly formed slices encounter an increasing amount of actin, leading to a rise in the density of these fresh slices. Furthermore, over extended time intervals, slices are expected to undergo elastic relaxation, which can be inferred from a declining density as time progresses. This phenomenon of layering densification and subsequent relaxation is clearly depicted in Figure 6.8 (Right). In this figure, each data point represents the average density within a volume centered on a segment of the fiber. The color code denotes the time of appearance of each layer. On the left side of the figure, we depict the velocities of all fiber segments, still labeled with their respective appearance times. Intriguingly, it becomes evident that the velocity of a slice does not depend on its position within the network, indicating a homogeneous growth pattern.

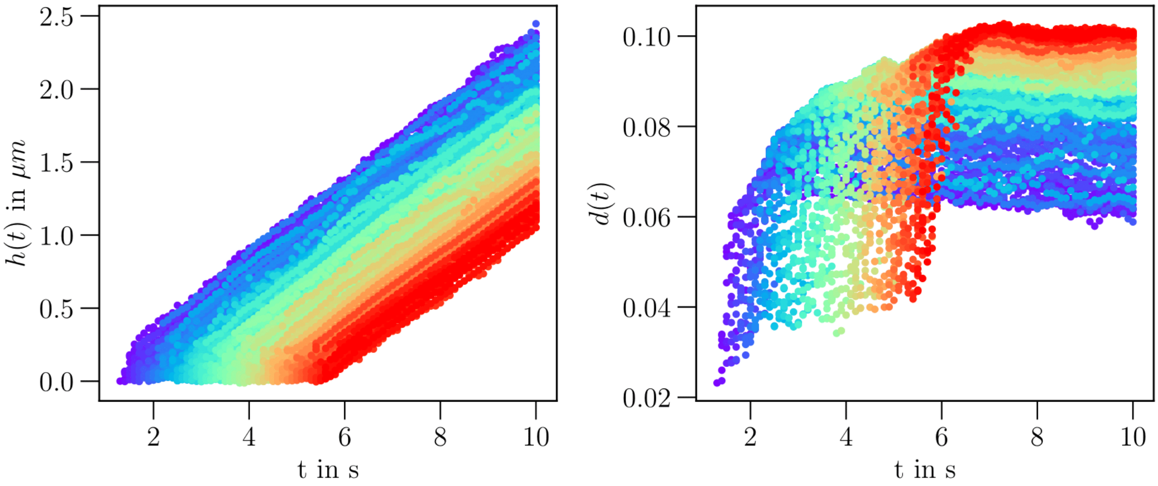

Figure 6.8: Evolution of slices with Height $h(t)$ (Left) and density $d(t)$ on (Right) as a function of time $t$. The color code represents the appearance time. For each point the density is calculated inside the slice centered on the point position and with a height $\delta z = 0.2$ $\mu$m. Here, $f_s = \text{inf}$ pN and $k_{Arp2/3} = 1378$ $\mu$m$^{-2}$.s$^{-1}$

It is essential to highlight that the presented data have been obtained from a system characterized by a high $k_{Arp2/3}$ rate. Nevertheless, we have encountered challenges in constructing a comprehensive model that accounts for both the evolution of slices and describes both the densification and relaxation phenomena. Therefore, we propose a simplified framework based on straightforward assumptions.

Overall, the instantaneous velocity $v_\tau(t)$ of the network can be expressed as:

$$v_\tau(t) = v(t) + h(t)\bar{\dot{\epsilon}}(t) \ , \ \bar{\dot{\epsilon}}(t) = \int_0^{h(t)} \frac{dx}{h(t)} \partial_t \epsilon(x,t) \tag{6.3}$$

Here, $v(t)$ stands for the velocity induced by both polymerization and the drag of the network, while $h(t)\bar{\dot{\epsilon}}(t)$ represents the elastic relaxation of the network.

As evident from Figure 6.8 (Right), while density relaxation does occur, it can be reasonably neglected at the time scales of our observations. In fact, the most notable density relaxation observed is approximately 10% over a time span of approximately 10 s. This observation has been corroborated for lower values of $k_{Arp2/3}$, which are closer to those employed in our previous simulations, as shown in the Appendix A.5 in Figure A.17. Thus, we assume that:

$$|h(t)\bar{\dot{\epsilon}}(t)| \ll v(t) \Rightarrow v_\tau(t) \simeq v(t) \tag{6.4}$$

In this approach, we conceptualize our system as comprising polymerizing fibers exerting force against a drag that progressively increases with time, denoted as $\sigma_0(t)$. Given that growing fibers ultimately reach their maximum length, the relationship between the drag $\sigma_0(t)$ and the velocity $v(t)$ becomes straightforward. Moreover, under the assumption that we are still operating within the entanglement regime, we can make use of Equation 6.1.

As a result, we employ the following equations:

$$\begin{aligned} \sigma_0(t) &= \frac{\gamma_0 \; N_{actin}(t)}{S} \; v(t) \\ v(t) &= j \; \kappa^{2/7} \; r^{-8/7} \; \sigma_0(t)^{-2/7} \end{aligned} \tag{6.5}$$

With $j = ks_0\ell_0$, and $N_{Actin}(t) = kSt$. $S$ is the surface of the enclosure and $s_0$ the cross section of a filament, $\gamma_0$ is the drag of a fiber of length $\ell_0$:

$$\gamma_0 = \frac{3\pi\eta\ell_0(t)}{\ln\left(\frac{\ell_0(t)}{2r}\right) + 0.312} \tag{6.6}$$

Then, mixing both equations in 6.5, we derive expressions for growth velocity and density:

$$\begin{aligned} v(t) &= t^{-2/9}\gamma_0^{-2/9}\kappa^{2/9}r^{8/9}k^{5/9}(s_0\ell_0)^{7/9} \\ \rho(t) &= t^{2/9}\gamma_0^{2/9}\kappa^{-2/9}r^{-8/9}k^{4/9}(s_0\ell_0)^{2/9} \end{aligned} \tag{6.7}$$

Thus, from previous equations we can derive a simple scaling of $v(t)$ and $\rho(t)$ with $k$ as the main parameter.

$$\begin{aligned} v(t) &\propto v_0(k)t^{-2/9} \\ \rho(t) &\propto \rho_0(k)t^{2/9} \end{aligned} \tag{6.8}$$

This implies:

$$h(t) \propto \frac{9}{7}v_0 t^{7/9} \tag{6.9}$$

In Figure 6.9, we present power-law fits for the position $h(t)$ (Left) and the density $\rho(t)$. We have chosen to retain only fits that achieve a coefficient of determination $R^2$ of at least 0.9. Notably, we excluded systems with lower values of $k_{Arp2/3}$, specifically those below 200 $s^{-1}$ in our study. The observed deviations from the theoretical predictions can be attributed to a combination of factors, including discrepancies with entanglement theory and the presence of significant elastic relaxation effects that cannot be disregarded. Systems with lower $k_{Arp2/3}$ values may require more time to establish a cohesive network capable of exerting a sufficiently high drag to enhance entanglement. Additionally, as illustrated in Figure 6.10, lower $k_{Arp2/3}$ values result in less regular networks that collectively exhibit a higher degree of density relaxation over time.

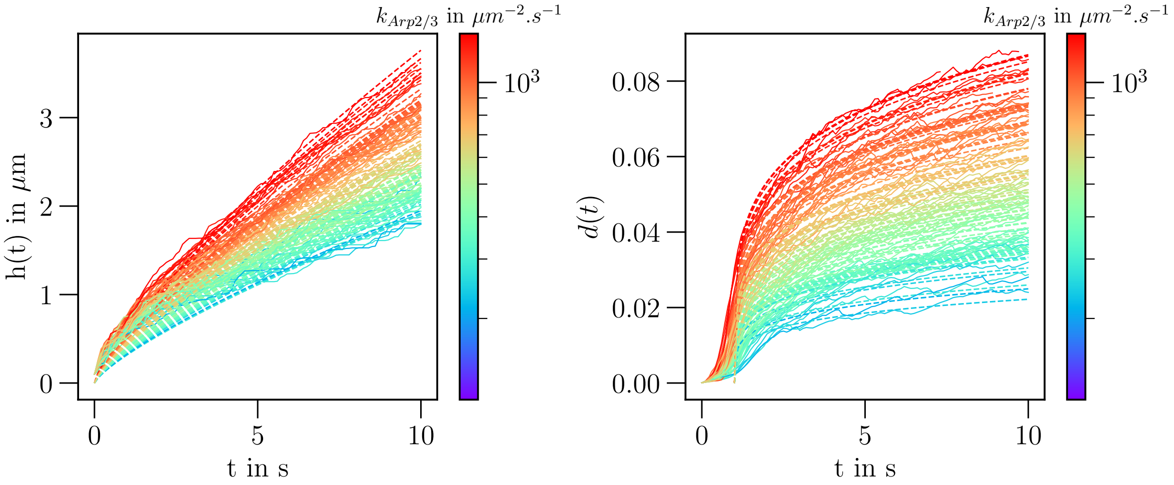

Figure 6.9: Power law fit of the height $h(t)$ (Left) and density $d(t)$ (Right) as a function of time $t$ for various $k_{Arp2/3}$ with $f_s = \text{inf}$ pN. For density we have started the fit at 1 s, after the first transitional growth phase

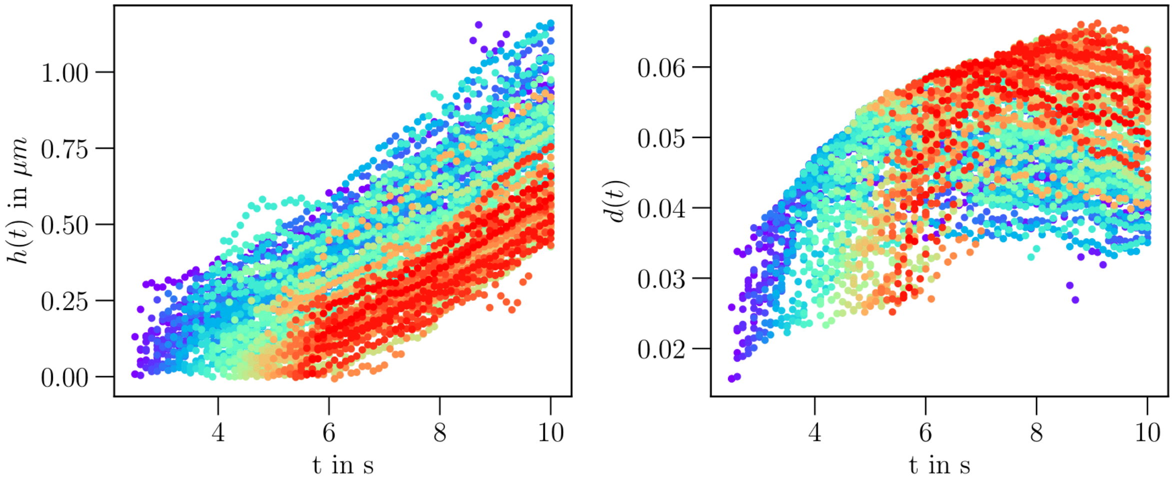

Figure 6.10: Evolution of slices with height $h(t)$ (Left) and density $d(t)$ on (Right) as a function of time $t$. The color code represents the appearance time. For each point the density is calculated inside the slice centered on the point position and with a height $\delta z = 0.2$ $\mu$m. Here, $f_s = \text{inf}$ pN and $k_{Arp2/3} = 390$ $\mu$m$^{-2}$.s$^{-1}$

Based on our previous power-law fits, we have directed our attention toward examining the rate dependencies of the pre-factors, namely $v_0$ and $d_0$. In Figure 6.11, we illustrate their dependence on $k_{Arp2/3}$ with a power-law fit. Notably, both exponents deviate from the anticipated values according to our theory, although they are not significantly divergent. To elucidate the origins of these discrepancies, further investigations and a more precise analysis are warranted.

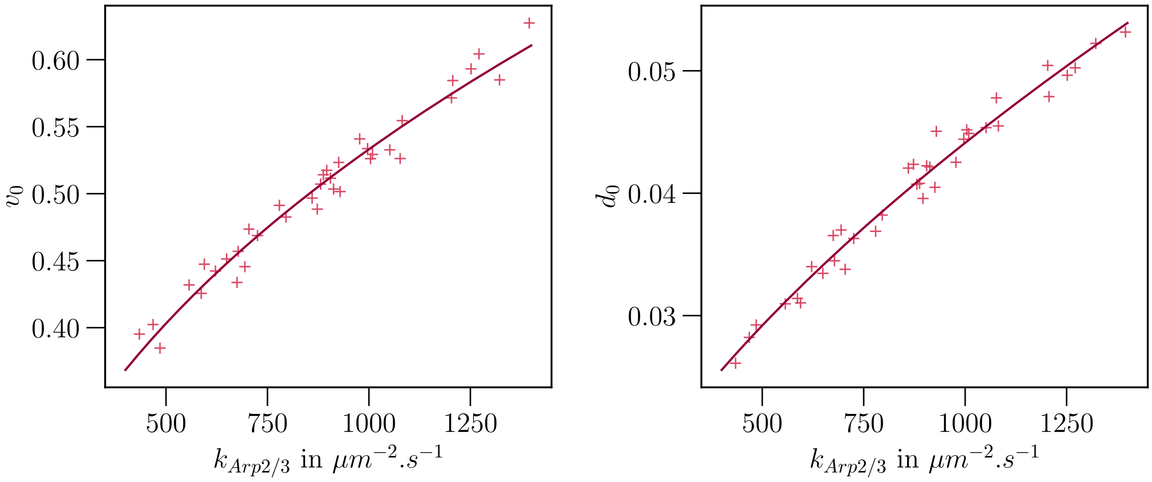

Figure 6.11: Pre-factors of the power law $v_0$ (Left) and $d_0$ (Right) as a function of $k_{Arp2/3}$. The fit is made with a power law function in $k_{Arp2/3}$ with respectively exponents 5/9 and 4/9 as expected from theory.

Finally, the flux derived from the pre-factors $v_0$ and $d_0$ aligns precisely with the expectations based on the simulation setup, as exemplified in Figure 6.12.

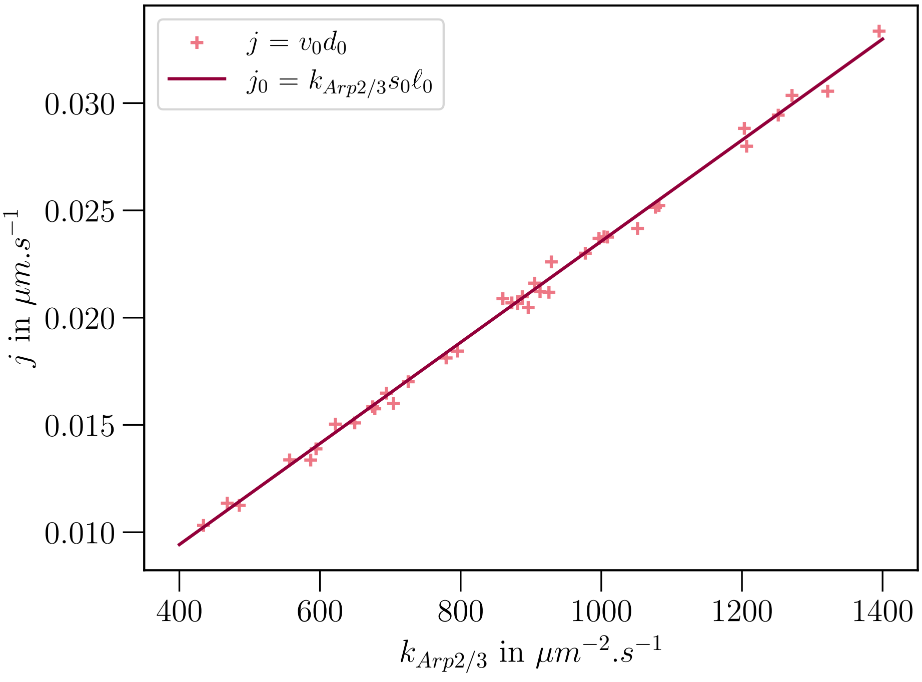

Figure 6.12: Flux of actin $j$ in $\mu$m.s$^{-1}$ as a function of $k_{Arp2/3}$. Comparison between the points from the power law fit of $v_0$ and $j_0$ and what is expected from the model.

# Conclusion

Within the scope of our study, we have undertaken a comprehensive exploration of critical mechanical aspects pertaining to force generation in branched actin networks, with a particular focus on the pivotal roles played by stress and stall force. Our findings have encompassed several key aspects: Firstly, we have validated the predictions of entanglement theory concerning the definition of network characteristics via its responses to external stress, as expected from experiments. Furthermore, we have introduced the stress induced by the drag of the network as a limiting factor of its expansion and have expanded the scope of the theoretical framework. Secondly, our investigation has unveiled the existence of a threshold transition associated with stall force, a critical point at which motion becomes feasible irrespective of the specific stall force magnitude. Remarkably, within our dense systems, we have observed a notable accumulation of fibers at the leading edge, while fiber density tends to diminish under low-stress conditions. This phenomenon, resembling a condensation transition, bears resemblance to observations made by Tsekouras et al. [95] in the context of parallel growth. It would be of interest to provide a more detailed quantification of this transition by determining among other quantities the precise stress values at which it occurs. However, it is worth noting that extracting any discernible orientation order from our results may prove challenging, given the seemingly random filament orientations.

# Discussion

Finally, we end this first part by assessing the constraints inherent to our numerical setup and the associated interpretations.

## Force generation model

To enhance the fidelity of our setup, as previously elucidated, one potential avenue is to increase the size of the system in an effort to approximate the experimental conditions outlined by Bieling et al. Furthermore, we posit that increasing the steric repulsion coefficient $K_{steric}$ and reducing the confinement coefficient $K_{confine}$ may yield a simulation environment that better mirrors actual filament interactions while reducing fluctuations of the AFM.

Furthermore, a way to improve the biological relevance of the setup involves the inclusion of capping proteins, instead of emulating their actions by imposing a maximum reachable filament length. Subsequent advancements could entail the incorporation of additional ABP, such as crosslinkers, to more faithfully replicate the complexity of biological systems.

## Entanglement theory

We delineate several limitations of the entanglement theory in the context of our study. Firstly, this theoretical framework does not account for the polymerization process, wherein the number of filaments in the system increases over time. This increase in filament number has multifaceted effects, including an associated rise in drag. Besides, the theory does not explicitly address filament branching when the distance between contact points ($\xi$) is smaller than the length of individual fibers. Notably, the spacing between branching points may emerge as a pivotal parameter, akin to another characteristic length scale $\xi_{Arp2/3}$. Intuitively, this distance should diminish with increasing filament density since more fibers are available for binding. Consequently, $\xi_{Arp2/3}$ should exhibit a scaling behavior analogous to that of $\xi$.

Secondly, we encountered challenges in fitting the theoretical predictions of entanglement theory, specifically with respect to parameters such as filament radius ($r$) and bending rigidity ($\kappa$). The inability to establish a scaling relationship may be attributed, in part, to the value of the steric hindrance coefficient ($K_{steric}$), which, if increased, might enable the system to more accurately perceive the actual filament radius ($r$). Additionally, as energy is stored in both bending elasticity and Arp2/3 link elasticity, elevating the stiffness of the Arp2/3 interactions could potentially emphasize the bending response and contribute to resolving the discrepancies observed between our results and the theoretical predictions.

## Stall force transition model

In our analysis of stall force transitions, we have encountered a challenge in formulating an explicit expression for the surface transition value $s_{tr}$, which does not readily correlate with any straightforward geometric or surface-related parameter in the system. We suggest that this transition value might be contingent on the bending rigidity ($\kappa$). For instance, we speculate that fibers with infinite rigidity should exhibit a surface transition value ($s_{tr}$) that approximates the initial surface coverage ($s_0$). This conjecture hints at a potential relationship between bending rigidity and the observed transition behavior, which warrants further investigation and analysis.

## Drag dominated regime and free growth

In general, our analysis of free actin network growth indicates that branched actin networks consistently adhere to the principles outlined in entanglement theory, whether stress is imposed externally (e.g., by AFM) or arises due to the escalating drag generated within the network. One limitation of this approach is the necessity to generate a sufficiently large network to exert substantial stress on pre-existing fibers.

From a biological perspective, one limitation arises from our simplified treatment of drag, which should ideally consider the influence of hydrodynamic interactions. Recent developments have introduced a novel method that models ensembles of fibers as porous mediums [113] and were successfully applied in the study of mitotic spindle positioning [114]. We believe that a more accurate treatment of drag, accounting for hydrodynamic interactions, would enhance the biological relevance of our study, although it is expected to preserve the fundamental stress adaptation mechanisms we have observed.

# Part II

# An example of parameter space compression on branched actin

# Introduction

> *With four parameters I can fit an elephant, and with five I can make him wiggle his trunk.*
>
> **von Neumann to Fermi**

In science, success often hinges on the ability to formulate efficient theories that can predict phenomena within specific time and length scales. Consequently, it is not always necessary to delve into the underlying layers to achieve an effective description of a system. For instance, the mean-field approach in fluid mechanics does not demand a precise understanding of quantum mechanics at the molecular level. Similarly, thermodynamics can abstract away from the stochastic origins of diffusion and heat transfer. Thus, in physics, many lower-level theories can be systematically coarse-grained or *renormalized* into macroscopic effective models. This idea underscores the effective hierarchical nature of models [6].

Building models is a challenging endeavor, and there may be a temptation to incorporate as many parameters as possible in an attempt to enhance their performance. However, the inclusion of unnecessary parameters can obscure the significance of the pivotal ones, ultimately resulting in a less interpretable model. In summary, complex models can resemble black boxes, a situation typically avoided in physics for the sake of clarity. Therefore, a significant scientific challenge lies in discerning the pertinent directions within parameter space to make sense of complex models. Fortunately, in various scientific domains, the exploration of parameter space has underscored the hierarchy hypothesis, as demonstrated in [115]. As depicted in Figure 2.1, critical predictions often rely on a small number of parameter combinations, followed by a series of geometrically less significant ones. This recurring attribute, referred to as *sloppiness*, aligns with findings previously emphasized by the renormalization group (RG) [116].

Furthermore, various techniques have been proposed since the 1980s to address the parameter space problem, offering diverse solutions to the challenge. In the 1980s, classical principal-component analysis emerged as a technique to reduce ordinary differential equations (ODE)-based models of biochemical systems [117]. More recently, the manifold boundary approximation method has been developed to fit data while minimizing dimensionality [118], and fitness-based asymptotic parameter reduction can identify the *core working module* of a model [119]. Additionally, other machine-learning approaches can construct realistic models with a minimal number of parameters, such as through the use of Bayesian information criterion [120]. However, it is worth noting that these methods primarily target ODE-based models, highlighting the need for universal techniques applicable to stochastic computational systems.

More recently, Parameter Space Compression (PSC) [121] has proposed new reasons to explain why fundamental models operate successfully with a minimum set of parameters. We rely on this foundational idea for our work. Here, in this second part, we first introduce the properties of Fisher information, a statistical quantity upon which PSC is defined. We then detail the main results associated with PSC before presenting our own approach and results applied to branched actin systems.

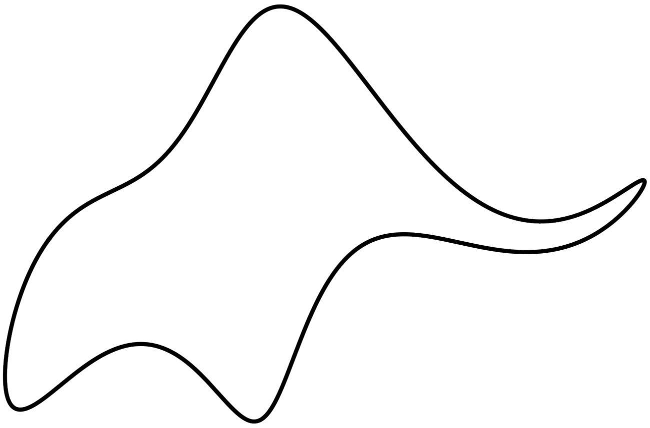

Figure 1: A Fermi-Neumann elephant based on Fourier analysis, Equations 1, from [122].

$$\begin{cases} x(t) = -60\cos(t) + 30\sin(t) - 8\sin(2t) + 10\sin(3t) \\ y(t) = 50\sin(t) + 18\sin(2t) - 12\cos(3t) + 14\cos(5t) \end{cases} \tag{1}$$

# Chapter 1

# The Fisher information

## 1.1 Introduction

In this section, we introduce the Fisher information and its associated properties for continuous variables, which serve as the basis for our analysis of parameter space compression. It is worth noting that much of the foundational concepts in this area trace back to the pioneering work of Fisher, as documented in his seminal publication [123].

### 1.1.1 Intuitive approach

Here we qualitatively introduce the concept of Fisher information, denoted as $\mathcal{I}(\theta)$, which serves as a measure of the amount of information contained in an observable variable $X$ regarding an unknown parameter $\theta$. This parameter $\theta$ is intrinsic to the probability density function $f_\theta(X)$ upon which the observed data $X$ depends. The overall objective is to determine the *true* value of $\theta$ based on the available data. We commonly call $f_\theta(X)$ the likelihood function. In essence, if the probability density function $f_\theta$ exhibits a sharp and well-defined peak in response to changes in $\theta$, it indicates that the data is conducive to accurately determining the *true* value of $\theta$ from the observations. Conversely, if the probability density function $f_\theta$ is flat and spread out, estimating the actual *true* value of $\theta$ necessitates a larger sample size, akin to using the entire population for sampling.

As an example, consider a normal distribution where the mean value is contingent on a parameter $\theta$. Figure 1.1 illustrates two scenarios: on the left panel, the distribution is moderately sensitive to changes in the parameter, while on the right panel, the same parameter change results in a more significant alteration of the distributions. Consequently, in the second case, we can envision that $f_\theta$ is sharply peaked concerning changes in $\theta$, while $f_\theta$ in the first case is less sensitive. Later in our discussion, we will refer to parameters as either *stiff* (right panel) or *sloppy* (left panel) based on these characteristics.

More generally, the Fisher Information has shown great interest in other scientific fields such as natural gradient descent in neural networks. In the following, we will define properly this quantity.

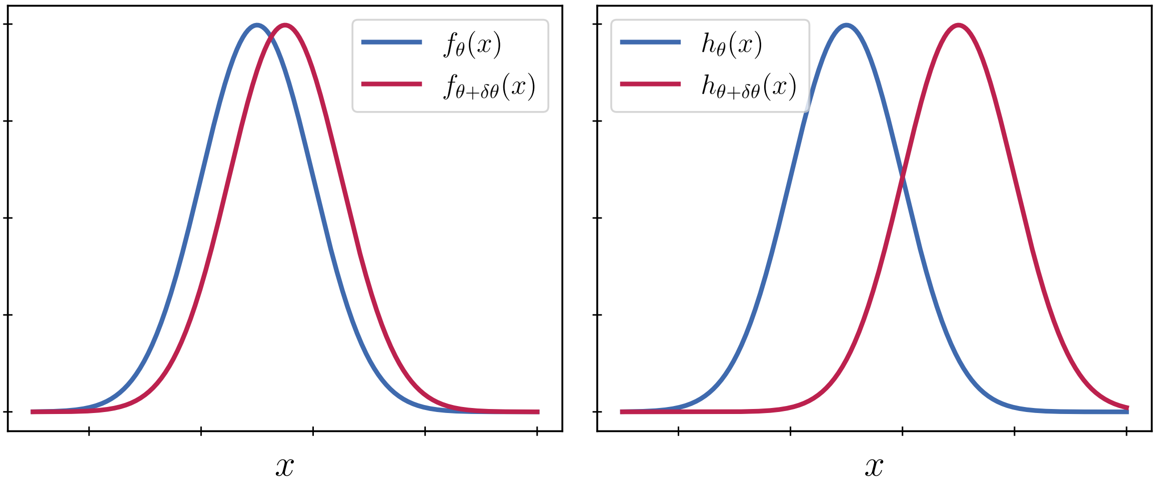

Figure 1.1: Scheme of the variation of Gaussian distribution of fixed standard deviation whose mean is a function of a parameter $\theta$ and is whether slightly (Left) or strongly (Right) affected by a shift of the parameter.

### 1.1.2 Definition

We start by defining $\mathcal{L}(\theta)$, the log-likelihood as:

$$\mathcal{L}(\theta|X) = \log f_\theta(X) \tag{1.1}$$

The score, denoted as $S(\theta|X)$, is the gradient of the log-likelihood function concerning changes in the parameter $\theta$. It quantifies the sensitivity of the log-likelihood to alterations in parameter values:

$$S(\theta|X) = \frac{\partial}{\partial\theta}\log f_\theta(X) \tag{1.2}$$

It is crucial to emphasize that the quantities we derive, namely $\mathcal{L}(\theta)$ and $S(\theta)$, are estimations based on the observed data $X$. The Fisher information, denoted as $\mathcal{I}(\theta)$, is formally defined as the variance of the score:

$$\mathcal{I}(\theta) = \mathbb{V}\left[S(\theta|X)\right] \tag{1.3}$$

Subsequently, because the expected score, denoted as $\mathbb{E}\left[S(\theta)\right]$, equals zero, we can simplify the expression of $\mathcal{I}(\theta)$. Specifically, under certain regularity conditions (which are typically satisfied), we can interchange integration and differentiation. Indeed, we have:

$$\begin{aligned}
\mathbb{E}\left[\frac{\partial}{\partial\theta}\log f_\theta(X)\right] &= \int\left[\frac{\frac{\partial}{\partial\theta}f_\theta(x)}{f_\theta(x)}\right]f_\theta(x)\mathrm{d}x \\
&= \int\frac{\partial}{\partial\theta}f_\theta(x)\mathrm{d}x \\
&= \frac{\partial}{\partial\theta}\int f_\theta(x)\mathrm{d}x \\
&= 0
\end{aligned} \tag{1.4}$$

Furthermore, using the variance formula for any random variable $Z$, which states that $\mathbb{V}[Z] = \mathbb{E}\left[Z^2\right] - \mathbb{E}[Z]^2$, we can straightforwardly derive:

$$\mathcal{I}(\theta) = \mathbb{E}\left[\left(\frac{\partial}{\partial\theta}\log f_\theta(X)\right)^2\right] \tag{1.5}$$

Which can also be written as:

$$\boxed{\mathcal{I}(\theta) = \int_{\mathbb{R}}\left(\frac{\partial}{\partial\theta}\log f_\theta(x)\right)^2 f_\theta(x)\mathrm{d}x} \tag{1.6}$$

It is worth noting that the Fisher information is not contingent on any specific observation, as the random variable $X$ has been averaged out. Naturally, $\mathcal{I}(\theta) \geq 0$, as expected for a variance. In intuitive terms, the Fisher information quantifies the dispersion of the Score, implying that a large Fisher information signifies a dispersed score function.

For instance, let us designate $\hat{\theta}$ as a good estimator of $\theta$, typically the one that maximizes the log-likelihood $\mathcal{L}(\theta|X)$. Essentially, a high Fisher information suggests that $\hat{\theta}$ will provide more information about $X$ than if the Fisher information were smaller. In other words, the Fisher information determines the rate at which the observed score converges towards the true score function.

### 1.1.3 An alternative definition

In this section, we introduce an alternative definition of the Fisher information, which possesses the advantage to highlight the geometric nature of this quantity by revealing a second-order derivative. To begin, assuming that $f_\theta$ is twice differentiable, we observe:

$$\begin{aligned}\frac{\partial^2}{\partial\theta^2}\log f_\theta(x) &= \frac{\partial}{\partial\theta}\left[\frac{\frac{\partial}{\partial\theta}f_\theta(x)}{f_\theta(x)}\right] \\ &= \frac{\frac{\partial^2}{\partial\theta^2}f_\theta(x)}{f_\theta(x)} - \left[\frac{\frac{\partial}{\partial\theta}f_\theta(x)}{f_\theta(x)}\right]^2 \\ &= \frac{\frac{\partial^2}{\partial\theta^2}f_\theta(x)}{f_\theta(x)} - \left[\frac{\partial}{\partial\theta}\log f_\theta(x)\right]^2\end{aligned} \tag{1.7}$$

Once again, if we presume that we can interchange integration and differentiation, we can demonstrate that the expected value of the first term in the equality becomes zero:

$$\begin{aligned}\mathbb{E}\left[\frac{\frac{\partial^2}{\partial\theta^2}f_\theta(x)}{f_\theta(x)}\right] &= \int\left[\frac{\frac{\partial^2}{\partial\theta^2}f_\theta(x)}{f_\theta(x)}\right]f_\theta(x)\mathrm{d}x \\ &= \int\frac{\partial^2}{\partial\theta^2}f_\theta(x)\mathrm{d}x \\ &= \frac{\partial^2}{\partial\theta^2}\int f_\theta(x)\mathrm{d}x \\ &= 0\end{aligned} \tag{1.8}$$

Thus we obtain an alternative definition of the Fisher information:

$$\boxed{\mathcal{I}(\theta) = -\mathbb{E}\left[\frac{\partial^2}{\partial\theta^2}\log f_\theta(x)\right]} \tag{1.9}$$

Consequently, the Fisher information can be construed from a geometric perspective as the local curvature of the log-likelihood curve. In the vicinity of the maximum likelihood estimate, a low Fisher information implies that the maximum appears to be relatively *blunt*. Conversely, a high Fisher information signifies that the maximum is characterized by a sharper and more pronounced peak in the likelihood curve.

### 1.1.4 The Cramer-Rao bound

Interestingly, we can demonstrate that the precision with which we can estimate $\theta$ is constrained by the Fisher information. Technically, the Cramer-Rao bound asserts that the inverse of the Fisher information serves as a lower bound for the variance of any unbiased estimator of $\theta$. We will now outline one method to derive this result.

Let us start by considering an unbiased estimator of $\theta$, denoted as $\hat{\theta}(X)$. By unbiased, we mean:

$$\begin{aligned} &\mathbb{E}\left[\hat{\theta}(X) - \theta|\theta\right] = 0 \\ \iff &\int \left(\hat{\theta}(x) - \theta\right) f_\theta(x)\mathrm{d}x = 0 \end{aligned} \tag{1.10}$$

As this is true for any value of $\theta$, we obtain:

$$\begin{aligned} &\frac{\partial}{\partial\theta}\int \left(\hat{\theta}(x) - \theta\right) f_\theta(x)\mathrm{d}x = 0 \\ \iff &\int \left(\hat{\theta}(x) - \theta\right) \frac{\partial f_\theta(x)}{\partial\theta}\mathrm{d}x - \int f_\theta(x)\mathrm{d}x = 0 \end{aligned} \tag{1.11}$$

Therefore, as $f_\theta$ is a probability density function (PDF), it satisfies:

$$\int f_\theta(x)\mathrm{d}x = 1 \tag{1.12}$$

The next step involves a re-expression of the first derivative of $f_\theta$ as follows:

$$\frac{\partial f_\theta(x)}{\partial\theta} = f_\theta(x)\frac{\partial \log f_\theta(x)}{\partial\theta} \tag{1.13}$$

Using the two aforementioned facts, equation 1.11 can be rewritten as follows:

$$\int \left(\hat{\theta}(x) - \theta\right) f_\theta(x)\frac{\partial \log f_\theta(x)}{\partial\theta}\mathrm{d}x = 1 \tag{1.14}$$

Then, we use a clever factorization that allows for the application of the Cauchy-Schwartz inequality:

$$\int \left[\left(\hat{\theta}(x) - \theta\right)\sqrt{f_\theta(x)}\right]\left[\frac{\partial \log f_\theta(x)}{\partial\theta}\sqrt{f_\theta(x)}\right]\mathrm{d}x = 1 \tag{1.15}$$

Hence, squaring the integral enables us to apply the Cauchy-Schwartz inequality:

$$\left(\int \mathrm{d}x \left[\left(\hat{\theta}-\theta\right)\sqrt{f_\theta}\right]\left[\frac{\partial \log f_\theta}{\partial \theta}\sqrt{f_\theta}\right]\mathrm{d}x\right)^2 \leq \int \mathrm{d}x \left(\hat{\theta}-\theta\right)^2 f_\theta \cdot \int \mathrm{d}x \left(\frac{\partial}{\partial \theta}\log f_\theta\right)^2 f_\theta \tag{1.16}$$

The first bracket represents the variance of the estimator $\hat{\theta}$, while the second bracket corresponds to the Fisher information. By rearranging the expression, we arrive at:

$$\boxed{\mathbb{V}(\hat{\theta}) \leq \frac{1}{\mathcal{I}(\theta)}} \tag{1.17}$$

The inverse of the Fisher information is an upper-bound of the variance of $\hat{\theta}$.

## 1.2 Multi-parametric case

The FI can naturally be extended to multi-parametric cases when the probability density function is defined upon several parameters.

### 1.2.1 Definition

In cases involving $p$ parameters, where $\theta$ represents a $p \times 1$ vector, denoted as $\theta = (\theta_1, \ldots, \theta_p)^{\mathrm{T}}$, the Fisher information assumes the structure of a $p \times p$ matrix. The typical element of the Fisher information matrix (FIM), designated as $\mathbf{I}$, is given by:

$$[\mathbf{I}(\theta)]_{i,j} = \mathbb{E}\left[\left(\frac{\partial}{\partial \theta_i}\log f_\theta(X)\right)\left(\frac{\partial}{\partial \theta_j}\log f_\theta(X)\right)\right] \tag{1.18}$$

Similarly, under some regularity conditions the matrix can be written as:

$$[\mathbf{I}(\theta)]_{i,j} = -\mathbb{E}\left[\frac{\partial^2}{\partial \theta_i \partial \theta_j}\log f_\theta(X)\right] \tag{1.19}$$

It can be demonstrated that the Fisher information matrix (FIM) is a positive semi-definite matrix, which can be expressed as: $\left\{x^T \mathbf{I} x \geq 0,\ \forall x \in \mathbb{R}^p - 0\right\}$. This is equivalent to stating that all eigenvalues of $\mathbf{I}$ are non-negative. Since $\mathbf{I}$ is a real symmetric matrix, it can be diagonalized, as per the Spectral theorem. When the Fisher information matrix $\mathbf{I}$ is strictly positive-definite, it defines a Riemannian metric in an N-dimensional parameter space. In the realm of information geometry, this metric is explored and analyzed as the Fisher information metric [124]. In the next section we explicitly state this result, with the Kullbach-Leibler divergence.

### 1.2.2 The Kullbach - Leibler divergence and information geometry

In mathematical statistics, the Kullback-Leibler divergence is a metric used to quantify the dissimilarity between two probability distributions, denoted as $P$ and $Q$. It is defined as follows:

$$D_{KL}(P||Q) = \sum_x P(x)\log\left(\frac{P(x}{Q(x)}\right) \tag{1.20}$$

Strictly speaking, the Kullback-Leibler divergence is not a distance because it has an asymmetric definition: In general, $D_{KL}(P||Q) \neq D_{KL}(Q||P)$. In qualitative terms, it assesses how well distribution $Q$ can predict data generated by distribution $P$.

Now, let us consider two probability distributions with parameters infinitesimally close to each other: $P_\theta$ and $P_{\theta+\delta\theta}$. The infinitesimal Kullback-Leibler divergence takes on the following form:

$$D_{KL}(P_\theta||P_{\theta+\delta\theta}) = g_{\mu\nu}\delta\theta^\mu\delta\theta^\nu + O\delta\theta^3 \tag{1.21}$$

We provide calculations leading to the earlier results in Appendix B.1. Specifically, $g_{\mu\nu}$ is the Fisher information matrix and is expressed as follows:

$$g_{\mu\nu}(\theta) = -\sum_x P_\theta(x)\frac{\partial^2 \log f_\theta(x)}{\partial\theta_\mu\partial\theta_\nu} \tag{1.22}$$

Hence, the local quadratic approximation of the KL-divergence unveils the role of the Fisher information matrix (FIM) as a metric on parameter space. More precisely, it defines a Riemannian manifold known as the statistical manifold, where each point corresponds to a probability distribution, as depicted in Figure 1.2. It can be rigorously demonstrated that the tensor $g_{\mu\nu}$ satisfies all the mathematical prerequisites of a Riemannian metric, although we will not delve into the technical details, which are well-documented in the literature [124]. This outcome establishes the groundwork for the field of information geometry, where distances on the statistical manifold quantify how distinguishable two models are from their data in dimensionless units of their standard deviations.

Naturally, Equation 1.22 can be reformulated in a continuous form as follows:

$$g_{\mu\nu}(\theta) = -\int \frac{\partial^2 \log f_\theta(x)}{\partial\theta_\mu\theta_\nu} f_\theta(x)\mathrm{d}x \tag{1.23}$$

Or, equivalently:

$$g_{\mu\nu}(\theta) = \int \frac{\partial \log f_\theta(x)}{\partial\theta_\mu}\frac{\partial \log f_\theta(x)}{\partial\theta_\nu} f_\theta(x)\mathrm{d}x \tag{1.24}$$

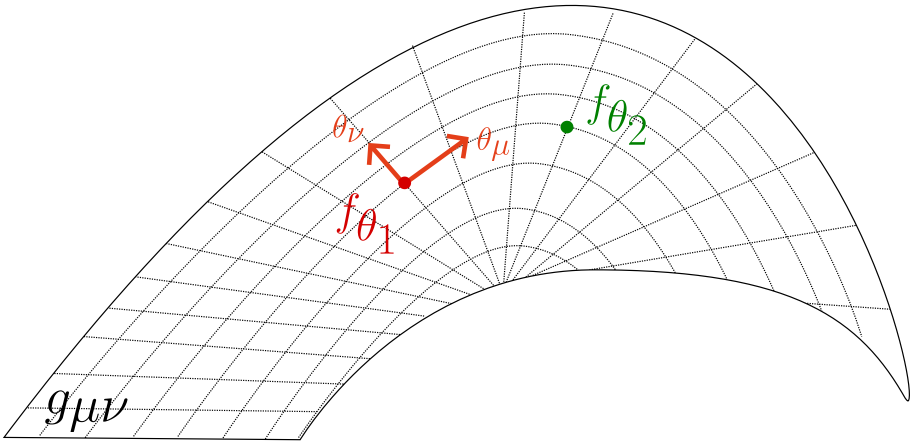

Figure 1.2: Representation of a statistical manifold upon which the density probability $f_\theta$ is defined with associated metric $g_{\mu\nu}$. Arrows associated to $\theta_\mu$ and $\theta_\nu$ represent displacements on the manifold.

### 1.2.3 Multi-parametric and multi-observable case

In cases involving $p$ parameters, and $n$ observables where $\mathbf{X}$ represents an $n \times 1$ vector, denoted as $\mathbf{X} = (X_1, \ldots, X_n)^{\mathrm{T}}$, the Fisher information still assumes the structure of a $p \times p$ matrix:

$$\boxed{[\mathbf{I}(\theta)]_{i,j} = \mathbb{E}\left[\left(\frac{\partial}{\partial \theta_i} \log f_\theta(\mathbf{X})\right)\left(\frac{\partial}{\partial \theta_j} \log f_\theta(\mathbf{X})\right)\right]} \tag{1.25}$$

Since our application (branched actin system) involves dealing with many observables in multi-parametric systems, we will focus on this form of interest. As Gaussian distributions are central to our study we introduce them as well as the specific associated form of the FIM in this context.

## 1.3 Multivariate Gaussian distribution

### 1.3.1 Definition

Let $X$ be a random variable following a Gaussian distribution $\mathcal{N}(\mu, \sigma)$, whose associated probability density function is:

$$f(x) = \frac{1}{\sigma\sqrt{2\pi}} \exp\left(-\frac{1}{2}\left(\frac{x-\mu}{\sigma}\right)^2\right) \tag{1.26}$$

We now consider a vector of random variables $\mathbf{X} = (X_1, \ldots, X_n)^{\mathrm{T}} \in \mathbb{R}^n = \Omega$. Let $\mu \in \mathbb{R}^n$ be the mean vector and $\mathbf{\Sigma} = [\sigma_{ij}]$ a $n \times n$ symmetric positive-definite covariance matrix:

$$\begin{aligned} \boldsymbol{\mu} &= (\mathbb{E}[X_1], \mathbb{E}[X_2], \ldots, \mathbb{E}[X_n])^{\mathrm{T}} \\ \mathbf{\Sigma}_{i,j} &= \mathbb{E}[(X_i - \mu_i)(X_j - \mu_j)] \end{aligned} \tag{1.27}$$

In order to clarify the notations, we will write $\boldsymbol{\mu}$ in this way:

$$\boldsymbol{\mu} = (\mu_1, \mu_2, \ldots, \mu_n)^{\mathrm{T}} \tag{1.28}$$

The multivariate Gaussian distribution $\mathcal{N}(\boldsymbol{\mu}, \mathbf{\Sigma})$ has associated probability density function:

$$\boxed{f(\mathbf{x}) = (2\pi)^{-n/2}|\mathbf{\Sigma}|^{-1/2} \exp\left(-\frac{1}{2}(\mathbf{x}-\boldsymbol{\mu})^{\mathrm{T}}\mathbf{\Sigma}^{-1}(\mathbf{x}-\boldsymbol{\mu})\right)} \tag{1.29}$$

With $\mathbf{\Sigma}^{-1}$ the inverse covariance matrix, also known as precision matrix, and $|\mathbf{\Sigma}|$ the determinant of the covariance matrix.

### 1.3.2 Gaussian FIM

Let $\mathbf{X}$ follow a $n$-multivariate Gaussian distribution parameterized by a vector $\theta$ of dimension $p$: $\mathbf{X} \sim \mathcal{N}(\boldsymbol{\mu}(\theta), \boldsymbol{\Sigma}(\theta))$. In this context the FIM has a particular form:

$$\boxed{[\mathbf{I}(\theta)]_{i,j} = \frac{\partial \boldsymbol{\mu}^{\mathsf{T}}}{\partial \theta_i} \boldsymbol{\Sigma}^{-1} \frac{\partial \boldsymbol{\mu}}{\partial \theta_j} + \frac{1}{2} \operatorname{Tr}\left( \boldsymbol{\Sigma}^{-1} \frac{\partial \boldsymbol{\Sigma}}{\partial \theta_i} \boldsymbol{\Sigma}^{-1} \frac{\partial \boldsymbol{\Sigma}}{\partial \theta_j} \right)} \tag{1.30}$$

$$\frac{\partial \boldsymbol{\mu}}{\partial \theta_i} = \begin{bmatrix} \frac{\partial \mu_1}{\partial \theta_i} & \frac{\partial \mu_2}{\partial \theta_i} & \cdots & \frac{\partial \mu_N}{\partial \theta_i} \end{bmatrix}^{\mathrm{T}} \tag{1.31}$$

$$\frac{\partial \boldsymbol{\Sigma}}{\partial \theta_i} = \begin{bmatrix} \frac{\partial \Sigma_{1,1}}{\partial \theta_i} & \frac{\partial \Sigma_{1,2}}{\partial \theta_i} & \cdots & \frac{\partial \Sigma_{1,N}}{\partial \theta_i} \\ \frac{\partial \Sigma_{2,1}}{\partial \theta_i} & \frac{\partial \Sigma_{2,2}}{\partial \theta_i} & \cdots & \frac{\partial \Sigma_{2,N}}{\partial \theta_i} \\ \vdots & \vdots & \ddots & \vdots \\ \frac{\partial \Sigma_{N,1}}{\partial \theta_i} & \frac{\partial \Sigma_{N,2}}{\partial \theta_i} & \cdots & \frac{\partial \Sigma_{N,N}}{\partial \theta_i} \end{bmatrix} \tag{1.32}$$

Computations leading to this result have been detailed in literature [125]. Interestingly, in the particular but very common case where the covariance matrix does not depend on the parameter $\theta$, $\boldsymbol{\Sigma}(\theta) = \boldsymbol{\Sigma}$, we obtain:

$$[\mathbf{I}(\theta)]_{i,j} = \frac{\partial \boldsymbol{\mu}^{\mathsf{T}}}{\partial \theta_i} \boldsymbol{\Sigma}^{-1} \frac{\partial \boldsymbol{\mu}}{\partial \theta_j} \tag{1.33}$$

Adopting the *tensor style*, we have:

$$\boxed{g_{\mu\nu} = \frac{\partial \boldsymbol{\mu}^{\mathsf{T}}}{\partial \theta_\mu} \boldsymbol{\Sigma}^{-1} \frac{\partial \boldsymbol{\mu}}{\partial \theta_\nu}} \tag{1.34}$$

In the following section, we will explore how Fisher information has been employed in the literature to compress the parameter space of physical systems. We will begin with the general concept introduced in Machta et al. [121] and then delve into a numerical implementation as demonstrated in Hsu et al. [126].

# Chapter 2

# State of the Art

## 2.1 Fisher information for Parameter Space Compression

### 2.1.1 Introduction

In their work, Machta et al. [121] expand upon the observation that multi-parameter models from various scientific fields primarily rely on a few *stiff* combinations of parameters, as already discussed in [115]. This recurring characteristic may lead one to interpret it as an inherent property that could potentially explain a form of universality, akin to the concept of renormalization group in physics.

To investigate this hypothesis further, they conducted an information-theoretic analysis on models for which the continuum limit or the renormalization group (RG) had already offered a satisfying explanation for the emergence of an effective model capable of abstracting away microscopic details.

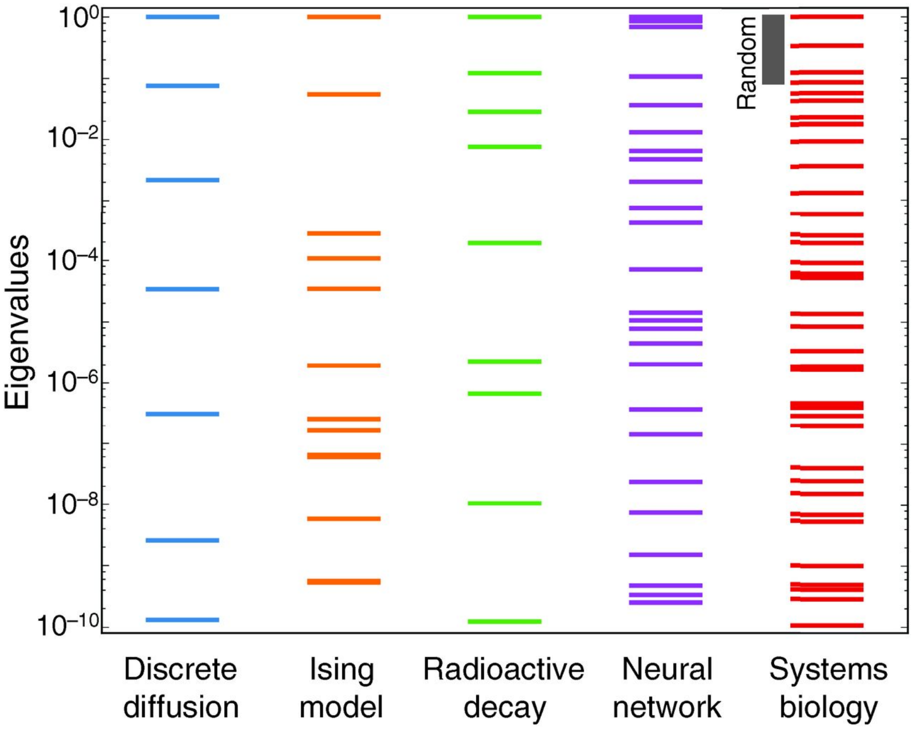

Figure 2.1: Eigenvalues of the FIM for various models. Eigenvalues are normalized to unit of stiffest value. The thick grey line accounts for the distribution of eigenvalues predicted by Wishart statistics often found in least square problems.

Building upon the definition of the Fisher Information Matrix (FIM) (see Equation 1.19), they derived a Gaussian metric for a hopping model of diffusion and a statistical mechanics metric for the Ising model of ferromagnetism. Intriguingly, in both cases, they demonstrated that at long time and length scales, analytical investigations yielded a similar hierarchical arrangement of eigenvalues corresponding to relevant macroscopic parameters (such as the diffusion constant in the first model). In this context, we will focus on the diffusion model as a straightforward proof of concept, while the second model explores the efficiency of the approach at phase transitions where microscopic fluctuations become significant, which is far from our considerations.

### 2.1.2 A hopping model of diffusion

Let us consider a simple microscopic model of stochastic motion on a discrete 1-dimensional lattice of sites. This system is governed by $2N+1$ parameters denoted as $\theta^{\mu}$ for $-N \leq \mu \leq N$. These parameters describe the probability that a particle will hop from site $j$ to site $j+\mu$ in a discrete time step, as illustrated in Figure 2.2. Consequently, the observables are represented by vector $\vec{y}$, which describes the densities of particles at time $t$. At the initial time, all particles are located at the origin, given by $\rho_0(j) = \delta_{j,0}$. Subsequently, after one time step, the distribution becomes:

$$\rho_1(j) = \theta^{j} \tag{2.1}$$

At long time and length scales, in the continuum limit, the particle density should be governed by the classical diffusion equation.

$$\frac{\partial \rho(x,t)}{\partial t} = D\frac{\partial^2 \rho}{\partial x^2} - v\frac{\partial \rho}{\partial x} \tag{2.2}$$

With $D$ the diffusion coefficient and $v$ the drift. Here, for the sake of simplicity we assume no particle creation.

Let us retrieve the characteristics of the diffusion equation using Parameter Space Compression. To tackle this problem, we employ a simplified version of the Gaussian model, which we will present here.

#### An example of the Gaussian metric

This approach, initially inspired by nonlinear least squares, involves a model in which the data vector $y^{j}$ is assumed to follow a normal distribution around a parameter-dependent mean $y_0^{j}(\theta)$ with a standard deviation $\sigma^{j}$. Therefore, the probability distribution of the data $\vec{y}$ given $\theta$ is expressed as follows:

$$P_{\theta}(\vec{y}) \propto \exp\left(-\frac{\left(y^{j} - y_0^{j}(\theta)\right)^2}{2(\sigma^{j})^2}\right) \tag{2.3}$$

Given this Gaussian distribution, it can be demonstrated that the FIM can be simply expressed as:

$$g_{\mu\nu} = \sum_{j} \frac{1}{\sigma^{j}}\frac{\partial y_0^{j}(\theta)}{\partial \theta_{\mu}}\frac{1}{\sigma^{j}}\frac{\partial y_0^{j}(\theta)}{\partial \theta_{\nu}} \tag{2.4}$$

In this simplified version of the Gaussian metric, it is assumed that there is no correlation between observables. Since the hopping events from one site to another are completely independent, the resulting observables in vector $\vec{x}$ are uncorrelated.

The uncertainties $\sigma^j$ do not depend on the parameters. In addition, using $\sigma^j = 1$ does not have an impact on the metric because all observables have the same dimension and are measurable with equal accuracy. This simplifies the expression to:

$$\boxed{g_{\mu\nu} = \sum_j J_{j\mu} J_{j\nu} \ ; \ J_{j\mu} = \frac{\partial y_0^j(\theta)}{\partial \theta_\mu}} \tag{2.5}$$

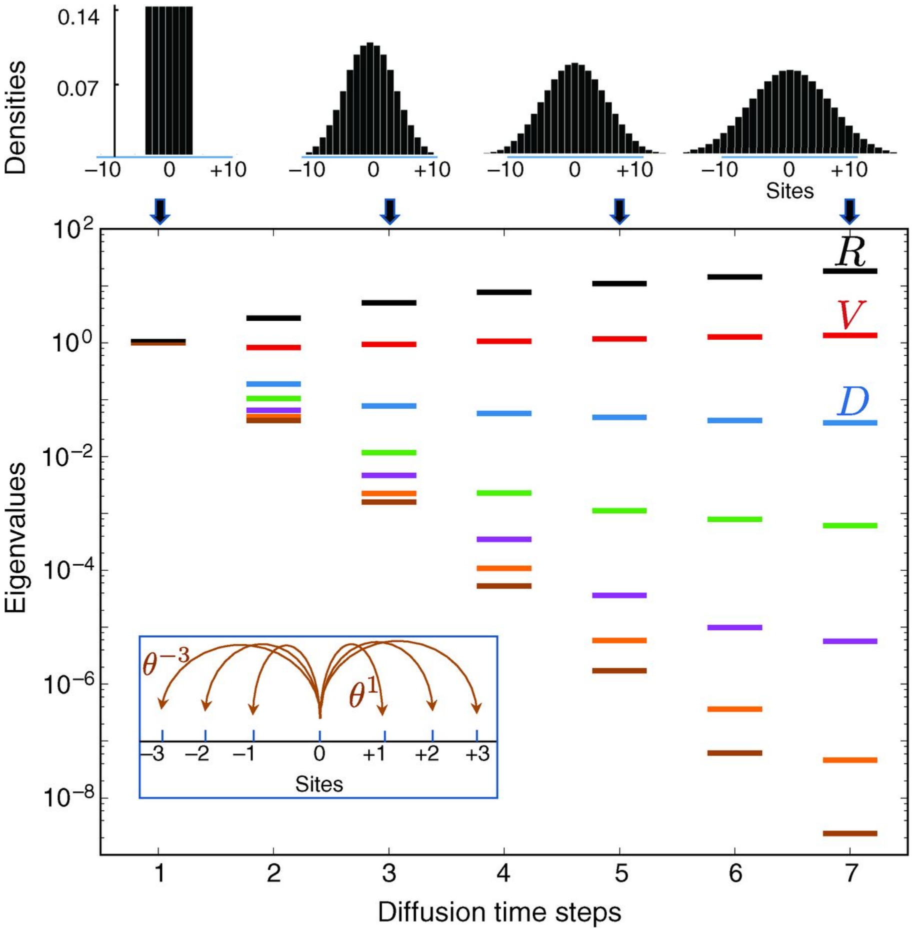

Figure 2.2: FIM eigenvalues of a model of stochastic motion on a 1D lattice. The seven parameters describe probabilities of transitioning to nearby sites (bottom, inset). Observations are taken after a given number of time steps for the case in which all parameters take the value qm $= 1/7$. The top row shows the resulting densities plotted at times t = 1, 3, 5, and 7. The bottom plot shows the eigenvalues of the FIM versus number of steps, with emerging $R, v$ and $D$, from [121]. $R$ being the rate of addition of particles when the mass is not conserved.

### Coarsening the diffusion equation at high scales

In our case, our observables are time-dependent, denoted as $\rho_t(j)$, which means the FIM also varies with time

$$g_{\mu\nu}(t) = \sum_j \frac{\partial \rho_t(j)}{\partial \theta_\mu} \frac{\partial \rho_t(j)}{\partial \theta_\nu} \tag{2.6}$$

After a single time step, the particle density distribution becomes $\rho_1(j) = \theta^j$. This simplifies the expression of the FIM to:

$$\begin{aligned} g_{\mu\nu}(1) &= \sum_j \frac{\partial\theta_j}{\partial\theta_\mu}\frac{\partial\theta_j}{\partial\theta_\nu} \\ &= \sum_j \delta_{j,\mu}\delta_{j,\nu} \\ &= \delta_{\mu\nu} \end{aligned} \tag{2.7}$$

Hence, it is clear that the FIM in this case has $2N+1$ eigenvalues, all with a value $\lambda = 1$. This is shown in Figure 2.2 after a single time step. In other words, all parameters are equally measurable. To discern global trends and dependencies, one would need to study the behavior of the FIM over multiple time steps.

In order to calculate the density of particles at position $j$ and time $t$ $\rho_t(j)$ one can introduce the Fourier transform of the hopping rates and of the particle density:

$$\begin{aligned} \tilde{\theta}^k &= \sum_{\mu=-N}^{N} e^{-ik\mu}\theta^\mu \\ \tilde{\rho}_t^k &= \sum_{\mu=-\infty}^{\infty} e^{-ikj}\rho_t(j) \\ \rho_t(j) &= \frac{1}{2\pi}\int_{-\pi}^{\pi} \mathrm{d}k e^{ikj}\tilde{\rho}_t^k \end{aligned} \tag{2.8}$$

The density distribution at time $t$ is the convolution between the density at $t-1$ and the hopping rates. In the Fourier space, this becomes:

$$\tilde{\rho}_t^k = \tilde{\theta}^k \tilde{\rho}_{t-1}^k \tag{2.9}$$

Initially all particles are at the origin i.e. $\rho_0(j) = \delta_{j,0}$, which translates as $\tilde{\rho}_0^k = 1$. Thus, we obtain:

$$\begin{aligned} \tilde{\rho}_t^k &= (\tilde{\theta}^k)^t \\ \rho_t(j) &= \frac{1}{2\pi}\int_{-\pi}^{\pi} \mathrm{d}k e^{ikj}(\tilde{\theta}^k)^t \end{aligned} \tag{2.10}$$

Subsequently, we get:

$$\begin{aligned} J_{j\mu}^t = \partial_\mu\rho_t(j) &= \frac{t}{2\pi}\int_{-\pi}^{\pi} \mathrm{d}k e^{ik(j-\mu)}(\tilde{\theta}^k)^{t-1} \\ g_{\mu\nu}(t) &= \frac{t^2}{2\pi}\int_{-\pi}^{\pi} \mathrm{d}k e^{ik(\mu-\nu)}(\tilde{\theta}^k)^{t-1}(\tilde{\theta}^{-k})^{t-1} \end{aligned} \tag{2.11}$$

The examination of the eigenvalues of the Fisher Information Matrix (FIM) resulted in the sloppy spectrum depicted in Figure 2.2, obtained from numerical computations. This analysis enables us to identify the three stiffest eigendirections of $g_{\mu\nu}$, which correspond to the three terms of the diffusion equation at later times (when we consider a creation term $R$).

In addition, by assuming that all hopping rates $\theta_\mu$ are positives and that their sum is equal to one, then they are each less than 1. Thus, logically at late time $t$, the integral is predominantly influenced by small values of $k$, low spatial frequencies. Therefore, for small values of $k$, we have:

$$\begin{aligned}\tilde{\theta}^k &= \sum_{\mu=-N}^{N} e^{-ik\mu}\theta^\mu \\ &\approx \left(1 - ikv - \Delta\frac{k^2}{2}\right) + o(k^3) \\ &= e^{-ikv - D\frac{k^2}{2}} + o(k^3)\end{aligned} \tag{2.12}$$

Hence, we retrieve the drift $v$ and the diffusion constant $D$:

$$\begin{aligned}v &= \sum_\mu \mu\theta^\mu \\ \Delta &= \sum_\mu \mu^2\theta^\mu \\ D &= \Delta - v^2\end{aligned} \tag{2.13}$$

Thus, for late times, it is possible to extend the domain of the integral as high frequency terms vanish exponentially. The FIM can be approximated as:

$$g_{\mu\nu}(t) \approx \frac{t^2}{2\pi}\int_{\infty}^{\infty} \mathrm{d}k e^{ik(\mu-\nu)} e^{-Dtk^2} \tag{2.14}$$

Using results from Gaussian integrals, this becomes:

$$g_{\mu\nu}(t) \simeq \frac{t^2}{(Dt)^{1/2}} e^{-(\mu-\nu)^2/4Dt} \tag{2.15}$$

This can be expanded in powers of the small parameter $-(\mu-\nu)^2/4Dt$. Then, we obtain:

$$g_{\mu\nu}(t) \simeq \sum_{n=0}^{\infty} \frac{(-1)^n(\mu-\nu)^{2n}}{n!(4Dt)^{n+1/2}} \tag{2.16}$$

Thus, each term of the series contributes to an eigenvalue that scales as:

$$\boxed{\lambda_n \simeq t^2 \left(\frac{Dt}{N^2}\right)^{-n-1/2} \qquad n \geq 0} \tag{2.17}$$

Consequently, after several time steps, a hierarchy of eigenvalues naturally emerges, capturing the macroscopic characteristics of the system.

Hence, this diffusion model has effectively demonstrated, as a proof of concept, how PSC offers a methodology for unveiling the inherent sloppiness inherent in multi-parameter models by simplifying the coarsening the observables. It enables the distinction between *stiff* and *sloppy* parameters, effectively capturing high-scale collective behaviors while discarding irrelevant changes. In practice, PSC compresses the higher moments of the distribution (such as skewness or kurtosis), whose contribution diminish over time, as illustrated in Figure 2.2. This suggests that the primary characteristics of stochastic variables can be encapsulated in variations of mean and variance.

## 2.2 A numerical implementation

Hsu et al. [126] extended the application of PSC by introducing a numerical approach that can be employed with computational models. This expansion allowed PSC to be applied to a broader range of systems, including those that lack analytical solutions. They verified the robustness of their method using analytical models of random walks and protein production before applying it to the microtubule dynamic instability problem. While we will not delve into the details of the random walk and protein production systems, we will explore their computational approach and the outcomes of their study concerning microtubule instability.

### 2.2.1 A simplification of the Gaussian metric

Let us present their overall approach. Regarding the observables, rather than assuming a specific probabilistic model, they make an assumption about the deviations of the noisy probability from the true model. Specifically, they assume that these deviations follow a Gaussian distribution with respect to the true model. Let us walk through the derivation. We begin with the assumption that our model observable is defined by the PDF $f_\theta(x)$. We also introduce $d_i$ as the experimentally measured probability of the value $x_i$. Note that $d_i$ deviates from the true value $f_\theta(x_i)$ due to measurement error:

$$d_i = f_\theta(x_i) + \sigma_i r_i \tag{2.18}$$

The measurement error $r_i$ is assumed to be Gaussian distributed, centered in 0 with variance 1. $\sigma_i$ accounts for the local variance measurement which should depend on observable $x$.

$$r_i(\theta) = \frac{d_i - f_\theta(x_i)}{\sigma_i} \tag{2.19}$$

Logically, errors $\{r_i\}$ are independent and the PDF of the residuals $\vec{r} = \{r_i\}$ is:

$$p_\theta(\vec{r}) = \frac{1}{(2\pi)^{M/2}} \exp\left(-\frac{1}{2}\sum_{i=1}^{M} r_i(\theta)^2\right) \tag{2.20}$$

with $M$ the number of points on the curve where we try to fit the data.

Hence, we define $g_{\mu\nu}$ as the FIM of the residuals $\vec{r}$. As $\vec{r}$ is Gaussian distributed, the computations are straightforward, obtaining a form close to Equation 1.34.

$$\begin{aligned} g_{\mu\nu} &= \left\langle -\frac{\partial^2 \log p_\theta(\vec{r})}{\partial\theta_\mu \partial\theta_\nu} \right\rangle \\ &= \left\langle \frac{\partial^2 \sum_i \frac{1}{2} r_i^2}{\partial\theta_\mu \partial\theta_\nu} \right\rangle \\ &= \sum_i \left\langle r_i \frac{\partial^2 r_i}{\partial\theta_\mu \partial\theta_\nu} + \frac{\partial r_i}{\partial\theta_\mu}\frac{\partial r_i}{\partial\theta_\nu} \right\rangle \\ &= \sum_i \left\langle r_i \frac{\partial^2 r_i}{\partial\theta_\mu \partial\theta_\nu} \right\rangle + \left\langle \frac{\partial r_i}{\partial\theta_\mu}\frac{\partial r_i}{\partial\theta_\nu} \right\rangle \end{aligned} \tag{2.21}$$

By substituting the expressions for $\{r_i\}$ as defined in Equation 1.34, we find that the first term vanishes. Indeed, $d_i$ is independent of $\theta$, and $f_\theta(x_i)$ does not depend on $r_i$. This leads to $-\sum_i \partial_{\mu\nu} f_\theta(x_i) < r_i >$, where $< r_i >=0$. Regarding the second term, it becomes fully deterministic as follows:

$$\frac{\partial r_i}{\partial \theta_\mu} = -\frac{1}{\sigma_i}\frac{\partial f_\theta(x_i)}{\partial \theta_\mu} \tag{2.22}$$

Finally, we obtain:

$$\boxed{g_{\mu\nu}(t) = \sum_i \frac{1}{\sigma_i^2}\frac{\partial f_\theta(x_i,t)}{\partial \theta_\mu}\frac{\partial f_\theta(x_i,t)}{\partial \theta_\nu}} \tag{2.23}$$

The expression presented is a straightforward function of the Jacobian matrix concerning its parameters. Besides, the main strength of the results lies in the fact that they are purely determined by the model $f_\theta(x,t)$, as $\vec{r}$ has been averaged out. For practical reasons, all $\sigma_i$ were assumed to be equal to 1. In addition, as biological models often mix rates and energies, the authors proposed to rescale kinetic rates by using their logarithm as rates are exponentially related to the rescaled energy (in $k_B T$ units):

$$\frac{\partial f_\theta(x)}{\partial \log(\theta_\mu)} = \frac{\partial f_\theta(x)}{\partial \theta_\mu}\theta_\mu \tag{2.24}$$

Therefore, the final expression is:

$$g_{\mu\nu}(t) = \sum_i \frac{\partial f_\theta(x_i,t)}{\partial \theta_\mu}\frac{\partial f_\theta(x_i,t)}{\partial \theta_\nu}\theta_\mu^{\alpha_\nu}\theta_\nu^{\alpha_\nu} \tag{2.25}$$

where $\alpha_\mu = 0$, if $\theta_\mu$ is an energy and $\alpha_\mu = 1$, if $\theta_\mu$ is a kinetic rate.

Numerically, the finite derivatives are evaluated this way:

$$\frac{\partial f_\theta(x,t)}{\partial \theta_\mu} = \frac{f_\theta(x,t \mid \theta_\mu + \Delta\theta_\mu) - f_\theta(x,t \mid \theta_\mu - \Delta\theta_\mu)}{2\Delta\theta_\mu} \tag{2.26}$$

The initial step involves the generation of a set of probability distributions denoted as $f_\theta(x,t \mid \theta_\mu \pm \Delta\theta_\mu)$, totaling $2N+1$ distributions for each observable $x$. Notably, even though the choice of $\Delta\theta$ is arbitrary, authors suggest that the most robust choice to obtain significant changes while avoiding artifacts and numerical instabilities was to vary energies by $0.05 k_B T$ (which means a 5% change for kinetic rates). Subsequently, these probability distributions enable the computation of the time-dependent FIM, as depicted in Equation 2.25, specifically for the observable $x$. The resultant eigenvalues derived from this computation yield time-varying eigendirections.

### 2.2.2 Application to the microtubule dynamics

We now present the outcomes obtained through the numerical methodology, applied to a model representing microtubule growth. As previously elucidated in section 1.1.1, microtubules undergo dynamic instability, a stochastic process involving intermittent transitions between growth and shrinkage phases. This intricate non-equilibrium phenomenon was initially simulated in the 1980s [127] [128] and continues to captivate the interest of the computational biology community [129]. Over the years, numerous models of increasing complexity have been introduced to comprehend this phenomenon. However, in contemporary research, the pursuit is to construct a minimal model capable of retaining predictive power. Consequently, the application of PSC becomes appropriate in ascertaining whether these models exhibit an inherent low-dimensional structure that manifests through *sloppiness*.

### A microtubule growth model

The model used draws inspiration from the seminal work of VanBuren et al. [130], which has undergone several adaptations in the literature. This model is visually represented in Figure 2.3 (Top). In essence, it hinges on the principle of tubulin dimers associating end-to-end to form protofilaments. These longitudinal bonds are characterized by variations in Gibbs free energy denoted as $\Delta G^o_{long}$. To construct the tubular structure, 13 protofilaments are interconnected with a parameter denoted as $\Delta G^o_{lat}$.

The rate at which these associations occur is represented by $k_+$. Additionally, tubulin undergoes hydrolysis of GTP (Guanosine Triphosphate), a process known as GTPase, which occurs at a constant rate denoted as $k_H$. The hydrolysis of GTP and subsequent release of phosphate weakens the bonds between subunits within the polymer, ultimately giving rise to the phenomenon of dynamic instability. Specifically, the association of new GDP-tubulin subunits is accompanied by an increase in energy denoted as $\Delta\Delta G^o_{lat}$. The selection of these model parameters aligns with existing literature [131], as illustrated in Figure 2.3 (Top). The process was simulated using Gillespie algorithm [132] and they successfully replicate experimental data derived from *in vitro* reconstitutions [133]. In summary, microtubules undergo growth as long as their end is shielded by a GTP-tubulin cap. However, once this cap disappears, growth transitions to shrinkage, a phenomenon referred to as catastrophe.

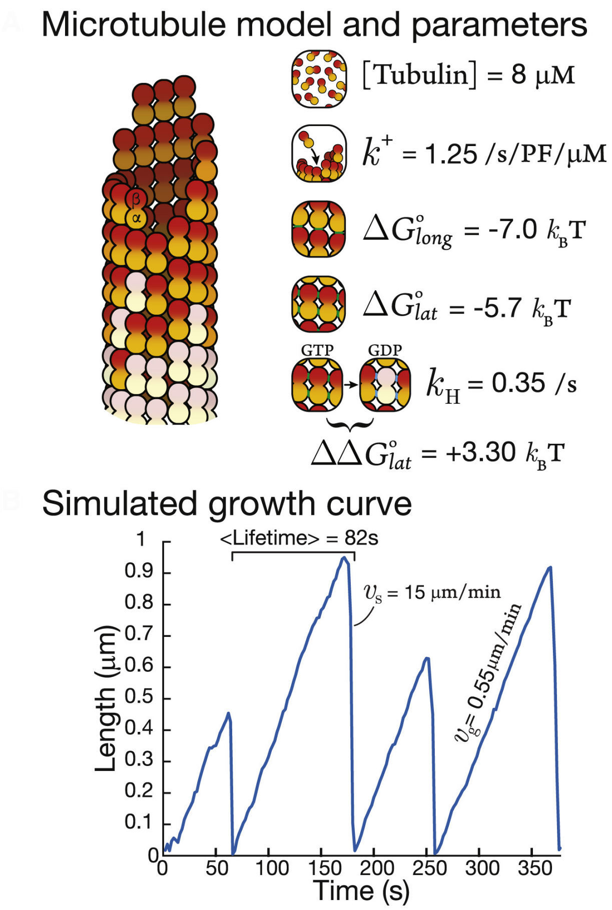

Figure 2.3: (Top) Base model of microtubule simulations dynamics, (Bottom) plot of the length as a function of time for one simulation, adapted from [126].

### Numerical PSC results

In order to streamline the model, all five parameters, namely $\Delta G^o_{long}$, $\Delta G^o_{lat}$, $k_+$, $k_H$, and $\Delta\Delta G^o_{lat}$, were systematically varied around their initial values. Four distinct observables were subsequently measured: the microtubule length, the decay constant characterizing the conversion of GTP-tubulin into GDP-tubulin, the microtubule lifetime, and the post-catastrophe rate. Notably, the length and decay constant could be continuously tracked throughout the simulation duration, distinguishing them from the other observables. The numerical FIM analysis yielded an eigenvalues hierarchy, conforming to expectations. In general, all independent observables underscored the preeminence of a single eigenvalue that gradually emerged over time, a phenomenon clearly illustrated in Figure 2.4, which pertains to microtubule length. Within the same figure, the primary eigenvector decomposition is represented as a percentage of the initial parameters. Remarkably, it became evident that $\Delta G^o_{long}$ and $\Delta G^o_{lat}$ played pivotal roles in determining microtubule length.

Although this analysis elucidated that most observables could be characterized by a single effective parameter, it did not provide insights into the extent to which the key factor influencing microtubule length also influenced observables such as the decay rate. Subsequently, to discern shared effective parameters, the authors conducted a Singular Value Decomposition (SVD) analysis by merging eigenvectors from all observables. The number of prominent singular values obtained from this analysis offer insights into how many dimensions are required to accurately represent the original matrix. In a sense, SVD can be regarded as a generalization of diagonalization, applicable to non-square matrices. The SVD analysis yielded a *sloppy* distribution of singular values, with two dominant ones, signifying a two-dimensional characterization of the problem. The first vector, primarily influenced by the energy of lattice bonds ($\Delta G^o_{long}$ and $\Delta G^o_{lat}$), accounted for *polymerization*. The second vector is associated with the binding and unbinding dynamics of dimers ($k^+$ and $\Delta\Delta G^o_{lat}$) and represents a GTP-cap parameter. Intriguingly, these two parameters formed a two-dimensional "ribbon" within the five-dimensional parameter space.

While this approach has successfully revealed the sloppy nature of a microtubule model, as well as its underlying dimensions, we have also identified several limitations. These limitations serve as the foundation upon which we base our own iteration of numerical PSC in the subsequent chapter.

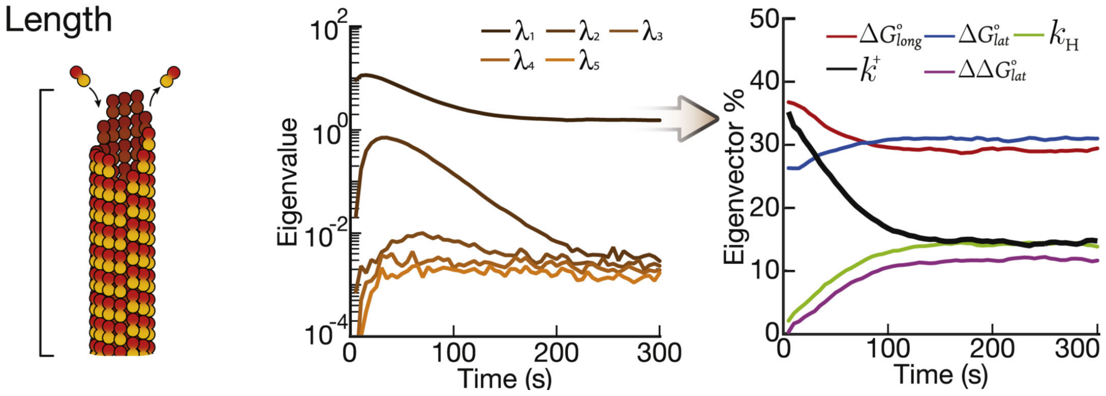

Figure 2.4: Numerical PSC for the five parameter microtubule model. Eigenvalues and main eigenvector decomposition as a function of time in s, adapted from [126].

# Chapter 3

# Toward a local Gaussian approximation[1]

## 3.1 Limits and potential improvements of the numerical approach

In this section, we articulate the motivations behind the development of our novel numerical PSC method by listing the limitations introduced by the approach employed by Hsu et al.

### 3.1.1 The inner dimension of the model

The observables derived from the microtubule study can, for the most part, be reasonably approximated using common PDFs such as Gaussian, exponential, or Gamma distributions. For example, as depicted in Figure 3.1, the probability density of the microtubule length conforms to an exponential model, while the decay constant can be effectively modeled as a Gaussian distribution.

Thereafter, it is crucial to emphasize that a PDF can be completely characterized by its cumulants, which represent mathematical functions derived from the underlying probability parameters. Furthermore, it is worth noting the direct connection between the conventional FIM and a FIM constructed based on the cumulants, as elaborated upon in the work of Prasad et al. [134]. Consequently, one can expect that an exponential decay model would be associated with a one-dimensional parameter space, represented by the parameter $\lambda$, while a Gaussian model would require a two-dimensional parameter space to adequately capture its characteristics, involving parameters for mean and variance.

Our primary goal in this context is to demonstrate that the FIM methodology introduced by Hsu et al. inherently yields a rank-1 matrix when applied to scenarios involving one-parameter models, such as Gaussian distributions with fixed widths or exponential distributions. To begin our analysis, we revisit the expression of the approximated FIM, particularly when the probability density function is not time-dependent:

$$g_{\mu\nu} = \sum_i \frac{1}{\sigma_i^2} \frac{\partial f_\theta(x_i)}{\partial \theta_\mu} \frac{\partial f_\theta(x_i)}{\partial \theta_\nu} \tag{3.1}$$

Let us approximate this sum as an integral by considering the step size $\Delta x$ between sampled points. We also consider that the uncertainties on probability measurements do not depend on the sampled point: $\sigma_i = \sigma_\alpha$, which leads to:

$$g_{\mu\nu} \simeq \frac{1}{\sigma_\alpha^2 \Delta x} \int \mathrm{d}x \frac{\partial f_\theta(x)}{\partial \theta_\mu} \frac{\partial f_\theta(x)}{\partial \theta_\nu} \tag{3.2}$$

---

[1] sorry for the spoiler...

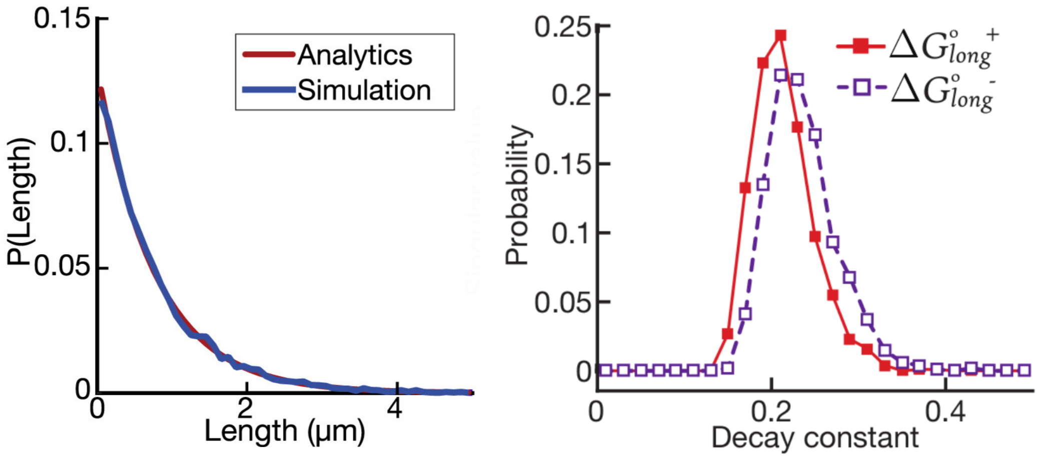

Figure 3.1: (Left) Probability distribution of the length from simulations and analytic expression from an exponential law modelling. (Right) Plot of the decay constant distribution for two $\Delta G^{o}_{long}{}^{\pm}$ values. We observe the shift of the PDF when switching the parameter. Adapted from [126]

### Gaussian example

First, let us assume that $f_\theta(x)$ is a Gaussian probability density function, whose mean is a function of $\theta$ but not its variance:

$$f_\theta(x) = \frac{1}{\sigma\sqrt{2\pi}} e^{(x-x_0(\theta))^2/(2\sigma^2)} \tag{3.3}$$

Thus, we have:

$$g_{\mu\nu} \simeq \frac{1}{\sigma_\alpha^2 \Delta x} \int \mathrm{d}x \frac{1}{4\sigma^4} f_\theta(x)^2 (x - x_0(\theta))^2 \frac{\partial x_0(\theta)}{\partial \theta_\mu} \frac{\partial x_0(\theta)}{\partial \theta_\nu} \tag{3.4}$$

To make things more concise, we write $\frac{\partial x_0(\theta)}{\partial \theta_\mu} = \partial_\mu x_0$:

$$g_{\mu\nu} \simeq \frac{1}{4\sigma_\alpha^2 \Delta x \sigma^2} \frac{\partial_\mu x_0 \, \partial_\nu x_0}{\sigma^2} \int \mathrm{d}x f_\theta(x)^2 (x - x_0(\theta))^2 \tag{3.5}$$

Or, we retrieve here the expression of the Gaussian FIM for a unique observable:

$$G_{\mu\nu} = \frac{\partial_\mu x_0 \, \partial_\nu x_0}{\sigma^2} \tag{3.6}$$

This leads to:

$$g_{\mu\nu} \simeq \frac{G_{\mu\nu}}{4\sigma_\alpha^2 \Delta x \sigma^2} \int \mathrm{d}x f_\theta(x)^2 (x - x_0(\theta))^2 \tag{3.7}$$

Then, as the integral remains to be calculated we start by re-expressing $f_\theta^2$:

$$\begin{aligned} f_\theta(x)^2 &= \frac{1}{\sigma^2 2\pi} e^{(x-x_0(\theta))^2/\sigma^2} \\ &= \frac{1}{\sigma\sqrt{2\pi}} \frac{1}{\sigma\sqrt{2\pi}} e^{(x-x_0(\theta))^2/2(\sigma/\sqrt{2})^2} \\ &= \frac{1}{\sigma\sqrt{4\pi}} \frac{1}{\sqrt{2\pi}\frac{\sigma}{\sqrt{2}}} e^{(x-x_0(\theta))^2/2(\sigma/\sqrt{2})^2} \end{aligned} \tag{3.8}$$

We define $\Sigma = \sigma/\sqrt{2}$,

$$f_\theta(x)^2 = \frac{1}{\sigma\sqrt{4\pi}}\frac{1}{\sqrt{2\pi}\Sigma}e^{(x-x_0(\theta))^2/2\Sigma^2} \tag{3.9}$$

Then, the integral becomes:

$$\begin{aligned} I &= \int \mathrm{d}x f_\theta(x)^2(x-x_0(\theta))^2 \\ &= \frac{1}{\sigma\sqrt{4\pi}}\int \mathrm{d}x \frac{1}{\sqrt{2\pi}\Sigma}e^{(x-x_0(\theta))^2/2\Sigma^2}(x-x_0(\theta))^2 \\ &= \frac{\Sigma^2}{\sigma\sqrt{4\pi}} \\ &= \frac{\sigma}{4\sqrt{\pi}} \end{aligned} \tag{3.10}$$

Finally, the metric becomes:

$$\boxed{g_{\mu\nu} \simeq \frac{G_{\mu\nu}}{16\sqrt{\pi}\sigma_\alpha^2\Delta x\sigma}} \tag{3.11}$$

Thus, for a Gaussian PDF, the Hsu metric is directly proportional to the the single observable Gaussian metric with mean dependency.

### Exponential example

As another example, we consider that $f_\theta(x)$ is an exponential probability density function defined over $\mathbb{R}^+$, whose unique parameter $\lambda$ is a function of $\theta$:

$$f_\theta(x) = \lambda(\theta)e^{-\lambda(\theta)x} \tag{3.12}$$

Here we write the metric $h_{\mu\nu}$

$$\begin{aligned} h_{\mu\nu} &\simeq \frac{1}{\sigma_\alpha^2\Delta x}\int \mathrm{d}x\ \partial_\mu\lambda\ \partial_\nu\lambda\,(1-\lambda x)^2\,e^{-2\lambda x} \\ &\simeq \frac{\partial_\mu\lambda\ \partial_\nu\lambda}{\sigma_\alpha^2\Delta x}\int \mathrm{d}x\left(1-2\lambda x+(\lambda x)^2\right)e^{-2\lambda x} \\ &\simeq \frac{\partial_\mu\lambda\ \partial_\nu\lambda}{\sigma_\alpha^2\Delta x}\left[\int \mathrm{d}xe^{-2\lambda x} - \int \mathrm{d}x2\lambda xe^{-2\lambda x} + \int \mathrm{d}x(\lambda x)^2e^{-2\lambda x}\right] \\ &\simeq \frac{\partial_\mu\lambda\ \partial_\nu\lambda}{\sigma_\alpha^2\Delta x}\left[-\frac{1}{2\lambda} - \frac{2\lambda}{2\lambda} + \frac{1}{4\lambda}\int \mathrm{d}u\ u^2e^{-u}\right] \end{aligned} \tag{3.13}$$

In the last step, we performed a change of variable with $u = 2\lambda x$ for the last integral which is a Gamma function:

$$\int \mathrm{d}u\ u^2e^{-u} = \Gamma(3) \tag{3.14}$$

Or, a property of the Gamma function is:

$$\Gamma(n) = (n-1)! \tag{3.15}$$

Finally, the metric is:

$$h_{\mu\nu} \simeq -\frac{\partial_\mu \lambda \; \partial_\nu \lambda}{\sigma_\alpha^2 \Delta x} \tag{3.16}$$

In addition, it can be shown that the metric associated to an exponential PDF is :

$$H_{\mu\nu} = -\frac{\partial_\mu \lambda \; \partial_\nu \lambda}{\lambda^2} \tag{3.17}$$

Thus, we obtain:

$$\boxed{h_{\mu\nu} \simeq \frac{\lambda^2 H_{\mu\nu}}{\sigma_\alpha^2 \Delta x}} \tag{3.18}$$

Therefore, in both cases, it is feasible to establish an association between the metric computed using the Hsu method and the intrinsic metric of the one-dimensional model.

### A rank one matrix by construction

With this consideration in mind, our objective is to demonstrate that this metric ultimately results in a rank-one matrix. To illustrate this point, we begin with the single Gaussian example $G_{\mu\nu}$:

$$G_{\mu\nu} = \frac{\partial_\mu x_0 \; \partial_\nu x_0}{\sigma^2} \tag{3.19}$$

We define $V$ as the re-scaled partial derivative vector, with $V \in \mathbb{R}^p$:

$$V = \frac{1}{\sigma}(\partial_1 x_0, \partial_2 x_0, \cdots, \partial_p x_0)^t \tag{3.20}$$

Thus the FIM $G$ can be expressed as:

$$G = V \cdot V^t \tag{3.21}$$

Let us demonstrate that G is a rank one matrix. We consider a vector $X \in \mathbb{R}^p$. We have:

$$\begin{aligned} GX &= \left(VV^t\right) X \\ &= V \left(V^t X\right) \end{aligned} \tag{3.22}$$

Since $V^t X$ is a scalar we call it $k$ and write:

$$GX = kV \tag{3.23}$$

From this it follows that if $X$ is an eigenvector of $G$, it must be a multiple of $V$. In other words, the eigenspace of G is:

$$span(X) = \{\alpha V \; , \; \alpha \in \mathbb{R}\} \tag{3.24}$$

Thus, $G$ is a rank-1 matrix whose only eigendirection is $V$.

Naturally, it follows that an exponential metric obtained from Equation 3.18 would yield the same outcome. In conclusion, metrics derived from both a basic Gaussian probability and an exponential probability distribution will exhibit a rank of 1, limiting the amount of information that can be collected from such analyses. This leads us to think that it might be necessary to consider multiple observables in such situations to characterize a system.

### 3.1.2 Eigenspaces sensitivity to the numerical integration

Furthermore, we suppose that one limitation of the numerical analysis of the FIM stems from its sensitivity to the numerical integration method. In this context, we present various techniques for computing the FIM and assess the sensitivity of the resultant eigenspace to numerical parameters. To streamline our analysis, we concentrate on a Gaussian distribution associated with a single observable. Notably, both the mean and the standard deviation of this distribution are products of power laws that involve parameters.

$$f_\theta(x) = \frac{1}{\sigma(\theta)\sqrt{2\pi}} e^{-(x-x_0(\theta))/(2\sigma^2(\theta))}, \text{ with } x_0(\theta) = \prod_i^p \theta_i^{\alpha_i} \ , \ \sigma(\theta) = \prod_i^p \theta_i^{\beta_i} \tag{3.25}$$

$\{\alpha_i\}$ and $\{\beta_i\}$ are generated randomly as integers between 1 and 5. We derive the expression of the FIM, adapting Equation 1.30 to our context:

$$g_{\mu\nu} = \frac{x_0^2 \alpha_\mu \alpha_\nu}{\sigma^2 \theta_\mu \theta_\nu} + 2\frac{\beta_\mu \beta_\nu}{\theta_\mu \theta_\nu} \tag{3.26}$$

To ensure the absence of sloppy parameters, all parameters $\theta_\mu$ were normalized to a value of 1. Consequently, our expectation was that the eigenanalysis would reveal the emergence of two eigenvalues. Following this, we performed an eigenvalue analysis, relying on the exact computation of the FIM with a parameter count of $p = 5$. This analysis yielded two eigenvalues of substantial magnitude (approximately $\approx 10$), accompanied by three eigenvalues of notably smaller values (approximately $\approx 10^{-15}$). It follows logically that our system exhibits two distinct dimensions, aligning with the two parameters that govern the probability distribution $x_0$ and $\sigma$.

#### Numerical integration of the FIM

Using the exact PDF defined above, we performed a numerical integration process of step size d$x$ to calculate the FIM based on:

$$g_{\mu\nu} \simeq -\int \mathrm{d}x f_\theta(x) \frac{\delta \log f_\theta(x)}{\delta\theta_\mu} \frac{\delta \log f_\theta(x)}{\delta\theta_\nu} \tag{3.27}$$

We examined the effects of two key numerical parameters: the differentiation parameter $\delta\theta$ and the integration step d$x$ on the eigenvalues, as depicted in Figure 3.2.

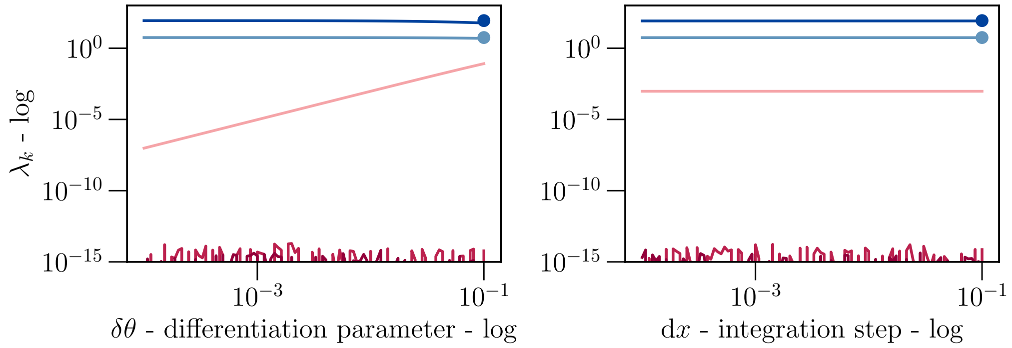

Figure 3.2: Numerical FIM: Eigenvalues as a function of $\delta\theta$ (Left) and d$x$ on (Right). The blue dots are the eigenvalues obtained from the exact FIM analysis. By default $dx$=0.01 and $\delta\theta$=0.01.

Notably, our numerical integration introduced a third eigenvalue with a magnitude on the order of $10^{-3}$ independently of the integration step. Furthermore, it is evident (Left) that the magnitude of this third eigenvalue exhibits a direct correlation with variations in the differentiation parameters, increasing with $\delta\theta$. In essence, these findings strongly suggest that artifacts arising from numerical integration have the potential to yield unexpected eigenvalues.

### FIM obtained from a discrete sampling

Thereafter, we proceeded with the numerical computation of the FIM first sampling the PDF from a Gaussian number generator. In fact, for each parameter $\theta_\mu$, two histograms of size $S$ were generated to compute the required derivative (on $\theta_\mu$ and $\theta_\mu + \delta\theta$. Subsequently, we applied the numerical integration procedure to the sampled distributions. Once again, we examined the influence of the differentiation parameter $\delta\theta$, the integration step $\mathrm{d}x$ as well as the sample size $S$ as depicted in Figure 3.3. Our analysis revealed that the eigenvalues exhibit a strong dependence on the sample size $S$, bin size $dx$, and differentiation step $\delta\theta$ once again revealing the emergence of unexpected high eigenvalues.

Therefore, to mitigate the influence of these unexpected eigenvalues, it becomes imperative to employ a large sample size and carefully balanced values of $\delta\theta$ and $\mathrm{d}x$ allowing for a trade-off between the precision of the leading eigenvalues and the vanishing of the others. Consequently, this underscores the necessity for a methodology to obtain a precise FIM in the presence of finite sampling and numerical integration. With this objective in mind, it is worth noting that obtaining the entire global shape variation of the PDF may not be an essential requirement, as one might consider primarily capturing the principal changes in the PDF with respect to parameters, specifically focusing on mean and variance.

This consideration leads us to contemplate that for PDFs closely resembling Gaussians, the FIM for the overall system could be approximated as the one of a multivariate Gaussian distribution, as delineated in Equation 1.30, which we reiterate here:

$$[\mathbf{I}(\theta)]_{i,j} = \frac{\partial \boldsymbol{\mu}^{\mathsf{T}}}{\partial \theta_i} \boldsymbol{\Sigma}^{-1} \frac{\partial \boldsymbol{\mu}}{\partial \theta_j} + \frac{1}{2} \operatorname{Tr}\left( \boldsymbol{\Sigma}^{-1} \frac{\partial \boldsymbol{\Sigma}}{\partial \theta_i} \boldsymbol{\Sigma}^{-1} \frac{\partial \boldsymbol{\Sigma}}{\partial \theta_j} \right) \tag{3.28}$$

Indeed, drawing from our previous findings, we aim to underscore the importance of handling multiple observables (which implies working with multivariate distributions) in order to circumvent the emergence of rank-1 matrices.

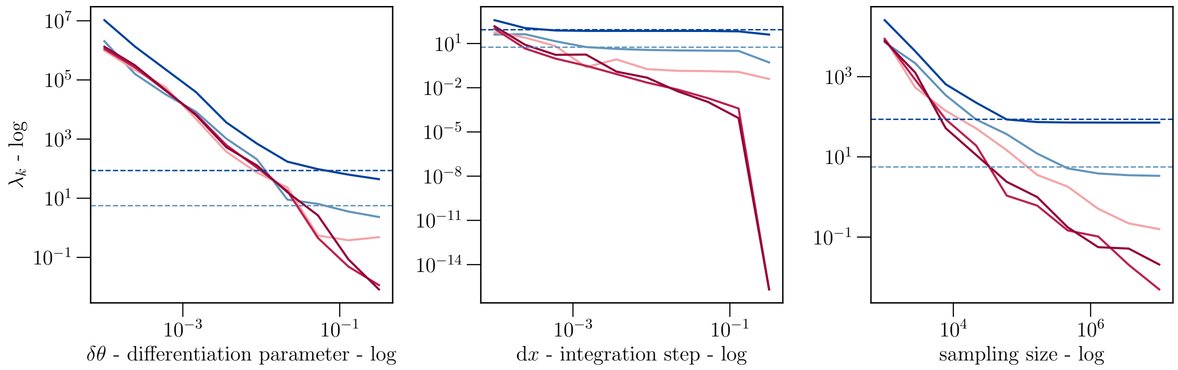

Figure 3.3: Sampling FIM: Eigenvalues as a function of $\delta\theta$ (Left) and $\mathrm{d}x$ on (Right). The dotted-lines represent the eigenvalues obtained from the exact FIM analysis. By default $dx = 0.01$, $\delta\theta = 0.01$ and $S = 100000$

Hence, the FIM is just dependent on variations of the mean and of covariance that are numerically easy to track:

$$\begin{aligned}\frac{\partial \boldsymbol{\mu}}{\partial \theta_j} &\simeq \frac{\delta \boldsymbol{\mu}}{\delta \theta_j}\\ \frac{\partial \boldsymbol{\Sigma}}{\partial \theta_i} &\simeq \frac{\delta \boldsymbol{\Sigma}}{\delta \theta_i}\end{aligned} \tag{3.29}$$

Furthermore, by incorporating a covariance correction to disentangle information, this approach offers the added benefit of accounting for correlations between observables. Consequently, it becomes feasible to investigate observables that do not exhibit scaling behavior akin to energies or kinetic rates.

### 3.1.3 Gaussian FI as a limit of the Gamma FI

Nonetheless, while the Gaussian approximation appears promising, it is prudent to assess its consistency when dealing with a skewed and peaked distribution. In this context, we examine the Fisher information (FI) for a one-dimensional problem, specifically focusing on the example of a Gamma distribution. We estimate the divergence between the FI of the Gamma distribution and the Gaussian FI with the same mean and variance, as a function of the skew parameter. Our objective is to gauge to what extent skewed distributions can be approximated as Gaussian distributions in the low skewness limit. Naturally, we anticipate that the ratio will approach 1 as the skewness parameter approaches zero.

Let us define $f_\theta(x)$ and $h_\theta(x)$, respectively Gaussian and Gamma PDF.

$$f_\theta(x) = \frac{e^{(x-x_0(\theta)/(2\sigma^2)}}{\sqrt{2\pi\sigma^2}} \tag{3.30}$$

$$h_\theta(x) = \frac{x^{k(\theta)-1} e^{-x/\Lambda(\theta)}}{\Gamma(k(\theta))\Lambda(\theta))^{k(\theta)}} \tag{3.31}$$

With $k$ the shape parameter and $\Lambda$ the scale parameter. We recall the definition of the $\Gamma$ function:

$$\Gamma(x) = \int_0^{+\infty} \mathrm{d}t\ t^{x-1} e^{-t} \tag{3.32}$$

In order to ensure that both probability distributions will have same mean and variance, we specify:

$$\begin{aligned}k &= \frac{x_0^2}{\sigma^2}\\ \Lambda &= \frac{\sigma_2}{x_0}\end{aligned} \tag{3.33}$$

For both distributions the FI is:

$$\begin{aligned}I_f(\theta) &= -\frac{x_0'(\theta)^2}{\sigma^2}\\ I_g(\theta) &= \frac{x_0'(\theta)^2\left[3\sigma^2 - 4\psi^1(x_0(\theta)^2/\sigma^2)x_0(\theta)^2\right]}{\sigma^4}\end{aligned} \tag{3.34}$$

With $\psi^m(z)$, the polygamma function defined as:

$$\psi^m(z) = \frac{\mathrm{d}^{m+1}}{\mathrm{d}z^{m+1}} \ln \Gamma(z) \tag{3.35}$$

Then, we can rewrite this as a function of the skewness $s$:

$$s = \frac{2}{\sqrt{k}} \tag{3.36}$$

Thus the ratio between Gaussian and Gamma information is:

$$\boxed{\eta(s) = -3 + \frac{16\psi^1\left(\frac{4}{s^2}\right)}{s^2}} \tag{3.37}$$

In Figure 3.4 (Right), we plot the ratio $\eta$ as a function of the skew $s$. As expected, as $s$ goes to 0, the Gamma FI converges to the Gaussian FI.Thus, this result supports the idea that the effective Gaussian approach is appropriate in the low skew regime. In the appropriate context, we insist on its promising interest to capture main cumulants variations despite finite sampling.

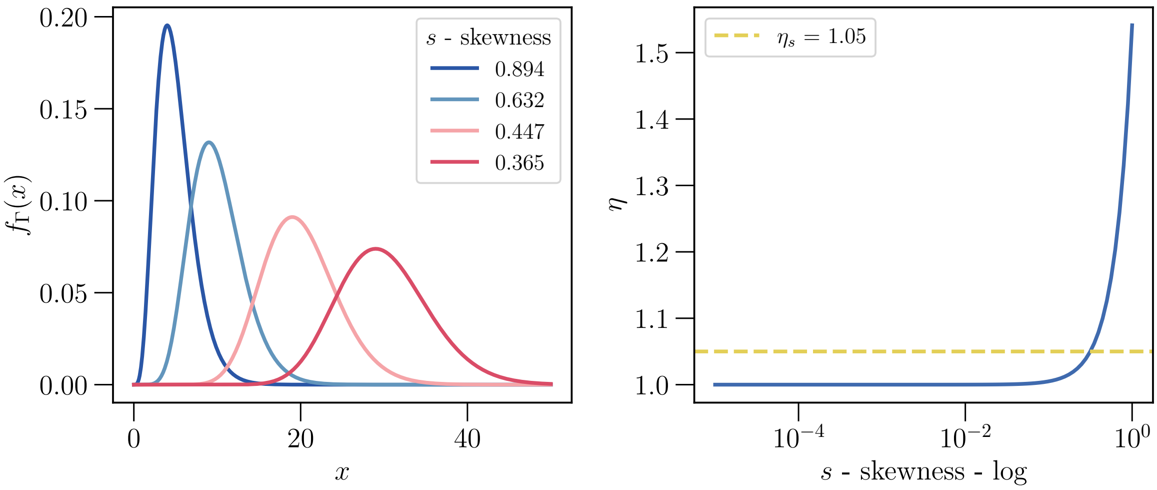

Figure 3.4: (Left) Plot of different PDF $f_\Gamma(x)$ for various skewness values $s$. (Right) Ratio of FI $\eta(s)$ as a function of skewness $s$ in log scale. We arbitrarily plot $\eta_s = 1.05$ as a transition threshold.

## 3.2 Introducing a local Gaussian approach for numerical PSC

In the end, we aim to conclude this section by introducing our own approach of numerical PSC. To compute the Fisher Information Matrix, we adopt an approach that presumes the local Gaussian behavior of our observables. This Gaussian assumption is considered suitable because it effectively captures the primary alterations in the probability density function, mainly the mean and variance, without assuming significant changes in its shape.

In particular, we aim to quantify the impact of the add of an observable to the eigenspace of the system. Before presenting a simple geometrical interpretation let us derive the iteration process computations.

### 3.2.1 Iteration process

As first hypothesis, we assume that the covariance matrix does not depend on the vector parameter $\theta$ : $\mathbf{X}_k \sim \mathcal{N}_k(\boldsymbol{\mu_k}(\theta), \boldsymbol{\Sigma}_k)$. Here $\mathbf{X}_k$ is a random vector of size $k$ which accounts for $k$ observables.

We start from the definition of the FIM:

$$[\mathbf{I}(\theta)]^k_{i,j} = \frac{\partial \boldsymbol{\mu}^{k,\mathsf{T}}}{\partial \theta_i} \boldsymbol{\Sigma}^{-1,k} \frac{\partial \boldsymbol{\mu}^k}{\partial \theta_j} \tag{3.38}$$

Then, we would like to know what happens to the FIM when we increase the size of the vector by adding one observable: $\mathbf{X}_{k+1} \sim \mathcal{N}_{k+1}(\boldsymbol{\mu_{k+1}}(\theta), \boldsymbol{\Sigma}_{k+1})$, which can be expressed as:

$$\mathbf{X}_{k+1} = \mathbf{X}_k + X_{k+1} \cdot \mathbf{e_{k+1}} \tag{3.39}$$

After performing calculations, we obtained for $[\mathbf{I}(\theta)]^{k+1}_{i,j}$:

$$[\mathbf{I}(\theta)]^{k+1}_{i,j} = [\mathbf{I}(\theta)]^k_{i,j} + \sum_{l=1}^{k} \sigma^{-1}_{l,k+1} \left[ \frac{\partial \mu^l}{\partial \theta_i} \frac{\partial \mu^{k+1}}{\partial \theta_j} + \frac{\partial \mu^l}{\partial \theta_j} \frac{\partial \mu^{k+1}}{\partial \theta_i} \right] + \sigma^{-1}_{k+1,k+1} \frac{\partial \mu^{k+1}}{\partial \theta_i} \frac{\partial \mu^{k+1}}{\partial \theta_j} \tag{3.40}$$

In the special case when there is no covariance between our random variables, we get :

$$\boxed{[\mathbf{I}(\theta)]^{k+1}_{i,j} = [\mathbf{I}(\theta)]^k_{i,j} + \frac{\partial \mu^{k+1}}{\partial \theta_i} \frac{\partial \mu^{k+1}}{\partial \theta_j} \sigma^{-1}_{k+1,k+1}} \tag{3.41}$$

From the previous result, we can extrapolate that the FIM of the whole vector can be expressed as the sum of the FIM for each random variable as a first approximation.

$$\mathbf{I}(\theta) = \sum_{l=1}^{k} \mathbf{I}^l(\theta) \tag{3.42}$$

Intuitively even though the previous results relies on a strong approximation we presume that it provides a great sensation of what is stake. Basically, by adding a new observable we load the global FIM with its associated information. Covariance weights the information increase.

### 3.2.2 Geometrical interpretation of sensitivity modes

The analysis of the eigenvectors and corresponding eigenvalues of the FIM unveils the hierarchical structure of sensitivity modes within parameter space aiding in the discrimination between stiff and sloppy directions.

Here, we propose a straightforward geometric analysis of our methodology. First, let us consider a single Gaussian observable, where the primary influence is associated with variations of its mean. For the sake of simplicity, we neglect the impact of variance dependency on parameters. In this context, and as previously discussed in subsection 3.1.1, the system is associated to a single direction in the parameter space, represented by the vector $v_1$ in Figure 3.5. Now, if we introduce another observable, it can either reinforce the existing direction, generate a new direction represented by $v_2$ or induce a rotation in the system. As we accumulate more observables, our objective is to obtain the proper basis of the biophysical system within the parameter space. In the following chapter we detail on our results concerning this numerical PSC procedure applied to our branched actin system.

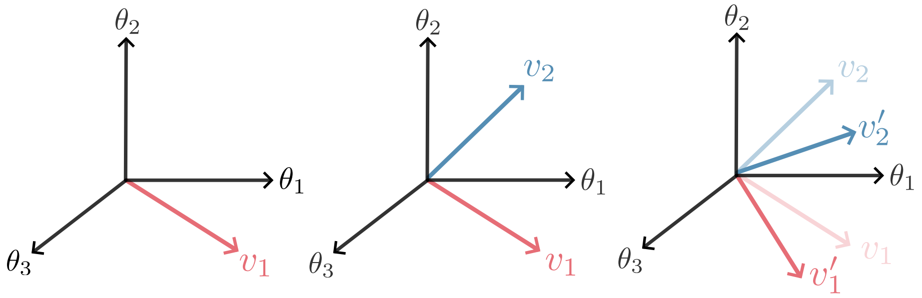

Figure 3.5: The addition of a new observable to the FIM can lead to the appearance of a new sensitivity mode $v_2$ or to the rotation of the overall basis.

# Chapter 4

# Application to our branched actin system

## 4.1 Simulation model

### 4.1.1 Setup

Here, we introduce the branched actin system to which we have applied numerical PSC. This system closely resembles the one studied in the first part of the thesis (refer to subsection 5.2 for a detailed description), with a few minor variations. However, a significant modification lies in the use of a dashpot with a constant drag coefficient denoted as $\gamma_0$ as opposed to the AFM used previously. The simulation model is schematically represented in Figure 4.1. A example on configuration file is proposed in Appendix B.2.1. In addition, it is worth noting that we conducted this study prior to the work presented in the first part of the thesis, when the numerical AFM had not yet been implemented. Nevertheless, the dashpot offers the advantage of simplicity, as it can be adjusted with a single parameter to monitor $\gamma_0$ (refer to subsection 5.2.1 for a comparison).

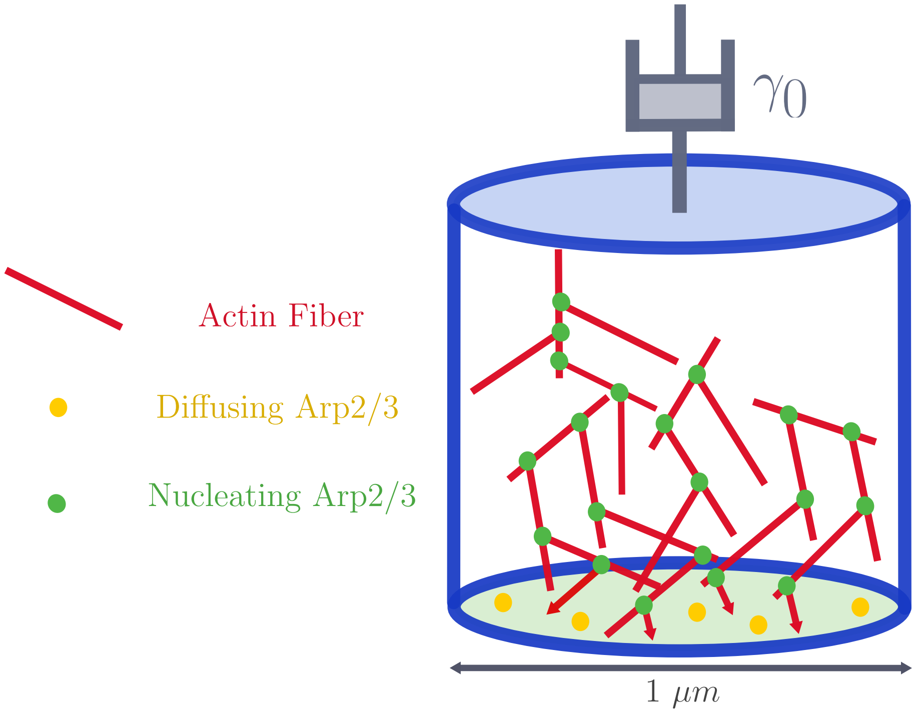

Figure 4.1: Scheme of the simulation system: A branched actin network is growing from the bottom and facing a constant drag $\gamma_0$.

For the sake of simplicity, we used infinite stall force fibers ($f_s = \text{inf pN}$) with a constant velocity of $v_{pol} = 1$ $\mu$m.s$^{-1}$. While we did not include the stall force $f_s$ in our sloppiness analysis, we believe it could have served as an judicious bridge between the two parts of the thesis. Additionally, $K_{conf}$ was set to 100 pN.$\mu$m$^{-1}$, with the understanding that its parameter value is not as critical in this setup as there is no involvement of an AFM. The steric stiffness $K_{steric}$ was configured at 400 pN.$\mu$m$^{-1}$, which, while still acceptable, should be elevated to enhance the relevance and precision of our results. Notably, our situation can be likened to the one depicted in Figure 5.6, as we encountered induced stresses $\sigma$ on the order of 600 Pa. This adjustment in $K_{steric}$ accounts for the overall reduction in velocity compared to the first part of the study. As expected, the growth of the network induces the motion of the piston at a constant velocity after a brief exponential transition period, as illustrated in Figure 4.2 (Right). In essence, the dynamics of the piston is governed by:

$$\begin{aligned} F_{Actin} &= \gamma_0 v_s \\ \iff \sigma_0 S &= \gamma_0 v_s \end{aligned} \tag{4.1}$$

The value of $\gamma_0$ was intentionally set to a relatively high value, approximately 5000 pN.s.$\mu$ m$^{-1}$, to effectively neglect the influence of network drag, denoted as $\gamma_{net}$. Our study revealed that the contribution of $\gamma_{net}$ did not surpass 300 pN.s.$\mu$m$^{-1}$, as illustrated in Appendix B.2.2, Figure B.1.

### 4.1.2 Observables estimation

Our study focused on a set of five parameters and four observables. The parameters under consideration are as follows: the Arp2/3 adding rate $k_{Arp2/3}$, the drag coefficient of the dashpot $\gamma_0$, the length of actin fibers $\ell_0$, the bending rigidity of the fibers $\kappa$, and the radius of the fiber $r_0$. We posit that all these parameters collectively determine the mechanics of the actin network. From our investigation, we aimed to extract the following observables: the velocity $v_s$, the stationary density $\rho_s$, the applied stress $\sigma_0$ and an elastic response modulus Y.

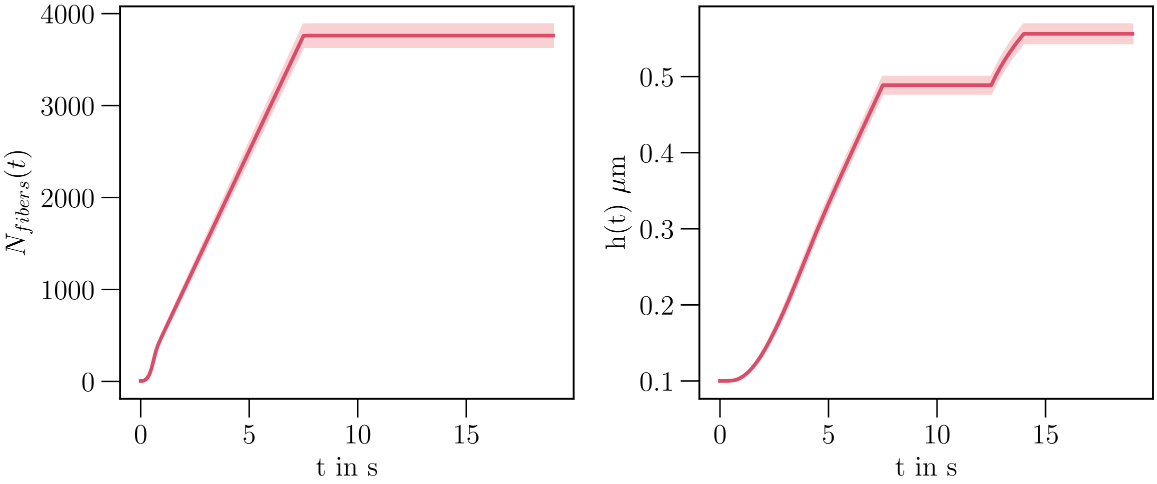

Figure 4.2: (Left) Number of fibers $N_{fibers}$ and height $h(t)$ (Right) as a function of time. The thick line is the mean value obtained over 300 simulations with small $k_{Arp2/3}$ variation. The shaded area delimits the standard deviation.

The following table presents the original values of our parameters:

| $k_{Arp2/3}$ | $\gamma_0$ | $\ell_0$ | $\kappa$ | $r_0$ |
|---|---|---|---|---|
| 500 $s^{-1}$ | 5000 pN.s.$\mu$m$^{-1}$ | 0.3 $\mu$m | 0.004 pN.$\mu$m$^2$ | 0.005 $\mu$m |

We let the system grow, and after $\tau_1 = 7.5$ seconds, we froze it by setting $\gamma$ to infinity, which effectively halts growth. Simultaneously, we set $k_{Arp2/3}$ to 0, which stopped the addition of new fibers, as illustrated in Figure 4.2. After 5 seconds, at $\tau_2 = 12.5$ seconds, we allowed the network to relax by resetting $\gamma_0$ to its initial value. Finally, at $\tau_3 = 14.5$ seconds, we returned to the infinite drag condition. In Appendix B.2.2, Figure B.1 we illustrate the evolution of the stored elastic energy all along these steps. Elastic relaxation is explicit here. In the initial phase, we determined the stationary velocity $v_s$ through a linear fit, as well as the applied stress $\sigma$ (according to Equation 4.1). Naturally, we expect these observables to provide the same information.

Figure 4.3 displays the evolution of density and force throughout these steps. The density $\rho$ rapidly increases before reaching its steady-state value. This value remains constant during the stall phase but exponentially decreases when $\gamma_0$ is reset to its initial value before stabilizing at a new plateau. From the first plateau we extract the stationary density value $\rho_s$. A similar behavior is observed for the measured Force F. Based on this data, we extract an estimation of the elastic modulus Y. Below, we elaborate on our method, which is derived from a minimalist elastic model.

### An elastic modulus measurement

During the relaxation step, we assume that the primary response of our network is elastic. As a result, we propose the following linear Hookean elastic model, which possesses the advantage of diverging for compressive forces.

$$F = -YS\left(\frac{\ell - \ell_0}{\ell_0}\right) \tag{4.2}$$

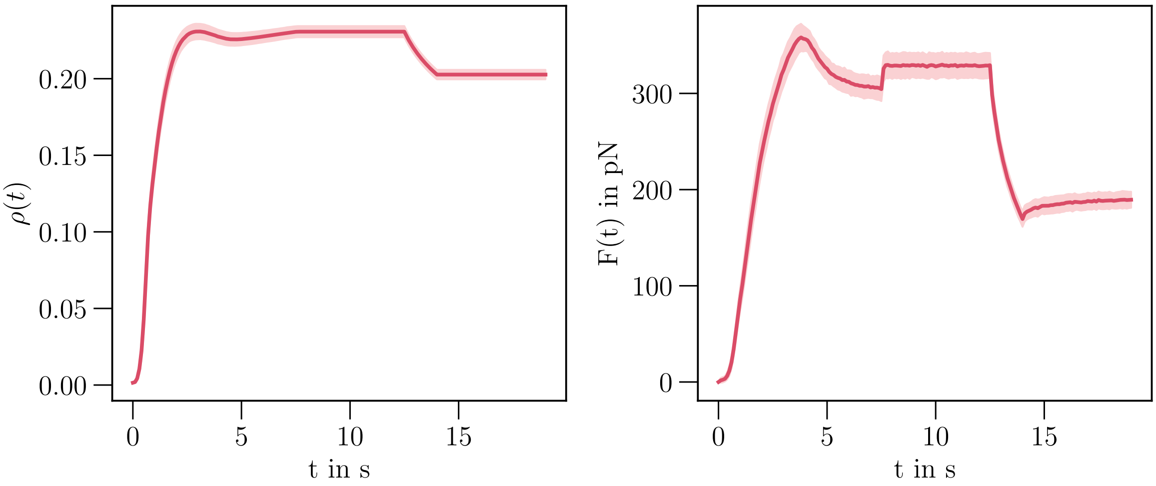

Figure 4.3: (Left) Density $\rho(t)$ and force F (Right) as a function of time. The thick line is the mean value obtained over 300 simulations with small $k_{Arp2/3}$ variation. The shaded area delimits the standard deviation.

Thus, from the two previous Figures (4.2, 4.3) we obtain the following system with the two set ($\ell_1$,$F_1$) and ($\ell_2$,$F_2$) one for each stall phase:

$$\begin{cases} F_1 = -YS\left(\dfrac{\ell_2 - \ell_0}{\ell_0}\right) \\ F_2 = -YS\left(\dfrac{\ell_2 - \ell_0}{\ell_0}\right) \end{cases} \tag{4.3}$$

Hence, with this two points it is possible to estimate the value of Y:

$$\boxed{Y = \frac{F_2 - F_1\left(\frac{\ell_1}{\ell_2}\right)}{S\left(\frac{\ell_1}{\ell_2} - 1\right)}} \tag{4.4}$$

We obtained modulus of the order of 1 kPa, which is accordance with the experimental studies on branched actin mechanics that we discussed in subsection 2.3.2, [86] [87] [89]. Having outlined our method for estimating the relevant observables, we proceed to assess the statistical consistency of our stochastic simulations.

## 4.2 Results

In this section, our objective is to compute the Gaussian FIM for our system under the assumption that variance modifications are neglected:

$$g_{\mu\nu} = \frac{\partial \boldsymbol{\mu}^{\mathsf{T}}}{\partial \theta_\mu} \boldsymbol{\Sigma}^{-1} \frac{\partial \boldsymbol{\mu}}{\partial \theta_\nu} \tag{4.5}$$

We first check the consistency of our estimation of $\boldsymbol{\mu}$, before dealing with $\boldsymbol{\Sigma}$.

### 4.2.1 Estimation of the PDF

In Figure 4.4 (Left), we present the histogram estimation for the PDF of the velocity for our actin system, with a higher value of $k_{Arp2/3}$ at 2000 $s^{-1}$. We conducted the same stochastic simulation a thousand times, resulting in a thousand different estimations of the stationary velocity $v_s$. Additionally, we fitted a Gaussian PDF to the data.

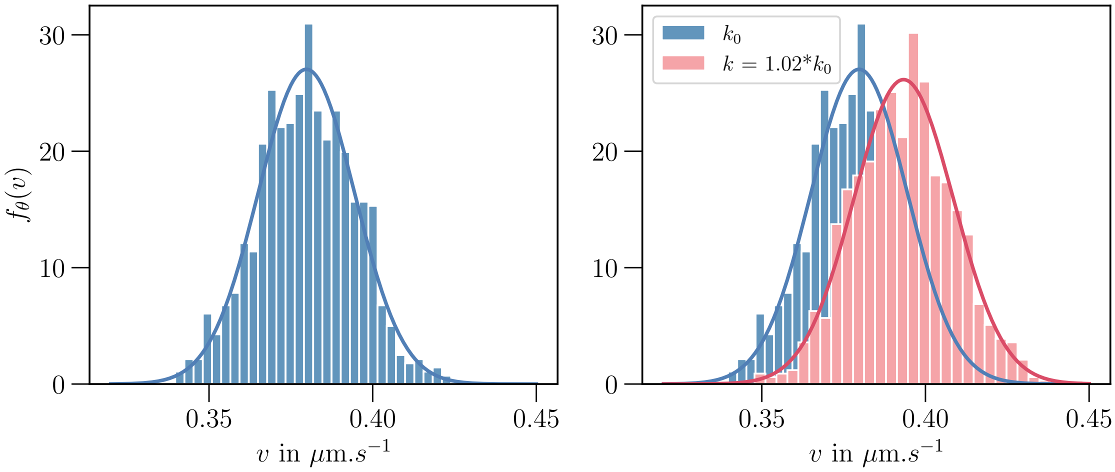

Figure 4.4: (Left) Histogram and Gaussian fit for the PDF $f_\theta(v)$. (Right) Effects of a shift of 2% on $k_{Arp2/3}$ on the PDF with $k_0$ 2000 $s^{-1}$.

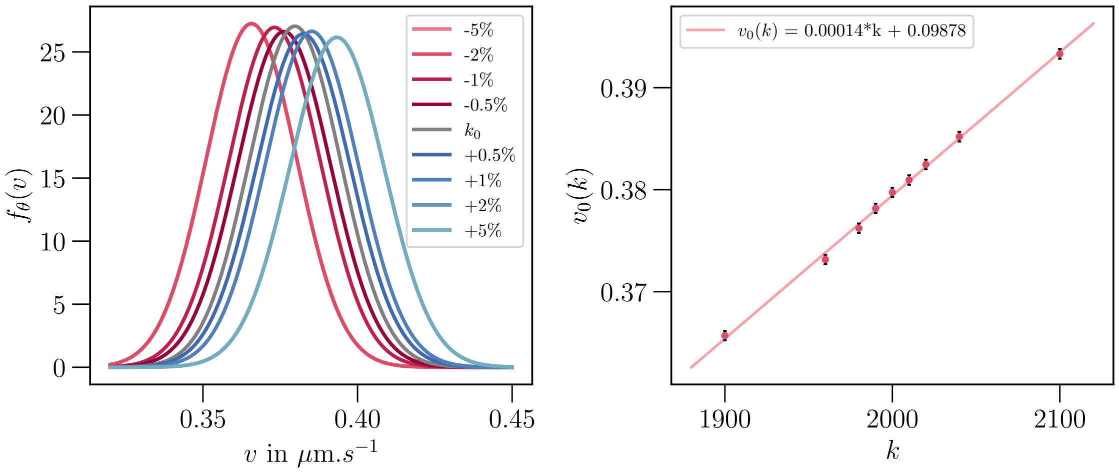

Figure 4.5: (Left) Multiple Gaussian Fit of shifted PDF for various $k_{Arp2/3}$ modifications. (Right) Mean value of the Gaussian as a function of the value of $k_{Arp2/3}$, with a linear fit. Small black lines are the standard error of the mean (SDEM).

Consequently, the Gaussian hypothesis aligns well with the displayed data. When we introduce a small variation in $k_{Arp2/3}$ by increasing its value by 2%, we observe a significant shift in the mean of the PDF with minimal alteration to its variance, further reinforcing our confidence in our primal hypothesis. We conducted similar simulations with shifts in the range of [-5%, +5%] and fitted the resulting histograms with Gaussian PDFs. The various Gaussian shapes are presented in Figure 4.5 (Left), and the corresponding mean values as a function of $k_{Arp2/3}$ are shown on the right side of the figure. Consequently, from this plot, it is straightforward to extract the slope, which corresponds to the first partial derivative of the mean:

$$\frac{\partial v_0}{\partial k} \approx \frac{\delta v_0}{\delta k} \tag{4.6}$$

Nonetheless, it is important to note that this technique demands a considerable number of simulation points to obtain the mean of the Gaussian $v_0(k)$ for various values of $k$. Despite this drawback, we chose to maintain the [-5%, +5%] interval around the central parameter point as a reasonable variation range for estimating the first-order derivative. In the subsequent section, we introduce our more computationally efficient method for estimating mean and covariance.

### 4.2.2 Partial derivative and covariance estimation

We transitioned to a broader sampling approach by simulating the system for random points within the [-5%, +5%] range. More precisely, we randomly selected one parameter within the [-5%, +5%] range around its initial value while keeping the others constant (as shown in Table 4.1.2) to calculate partial derivatives. For each parameter, we conducted 300 simulations, recorded the associated observable values ($v_s$, Y, $\rho_s$, and $\sigma$), and fitted the data using a linear model. Consequently, we obtained partial derivatives for all pairs of observables and parameters. Figure 4.6 depicts scatter plots illustrating the relationship between observables and variations in $\overline{k_{Arp2/3}}$ (where $\overline{k_{Arp2/3}} = k_{Arp2/3}/S$). We performed a series of bootstrap tests on the slope evaluations for each observable parameter couple, to quantify the variance of the estimation. We based our analysis on 300 bootstrap samples. The results are presented as a boxplot in Figure 4.7 for the $k_{Arp2/3}$ case.

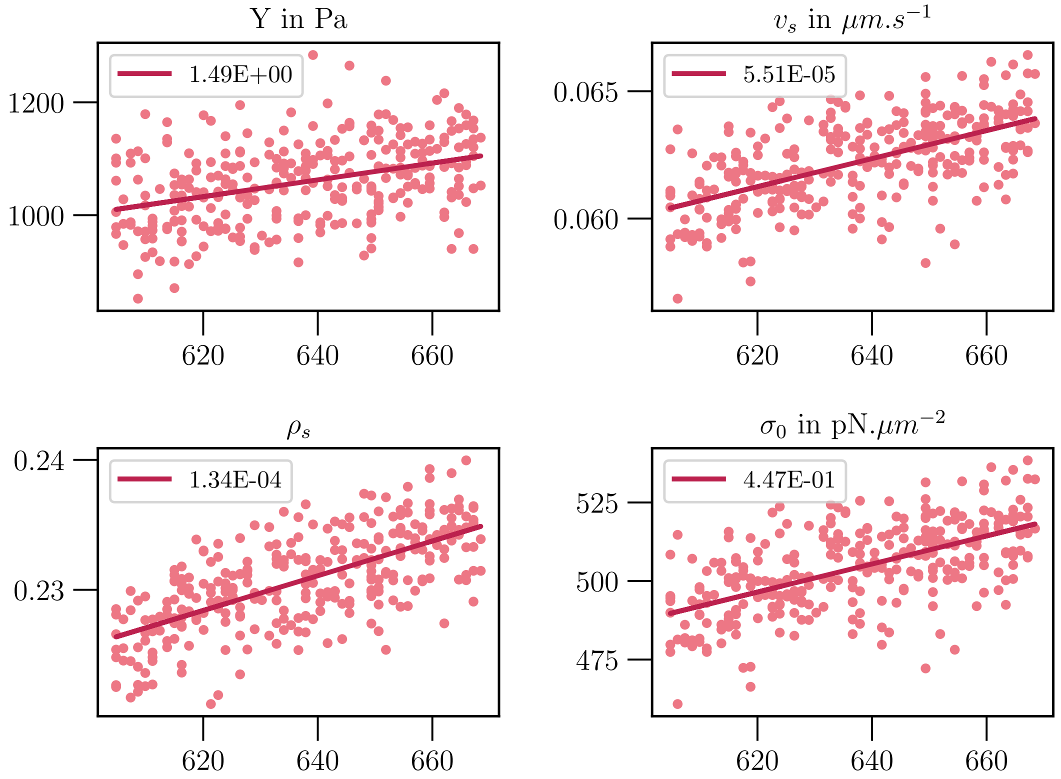

Figure 4.6: Scatters plots of observables values as a function of $\overline{k_{Arp2/3}}$ ($k$) in s$^{-1}$.$\mu$m$^{-2}$. The thick line is obtained through a local linear fit which provides the slope.

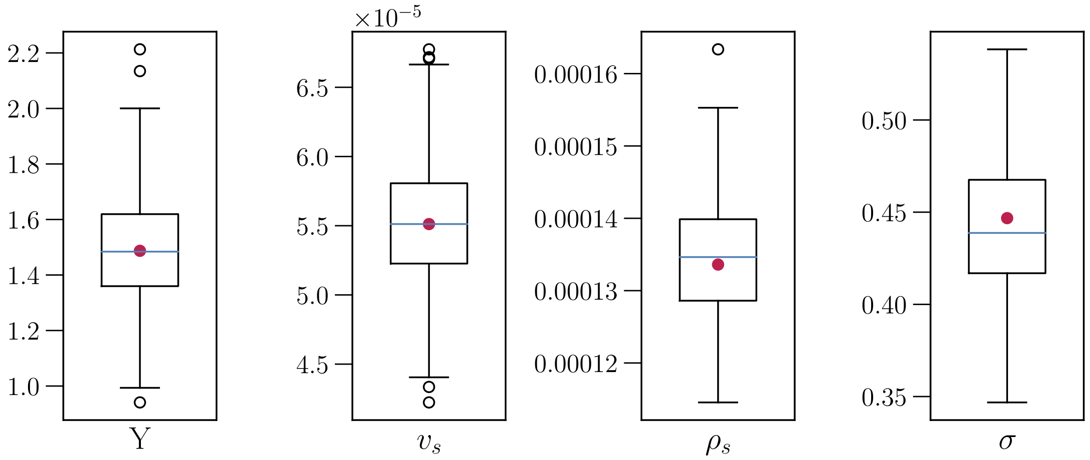

Figure 4.7: Bootstrap test on the different slopes estimation for the $k_{Arp2/3}$ parameter. The red dot is the original value.

Now, we proceed with the calculation of the covariance matrix $\boldsymbol{\Sigma}$ to ultimately derive $g_{\mu\nu}$ (Equation 4.5). Let us examine the covariance between an observable $X_i$ and another observable $X_j$ (e.g., Y and $v_s$). With $N$ simulation points, we can obtain an unbiased estimator for the term $\boldsymbol{\Sigma}_{i,j}$ in the covariance matrix $\boldsymbol{\Sigma}$:

$$\boldsymbol{\Sigma}_{i,j} = \frac{1}{N-1} \sum_{k=1}^{N} \left(X_{i,k} - \boldsymbol{\mu}_i\right) \left(X_{j,k} - \boldsymbol{\mu}_j\right) \tag{4.7}$$

Here, $X_{i,k}$ represents an output of the random variable $X_i$ (e.g., one data point for $v_s$), and $\boldsymbol{\mu}_i$ is the mean value of $X_i$. We applied this method to the five sets of simulations, resulting in five covariance matrices. We then calculated the average of these covariance matrices, we used this one as estimator for $\boldsymbol{\Sigma}$. While this approach may neglect slight variations induced by changes in parameters, we assume that covariance does not depend on the parameters. In Figure 4.8, we plot the normalized distance between the averaged covariance matrix $\boldsymbol{\Sigma}$ and the one associated to each observable $\boldsymbol{\Sigma}_u$. This plot comforts us in our mean covariance hypothesis. This quantity is written as:

$$d(\boldsymbol{\Sigma}, \boldsymbol{\Sigma}_u) = \frac{||\boldsymbol{\Sigma} - \boldsymbol{\Sigma}_u||}{||\boldsymbol{\Sigma}||} \tag{4.8}$$

With:

$$||\boldsymbol{\Sigma}|| = \sqrt{\sum_{i=1}^{n} \sum_{j=1}^{n} \left(\boldsymbol{\Sigma}_{i,j}\right)^2} \tag{4.9}$$

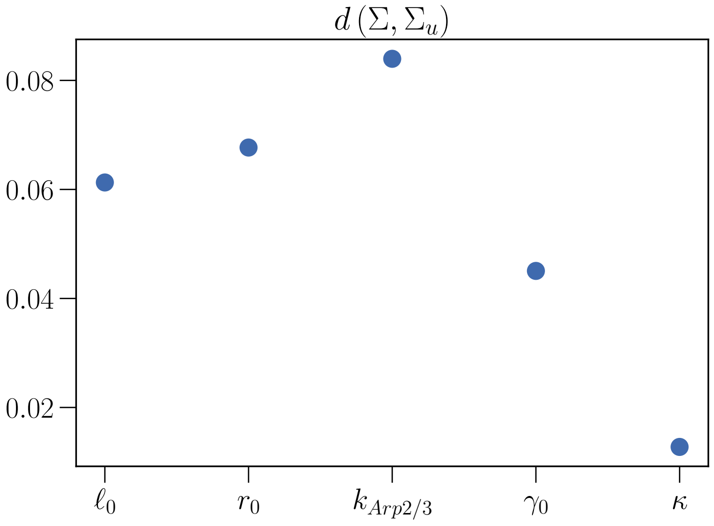

Figure 4.8: Normalized distance between the averaged covariance matrix $\boldsymbol{\Sigma}$ and the one associated to each observable $\boldsymbol{\Sigma}_u$.

Therefore, we have extracted partial derivatives and estimated covariance, for our FIM computation. Data related to shifts and bootstrap tests in other parameters can be found in Appendix B.2.3. With these preparations completed, we now move on to compute the FIM, and in the next section, we will present the results and provide interpretations based on eigen-analysis.

### 4.2.3 Eigen-analysis

Firstly, we computed the FIM for individual observables, and as anticipated, we obtained one-dimensional (1D) eigen-spaces. Figure 4.9 illustrates the eigenvalue rankings on a logarithmic scale for each observable. In all cases, only one dominant direction emerges in the phase space

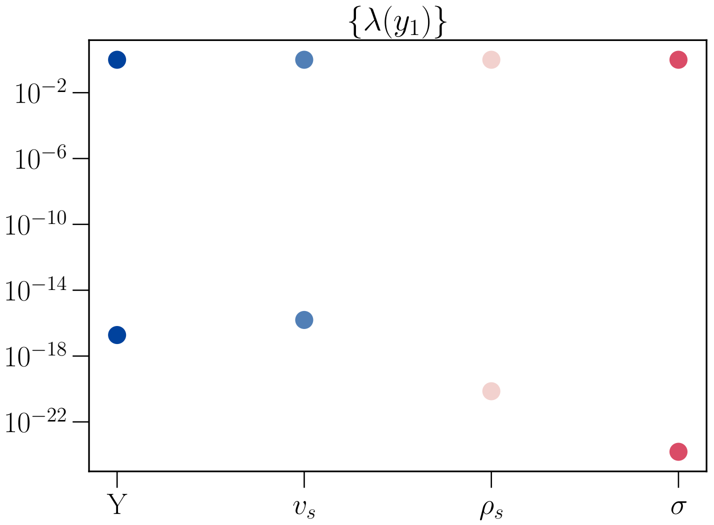

Figure 4.9: Ranking of the eigenvalues of the FIM computed for single observables. VValues have been re-scaled by the highest eigenvalue.

Therefore, we expanded our analysis by computing the FIM for different combinations of observables, merging two and three of them before computing the total FIM. Figure 4.10 displays the results of our eigenvalue rankings. In most cases, a single dominant direction is followed by a rather distant one. It becomes evident that our system can primarily be characterized by a single compressed parameter. Therefore, we assume that most of what follows in this result can be interpreted as noise or less significant information.

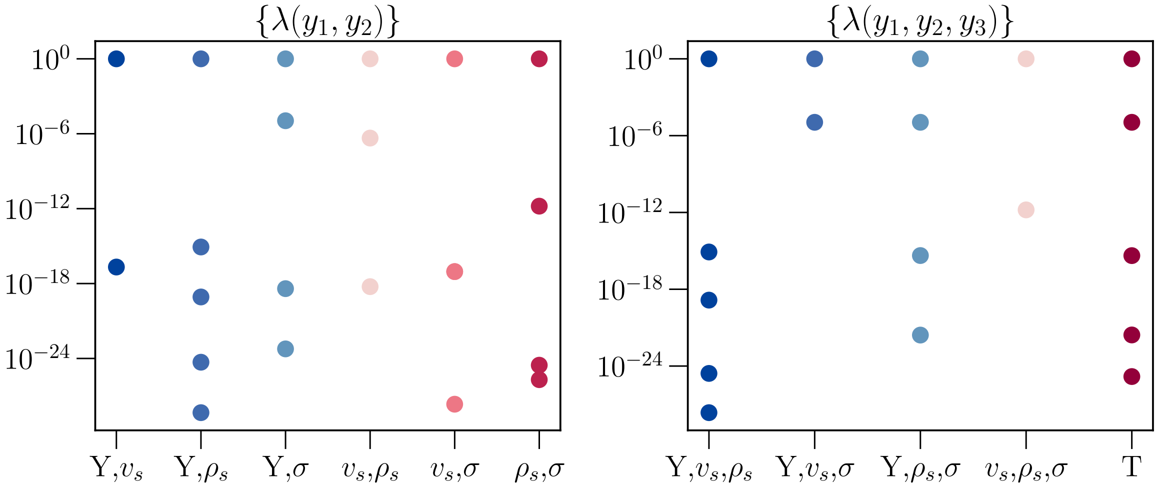

Figure 4.10: Ranking of the eigenvalues of the FIM computed for two (Left) and three (Right) combined observables. The combination of all observables is designated as T. Values have been re-scaled by the highest eigenvalue.

However, as a second eigenvalue appears to emerge from the ground ensemble, we have decided to take it into account in the following analysis. In Figure 4.11, we present the normalized projection of individual observable eigenvectors $u_i$ onto the first and second eigenvectors $w_{\lambda_1}$ and $w_{\lambda_2}$. Projections are calculated using a simple scalar product between the two vectors of interest. Consequently, individual sensitivity modes are mostly oriented along the same direction, the main mode of the system. This observation further reinforces the dominance of a single compressed parameter in characterizing the system's behavior.

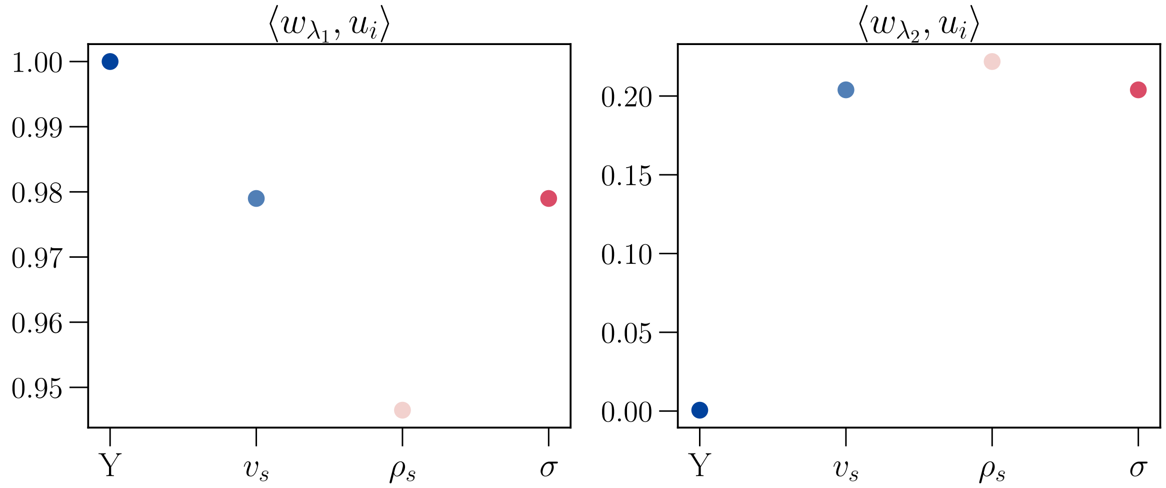

Figure 4.11: (Left) Scaled scalar product between the first eigenvector of the system $w_{\lambda_1}$ and the first eigenvector associated to a single a observable $u_i$. (Right) Same plot for the second eigenvector of the system $w_{\lambda_2}$.

In Figure 4.12, we illustrate the decomposition of the two main eigenvectors, $w_{\lambda_1}$ and $w_{\lambda_2}$, in terms of the percentage contribution of our initial parameters. It appears that a combination of $r_0$ and $\kappa$ plays a dominant role in determining the behavior of our system in the phase space. In the next paragraph, we will aim to develop a simple analytical model which confirms our one dimension space eigen-space.

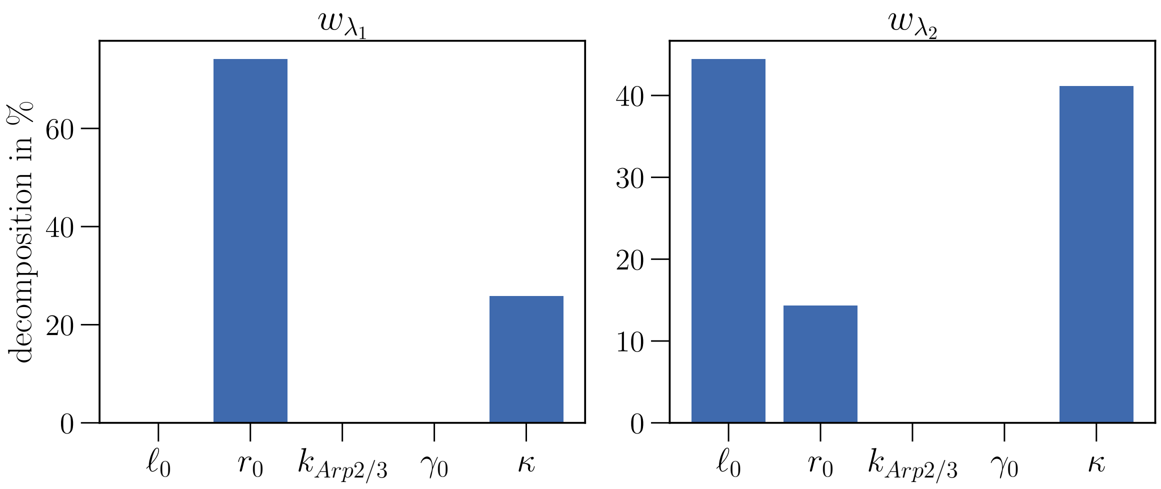

Figure 4.12: Decomposition in percentage of the initial parameters of the two main eigenvectors $w_{\lambda_1}$ (Left) and $w_{\lambda_2}$ (Right).

### 4.2.4 Analytical solution

During the growth phase, the balance of stresses leads to the following equation:

$$\sigma_0 S = \gamma_0 v_S \tag{4.10}$$

In addition as $f_s$ is infinite, the flux of actin is conserved which induces:

$$j = \rho_s v_s \tag{4.11}$$

Besides, $j$ the density of flux of actin can be expressed as the volume of actin entering the system per unit of time:

$$j = \frac{\pi k_{Arp2/3} \ell_0 r_0^2}{S} \tag{4.12}$$

Thus, by mixing (4.10), (4.11) and (4.12), we get:

$$\sigma_0 = \frac{\pi k_{Arp2/3} \ell_0 r_0^2 \gamma_0}{\rho_s S^2} \tag{4.13}$$

Moreover, we can add to this entanglement mechanical equations that predict the scalings of $\rho_s$ and Y, as discussed in the previous part in section 4:

$$\begin{aligned} \rho_s &= b^{8/7} \kappa^{-2/7} \sigma_0^{2/7} \\ Y &= b^{-4/7} \kappa^{1/7} \sigma_0^{6/7} \end{aligned} \tag{4.14}$$

Thus, we finally obtain the following scaling for $\sigma_0$:

$$\boxed{\sigma_0 \sim (\ell_0 k \gamma_0)^{7/9} r_0^{6/9} \kappa^{2/9}} \tag{4.15}$$

Afterwards, it is, to an exception, possible to express the other observables as a function of $\sigma$ and of an other parameter $\alpha$:

$$\begin{aligned} v_s &= \frac{\sigma_0}{\gamma_0} \\ \rho_s &= \frac{\alpha}{\sigma_0} \\ Y &= \frac{\sigma_0^{3/2}}{\sqrt{\alpha}} \end{aligned} \tag{4.16}$$

With $\alpha$ defined as:

$$\boxed{\alpha = k r_0^2 \ell_0 \gamma_0} \tag{4.17}$$

Thus, we have nearly assessed the inner dimensionnality of our system. However, it is important to note that this particular setting of compressed parameters is just one among many others, and it cannot be directly used to compare with the directions resulting from the FIM analysis. Performing such a comparison would indeed require a more elaborate analysis that we have not undertaken. We address this point in the discussion that follows.

# Conclusion

Let us summarize what we have achieved. Within the scope of this study, we have introduced a novel numerical implementation of PSC, a method designed to quantify the inner dimension of complex multi-parameter models. Our application of this approach was focused on a branched actin system. Notably, we aimed to push the boundaries of previous analyses by concentrating on key statistical cumulants, namely mean and variance, as the primary variables of interest. This approach allowed us to circumvent the need for a comprehensive examination of the entire PDF across parameter variations to calculate the FIM. Thus, within this hypothesis we delved into the Gaussian approximation framework, emphasizing the importance of incorporating multiple observables in the analysis to maximize the quantity of information captured. We made the critical assumption that this hypothesis holds true, particularly when dealing with PDFs characterized by low skewness. The eigen-analysis of the Gaussian FIM uncovered sensitivity modes within the parameter space, with the primary modes associated with the most substantial variations in the system's behavior. Those main directions are associated to the inner dimensionnality of the system under investigation. We conducted this methodology on our branched actin system finding an inner dimension of two, whose value was substantiated by a simple analytic model.

# Discussion

We now turn our attention to the limits of our work and outline potential avenues for future improvements and research.

### Simulation setup and Gaussian FIM approach

Firstly, one could be tempted to increase the steric stiffness parameter, $K_{steric}$, in our simulations. Doing so would reduce filament overlap, thereby increasing the reliability of our results. While this would imply increase computational costs, the gains in result robustness would be substantial. Secondly, the precision of our elastic modulus measurement should be refined. A viable approach could involve conducting repeated small relaxation-compression steps to yield an averaged value over multiple measurements, ensuring a linear response and mitigating hysteresis effects. In addition, linking the model predictions to the FIM results is something that remains to be studied notably by introducing more complex propositions.

Moreover, we consider the incorporation of additional novel observables into our analysis. These observables could offer different types of information, potentially enriching our understanding of the system. As previously discussed, the orientation order is one such candidate, as explored in the Conclusion of the first part of our study. The question arises as to how many observables are truly necessary to adequately characterize our system. While one might argue for limiting observations to what is accessible in during experiments, we think there is merit in exploring the full spectrum of possibilities. Determining the optimal number of sufficient observables to provide high quality information promises to be an intriguing area for future research.

### Guidelines for the future

As we conclude our work, we propose some promising directions for further investigations related to PSC. Beyond augmenting the number of observables and refining precision, we contemplate introducing additional parameters to modulate the system's behavior. For example, assessing the impact of cross-linkers on the sensitivity modes could be a valuable endeavor. Previous research has indicated that while crosslinkers affect network stiffness, they do not qualitatively alter the stress-stiffening curve, suggesting a minor influence on the compressed space [87]. However, this idea would necessitate a comparison of manifolds embedded in parameter spaces of varying dimensions. Additionally, exploring the predictive capacity of a manifold built on compressed parameters, particularly in scenarios with a reduced dimensionality (e.g., 2 dimensions in a 5-dimensional parameter space for our case) is of particular interest at short time.

In a broader context, such research could provide valuable insights for theoreticians seeking to construct minimalist yet potent models, particularly when addressing systems with numerous potential mechanisms [135].

# Appendix

# Appendix A

# The stress adaptation of growing branched actin networks

## A.1 Force generation model

### A.1.1 Cytosim simulation parameters

Here we will review the main elements of the configuration file that setup the parameters of a simulation. $k_B T = 0.0042$ pN.$\mu$m accounts for $T \simeq 304$ K. The viscosity $\eta$ is set to 0.1 Pa.s, which is in accordance with most experimental measures: the viscosity of the cytoplasm being a few hundred times the viscosity of water ($\eta_{water} \approx 0.001$ Pa.s) [69]. The `time_step` is set to 0.0005 s.

`max_displacement` of the AFM is 0.002 per `time_step`, which means a maximum displacement of 4 $\mu$m per second, a velocity that had never been reached in our study.

The bending `rigidity` of actin $\kappa$ is set to 0.04 pN.$\mu$m, which means a persistence length $\ell_p \simeq 9.52$ $\mu$m, in accordance with literature [17]. The segmentation d$s$ is 0.03 $\mu$m, which means 10 points by fibers when they reach their maximum length.

Arp2/3 stiffness of the link was arbitrarily set to 0.5 $pN.rad^{-1}$.

For this simulation example, considering the number of frame `nb_frames`, the number of steps `nb_steps` and the `time_step`, we obtain the frame step $\tau = 0.1$ s.

```
set simul system

{
        dim = 3
        kT = 0.0042
        time_step = 0.0005
        steric = 1, 5000,
        viscosity = 0.1
        display = ( point_value=0.01; style=3; back_color=white;
        window_size=1920,1080; zoom=0.5; rotation= 0.81 -0.59 0 0;)
}

set space core
{
        shape = afm
        viscosity = 0.1
```

```
        stiff_piston = 0
        leq_piston = 0.1
        display = (color = 0x0000FF88; visible=1)
}

new core
{
        radius = 0.5
        top = 0.1
        bottom = 0
        max_displacement = 0.002
        aimed_force = 700
        attenuation = 1
}

set space base
{
    shape = cylinderZ
    display = ( color=0x0000FF44; visible=1 )
}

new base
{
        radius = 0.5
        top = 0.005
        bottom = 0
}

set fiber actin
{
        rigidity = 0.04
        drag_radius = 0.005
        segmentation = 0.03
        confine = inside, 1000, core
        lattice = 1, 0.00275
        activity = grow
        growing_speed = 1
        growing_off_speed = -0.1
        growing_force = 17.433288221999874
        min_length = 0
        max_length = 0.3
        persistent = 1
        display = (style = line; line_width = 1; color=red, dark_red)
        steric = 1, 0.005
}

new 1 actin
{
        length = 0.01
        position = 0 0 0
        orientation = 1 1 0
```

```
}

new 1 actin
{
        length = 0.01
        position = 0.25 0.25 0
        orientation = 1 1 0
}

new 1 actin
{
        length = 0.01
        position = 0.25 -0.25 0
        orientation = 1 1 0
}

new 1 actin
{
        length = 0.01
        position = -0.25 -0.25 0
        orientation = 1 1 0
}

new 1 actin
{
        length = 0.01
        position = -0.25 0.25 0
        orientation = 1 1 0
}

set hand activator
{
        binding = 1000, 0.01
        unbinding  = 0, inf
        display = (size=3; width=1; color=red, dark_red; visible=1;)
}

set hand nucleator
{
        unbinding = 0, inf
        activity = nucleate
        nucleate = 1000, actin, (length=0.0055;)
        display = (size=3; width=1; color=green; visible=1;)
}

set couple arp23
{
        hand1 = activator
        hand2 = nucleator
        diffusion = 1
        stiffness = 100
```

```
        activity = fork
        torque = 0.5, 1.23
        trans_activated = 1
        confine = surface,, base
}

run system
{
        nb_steps = 10000
        nb_frames = 50
        event = 500 , (new 1 couple arp23 (disc 0.1 at 0 0 0.001))
}
```

### A.1.2 AFM parameters and confinement stiffness

The first part of the following piece of code computes the total force applied by counting the difference in position between the point considered and the current position of the tip: `(pos.ZZ - T)`. When this difference is positive it is multiplied by $K_{confine}$ (`stiff` here) and added to the `force_`.

The second part computes the next position of the tip `top_` by comparing the target force `aimed_force_` and the previously measured one `force_`. `top_` cannot be greater than `max_displ_` and less than `leq_piston`.

```
void SpaceForcePiston::setInteraction(Vector const& pos, Mecapoint const& pe,
Meca & meca, real stiff, const real rad, const real B, const real T) const
{
#if ( DIM >= 3 )
   SpaceCylinderZ::setInteraction(pos, pe, meca, stiff, rad, B, T);
   if ( pos.ZZ > T )
    {
                force_ += stiff * ( pos.ZZ - T);
        df_dx_ -= stiff;
    }
#endif
}

//---------------------------------------------------------------------------
///    Update cylinder height
//---------------------------------------------------------------------------

void SpaceForcePiston::step()
{
    if (std::abs(df_dx_)>0 & std::abs(force_)>0) {
        real dx = (aimed_force_-force_)/(attenuation_*df_dx_);
        if (std::abs(dx)>max_displ_) {
            dx = dx * max_displ_ /std::abs(dx);
        }
        top_ += dx;
        if (top_< prop->leq_piston ) { top_ = prop->leq_piston ;}
```

```
    }

    last_force = force_;
    df_dx_ = 0;
    reset_force();
}
```

The following plot Figure A.1 accounts for the effect of $K_{confine}$ on the velocity of the system for three different stress values at infinite stall force. We conclude from this graph that for $K_{confine}$ in the range [50, 2000] Pa the behavior is rather similar, although more stable for smaller values.

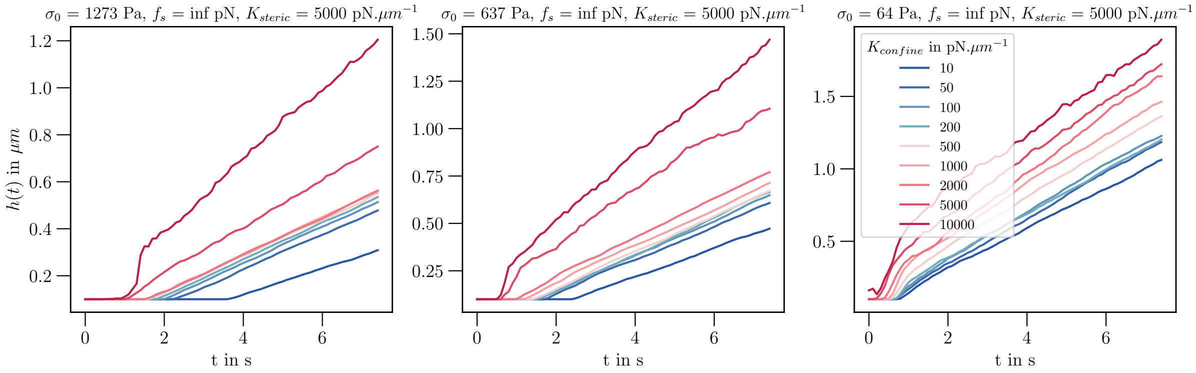

Figure A.1: Height $h(t)$ as a function of time $t$ for various confinement stiffness parameters $K_{confine}$ under three stress $\sigma_0$: 1273 Pa (Right), 636 Pa (Center) and 64 (Right). $f_s$ = inf pN, $K_{steric}$ = 5000 pN.$\mu$m$^{-1}$.

Previous plots had been done with an attenuation parameter of 1, we show in Figure A.2 that it does not have an impact on the velocity.

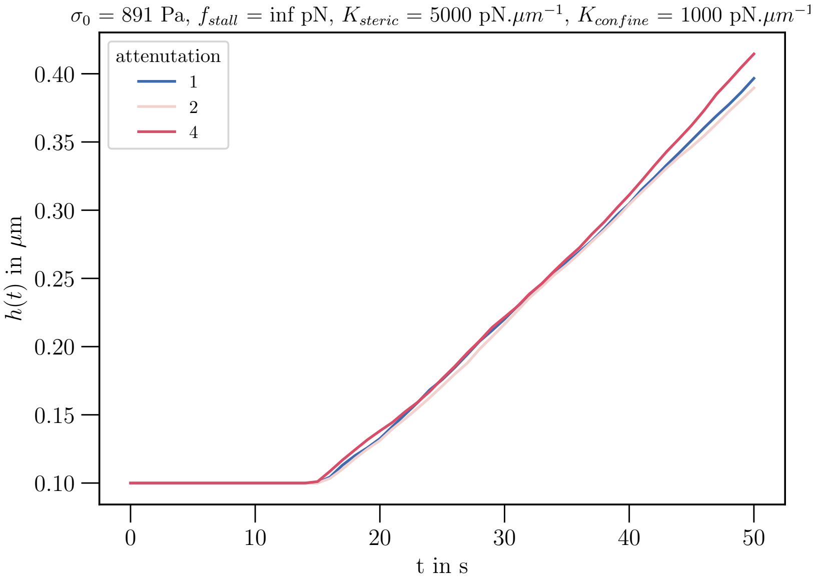

Figure A.2: Height $h(t)$ as a function of time $t$ for various attenuation parameters.

### A.1.3 Activation of Arp2/3

Arp2/3 is quickly activated in our system turning from a Free-Free (FF) state to and Activated-Activated (AA) state. The set up of a steady state takes approximately 1s, to setup the steady-state, see Figure A.3. Indeed at the beginning there are not enough fibers to bind to nucleators. On Figure A.3 (Right) we see that time to reach the plateau slightly depend on $\sigma_0$. With higher stress we reduce the transition time, as the network gets denser and we have more accessible fibers to nucleate on.

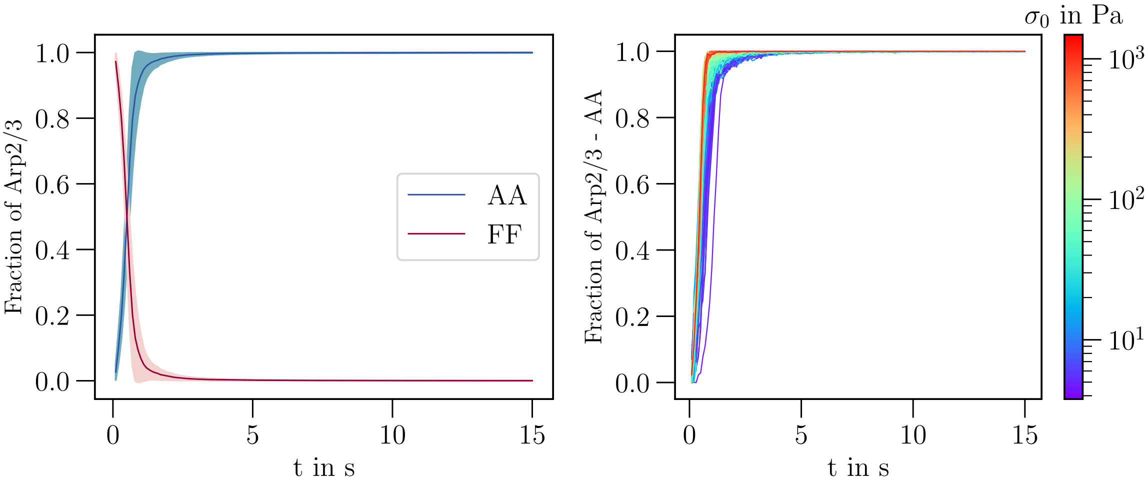

Figure A.3: (Left) Mean fraction of Arp2/3 AA (Activated-Activated) and FF (Free-Free) with respect to time, shaded part are standard deviation bounds. (Right) Detail on the AA curve for different stress values.

## A.2 Infinite stall force

### A.2.1 Estimation of velocity and density

In order to extract velocity from our position data we used a simple gradient method combined with a Savitzky-Golay filter. Basically, we define $n$ fitting intervals each centered on a data point $(x_0, y_0)$ (whenever it is possible) whose width is $2\ell + 1$. We also consider a polynomial of degree $d$, $P_d$ with $d < 2\ell + 1$. For each interval we do a regression and minimize the mean squared error to obtain the best fitting polynomial function $P_d^*$. Then we defined the smoothed value $y^* = P_d^*(x_0)$. This technique has the advantage of being less abrupt than a simple rolling average.

In Figure A.4 (Left) we plot the smoothed velocity for various $\sigma_0$ with parameters $p = 3$ and $l = 20$. Brown dotted lines delimit the fitting region to estimate the stationary velocity. For small $\sigma_0$ we can observe the slow down of the system which forces us to average for small time interval to neglect drag-induced effects. To estimate the stationary density we simply compute the average over the last frames, see Figure A.4 (Right).

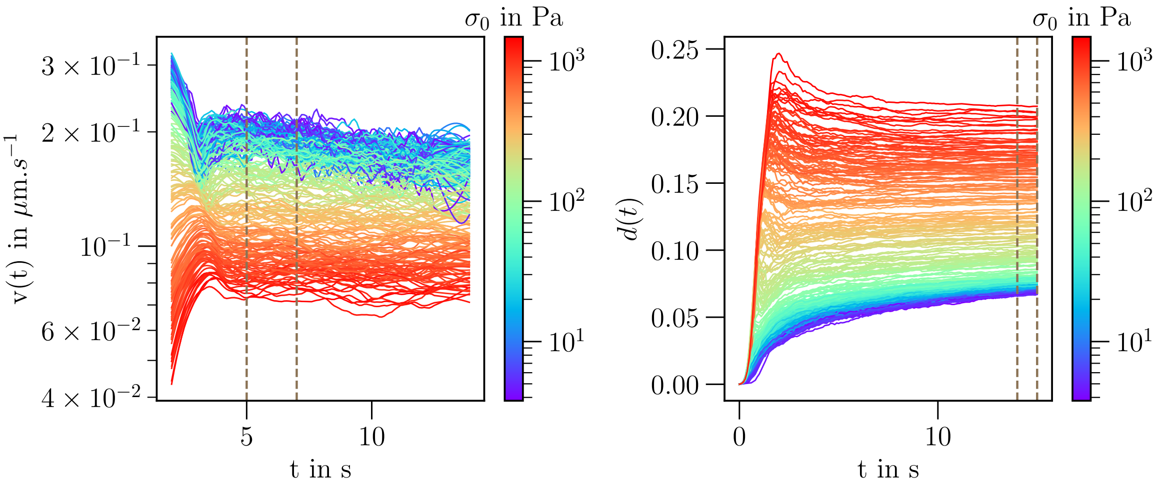

Figure A.4: (Left) Instantaneous velocity fitted with a Savitzky-Golay filter as a function of time for different stress $\sigma_0$, with $f_s = \inf$ pN. Brown dotted lines delimit the fitting region, between 5s and 7s. (Right) Brown dotted lines delimit the fitting region for the estimation of the stationary density, between 14s and 15s.

To establish the consistency of our measurements we performed a Bootstrap test on the velocity slope $\eta_{v_s}$ and on the density slope $\eta_{d_s}$. We sampled without replacement on the original fitting ensemble and obtained $N_{samples} = 300$ bootstrap ensembles and conducted the same power law fitting for each. We represent the obtained box plots on Figure A.5, for our infinite stall force simulations. Our original measurement (red cross) overlaps with the bootstrap mean (orange line).

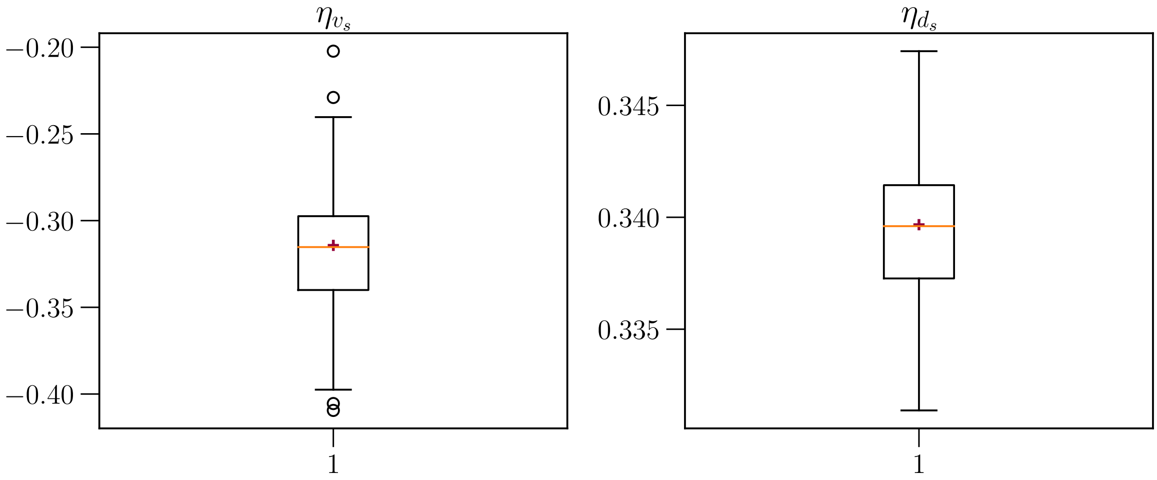

Figure A.5: Bootstrap test on the exponent for velocity $\eta_{v_s}$ on (Left) and $\eta_{d_s}$ on (Right). The test has been done for $N_{sample} = 300$ times. For each figure, the red cross is the original value while the orange line represents the bootstrap mean.

### A.2.2 Flux of actin

From Figure A.6 (Left), we see that the volume of actin doesn't depend on the applied stress for infinite stall force fibers. From the (Right) one we conclude that the mean length of fibers $\langle \ell(t) \rangle$ reaches a value near its maximum possible one independently of the stress $\sigma_0$.

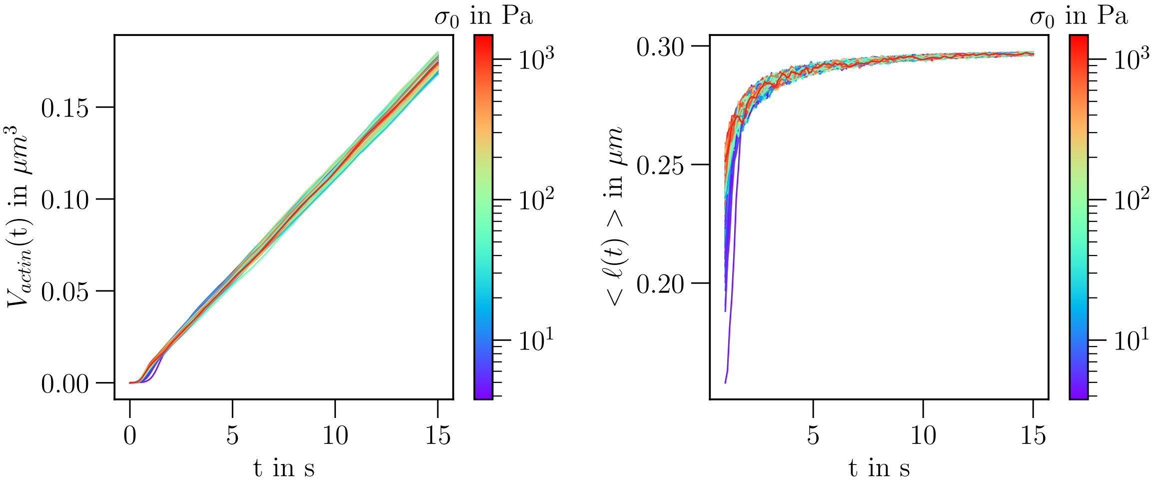

Figure A.6: Total volume of actin $V_{actin}(t)$ on (Left) and mean length of fibers $\langle \ell(t) \rangle$ (Right) as a function of time for different stress $\sigma_0$, with $f_s = \inf$ pN.

### A.2.3 Energy

#### Fibers energy

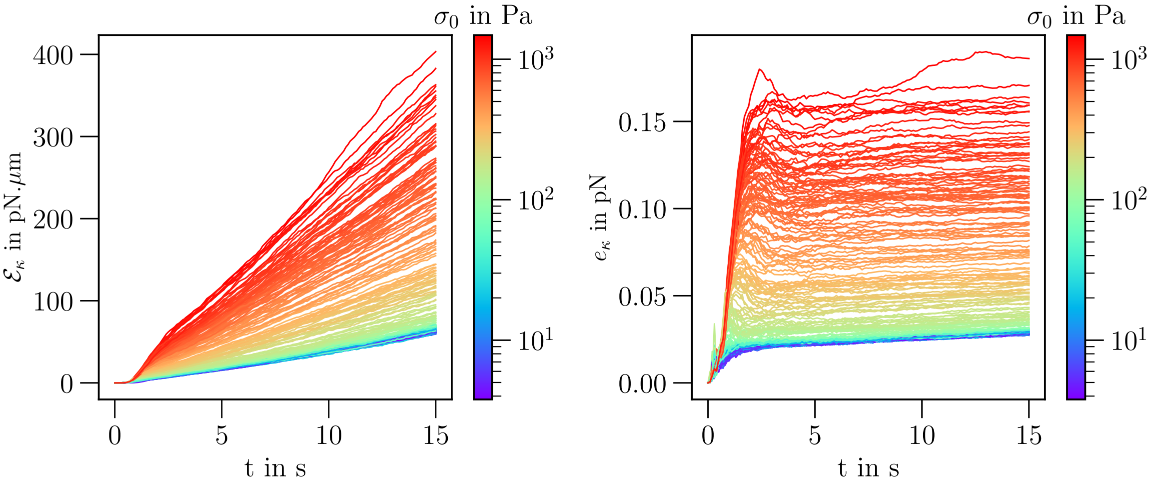

Figure A.7: (Left) Fibers bending energy as a function of time $t$ for various stress $\sigma_0$ in Pa. (Right) Fibers bending energy per fiber length, with $f_s = \inf$ pN.

Directly from data we obtain the stored elastic energy though the bending rigidity of fibers. We represent on Figure A.13 (Left) the overall elastic energy as a function of time. Notably, we see on the (Right) Figure that the energy per unit of length increases significantly with increasing $\sigma_0$, which accounts for enhanced flexion. Bending of fibers as well as entanglement might be the main source of the overall network elasticity.

**Arp2/3 energy**

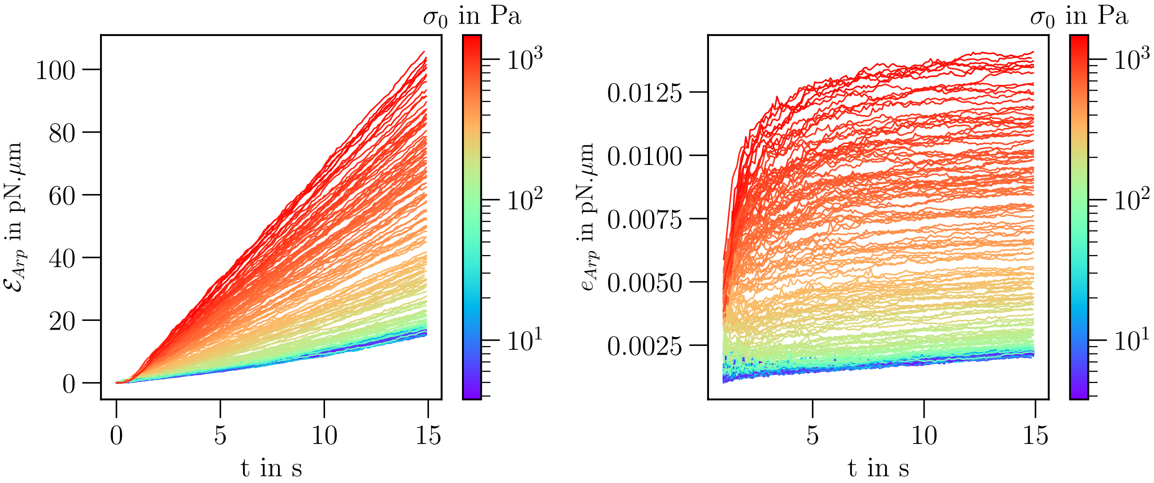

Figure A.8: (Left) Arp2/3 elastic energy as a function of time $t$ for various stress $\sigma_0$ in Pa. (Right) Arp2/3 elastic energy per Arp2/3, with $f_s$ = inf pN.

As Arp2/3 couples exhibit a finite rigidity between hands, it is possible to store elastic energy in their deformation. Similarly, we obtain the overall energy stored Figure A.8 (Left) as well as the energy per Arp2/3 which reaches an almost stationary state (Right).

## A.3 Finite stall force

### A.3.1 Velocity and density

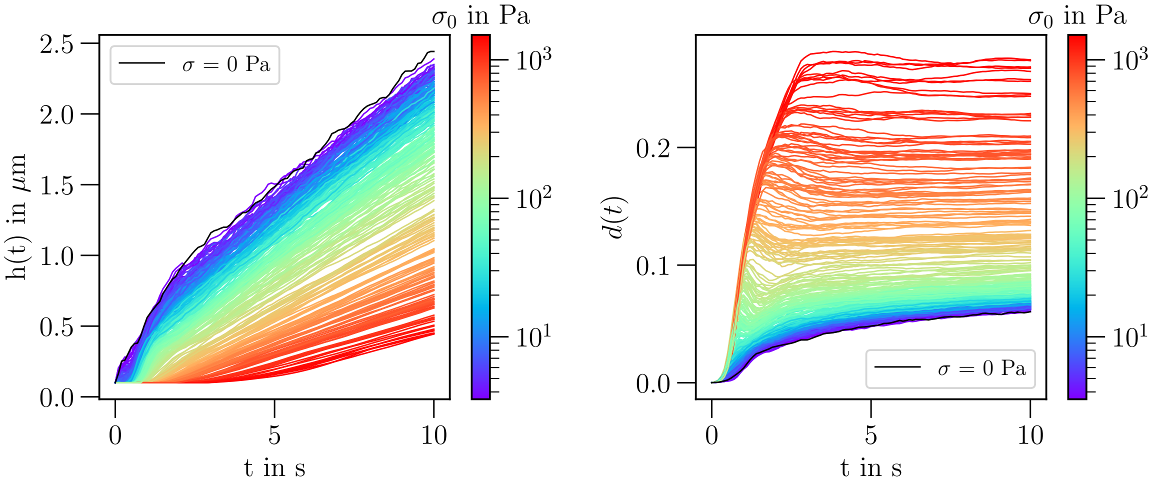

Figure A.9: Height $h(t)$ (Left) and density $d(t)$ (Right) of the network as a function of time $t$ for various stress $\sigma_0$ with $f_s$ = 3.87 pN.

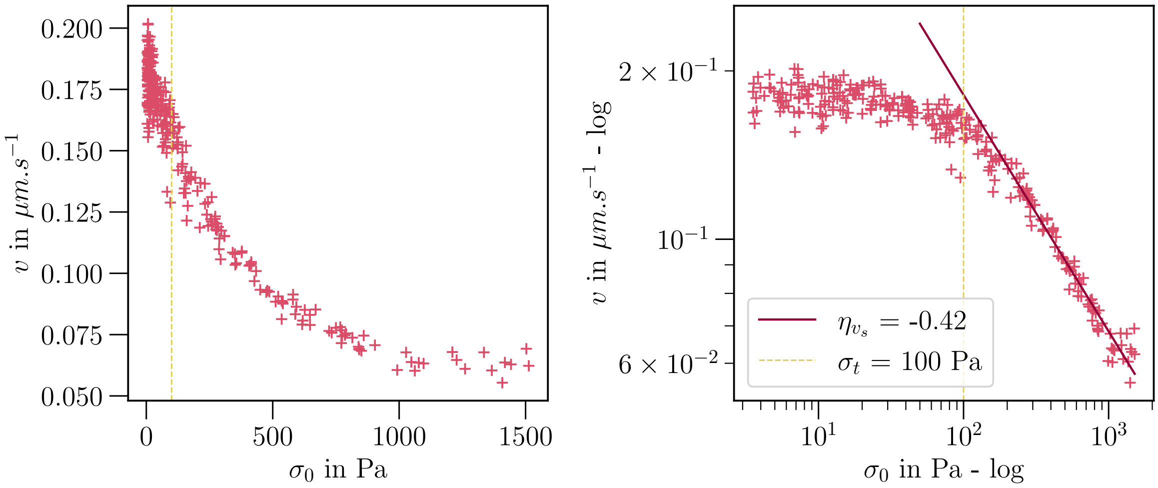

Figure A.10: Near-stationary velocity for various stress in normal (Left) and log-log scales (Right), with $f_s = 3.87$ pN. We see a power-law behavior for high stress after a constant value phase that ends around 100 Pa (yellow dotted line). The fit for the power-law scaling is represented in the log-log plot.

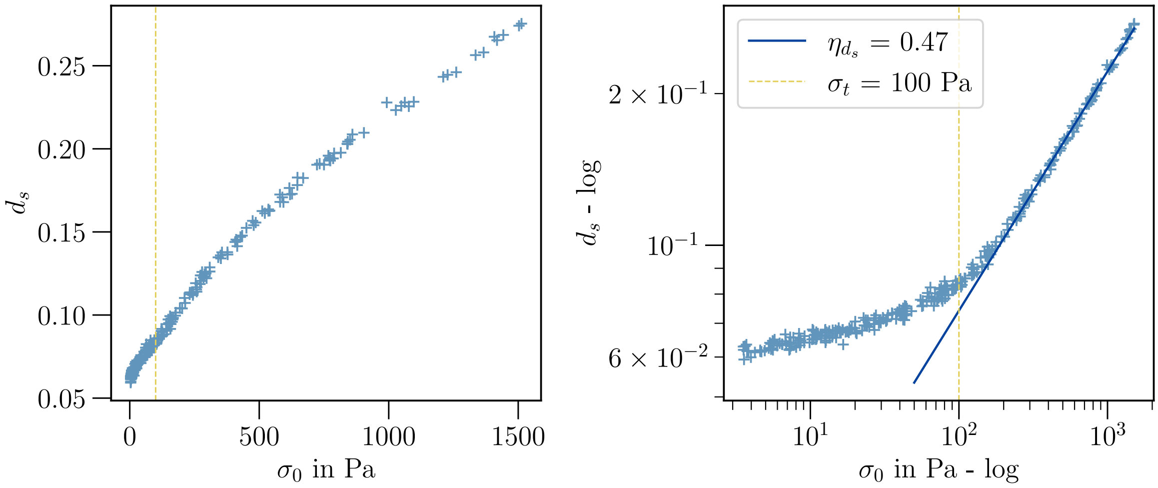

Figure A.11: Near-stationary density for various stress in normal (Left) and log-log scales (Right), with $f_s = 3.87$ pN. We see a power-law behavior for high stress after a constant value phase that ends around 100 Pa (yellow dotted line). The fit for the power-law scaling is represented in the log-log plot.

For finite stall force simulations, $f_s = 3.87$ pN, we obtain the same two phase behavior as the infinite stall force one. The entanglement threshold is shifted to higher stresses. Also, we see that the free growth ($\sigma = 0$ Pa) has a behavior close to the small $\sigma_0$ networks.

### A.3.2 Flux of actin

Here, for high stress, we observe a decrease of the flux of actin at early times before reaching the constant flux steady state, see Figure A.12. We observe the same delay for the mean length with high decrease at the beginning, before reaching a stationary value.

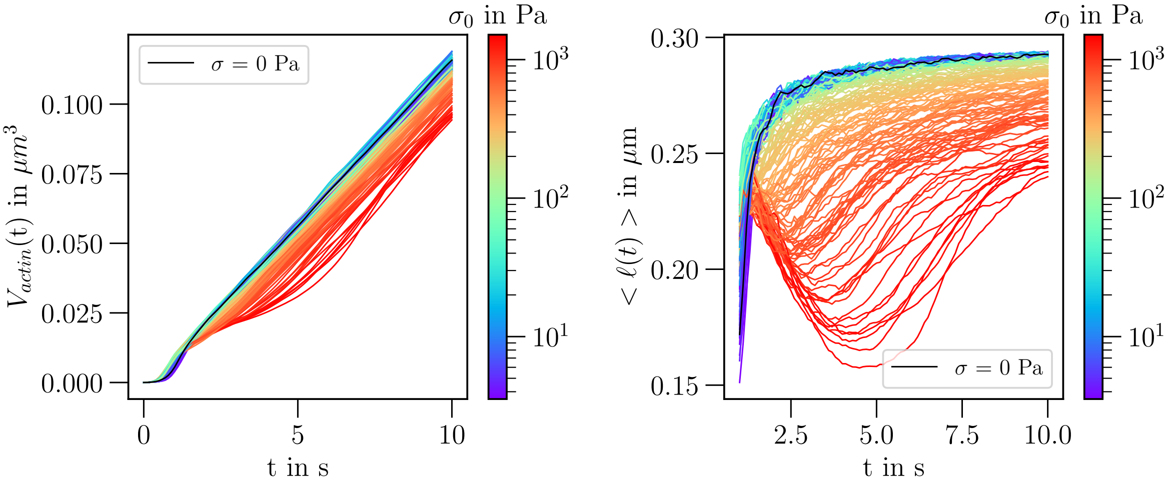

Figure A.12: Total volume of actin $V_{actin}(t)$ on (Left) and mean length of fibers $\langle \ell(t) \rangle$ (Right) as a function of time for different stress $\sigma_0$, with $f_s = 3.87$ pN.

### A.3.3 Energy

In the same way as before with infinite stall force fibers, we obtain an increase of the stored elastic energy as well as the Arp2/3 energy with increasing $\sigma_0$. Notably, free growing networks exhibit a non-vanishing elastic energy, which accounts for entanglement of the network.

#### Fibers energy

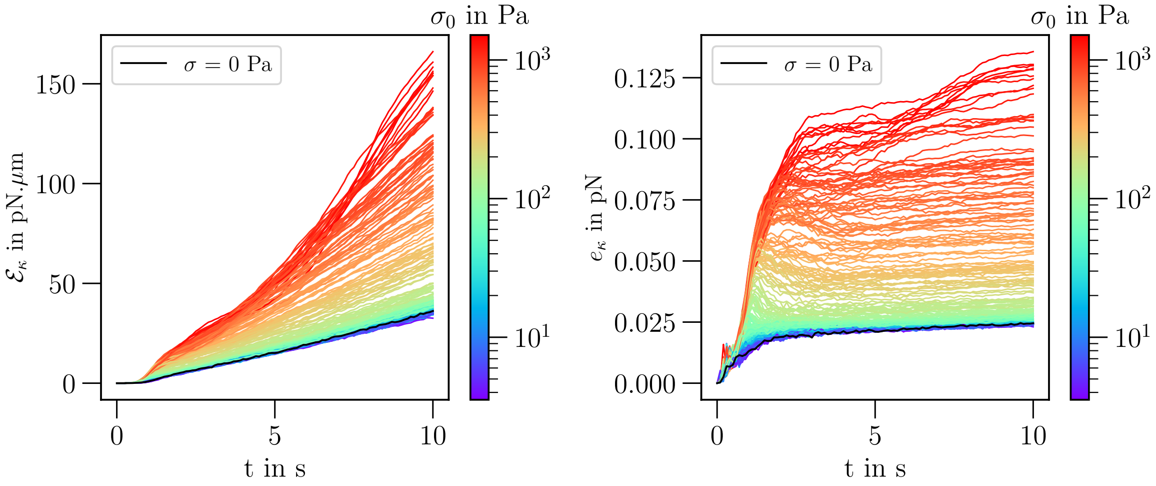

Figure A.13: Fibers bending energy as a function of time $t$ for various stress $\sigma_0$ in Pa on (Left). Fibers bending energy per fiber length on (Right), with $f_s = 3.87$ pN.

**Arp2/3 energy**

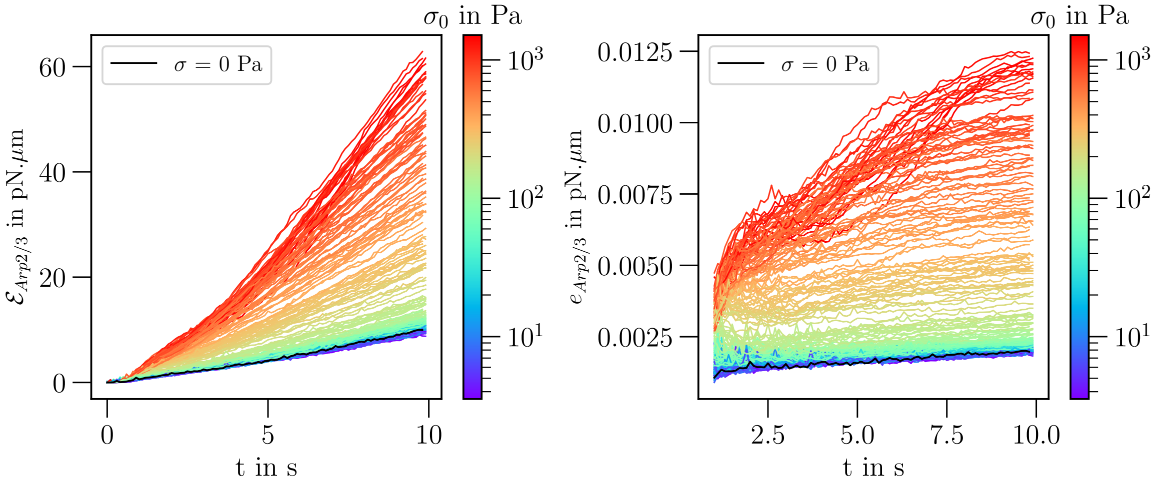

Figure A.14: Arp2/3 elastic energy as a function of time $t$ for various stress $\sigma_0$ in Pa on (Left). Arp2/3 elastic energy per Arp2/3 on (Right), with $f_s = 3.87$ pN.

## A.4 Stall force transition

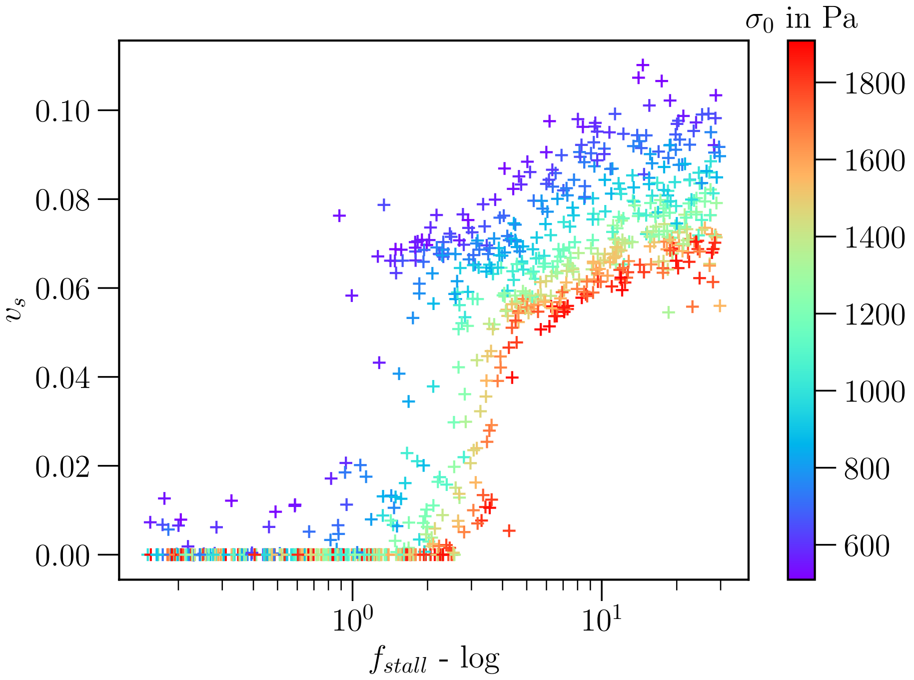

Figure A.15: Velocity vs stall force for different stress values at the stall force transition.

## A.5 Free growth

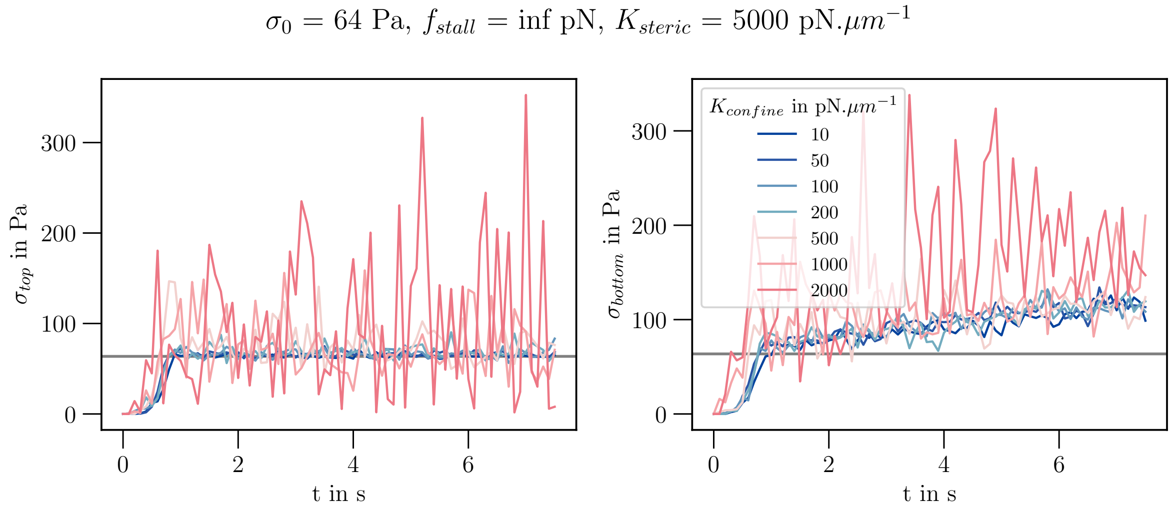

Figure A.16: Stress measured by penetration length computation for top $\sigma_{top}$(Left) and bottom $\sigma_{bottom}$ (Right) as a function of time $t$ for various $K_{confine}$, with: $\sigma_0 = 64$ Pa, $f_s =$ inf pN and $K_{confine} = 5000$ pN.$\mu m^{-1}$

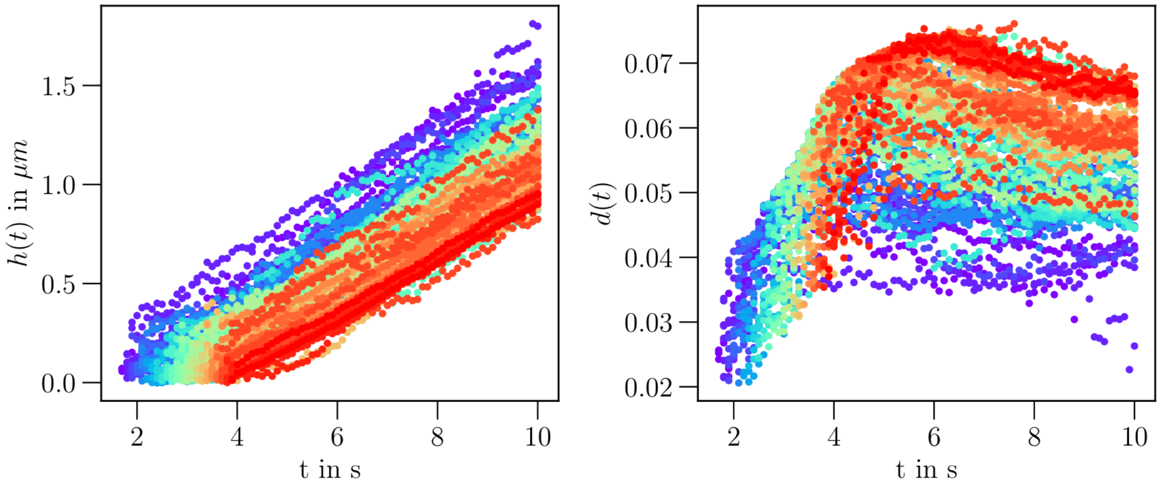

Figure A.17: Evolution of slices with height $h(t)$ (Left) and density $d(t)$ on (Right) as a function of time $t$. The color code represents the appearance time. For each point the density is calculated inside the slice centered on the point position and with a height $\delta z = 0.2$ $\mu$m. Here, $f_s =$ inf pN and $k_{Arp2/3} = 675$ $\mu$m$^{-2}$.s$^{-1}$

# Appendix B

# An example of parameter space compression on branched actin

## B.1 Quadratic form of the KL-divergence

Here we define the KL-divergence, and show how the Fisher information naturally appears when dealing with close PDF.

$$D_{KL}(P||Q) = \sum_x P(x) \log \left( \frac{P(x}{Q(x)} \right) \tag{B.1}$$

Thus,

$$\begin{aligned} D_{KL}(P_\theta||P_{\theta+\delta\theta}) &= \sum_x P_\theta(x) \log \left( \frac{P_\theta(x)}{P_{\theta+\delta\theta}(x)} \right) \\ &= \sum_x P_\theta(x) \log \left( \frac{P_\theta(x)}{P_\theta(x) + \delta\theta^\mu \partial_{\theta_\mu} P_\theta(x) + \delta\theta^\mu \delta\theta^\nu \partial_{\theta_\mu\theta_\nu} P_\theta(x) + O(\delta\theta^3)} \right) \\ &= -\sum_x P_\theta(x) \log \left( 1 + \frac{\delta\theta^\mu \partial_{\theta_\mu} P_\theta(x) + \delta\theta^\mu \delta\theta^\nu \partial_{\theta_\mu\theta_\nu} P_\theta(x) + O(\delta\theta^3)}{P_\theta(x)} \right) \end{aligned} \tag{B.2}$$

Then, as $P_\theta(x)$ is defined upon the maximum likelihood estimator:

$$\partial_{\theta_\mu} P_\theta(x) = 0 \tag{B.3}$$

Then,

$$\begin{aligned} D_{KL}(P_\theta||P_{\theta+\delta\theta}) &= -\sum_x P_\theta(x) \log \left( 1 + \frac{\delta\theta^\mu \delta\theta^\nu \partial_{\theta_\mu\theta_\nu} P_\theta(x) + O(\delta\theta^3)}{P_\theta(x)} \right) \\ &= -\sum_x \delta\theta^\mu \delta\theta^\nu \partial_{\theta_\mu\theta_\nu} P_\theta(x) + O(\delta\theta^3) \\ &= -\delta\theta^\mu \delta\theta^\nu \sum_x \partial_{\theta_\mu\theta_\nu} P_\theta(x) + O(\delta\theta^3) \\ &= g_{\mu\nu} \delta\theta^\mu \delta\theta^\nu + O(\delta\theta^3) \end{aligned} \tag{B.4}$$

But we have:

$$\begin{aligned}\partial_{\theta_\mu\theta_\nu}\log P_\theta(x) &= \partial_{\theta_\mu}\left(\frac{\partial_{\theta_\nu}P_\theta(x)}{P_\theta(x)}\right)\\ &= \frac{P_\theta(x)\partial_{\theta_\mu\theta_\nu}P_\theta(x)-\partial_{\theta_\mu}P_\theta(x)\partial_{\theta_\nu}P_\theta(x)}{P_\theta(x)^2}\\ &= \frac{\partial_{\theta_\mu\theta_\nu}P_\theta(x)}{P_\theta(x)}\end{aligned} \tag{B.5}$$

Which means:

$$\partial_{\theta_\mu\theta_\nu}P_\theta(x) = P_\theta(x)\partial_{\theta_\mu\theta_\nu}\log P_\theta(x) \tag{B.6}$$

Hence, the KL-divergence becomes:

$$\begin{aligned}D_{KL}(P_\theta||P_{\theta+\delta\theta}) &= -\delta\theta^\mu\delta\theta^\nu\sum_x P_\theta(x)\partial_{\theta_\mu\theta_\nu}\log P_\theta(x)+O(\delta\theta^3)\\ &= -\delta\theta^\mu\delta\theta^\nu\left\langle\partial_{\theta_\mu\theta_\nu}\log P_\theta(x)\right\rangle+O(\delta\theta^3)\end{aligned} \tag{B.7}$$

Finally, we obtain:

$$\boxed{D_{KL}(P_\theta||P_{\theta+\delta\theta}) = -\delta\theta^\mu\delta\theta^\nu g_{\mu\nu}+O(\delta\theta^3)} \tag{B.8}$$

## B.2 Results

### B.2.1 Example of a configuration file

```
set simul system
{
        dim = 3
        kT = 0.0042
        time_step = 0.0005
        steric = 1, 5000,
        viscosity = 0.1
        display = ( point_value=0.01; style=3; back_color=white;
        window_size=1920,1080; zoom=0.5; rotation= 0.81 -0.59 0 0;)
}

set space core
{
        shape = piston
        viscosity = 5000
        stiff_piston = 0
        leq_piston = 0.5
        display = (color = 0x0000FF88; visible=1)
}

new core
{
        radius = 0.5
        top = 0.1
        bottom = 0
}

set space base
{
    shape = cylinderZ
    display = ( color=0x0000FF44; visible=1 )
}

new base
{
        radius = 0.5
        top = 0.005
        bottom = 0
}

set fiber actin
{
        rigidity = 0.04
        drag_radius = 0.005
        segmentation = 0.01
        confine = inside, 100, core
        lattice = 1, 0.00275
        activity = grow
```

```
        growing_speed = 1
        growing_off_speed = 0
        growing_force = inf
        min_length = 0.01
        max_length = 0.3
        persistent = 1

}

new 1 actin
{
        length = 0.01
        position = 0 0 0
        orientation = 1 1 0
}

new 1 actin
{
        length = 0.01
        position = 0.25 0.25 0
        orientation = 1 1 0
}


new 1 actin
{
        length = 0.01
        position = 0.25 -0.25 0
        orientation = 1 1 0
}

new 1 actin
{
        length = 0.01
        position = -0.25 -0.25 0
        orientation = 1 1 0
}

new 1 actin
{
        length = 0.01
        position = -0.25 0.25 0
        orientation = 1 1 0
}

set hand activator
{
        binding = 1000, 0.01
        unbinding  = 0, inf
        display = (size=3; width=1; color=red, dark_red; visible=1;)
```

```
}

set hand nucleator
{
        unbinding = 0, inf
        activity = nucleate
        nucleate = 1000, actin, (length=0.0055;)
        display = (size=3; width=1; color=green; visible=1;)

}

set couple arp23
{
        hand1 = activator
        hand2 = nucleator
        diffusion = 1
        stiffness = 100
        activity = fork
        torque = 0.5, 1.23
        trans_activated = 1
        confine = surface,, base

}

new 1 arp23

run system
{
        nb_steps = 7500
        nb_frames = 75
        event = 500 , (new 1 couple arp23 (disc 0.1 at 0 0 0.001))
}

change core {viscosity = infinity;}

run system
{
        nb_steps = 5000
        nb_frames = 50
}

change core {viscosity = 5000;}

run system
{
        nb_steps = 2500
        nb_frames = 25
}

change core {viscosity = infinity;}
```

```
run system
{
        nb_steps = 5000
        nb_frames = 50
}
```

### B.2.2 Drag of the network and stored elastic energy

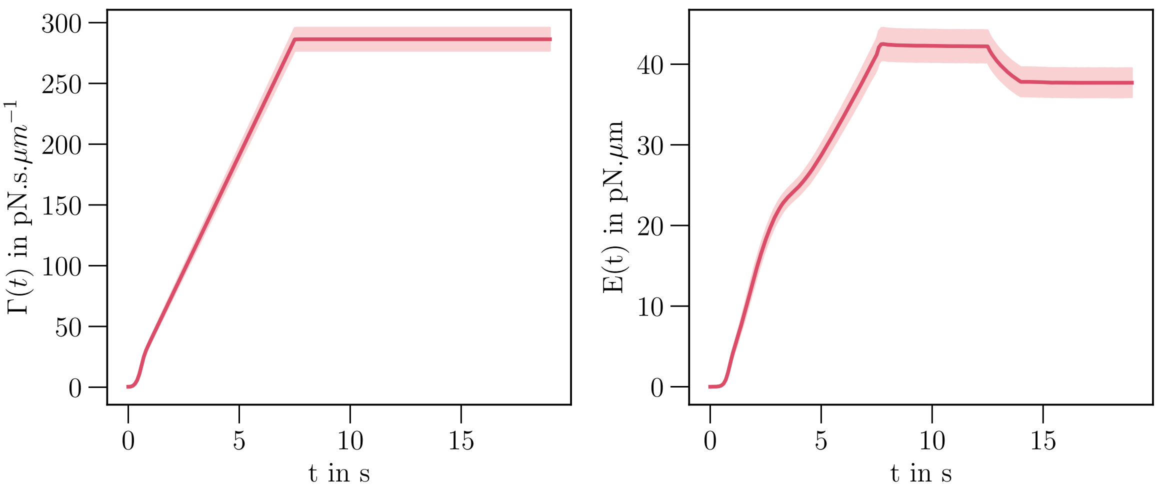

Figure B.1: (Left) Drag of the network Γ(t) in pN.s.$\mu$m$^{-1}$ and elastic energy E(t) in pN.$\mu$m (Right) as a function of time. The thick line is the mean value obtained over 300 simulations with small $k_{Arp2/3}$ variation. The shaded area delimits the standard deviation.

### B.2.3 Local slopes of the observables and bootstrap test

#### Bending rigidity - $\kappa$

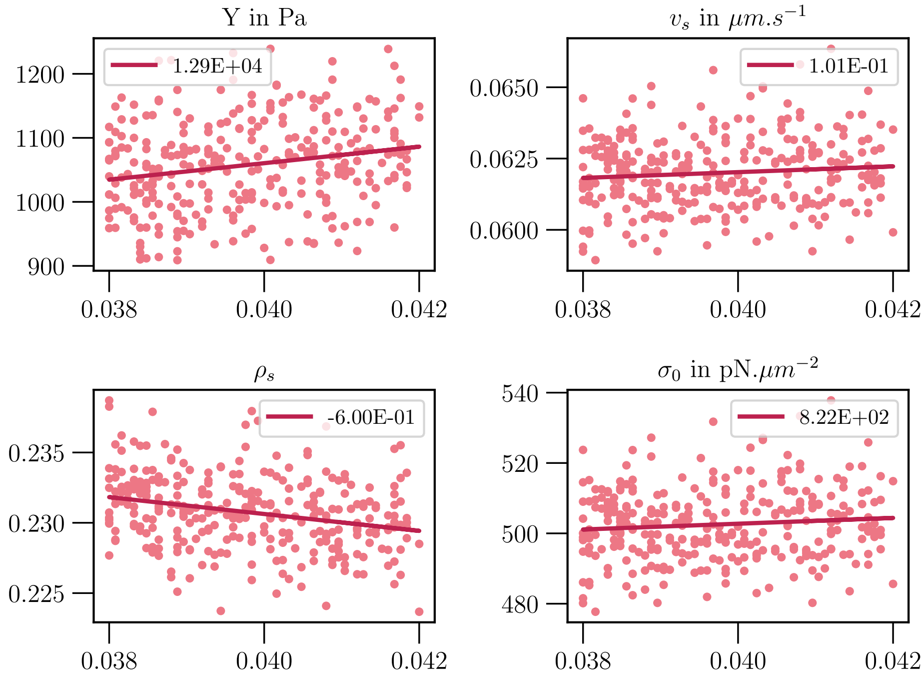

Figure B.2: Scatters plots of observables values as a function of $\kappa$ in pN.$\mu^2$. The thick line is obtained through a local linear fit which provides the slope.

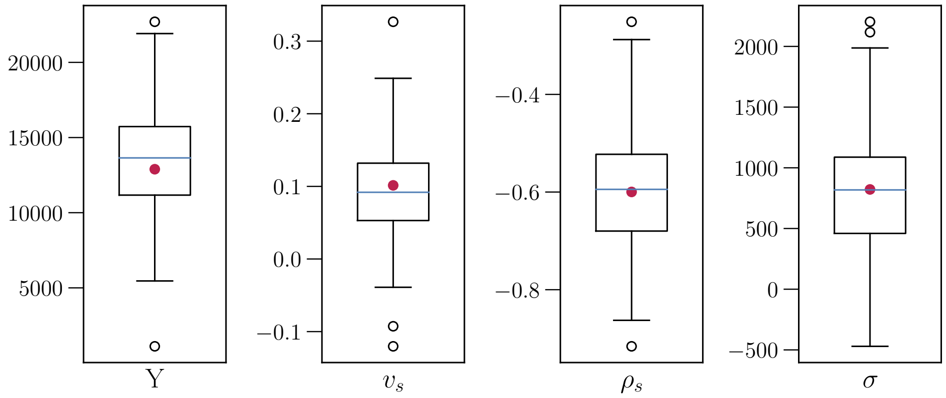

Figure B.3: Bootstrap test on the different slopes estimation for the $\kappa$ parameter. The red dot is the original value.

### Drag - $\gamma_0$

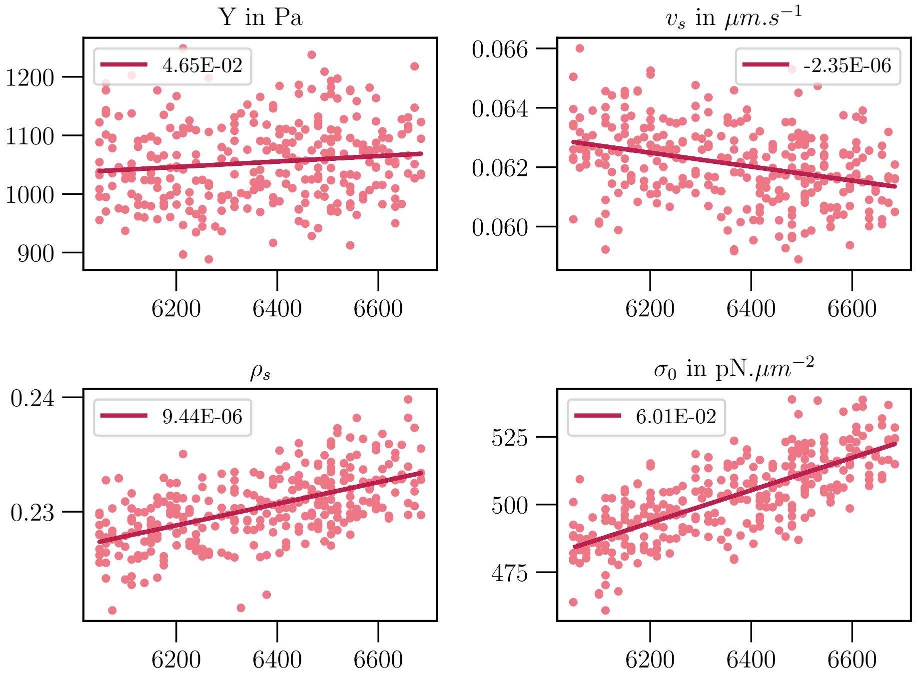

Figure B.4: Scatters plots of observables values as a function of $\gamma_0/S$ in pN.s.$\mu$m$^{-3}$. The thick line is obtained through a local linear fit which provides the slope.

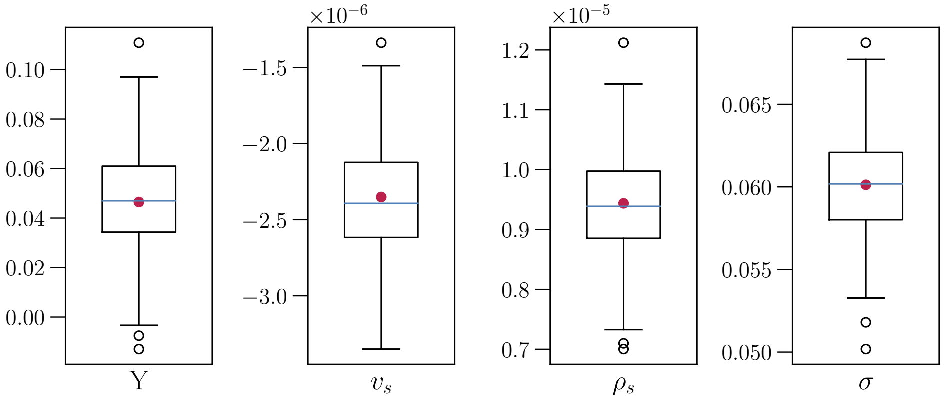

Figure B.5: Bootstrap test on the different slopes estimation for the $\gamma_0$ parameter. The red dot is the original value.

### Fiber radius - $r_0$

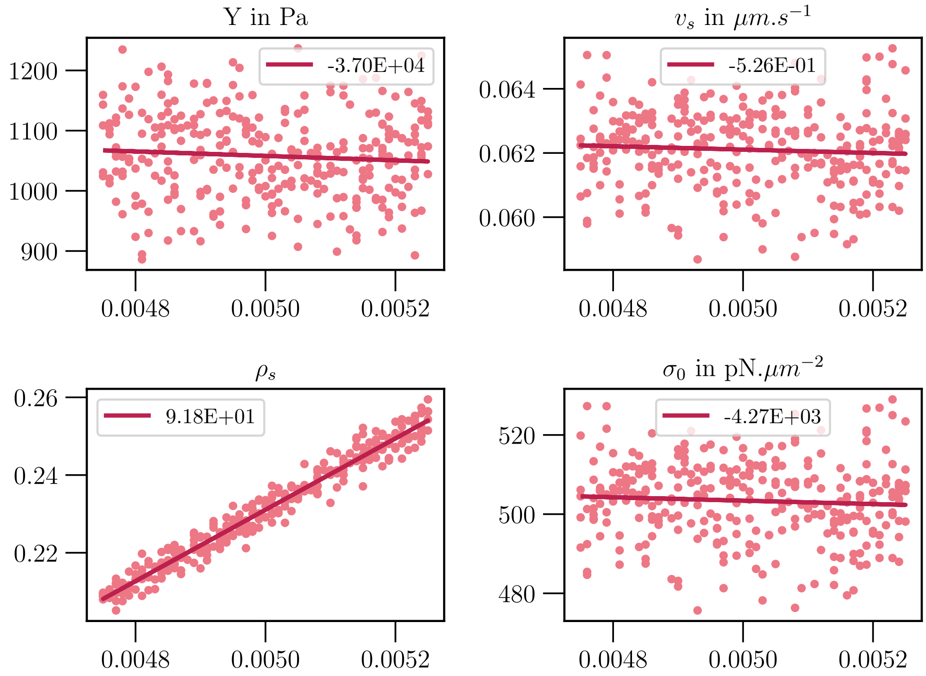

Figure B.6: Scatters plots of observables values as a function of $r_0$ in $\mu$m. The thick line is obtained through a local linear fit which provides the slope.

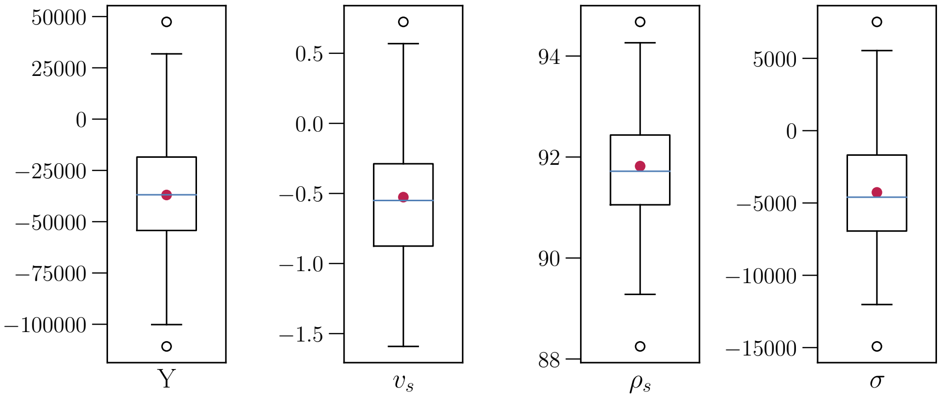

Figure B.7: Bootstrap test on the different slopes estimation for the $r_0$ parameter. The red dot is the original value.

### Fiber length - $\ell_0$

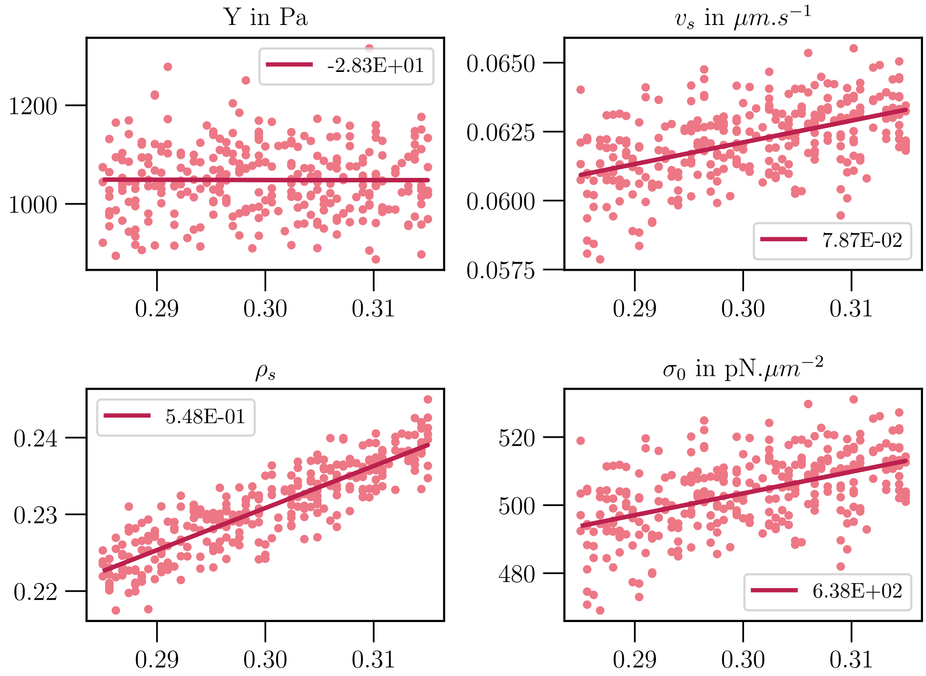

Figure B.8: Scatters plots of observables values as a function of $\ell_0$ in $\mu$m. The thick line is obtained through a local linear fit which provides the slope.

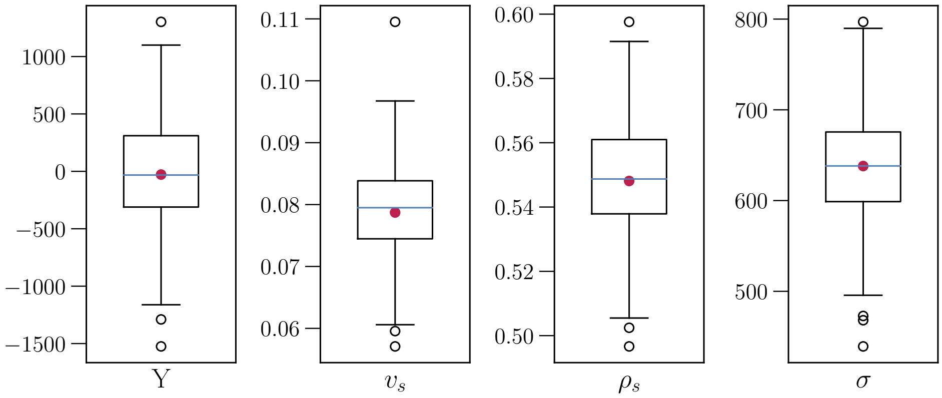

Figure B.9: Bootstrap test on the different slopes estimation for the $\ell_0$ parameter. The red dot is the original value.

# Bibliography

[1] Erwin Schrödinger. *What is Life? The Physical Aspect of the Living Cell.* Cambridge University Press, 1944.

[2] Ilya Prigogine. Time, Structure, and Fluctuations. *Science*, 201(4358):777–785, 1978.

[3] A M Turing. The chemical basis of morphogenesis. *Philosophical Transactions of the Royal Society of London. Series B, Biological Sciences*, 237(641):37–72, 1952.

[4] E M Purcell. Life at low Reynolds number. *American Journal of Physics*, 45(1):3–11, 1 1977.

[5] Laurent Blanchoin, Rajaa Boujemaa-paterski, Cécile Sykes, and Julie Plastino. Actin Dynamics, Archi-tecture, and Mechanics in Cell Motility. *Physiological Reviews*, 94(1):235–263, 2014.

[6] P W Anderson. More Is Different. *Science*, 177(4047):393–396, 1972.

[7] Michael Murrell, Patrick W. Oakes, Martin Lenz, and Margaret L. Gardel. Forcing cells into shape: The mechanics of actomyosin contractility. *Nature Reviews Molecular Cell Biology*, 16(8):486–498, 2015.

[8] Jasper Weinberg and David G. Drubin. Clathrin-mediated endocytosis in budding yeast. *Trends in Cell Biology*, 22(1):1–13, 2012.

[9] J. Victor Small, Monika Herzog, and Kurt Anderson. Actin filament organization in the fish keratocyte lamellipodium. *Journal of Cell Biology*, 129(5):1275–1286, 1995.

[10] Pascale Cossart and Christine Kocks. The actin-based motility of the facultative intracellular pathogen Listeria monocytogenes. *Molecular Microbiology*, 13(3):395–402, 8 1994.

[11] Alexander Mogilner and George Oster. Cell motility driven by actin polymerization. *Biophysical Journal*, 71(6):3030–3045, 1996.

[12] T. L. Hill. Microfilament or microtubule assembly or disassembly against a force. *Proceedings of the National Academy of Sciences of the United States of America*, 78(9 II):5613–5617, 1981.

[13] C. S. Peskin, G. M. Odell, and G. F. Oster. Cellular motions and thermal fluctuations: the Brownian ratchet. *Biophysical Journal*, 65(1):316–324, 1993.

[14] Matthew J. Footer, Jacob W.J. J Kerssemakers, Julie A. Theriot, and Marileen Dogterom. Direct measurement of force generation by actin filament polymerization using an optical trap. *Proceedings of the National Academy of Sciences of the United States of America*, 104(7):2181–2186, 2007.

[15] C. P. Broedersz and F. C. MacKintosh. Modeling semiflexible polymer networks. *Reviews of Modern Physics*, 86(3):995–1036, 7 2014.

[16] Arshad Desai and Timothy J. Mitchison. Microtubule polymerization dynamics. *Annual Review of Cell and Developmental Biology*, 13:83–117, 1997.

[17] F. Gittes, B. Mickey, J. Nettleton, and J. Howard. Flexural rigidity of microtubules and actin filaments measured from thermal fluctuations in shape. *Journal of Cell Biology*, 120(4):923–934, 2 1993.

[18] Nobutaka Hirokawa. Kinesin and Dynein Superfamily Proteins and the Mechanism of Organelle Transport. *Science*, 279(5350):519–526, 1 1998.

[19] Claire E. Walczak and Rebecca Heald. Mechanisms of Mitotic Spindle Assembly and Function. *International Review of Cytology*, 265(07):111–158, 2008.

[20] Hirokazu Tanimoto, Akatsuki Kimura, and Nicolas Minc. Shape-motion relationships of centering microtubule asters. *Journal of Cell Biology*, 212(7):777–787, 2016.

[21] Sandrine Etienne-Manneville. Cytoplasmic Intermediate Filaments in Cell Biology. *Annual Review of Cell and Developmental Biology*, 34(July):1–28, 2018.

[22] Kenneth C. Holmes, David Popp, Werner Gebhard, and Wolfgang Kabsch. Atomic model of the actin filament, 1990.

[23] W Kabsch, H G Mannherz, D Suck, E F Pai, and K C Holmes. Atomic structure of actin:DNase I complex, 1990.

[24] L. R. Otterbein, P. Graceffa, and R. Dominguez. The crystal structure of uncomplexed actin in the ADR state. *Science*, 293(5530):708–711, 2001.

[25] C. Frieden. Polymerization of actin: Mechanism of the Mg2+-induced process at pH 8 and 20°C. *Proceedings of the National Academy of Sciences of the United States of America*, 80(21 I):6513–6517, 1983.

[26] Balázs Gaszner, Miklós Nyitrai, Nóra Hartvig, Tamás Köszegi, Béla Somogyi, and József Belágyi. Replacement of ATP with ADP affects the dynamic and conformational properties of actin monomer. *Biochemistry*, 38(39):12885–12892, 1999.

[27] Takashi Fujii, Atsuko H. Iwane, Toshio Yanagida, and Keiichi Namba. Direct visualization of secondary structures of F-actin by electron cryomicroscopy. *Nature*, 467(7316):724–728, 2010.

[28] A. Ott, M. Magnasco, A. Simon, and A. Libchaber. Measurement of the persistence length of polymerized actin using fluorescence microscopy. *Physical Review E*, 48(3):R1642–R1645, 9 1993.

[29] H. Higuchi, T. Yanagida, and Y.E. Goldman. Compliance of thin filaments in skinned fibers of rabbit skeletal muscle. *Biophysical Journal*, 69(3):1000–1010, 9 1995.

[30] Pekka Lappalainen, Tommi Kotila, Antoine Jégou, and Guillaume Romet-Lemonne. Biochemical and mechanical regulation of actin dynamics, 12 2022.

[31] Thomas D. Pollard and John A. Cooper. Actin, a central player in cell shape and movement. *Science*, 326(5957):1208–1212, 2009.

[32] Isabelle Sagot, Saskia K. Klee, and David Pellman. Yeast formins regulate cell polarity by controlling the assembly of actin cables. *Nature Cell Biology*, 4(1):42–50, 2002.

[33] David Pruyne, Marie Evangelista, Changsong Yang, Erfei Bi, Sally Zigmond, Anthony Bretscher, and Charles Boone. Role of formins in actin assembly: Nucleation and barbed-end association. *Science*, 297(5581):612–615, 2002.

[34] François Ferron, Grzegorz Rebowski, Sung Haeng Lee, and Roberto Dominguez. Structural basis for the recruitment of profilin-actin complexes during filament elongation by Ena/VASP. *EMBO Journal*, 26(21):4597–4606, 2007.

[35] R. Dyche Mullins, John A. Heuser, and Thomas D. Pollard. The interaction of Arp2/3 complex with actin: Nucleation, high affinity pointed end capping, and formation of branching networks of filaments. *Proceedings of the National Academy of Sciences of the United States of America*, 95(11):6181–6186, 1998.

[36] Isabelle Rouiller, Xiao Ping Xu, Kurt J Amann, Coumaran Egile, Stephan Nickell, Daniela Nicastro, Rong Li, Thomas D Pollard, Niels Volkmann, and Dorit Hanein. The structural basis of actin filament branching by the Arp2/3 complex. *Journal of Cell Biology*, 180(5):887–895, 2008.

[37] Laura M. Machesky and Robert H. Insall. Scar1 and the related Wiskott-Aldrich syndrome protein, WASP, regulate the actin cytoskeleton through the Arp2/3 complex. *Current Biology*, 8(25):1347–1356, 1998.

[38] Peter Bieling, Scott D Hansen, Orkun Akin, Tai-De Li, Carl C Hayden, Daniel A Fletcher, and R Dyche Mullins. WH2 and proline-rich domains of WASP-family proteins collaborate to accelerate actin filament elongation. *The EMBO Journal*, 37(1):102–121, 2018.

[39] Thomas D. Pollard and John A. Cooper. Quantitative Analysis of the Effect of Acanthamoeba Profilin on Actin Filament Nucleation and Elongation. *Biochemistry*, 23(26):6631–6641, 1984.

[40] Marc Edwards, Adam Zwolak, Dorothy A. Schafer, David Sept, Roberto Dominguez, and John A. Cooper. Capping protein regulators fine-tune actin assembly dynamics. *Nature Reviews Molecular Cell Biology*, 15(10):677–689, 10 2014.

[41] Johanna Funk, Felipe Merino, Matthias Schaks, Klemens Rottner, Stefan Raunser, and Peter Bieling. A barbed end interference mechanism reveals how capping protein promotes nucleation in branched actin networks. *Nature Communications*, 12(1), 2021.

[42] Tai-De Li, Peter Bieling, Julian Weichsel, R. Dyche Mullins, and Daniel A. Fletcher. The molecular mechanism of load adaptation by branched actin networks. *eLife*, 11, 6 2022.

[43] Hugo Wioland, Berengere Guichard, Yosuke Senju, Sarah Myram, Pekka Lappalainen, Antoine Jégou, and Guillaume Romet-Lemonne. ADF/Cofilin Accelerates Actin Dynamics by Severing Filaments and Promoting Their Depolymerization at Both Ends. *Current Biology*, 27(13):1956–1967, 2017.

[44] Hugo Wioland, Antoine Jegou, and Guillaume Romet-Lemonne. Torsional stress generated by ADF/cofilin on cross-linked actin filaments boosts their severing. *Proceedings of the National Academy of Sciences of the United States of America*, 116(7):2595–2602, 2019.

[45] Paul Matsudaira. Actin crosslinking proteins at the leading edge, 1994.

[46] Thomas D. Pollard. Actin and actin-binding proteins. *Cold Spring Harbor Perspectives in Biology*, 8(8):1–18, 2016.

[47] D. H. Wachsstock, W. H. Schwartz, and T. D. Pollard. Affinity of alpha-actinin for actin determines the structure and mechanical properties of actin filament gels. *Biophysical Journal*, 65(1):205–214, 7 1993.

[48] Jingyuan Xu, Denis Wirtz, and Thomas D. Pollard. Dynamic cross-linking by $\alpha$-actinin determines the mechanical properties of actin filament networks. *Journal of Biological Chemistry*, 273(16):9570–9576, 1998.

[49] Poul M. Bendix, Gijsje H. Koenderink, Damien Cuvelier, Zvonimir Dogic, Bernard N. Koeleman, William M. Brieher, Christine M. Field, L. Mahadevan, and David A. Weitz. A quantitative analysis of contractility in active cytoskeletal protein networks. *Biophysical Journal*, 94(8):3126–3136, 2008.

[50] Sven K. Vogel, Zdenek Petrasek, Fabian Heinemann, and Petra Schwille. Myosin motors fragment and compact membrane-bound actin filaments. *eLife*, 2013(2):1–18, 2013.

[51] Tatyana M. Svitkina, Elena A. Bulanova, Oleg Y. Chaga, Danijela M. Vignjevic, Shin ichiro Kojima, Jury M. Vasiliev, and Gary G. Borisy. Mechanism of filopodia initiation by reorganization of a dendritic network. *Journal of Cell Biology*, 160(3):409–421, 2003.

[52] Alexander Mogilner and B. Rubinstein. The physics of filopodial protrusion. *Biophysical Journal*, 89(2):782–795, 2005.

[53] Jan Mueller, Gregory Szep, Maria Nemethova, Ingrid de Vries, Arnon D. Lieber, Christoph Winkler, Karsten Kruse, J. Victor Small, Christian Schmeiser, Kinneret Keren, Robert Hauschild, and Michael Sixt. Load Adaptation of Lamellipodial Actin Networks. *Cell*, 171(1):188–200, 9 2017.

[54] Guillaume Salbreux, Guillaume Charras, and Ewa Paluch. Actin cortex mechanics and cellular morphogenesis. *Trends in Cell Biology*, 22(10):536–545, 2012.

[55] Martin P. Stewart, Jonne Helenius, Yusuke Toyoda, Subramanian P. Ramanathan, Daniel J. Muller, and Anthony A. Hyman. Hydrostatic pressure and the actomyosin cortex drive mitotic cell rounding. *Nature*, 469(7329):226–231, 2011.

[56] Tatyana M. Svitkina, Alexander B. Verkhovsky, Kyle M. McQuade, and Gary G. Borisy. Analysis of the actin-myosin II system in fish epidermal keratocytes: Mechanism of cell body translocation. *Journal of Cell Biology*, 139(2):397–415, 1997.

[57] Sari Tojkander, Gergana Gateva, and Pekka Lappalainen. Actin stress fibers - Assembly, dynamics and biological roles. *Journal of Cell Science*, 125(8):1855–1864, 2012.

[58] Amsha Proag, Anaïs Bouissou, Thomas Mangeat, Raphaël Voituriez, Patrick Delobelle, Christophe Thibault, Christophe Vieu, Isabelle Maridonneau-Parini, and Renaud Poincloux. Working together: Spatial synchrony in the force and actin dynamics of podosome first neighbors. *ACS Nano*, 9(4):3800–3813, 2015.

[59] Marion Jasnin, Jordan Hervy, Stéphanie Balor, Anaïs Bouissou, Amsha Proag, Raphaël Voituriez, Jonathan Schneider, Thomas Mangeat, Isabelle Maridonneau-Parini, Wolfgang Baumeister, Serge Dmitrieff, and Renaud Poincloux. Elasticity of podosome actin networks produces nanonewton protrusive forces. *Nature Communications*, 13(1):3842, 7 2022.

[60] Stefan Linder. The matrix corroded: podosomes and invadopodia in extracellular matrix degradation. *Trends in Cell Biology*, 17(3):107–117, 2007.

[61] Margaret L. Gardel, Karen E. Kasza, Clifford P. Brangwynne, Jiayu Liu, and David A. Weitz. Mechanical Response of Cytoskeletal Networks. *Methods in Cell Biology*, (08):487–519, 2008.

[62] Enrique M. De La Cruz and Margaret L. Gardel. Actin mechanics and fragmentation. *Journal of Biological Chemistry*, 290(28):17137–17144, 2015.

[63] Enrique M. De La Cruz, Jeremy Roland, Brannon R. McCullough, Laurent Blanchoin, and Jean-Louis Martiel. Origin of Twist-Bend Coupling in Actin Filaments. *Biophysical Journal*, 99(6):1852–1860, 9 2010.

[64] L.D Landau and E.M Lifshitz. *Theory of Elasticity.* Pergamon Press, Oxford., 1986.

[65] M. L. Gardel, J. H. Shin, F. C. MacKintosh, L. Mahadevan, P. A. Matsudaira, and D. A. Weitz. Scaling of F-actin network rheology to probe single filament elasticity and dynamics. *Physical Review Letters*, 93(18):1–4, 2004.

[66] Gabor Forgacs, Ramsey A. Foty, Yinon Shafrir, and Malcolm S. Steinberg. Viscoelastic properties of living embryonic tissues: A quantitative study. *Biophysical Journal*, 74(5):2227–2234, 1998.

[67] K. Venkatesan Iyer, Romina Piscitello-Gómez, Joris Paijmans, Frank Jülicher, and Suzanne Eaton. Epithelial Viscoelasticity Is Regulated by Mechanosensitive E-cadherin Turnover. *Current Biology*, 29(4):578–591, 2019.

[68] Jing Xie, Javad Najafi, Rémi Le Borgne, Jean Marc Verbavatz, Catherine Durieu, Jeremy Sallé, and Nicolas Minc. Contribution of cytoplasm viscoelastic properties to mitotic spindle positioning. *Proceedings of the National Academy of Sciences of the United States of America*, 119(8), 2022.

[69] Javad Najafi, Serge Dmitrieff, and Nicolas Minc. Size- and position-dependent cytoplasm viscoelasticity through hydrodynamic interactions with the cell surface. *Proceedings of the National Academy of Sciences*, 120(9):2017, 2 2023.

[70] J. Liu, M. L. Gardel, K. Kroy, E. Frey, B. D. Hoffman, J. C. Crocker, A. R. Bausch, and D. A. Weitz. Microrheology probes length scale dependent rheology. *Physical Review Letters*, 96(11):1–4, 2006.

[71] Tobias T. Falzone, Martin Lenz, David R. Kovar, and Margaret L. Gardel. Assembly kinetics determine the architecture of $\alpha$-actinin crosslinked F-actin networks. *Nature Communications*, 3(May), 2012.

[72] G. H. Koenderink, M. Atakhorrami, F. C. MacKintosh, and C. F. Schmidt. High-frequency stress relaxation in semiflexible polymer solutions and networks. *Physical Review Letters*, 96(13):1–4, 2006.

[73] F. Gittes and F. C. MacKintosh. Dynamic shear modulus of a semiflexible polymer network. *Physical Review E - Statistical Physics, Plasmas, Fluids, and Related Interdisciplinary Topics*, 58(2):1241–1244, 1998.

[74] F. C. MacKintosh, J. Käs, and P. A. Janmey. Elasticity of Semiflexible Biopolymer Networks. *Physical Review Letters*, 75(24):4425–4428, 12 1995.

[75] M. L. Gardel, J. H. Shin, F. C. MacKintosh, L. Mahadevan, P. Matsudaira, and D. A. Weitz. Elastic behavior of cross-linked and bundled actin networks. *Science*, 304(5675):1301–1305, 5 2004.

[76] J. Liu, G. H. Koenderink, K. E. Kasza, F. C. MacKintosh, and D. A. Weitz. Visualizing the strain field in semiflexible polymer networks: Strain fluctuations and nonlinear rheology of F-actin gels. *Physical Review Letters*, 98(19):1–4, 2007.

[77] M. Tempel, G. Isenberg, and E. Sackmann. Temperature-induced sol-gel transition and microgel formation in $\alpha$-actinin cross-linked actin networks: A rheological study. *Physical Review E - Statistical Physics, Plasmas, Fluids, and Related Interdisciplinary Topics*, 54(2):1802–1810, 8 1996.

[78] Astrid Weins, Peter Kenlan, Stephanie Herbert, Tu C. Le, Ivan Villegas, Bernard S. Kaplan, Gerald B. Appel, and Martin R. Pollak. Mutational and biological analysis of $\alpha$-actinin-4 in focal segmental glomerulosclerosis. *Journal of the American Society of Nephrology*, 16(12):3694–3701, 12 2005.

[79] B. Wagner, R. Tharmann, I. Haase, M. Fischer, and A. R. Bausch. Cytoskeletal polymer networks: The molecular structure of cross-linkers determines macroscopic properties. *Proceedings of the National Academy of Sciences of the United States of America*, 103(38):13974–13978, 9 2006.

[80] M. L. Gardel, F. Nakamura, J. H. Hartwig, J. C. Crocker, T. P. Stossel, and D. A. Weitz. Prestressed F-actin networks cross-linked by hinged filamins replicate mechanical properties of cells. *Proceedings of the National Academy of Sciences of the United States of America*, 103(6):1762–1767, 2006.

[81] Rajat Rohatgi, Le Ma, Hiroaki Miki, Marco Lopez, Tomas Kirchhausen, Tadaomi Takenawa, and Marc W Kirschner. The Interaction between N-WASP and the Arp2/3 Complex Links Cdc42-Dependent Signals to Actin Assembly. *Cell*, 97(2):221–231, 4 1999.

[82] Thomas P. Loisel, Rajaa Boujemaa, Dominique Pantaloni, and Marie France Cartier. Reconstitution of actin-based motility of Listeria and Shigella using pure proteins. *Nature*, 401(6753):613–616, 1999.

[83] Yann Marcy, Jacques Prost, Marie-France Carlier, Cé Cile Sykes, and Cé Cile Sykes. Forces generated during actin-based propulsion: A direct measurement by micromanipulation, 2004.

[84] Sapun H Parekh, Ovijit Chaudhuri, Julie A Theriot, and Daniel A Fletcher. Loading history determines the velocity of actin-network growth. *Nature Cell Biology*, 7(12):1119–1123, 2005.

[85] Lisa A. Cameron, Matthew J. Footer, Alexander van Oudenaarden, and Julie A. Theriot. Motility of ActA protein-coated microspheres driven by actin polymerization. *Proceedings of the National Academy of Sciences*, 96(9):4908–4913, 4 1999.

[86] Ovijit Chaudhuri, Sapun H Parekh, and Daniel A Fletcher. Reversible stress softening of actin networks. *Nature*, 445(7125):295–298, 2007.

[87] Peter Bieling, Tai-de Li, Julian Weichsel, Bo Huang, Daniel A Fletcher, R Dyche Mullins, Peter Bieling, Tai-de Li, Julian Weichsel, Ryan Mcgorty, Pamela Jreij, Bo Huang, and Daniel A Fletcher. Force Feedback Controls Motor Activity and Mechanical Properties of Self-Assembling Branched Actin Networks Article Force Feedback Controls Motor Activity and Mechanical Properties of Self-Assembling Branched Actin Networks. *Cell*, 164(1-2):115–127, 2016.

[88] Thomas Pujol, Olivia Du Roure, Marc Fermigier, and Julien Heuvingh. Impact of branching on the elasticity of actin networks. *Proceedings of the National Academy of Sciences of the United States of America*, 109(26):10364–10369, 2012.

[89] Pierre Bauër, Joseph Tavacoli, Thomas Pujol, Jessica Planade, Julien Heuvingh, Olivia Du Roure, and Olivia Du Roure. A new method to measure mechanics and dynamic assembly of branched actin networks. *Scientific Reports*, 7(1):1–11, 12 2017.

[90] Jessica Planade, Reda Belbahri, Micaela Boiero Sanders, Audrey Guillotin, Olivia du Roure, Alphée Michelot, and Julien Heuvingh. Mechanical stiffness of reconstituted actin patches correlates tightly with endocytosis efficiency. *PLOS Biology*, 17(10):e3000500, 10 2019.

[91] T D Pollard. Rate constants for the reactions of ATP- and ADP-actin with the ends of actin filaments. *The Journal of cell biology*, 103(6):2747–2754, 12 1986.

[92] Juliet Lee, Michelle Leonard, Tim Oliver, Akira Ishihara, and Ken Jacobson. Traction forces generated by locomoting keratocytes. *Journal of Cell Biology*, 127(6 II):1957–1964, 1994.

[93] Marileen Dogterom and Bernard Yurke. Measurement of the force-velocity relation for growing microtubules. *Science*, 278(5339):856–860, 1997.

[94] Serge Dmitrieff and François Nédélec. Membrane Mechanics of Endocytosis in Cells with Turgor. *PLoS Computational Biology*, 11(10):1–15, 2015.

[95] Kostas Tsekouras, David Lacoste, Kirone Mallick, and Jean François Joanny. Condensation of actin filaments pushing against a barrier. *New Journal of Physics*, 13, 2011.

[96] Coraline Brangbour, Olivia du Roure, Emmanuèle Helfer, Damien Démoulin, Alexis Mazurier, Marc Fermigier, Marie France Carlier, Jérôme Bibette, and Jean Baudry. Force-velocity measurements of a few growing actin filaments. *PLoS Biology*, 9(4), 4 2011.

[97] Alexander Mogilner and George Oster. The polymerization ratchet model explains the force-velocity relation for growing microtubules. *European Biophysics Journal*, 28(3):235–242, 3 1999.

[98] G. Sander van Doorn, Cătălin Tănase, Bela M. Mulder, and Marileen Dogterom. On the stall force for growing microtubules. *European Biophysics Journal*, 29(1):2–6, 3 2000.

[99] J. Krawczyk and J. Kierfeld. Stall force of polymerizing microtubules and filament bundles. *EPL (Europhysics Letters)*, 93(2):28006, 1 2011.

[100] Sebastian Wiesner, Emmanuele Helfer, Dominique Didry, Guylaine Ducouret, Françoise Lafuma, Marie France Carlier, and Dominique Pantaloni. A biomimetic motility assay provides insight into the mechanism of actin-based motility. *Journal of Cell Biology*, 160(3):387–398, 2003.

[101] James L. McGrath, Narat J. Eungdamrong, Charles I. Fisher, Fay Peng, Lakshminarayanan Mahadevan, Timothy J. Mitchison, and Scot C. Kuo. The force-velocity relationship for the actin-based motility of Listeria monocytogenes. *Current Biology*, 13(4):329–332, 2003.

[102] Fabien Gerbal, Paul Chaikin, Yitzhak Rabin, and Jacques Prost. An elastic analysis of Listeria monocytogenes propulsion. *Biophysical Journal*, 79(5):2259–2275, 2000.

[103] A. E. Carlsson. Growth velocities of branched actin networks. *Biophysical Journal*, 84(5):2907–2918, 5 2003.

[104] Alex Mogilner and George Oster. Force generation by actin polymerization II: The elastic ratchet and tethered filaments. *Biophysical Journal*, 84(3):1591–1605, 2003.

[105] Kun Chun Lee and Andrea J. Liu. Force-velocity relation for actin-polymerization-driven motility from Brownian dynamics simulations. *Biophysical Journal*, 97(5):1295–1304, 9 2009.

[106] J. Clerk Maxwell. On the calculation of the equilibrium and stiffness of frames. *The London, Edinburgh, and Dublin Philosophical Magazine and Journal of Science*, 27(182):294–299, 4 1864.

[107] C. M. van Wyk. Note on the compressibility of wool. *Journal of the Textile Institute Transactions*, 37(12):T285–T292, 12 1946.

[108] Francois Nedelec and Dietrich Foethke. Collective Langevin dynamics of flexible cytoskeletal fibers. *New Journal of Physics*, 9, 2007.

[109] Julio Belmonte, Maria Leptin, and François Nédélec. A theory that predicts behaviors of disordered cytoskeletal networks.

[110] Gaëlle Letort, Antonio Z. Politi, Hajer Ennomani, Manuel Théry, Francois Nedelec, and Laurent Blanchoin. Geometrical and Mechanical Properties Control Actin Filament Organization. *PLoS Computational Biology*, 11(5):e1004245, 5 2015.

[111] Wenli Zhang. Experimental and Computational Analysis of Random Cylinder Packings With Applications. (December):162, 2006.

[112] Maria M. Tirado and José García De La Torre. Translational friction coefficients of rigid, symmetric top macromolecules. Application to circular cylinders. *The Journal of Chemical Physics*, 71(6):2581–2587, 1979.

[113] Ehssan Nazockdast, Abtin Rahimian, Denis Zorin, and Michael Shelley. A fast platform for simulating semi-flexible fiber suspensions applied to cell mechanics. *Journal of Computational Physics*, 329:173–209, 2017.

[114] Ehssan Nazockdast, Abtin Rahimian, Daniel Needleman, and Michael Shelley. Cytoplasmic flows as signatures for the mechanics of mitotic positioning. *Molecular Biology of the Cell*, 28(23):3261–3270, 2017.

[115] Ryan N. Gutenkunst, Joshua J. Waterfall, Fergal P. Casey, Kevin S. Brown, Christopher R. Myers, and James P. Sethna. Universally Sloppy Parameter Sensitivities in Systems Biology Models. *PLoS Computational Biology*, 3(10):e189, 10 2007.

[116] Serena Bradde and William Bialek. PCA meets RG. pages 1–8, 10 2016.

[117] S Vajda, P Valko, and T Turanyi. Principal Component Analysis of Kinetic Models. *International Journal of Chemical Kinetics*, 17:55–81, 1985.

[118] J Chem Phys, Mark K. Transtrum, Benjamin B. Machta, Kevin S. Brown, Christopher R. Myers, James P. Sethna, Bryan C. Daniels, Christopher R. Myers, and James P. Sethna. Perspective: Sloppiness and emergent theories in physics, biology, and beyond. *Journal of Chemical Physics*, 143(1), 7 2015.

[119] Thomas J Rademaker and Paul Franc. Article Untangling the Hairball : Fitness-Based Asymptotic Reduction of Biological Networks. pages 1893–1906, 2017.

[120] Bryan C. Daniels and Ilya Nemenman. Automated adaptive inference of phenomenological dynamical models. *Nature Communications*, 6(1):8133, 8 2015.

[121] Benjamin B. Machta, Ricky Chachra, Mark K. Transtrum, and James P. Sethna. Parameter space compression underlies emergent theories and predictive models. *Science*, 342(6158):604–607, 2013.

[122] Jürgen Mayer, Khaled Khairy, and Jonathon Howard. Drawing an elephant with four complex parameters. *American Journal of Physics*, 78(6):648–649, 6 2010.

[123] R. A. Fisher. On the mathematical foundations of theoretical statistics. *Philosophical Transactions of the Royal Society of London. Series A, Containing Papers of a Mathematical or Physical Character*, 222(594-604):309–368, 1 1922.

[124] Luigi Malagò and Giovanni Pistone. Information geometry of the Gaussian distribution in view of stochastic optimization. *FOGA 2015 - Proceedings of the 2015 ACM Conference on Foundations of Genetic Algorithms XIII*, pages 150–162, 2015.

[125] A. Klein and H. Neudecker. A direct derivation of the exact Fisher information matrix of Gaussian vector state space models. *Linear Algebra and Its Applications*, 321(1-3):233–238, 2000.

[126] Chieh-ting Jimmy Ting (Jimmy) Hsu, Gary J. Brouhard, Paul Franc, and Paul François. Numerical Parameter Space Compression and Its Application to Biophysical Models. *Biophysical Journal*, 118(6):1455–1465, 3 2020.

[127] Tim Mitchison and Marc Kirschner. Dynamic instability of microtubule growth. *Nature*, 312(5991):237–242, 11 1984.

[128] Y. D. Chen and T. L. Hill. Monte Carlo study of the GTP cap in a five-start helix model of a microtubule. *Proceedings of the National Academy of Sciences of the United States of America*, 82(4):1131–1135, 1985.

[129] Pavel Zakharov, Nikita Gudimchuk, Vladimir Voevodin, Alexander Tikhonravov, Fazoil I. Ataullakhanov, and Ekaterina L. Grishchuk. Molecular and Mechanical Causes of Microtubule Catastrophe and Aging. *Biophysical Journal*, 109(12):2574–2591, 2015.

[130] Vincent VanBuren, David J. Odde, and Lynne Cassimeris. Estimates of lateral and longitudinal bond energies within the microtubule lattice. *Proceedings of the National Academy of Sciences of the United States of America*, 99(9):6035–6040, 2002.

[131] Brian T. Castle and David J. Odde. Brownian dynamics of subunit addition-loss kinetics and thermodynamics in linear polymer self-assembly. *Biophysical Journal*, 105(11):2528–2540, 2013.

[132] Daniel T. Gillespie. Exact stochastic simulation of coupled chemical reactions. *Journal of Physical Chemistry*, 81(25):2340–2361, 1977.

[133] Sami Chaaban, Shashank Jariwala, Chieh Ting Hsu, Stefanie Redemann, Justin M. Kollman, Thomas Müller-Reichert, David Sept, Khanh Huy Bui, and Gary J. Brouhard. The Structure and Dynamics of C. elegans Tubulin Reveals the Mechanistic Basis of Microtubule Growth. *Developmental Cell*, 47(2):191–204, 2018.

[134] S. Prasad and N.C. Menicucci. Fisher Information With Respect to Cumulants. *IEEE Transactions on Information Theory*, 50(4):638–642, 4 2004.

[135] Philippe Bun, Serge Dmitrieff, Julio M Belmonte, Franç Ois, J Né Dé Lec, and J Né Dé Lec. A disassembly-driven mechanism explains F-actin-mediated chromosome transport in starfish oocytes.

# Contents